Understanding Carbon-Biomolecule Interactions for the Rational Design of Carbon-Based Biomaterials

A thesis presented to the University of Dublin, Trinity College for the degree of Doctor of Philosophy in Chemistry

by

Joana Marta Vasconcelos



Prof. Paula E. Colavita

School of Chemistry & CRANN

Trinity College Dublin

2018

Declaration

I declare that the work in this thesis it has not been submitted as an exercise for a degree at this or any other University and it is entirely my own work. Due acknowledgements and references are given to others were appropriate.

I agree that the TCD Library may lend or copy the thesis upon request, subject to the Irish Copyright Legislation.

Joana M. C. Vasconcelos,

January 2018

_____

Acknowledgements

First and foremost, I would like to thank my PhD supervisor Paula E. Colavita for her support and patience over the last 4 years. Without your encouragement, guidance and friendship the completion of this thesis would not have been possible. Truly, thank you!

I would also like to thank Jorge Carvalho Silva for the fantastic three months collaboration at the GREAT laboratory, I will definitely miss my cells and platelets. Acknowledgements also go to Michael Beckett and Maria Santos Martinez for their collaboration in my PhD project.

I have greatly enjoyed my time in Trinity College Dublin and this is in no small part due to the people I have met here; your friendships have been very much appreciated. I would like to thank the present and past members of ColavitaBestFriends: Fede, Ronan, Stefi, Michelle, Suoyuan, Daniela, Dee, James, Adam, Carlota, Khairul, Serban, Guido, Dil, Leti, Paraic and all the visiting researchers for making this journey a thoroughly enjoyable experience. Particularly, James and Adam thanks for the English corrections and the burritos, both were extremely needed for the last three months. I would also like to thank Stefano, Harrisson, Farzana, Rob, Raquel and Aurelie for their kind friendship over the last 4 years.

The Department of Chemistry is fortunate to have many talented students, professors and technical staff, from whom I have learned during my PhD research. There are some technical staff who have helped me tremendously throughout my PhD and need to be mentioned: Anne Marie, Teresa, Tess, Helen, Patsy, Maura, Fred and Manuel thank you very much for your support. I am also very grateful to Prof. John Boland for the access to AFM instrumentation and Dr. Shaun Mills for his precious assistance. I would also like to express my gratitude to Gavin McManus and Dermot Daly for their support in microscopy measurements.

My gratitude goes to Fede and Ronan, the first two people that I have met in Dublin and the best friends someone can ask for; your support and friendship made me believe that I could do something else than cleaning. I would also like to thank Dani for being there for me when nothing seems to work in the laboratory life. My Mitchy, our therapeutic evenings and numerous counselling wine sessions were the highlight of my PhD. Thank you so much for all the support, friendship and Shebbies (I think I should thank for that too)! You were there

dealing with all my accomplishments and failures and I will always be thankful for that. My favourite Italian turtle, Stefania Mazzarati! Words are not enough to describe our friendship and probably no one would understand our SteJo dialect anyway. I am truly happy that you are still alive, after 300 non-sense trips; I cannot thank you enough for being part of my PhD expedition, even if almost 2000 km away. My favourite Portuguese person in Dublin, and most likely the only one that I know, this acknowledgement is for you João Coelho. The Portuguese power in Dublin made me believe I could do this, and what better example than my favourite unicorn?

In Dublin, it is hard to find the perfect flatmate but not impossible and Maria Aline you are the proof of it! Could not ask for anyone else to share my journey with; our dinners, fridge's list, Google weekends and procrastination times helped me SO much to survive in Ireland.

Now it is time to thank the Portuguese people in my life, starting with my Lisbon team. Dica, Catxinha, Chico e Teresinha, you are amazing! Did not spend one single week in Dublin without receiving a supportive text or call from you. Also, my time in Lisbon this year was the best time in my life.. it is so good to know than even after 10 years absolutely nothing changed! *Obrigada foufuros!*

What is life without a family? I would like to thank everyone in my fantastic family for all the comfort and belief, you are the pillar of my success. There was not one single day that I didn't wish to be in Madeira with you, but all your support made me stay and go through this journey. Specially, Kutchy, Pipo, Faisca, Sergio, Elma e Chica thank you so much for everyday support.

My special gratitude goes to my parents; *Mãe e Pai quero que saibam que este doutoramento é o resultado da vossa dedicação e apoio incondicional. Devo-vos tudo e mais alguma coisa, mas acima de tudo, devo um MUITO OBRIGADA pela Joana Vasconcelos que me tornei.*

Last but not least my gratitude goes to my grandparents Dores, Alberto, Alzira e Agostinho; *Muito obrigada pela vossa relação de excelência com Deus, sem o vosso apoio seria impossível,*

"Porque metade do sucesso é uma velinha acesa."

Summary

When a biomaterial is exposed to biological fluids after implantation a series of events occur on their surface, starting with the adsorption of small biomolecules at the interface, followed by cell adhesion and further processes. The ability to control and modulate interfacial interactions between a material and its host is a key factor in the rational design of biodevices. Performance of carbon-based materials in biological media has been studied for decades and the desire to understand the impressive bioresponse towards carbon materials is still present nowadays. *In vivo* carbon performance is thought to depend on the composition/structure of an initially adsorbed protein/lipid layer; however, there is still a great controversy regarding the structure of the adsorbed layer and the role of this layer on the *in vivo* long-term bioresponse towards carbon-based biodevices. This thesis aims to contribute to a fundamental understanding both on the interactions of carbon thin films with model lipid assemblies and on the influence of carbon/lipid interactions on the long-term performance of carbon coatings.

Chapter I provides an overview on the fundamental physico-chemical properties of carbon biomaterials, along with the characterisation and applications of diamond-like carbon (DLC) films in the biomedical field. Concurrently, a description of lipids present in biological fluids is provided, with special emphasis on phospholipids. Additionally, the role of lipids on the bioresponse towards implanted materials is reported. In particular, lipid-carbon interaction is reviewed in relation to carbon surface properties and biological media composition. Finally, literature on the impact of lipid/carbon interactions on the long-term bioresponse towards carbon is examined.

The description of the most relevant experimental techniques used on this thesis is presented in Chapter II. The sputtering method utilised for DLC film deposition is illustrated along with the description of carbon surface ζ-potential measurements. Liposomes are characterised using dynamic light scattering (DLS) and ζ-potential techniques. Finally, the description of the *in situ* and *ex situ* techniques utilised for liposome/carbon interactions is reported.

Chapter III presents the physico-chemical characterisation of DLC films, with special emphasis on surface ζ-potential determinations of these surfaces. Bare amorphous carbon

(a-C), oxidised amorphous carbon (a-C:O) and hydrogen doped amorphous carbon (a-C:H) are characterised with regards to their surface morphology, chemistry, wettability and charge. Results suggest that materials have increasing graphitic content in the order a-C:H < a-C:O < a-C and also an increasing density of oxidised groups in the order a-C:H < a-C < a-C:O. Oxidation of a-C yields a highly hydrophilic surface (a-C:O) and a significant increase on its SFE polar component. In the case of the sp^3-rich surface, a-C:H shows a similar wettability and SFE values, when compared with a-C. Determination of surface ζ-potentials yield isoelectric points of pH_{iso} = 3.0-3.7 and pH_{iso} < 1.5 for a-C and a-C:O surfaces, respectively.

The influence of nature, type and preparation methods of phospholipid liposomes on their size and electrostatic stability is reported in Chapter IV. Phosphatidylcholine (PC) and phosphatidylserine (PS) are combined in 80:20 PC/PS liposomes and found to be electrostatically stable and homogeneously dispersed at all buffer conditions studied.

Chapter V includes *ex-situ* and *in-situ* studies on PC/PS liposome adsorption on carbon surfaces by using a combination of microscopic, spectroscopic and nanogravimetric techniques. *Ex-situ* results indicate that liposomes adsorb at a-C surfaces independent of the buffer being used. Liposome adsorption at a-C:O surfaces, however, is only observed when Ca^{2+} is added to the buffer. Further *in-situ* measurements confirm *ex-situ* observation and suggest that liposome adsorption on both a-C and a-C:O surfaces is made through intact vesicle adsorption at the interface, unless under conditions that promote liposome rupture.

In Chapter VI, the long term bioresponse towards carbon thin films is investigated through cellular compatibility studies on varying thin film surface properties. Results indicate that the adhesion of endothelial and fibroblast cells at carbon surfaces is slightly reduced on a-C:O, when compared to a-C. Additionally, the anti-thrombogenic and anti-fungal behaviours of carbon films is studied. Oxidised carbon shows a significant decrease in platelet and fungi adhesion and spread, when compared with a-C, which is attributed to a-CO's high hydrophilicity. These results show the potential of carbon films for biomedical applications and highlight carbon's performance as a biomaterial with a unique combination of high biocompatibility, anti-thrombogenic and anti-fungal behaviours.

Finally, Chapter VII includes an overall conclusion on the results obtained within this thesis and prospects of continuation of this work in terms of carbon interaction with biomolecules, in particular the role of lipids in the long-term bioresponse towards carbon films.

Table of Content

Acknowledgements i

Summary iii

Nomenclature x

List of Figures xii

List of Tables xix

List of Publications xx

List of Communications xxi

Chapter I – INTRODUCTION 1

1. Carbon Materials 2

1.1. Carbon Biomaterials 2

1.1.1. Diamond-Like Carbon (DLC) 4

1.1.2. DLC Coatings: Biomedical Applications 7

2. Biointeractions at Materials Interface 11

2.1. Phospholipids in Biological Media 13

2.2. Phospholipid Liposomes 16

2.3. Interactions of Liposomes with Macroscopic Surfaces 19

2.3.1. Factors Influencing Liposome/Surface Interactions 19

2.3.1.1. Influence of Buffer 20

2.3.1.2. Influence of Lipid Composition 22

2.3.1.3. Influence of Surface Physico-Chemical Properties 22

2.3.2. Liposome Interactions with Carbon Surfaces 25

2.4. DLCs Long-Term Bioresponse 27

3. Aim of this Thesis 29

4. References 30

Chapter II – EXPERIMENTAL TECHNIQUES **37**

1. Carbon Films Deposition 38
2. Liposomes Characterisation 39
   - 2.1. Dynamic Light Scattering (DLS) 39
   - 2.2. Particles ζ-Potential 41
3. Carbon Surface Characterisation 43
   - 3.1. Surface ζ-Potential 43
4. Carbon/Biomolecules Interaction 46
   - 4.1. Infrared Reflectance Absorption Spectroscopy (IRRAS) *ex situ* 46
   - 4.2. Fluorescence Microscopy 49
   - 4.3. Fluorescence Recovery after Photobleaching (FRAP) 51
   - 4.4. Atomic Force Microscopy (AFM) 52
   - 4.5. Scanning Electron Microscopy (SEM) 55
5. References 57

Chapter III – CARBON AND CARBON MODIFIED-THIN FILMS **59**

1. Introduction 60
2. Results and Discussion 61
   - 2.1. Physico-Chemical Characterisation of Amorphous Carbon Thin Films 61
   - 2.2. Surface ζ-Potential Determinations 69
     - 2.2.1. Characterisation of Particle Suspensions 69
     - 2.2.2. Characterisation of Nylon and PTFE Surfaces using Tracer Particles 70
     - 2.2.3. Determination of Carbon SZP using Tracer Particles 71
3. Discussion 73
4. Conclusions 75
5. Experimental 77

5.1. Chemicals and Materials 77

5.2. Preparation of Tracer Particle Suspensions 77

5.3. Preparation of Carbon Thin Films 78

5.4. Characterisation Methods 78

5.5. Surface ζ-potential Determinations 79

6. References 80

Chapter IV – PHYSICO-CHEMICAL CHARACTERISATION OF PHOSPHOLIPID LIPOSOMES **83**

1. Introduction 84

2. Results and Discussion 85

2.1. Characterisation of Phosphatidylcholine (PC) and 3-sn-Phosphatidyl-L-serine (PS) 85

2.2. Characterisation of Phospholipid Liposomes 87

2.2.1. Morrisey *vs* Freeze-Thaw Protocols for Preparation of PC Liposome: Size and Stability Study 87

2.2.2. Influence of PS on the Electrostatic Stability of PC-containing Liposomes 90

2.2.3. Influence of pH on the Electrostatic Stability of PC/PS Liposomes 91

2.2.4. Influence of Ionic Composition on the Electrostatic Stability of PC/PS Liposomes 93

3. Conclusions 95

4. Experimental 96

4.1. Chemicals and Materials 96

4.2. Liposome Preparation 96

4.3. Characterisation Methods 97

5. References 98

Chapter V – INTERACTION OF CARBON THIN FILMS AND PHOSPHOLIPID LIPOSOMES **101**

1. Introduction 102

2. Results 103

2.1. Influence of Surface Chemistry 103

2.2. Influence of Buffer pH 106

2.3. Influence of Buffer Ionic Composition 107

2.4. Study of Liposome Rupture 109

3. Discussion 111

3.1. Surface Chemistry Effects 111

3.2. Buffer Composition Effects 113

4. Conclusions 115

5. Experimental 116

5.1. Materials and Compounds 116

5.2. Liposome Preparation 116

5.3. Substrate Preparation 116

5.4. Adsorption Experiments 117

5.5. Characterisation Methods 117

6. References 118

Chapter VI – *IN VITRO BIORESPONSE TOWARDS CARBON THIN FILMS* **123**

1. Introduction 124

2. Results 125

2.1. Cytotoxicity 125

2.2. Endothelial Cells Culture 126

2.3. HFFF2 Fibroblasts Culture 130

2.4. Thrombogenicity 133

2.5. *Saccharomyces Cerevisiae* Biofilm Formation 135

3. Discussion 138

4. Conclusion 141

5. Experimental 141

5.1. Materials and Chemicals 141

5.2. In vitro Tests 142

5.2.1. Cytotoxicity 142

5.2.2. Fibroblasts and Endothelial Cells 143

5.2.3. Thrombogenicity 143

5.2.4. *Saccharomyces Cerevisiae* Biofilm 143

5.3. Characterisation methods 144

5.3.1. Spectrophotometer 144

5.3.2. Immunostaining 144

5.3.3. Scanning electron microscopy (SEM) 145

6. References 146

Chapter VII – CONCLUSIONS AND FUTURE WORK **149**

1. Conclusions 150

2. Future Work 151

Published Work **155**

Nomenclature

Abbreviations

a-C – Amorphous carbon

a-C:H – Hydrogen doped amorphous carbon

a-C:O – Oxidised amorphous carbon

AFM – Atomic force microscopy

AL – Amine-terminated latex beads

BSA – Bovine serum albumin

CNT – Carbon nanotubes

C_{cell} – Cell control

C^+ – Positive control

C^- – Negative control

C.I. – Confidence interval

DAPI – 4',6-diamidino-2-phenylindole

d(H) – Hydrodynamic diameter

DLC – Diamond-like carbon

DLS – Dynamic light scattering

DMEM – Dulbecco's modified eagle medium

DMSO – Dimethyl sulfoxide

EC – Endothelial cells

ECM – Extracellular matrix

ET – Tauc gap

FA – Focal adhesion

FBS – Fetal bovine serum

FRAP – Fluorescence recovery after photobleaching

FT-IR – Fourier transform infrared spectroscopy

GUV –Giant unilamellar vesicles

IRRAS – Infrared reflection-absorption spectroscopy

LUV – Large unilamellar vesicles

MLV – Multilamellar vesicles

ND – Nanodiamonds

OD – Optical density

OLV – Oligolamellar vesicles

PAb – Primary antibody

pC – Counterion concentration

pH – Potential of hydrogen

pH_{iso} – pH at isoeletric point

pKa – Acid dissociation constant

PC – Phosphatidylcholine

PDI – Poli-dispersive index

PE – Phosphatidylethanolamine

PECVD – Plasma-enhanced chemical vapour deposition

PS – Phosphatidylserine

PTFE – Polytetrafluoroethylene

PVD – Physical vapour deposition

QCM-D – Quartz crystal microbalance with dissipation

REV – Reverse-Phase Evaporation

Rms – Root mean square

SAb – Secondary antibody

SAPL – Surface active phospholipids

SEM – Scanning electron microscopy

SL – Sulfonated latex beads

SLB – Supported lipid bilayer

SLM – Supported lipid monolayer

sp^2 – Trigonally bonded carbon

sp^3 – Tetrahedrally bounded carbon

SUV – Small unilamellar vesicles

SVL – Supported vesicle layer

SZP – Surface ζ-potential

Ta-C – Tetrahedral amorphous carbon

UV – Ultra violet

wCA – Water contact angle

XPS – X-ray photoelectron spectroscopy

List of Figures

CHAPTER I

Figure 1.1. Example of a pyrocarbon-based mechanical heart valve (a) prior and (b) after implantation in the body, where thrombus formation is clearly visible.[46] 3

Figure 1.2. Ternary phase diagram of bonding in amorphous carbon-hydrogen alloys.[48] 5

Figure 1.3. Example of a talar (left) and tibial (right) components of an ankle joint replacement coated with DLC films (adapted from [31]). 9

Figure 1.4. SEM image of a ~14 mm length biodiamond stent produced by Plasmachem (adapted from [41]). 9

Figure 1.5. Diagram of biofilm formation at biomaterials surface. 11

Figure 1.6. Fundamental two building blocks of lipids, according to LIPID MAPS classification: ketoacyl and isoprene groups; adapted from [91]. 13

Figure 1.7. Representative structures of lipids, according to LIPID MAPS classification. In red are shown examples of lipids derived from condensation of ketoacyl subunits and in blue lipids derived from condensation of isoprene subunits; adapted from [91]. 14

Figure 1.8. Phospholipid structure: hydrophobic group, which includes two fatty acid chains and hydrophilic head group, which includes glycerol, phosphate and R groups. R group corresponds to choline, serine and ethanolamine in the case of phosphatidylcholine (PC), phosphatidylserine (PS) and phosphatidylethanolamine (PE), respectively. 15

Figure 1.9. Size and structure of liposomes defined as small unilamellar vesicles (SUV) d < 100 nm, large unilamellar vesicles (LUV) d > 100 nm, giant unilamellar vesicles (GUV) d > 1000 nm, oligolamellar vesicles (OLV) 100 < d < 500 nm or multilamellar vesicles (MLV) d > 500 nm (adapted from [117]). 18

Figure 1.10. Schematic representation of liposome interaction with macroscopic surfaces. **(a)** Inhibited adsorption, **(b)** intact vesicle adsorption (SVL), **(c)** formation of a supported lipid bilayer (SLB) and (d) formation of a supported lipid monolayer (SLM). 20

CHAPTER II

Figure 2.1. Schematic diagram of the vacuum chamber used on this thesis for thin film deposition. The sputtering guns accelerate ions to collide against titanium (left) and carbon (right) targets. 39

Figure 2.2. Example of an experimental correlation function. 40

Figure 2.3. Optical configuration for dynamic light scattering measurements. 41

Figure 2.4. Electric double layer surrounding a negative charged particle.[4] 42

Figure 2.5. Schematic diagram of the measured mobility as a sum of electrophoresis and electro-osmosis. 44

Figure 2.6. Plot of apparent ζ-potential as a function of surface displacement obtained for a standard polymer as a static surface using tracer particles with known ζ-potential of ~ -70 mV. 45

Figure 2.7. Optical configuration for surface ζ-potential measurements. 46

Figure 2.8. Incident and reflected electric field vectors and the correspondent plane polarisations: parallel (Ep) and perpendicular (Es) polarisations with regards to the plane of incidence. 47

Figure 2.9. Dependence on angle of incidence of p-polarised light on (1) reflectance $R0$, corresponding to the bare substrate and (2) adsorption depth ΔRp for 1-nm layer at Ti substrate; reproduced from [13]. 48

Figure 2.10. Jablonski diagram on the excitation and emission process of a common fluorophore. 49

Figure 2.11. (a) Excitation (dot line) and emission (full line) spectra of DAPI (blue), alexa fluor 488 (green) and acti-stain 555 (red). **(b)** Fluorescence image of HFFF2 cells adherent to Si surface with nucleus stained using DAPI (blue), primary antibody (pAb) stained against vinculin with Alexa Fluor 488 as the fluorophore (green) and F-actin stained using phalloidin (red). 50

Figure 2.12. Optical setup for fluorescence microscopy measurements. 51

Figure 2.13. Schematic of AFM configuration adapted from Jalili *et al.*[21]. 53

Figure 2.14. Schematic of tapping mode AFM operation adapted from Jalili *et al.*[21]. 54

Figure 2.15. Set-up of a scanning electron microscope (SEM).[25] 55

CHAPTER III

Figure 3.1. SEM image of a a-C film deposited on a Si substrate. 61

Figure 3.2. 10 × 10 µm AFM topographic images of **(a)** a-C, **(b)** a-C:H and **(c)** a-C:O surfaces. All surfaces roughness values were obtained from height profile determinations. 62

Figure 3.3. Survey XPS spectra on the region 600-200 eV of a-C, a-C:H and a-C:O surfaces showing C 1s and O 1s core level peaks. 62

Figure 3.4. XPS spectra of **(a)** a-C, **(b)** a-C:H and **(c)** a-C:O surfaces in the C 1s region; Shirley background and individual contributions are shown under each curve. 63

Figure 3.5. Tauc plots for a-C (red) and a-C:H (blue) films. Extrapolation of the linear fit (dot line) to the X-axis results in Tauc Gap values for both carbon surfaces. 65

Figure 3.6. Representative images (left) of water contact angle (wCA) measurements and correspondent wCA plots (right) of a-C:H, a-C and a-C:O thin films. 66

Figure 3.7. SFE acid (Y+) and base (Y-) components of a-C:H (red), a-C (green) and a-C:O (blue) thin films. 68

Figure 3.8. (a) Hydrodynamic size and **(b)** ζ-potential of sulfate latex (SL) and amine latex (AL) beads used as tracer particles for surface ζ-potential measurements. SL and AL beads were suspended in 100 µM PBS buffer (1.37 mM NaCl and 27 µM KCl) with total ionic strength of 1.80 ± 0.15 mM for all pH values studied. 69

Figure 3.9. Surface ζ-potential measurements of Nylon 6,6 and PTFE surfaces (blue data points) using SL beads as tracer particles. SL beads were suspended in 100 µM PBS buffer (1.37 mM NaCl and 27 µM KCl) and the ionic strength remained at 1.80 ± 0.15 mM for all pH studied (pC = 2.82). Surface ζ-potential values were normalized by the counterion concentration (pC) for both polymers (red data points). 70

Figure 3.10. Surface ζ-Potential of a-C, a-C:H and a-C:O surfaces obtained using SL (full) and AL (empty) beads as tracer particles, suspended in 100 µM PBS buffer, 1.80 ± 0.15 mM ionic strength, for all pH values studied. 72

CHAPTER IV

Figure 4.1. FT-IR spectra on the 4000 – 1000 cm^{-1} region of phosphatidylcholine (**PC**) and phosphatidylserine (**PS**); phospholipid main groups are assigned on the spectra. 86

Figure 4.2. SEM images of PC liposomes deposited on a Si substrate; white bars correspond to **(a)** 500 nm and **(b)** 50 nm. 87

Figure 4.3. (a) Example of a measurement on the PC liposome hydrodynamic size (d.nm) using the Freeze-thaw (**blue**) and Morrisey (**red**) protocols after extrusion through a Ø100 nm filter. **(b)** Hydrodynamic size of PC liposomes for Freeze-thaw protocol (**red**) and for Morrisey protocol (**blue**). Liposomes were extruded through a nylon membrane (450 nm pore diameter) followed by a second extrusion through another nylon membrane (100 nm pore diameter). The hydrodynamic size was measured immediately after extrusion, for t=30 min and for t=60 min. 88

Figure 4.4. Hydrodynamic diameter (**blue**) and ζ-potential (**green**) values of PC/PS liposomes regarding pH and its respective polidispersity index (PDI-**red**). 91

Figure 4.5. Hydrodynamic size (**blue**) of PC/PS liposomes in the absence and presence of 10 mM $CaCl_2$ and its respective polidispersity index (PDI-**red**). Liposomes were extruded through a nylon membrane (450 nm pore diameter). The hydrodynamic size was measured immediately after extrusion, for t=30 min and for t=60 min. 94

Figure 4.6. Apparent ζ-potential values of PC (**red**) and PC/PS (**blue**) liposomes in the absence (solid line) and presence (dot line) of $CaCl_2$ in the PBS solution. 94

CHAPTER V

Figure 5.1. IRRAS spectra on the 3200 – 800 cm^{-1} region of a-C, a-C:H and a-C:O surfaces after 1 h incubation of 1 mM PC/PS liposome in PBS at pH 7.4. 104

Figure 5.2. FRAP images obtained after incubation of PC/PS liposomes onto a-C, a-C:H and a-C:O surfaces. Each image is 250 µm x 250 µm and the photobleached area is 25 µm x 25 µm. After photobleaching at t=0', images are taken at one minute time intervals. (scale bar corresponds to 100 µm). 105

Figure 5.3. QCM-D monitoring of PC/PS liposome adsorption at a-C (top) and a-C:O (bottom) surfaces. After PBS injection, the PC/PS solution (0.40 mg/mL) was injected at 10 min and the interaction of PC/PS liposomes with a-C and a-C:O surfaces was monitored during 30 min; the surface was further rinsed with PBS. All frequencies 106

(left) and dissipations (right) are presented in the third overtone and measured in the range of 0 to -60 Hz and 0 - 12 x 10^{-6}, respectively.

Figure 5.4. IRRAS spectra in the 3000-2600 cm^{-1} region of a-C and a-C:O surfaces after 1 h incubation of PC/PS liposomes suspended in PBS buffer at different pH. The position of CH_2 stretching bands is indicated with dot lines. 107

Figure 5.5. (Top) Fluorescence measurements of a-C/a-C:O pattern for different pH. a-C:O is the darker area in the picture while a-C is the outer of that area. **(Bottom)** Table of relative fluorescence intensities emitted from the adsorption of PC/PS liposomes at a-C and a-C:O surfaces. 108

Figure 5.6. (a) IRRAS spectra in the region 3200-2650 cm^{-1} of a-C and a-C:O surfaces after 1 h incubation of liposomes suspended in PBS and PBS with 10 mM $CaCl_2$ at pH 7.4. The position of -CH_2 stretching bands is indicated with dotted lines. Fluorescence images of a-C:O patterned over the a-C surface after incubation in suspensions of fluorescently labelled PC/PS liposomes (1 mM PC/PS, 1 h) in PBS **(b)** and in PBS with 10 mM $CaCl_2$ **(c)** at pH 7.4; scale bar = 500 µm. 109

Figure 5.7. AFM images of a-C (left) and a-C:O (right) surfaces after incubation in 20 µL of 1 mM PC/PS suspensions in **(a)** PBS and **(b)** PBS with 10 mM $CaCl_2$ at pH 7.4. Height profiles (inset) show step edges of average 1.1 nm thickness in either absence or presence of Ca^{2+} (z-scale = 20 nm). 111

CHAPTER VI

Figure 6.1. Results of the cytotoxicity test of Si substrate, a-C and a-C:O films deposited on Si; values given as mean ± stdev. Negative and positive controls are represented in red. 125

Figure 6.2. Relative population of endothelial cells adherent at a-C and a-C:O surfaces comparative to control (C_{cell}) after 24 h of cell culture; values given as mean ± stdev. 127

Figure 6.3. Fluorescence images of rat aortic endothelial cells adherent to **(a)** a-C and **(b)** a-C:O surfaces. The nucleus (blue) and the F-actin cytoskeleton (red) were stained using DAPI and phalloidin, respectively. 127

Figure 6.4. Fluorescence images of focal adhesions (FA) of endothelial cells adherent to **(a)** a-C and **(b)** a-C:O surfaces stained with an antibody (pAb) stained against vinculin (green). Overlap of fluorescence images of pAb, nucleus and F-actin cytoskeleton at **(c)** a-C and **(d)** a-C:O surfaces; nucleus (blue) and F-actin cytoskeleton (red) were stained using DAPI and phalloidin, respectively. 128

Figure 6.5. Relative population of endothelial cells. Adhesion (day 1) and proliferation (days 3-9) at a-C and a-C:O surfaces compared to control (C_{cell}); values given as mean ± stdev. 129

Figure 6.6. Relative population of *HFFF2* cells adherent at a-C and a-C:O surfaces comparative to control (C_{cell}) after 24 h of cell culture; values given as mean ± stdev. 132

Figure 6.7. Fluorescence images of HFFF2 cells adherent to **(a)** a-C and **(b**) a-C:O surfaces. The nucleus (blue) and the F-actin cytoskeleton (red) were stained using DAPI and phalloidin, respectively. 132

Figure 6.8. Fluorescence images of focal adhesions (FA) of HFFF2 cells adherent to **(a)** a-C and **(b)** a-C:O surfaces with primary antibody (pAb) stained against vinculin (green). Overlap of fluorescence images of pAb, nucleus and F-actin cytoskeleton at **(c)** a-C and **(d)** a-C:O surfaces; nucleus (blue) and F-actin cytoskeleton (red) were stained using DAPI and phalloidin, respectively. 132

Figure 6.9. Relative population of fibroblasts, from the line HFFF2, adhesion (day 1) and proliferation (days 3-9) at a-C and a-C:O surfaces comparative to control (C_{cell}); values given as mean ± stdev. 133

Figure 6.10. (a) Dendritic (D) and **(b)** spread dendritic (SD) morphologies of adherent platelets on a-C films imaged with SEM; scale bars correspond to 3 µm and 1 µm, respectively. 134

Figure 6.11. SEM image of *in vitro* human platelet adherent at **(a)** a-C and **(b)** a-C:O surfaces (scale bar = 20 µm). 134

Figure 6.12. Platelet dendritic (D) and spread dendritic (SD) morphologies distribution and focal centres at a-C and a-C:O surfaces; each plot shows the platelet population in a 100×75 μm^2 area (mean ± stdev). 135

Figure 6.13. Example of *saccharomyces cerevisiae* (yeast) adsorption at carbon films; scale bar = 1 µm. 136

Figure 6.14. SEM images at low (top) and high (bottom) magnifications on the adhesion of yeast at **(a)** Si, **(b)** a-C and **(c)** a-C:O surfaces; scale bars corresponds to 40 µm (top) and 5 µm (bottom). 137

Figure 6.15. Percentage of covered surface (mean ± stdev) by collection of *saccharomyces cerevisiae* (yeast) on Si, a-C and a-C:O surfaces. 138

Figure 6.8. Water contact angles (wCAs) of a-C (green) and a-C:O (blue) surfaces and resume of results previously obtained in this chapter. Adhesion of endothelial and fibroblast cells are reported as relative cell population; platelets are reported as total platelet population and yeast as % area occupied. 139

CHAPTER VII

Figure 7.1. Relative population of *HFFF2* cells adherent at a-C and a-C:O surfaces, in the absence (solid bars) and presence (light bars) of a PC/PS lipid passivated layer. Results are shown comparative to control (C_{cell}) after 24 h of cell culture; values given as mean ± stdev. 152

Figure 7.2. Overlap of fluorescence images of HFFF2 cells adherent to **(a)(c)** a-C and **(b)(d)** a-C:O surfaces without (a and b) and with (c and d) a PC/PS lipid passivated layer at carbon surfaces. Nucleus (blue) and F-actin cytoskeleton (red) were stained using DAPI and phalloidin, respectively. Primary antibody (pAb) is stained against vinculin (green). 153

List of Tables

CHAPTER I

Table 1.1. Comparison of major physico-chemical properties of DLC with those of reference, i.e. diamond and graphite (adapted from [13, 48]). 6

Table 1.2. Outcomes of the interaction between liposomes and standard macroscopic surfaces; possible outcomes are: no liposome adsorption, supported lipid monolayer (SLM), bilayer (SLB) or vesicle layer (SVL). 24

CHAPTER III

Table 3.1. Water contact angle (θw) and total SFE (Ytot), its dispersive (YLW), acid (Y+) and base (Y-) components for a-C, a-C:H and a-C:O thin films. 67

Table 3.2. Summary of composition and properties of carbon thin films. 75

CHAPTER IV

Table 4.1. Assignment of major IR bands present on phospholipid groups.[25, 29-30] 85

Table 4.2. Hydrodynamic size, PDI and ζ-potential of PC (100) and PC/PS (80:20) liposomes. 91

List of Publications

Under Review Studies of lipid/carbon interactions: influence of surface and buffer chemistry on the adsorption of phospholipid liposomes.

Vasconcelos *et al.*

2017 **Vasconcelos, J. M.**; Zen, F.; Stamatin, S. N.; Behan, J. A.; Colavita, P.E., *Surf. Interface Anal.* ***2017***

2017 Browne, M. P., **Vasconcelos, J. M.**, Coelho J., O'Brien, M., Rovetta, A. A., McCarthy, E. K., Nolan, H., Duesberg, G. S., Nicolosi, V., Colavita, P. E., Lyon, M. E. G., *Sustainable Energy Fuels*, **2017**, 1, 207–216

2016 Esteban-Tejeda, L., Duff, T., Ciapetti, G., Angione, M. D., Myles, A., **Vasconcelos, J. M.**, Scanlan, E. M., Colavita, P.E., *Polymer*, **2016**, 106, 1-7

2016 Zen, F.; Angione, M. D.; Behan, J. A.; Cullen, R. J.; Duff, T.; **Vasconcelos, J. M.**; Scanlan, E. M.; Colavita, P. E., *Scientific Reports,* **2016**, 6, 24840.

2015 Marzorati S., **Vasconcelos J. M.**, Ding J., Longhi M., Colavita P. E., *Journal of Materials Chemistry A*, **2015**, 3, 18920

2014 Joao, C. F.; **Vasconcelos, J. M.;** Silva, J. C.; Borges, J. P., *Tissue engineering. Part B, Reviews*, **2014**, 20 (5), 437-54

List of Communications

2017 European Materials Research Society Spring Meeting, Strasbourg, France **(Oral)**

2016 European Materials Research Society Fall Meeting, Warsaw, Poland **(Oral)**

2016 27th International Conf. on Diamond and Carbon Materials, France **(Oral/Poster)**

2016 UK Surface Analysis Forum Summer Meeting, Ireland **(Oral/Poster)**

2016 3rd Centro de Química da Madeira Anual Meeting, Portugal **(Oral)**

2015 66th Irish Chemistry Colloquium, Ireland **(Oral)**

2015 1st ITN-SNAL Summer School, Italy **(Poster)**

2015 European Materials Research Society Spring Meeting, France **(Poster)**

2015 CRANN and AMBER Scientific Advisory Board Meeting, Ireland **(Poster)**

Chapter I

Introduction

Carbon-based materials, in particular diamond-like carbon (DLC) coatings, are widely used in many research fields, due to their outstanding physico-chemical properties. In biomedical applications, DLC materials display an exceptional performance as coatings for carbon-based biodevices. However, the origin of the long-term bioresponse towards DLC coatings is not fully understood; it is believed that a lipid/protein passivated layer ultimately defines the bioresponse towards DLC-coated material. Herein, the fundamental physico-chemical characterisation of DLC is discussed, along with the examination on the influence of DLC properties on the DLC/lipid interactions. Finally, DLC's long-term performance is reviewed with regards to cell, platelet and fungi adhesion at the interface.

1. Carbon Materials

In recent decades, carbon-based materials have become ubiquitous in a vast range of applications. Biomedical devices, sensing, electronics, therapeutics, catalysis, separation technologies and mechanical reinforcements, are just few examples of the diversity of carbon's applications. The potential of carbon materials in various fields is attributed to the wide range of physico-chemical properties of carbon allotropes. For instance, carbon nanomaterials, such as porous carbons, have found uses in gas separation, water purification and fuel cells.[1] Carbon nanotubes have found applications as energy storage and energy conversion devices, sensors and semiconductor devices.[2-6] Carbon nanofibers have been used as sensors, electrodes and electromagnetic shields[7-8] and graphene has been applied in the field of both photonics and electronics.[9] Carbon in the form of coatings and thin-films possesses unique properties which have led to applications as electrodes,[10] protective coatings,[11-12] and in the automotive sector.[13]

Of particular significance is the tremendous progress that has been made in the biomedical sector due to the excellent performance of carbon-based materials in biological media.[14-16] The choice of carbon materials for a wide range of biomedical applications, over other types of materials, is due to carbon's singular biocompatibility and tunability to the application that the biomaterial is design for. The following section is dedicated to the description of the biomedical applications of carbon-based devices, with special emphasis on the usage of carbon coatings in the biomedical field.

1.1. Carbon Biomaterials

Carbon materials are widely used in biological applications, in the form of nanoparticles, nanostructured scaffolds, coatings and thin films. Carbon often demonstrates excellent performance as a biomaterial, a notable example being that of nanostructured forms of carbon; nanotubes,[17-18] fullerenes,[19] carbon nanoparticles[20-22] and porous carbons[23-24] have all been investigated as promising candidates for therapeutic and diagnostic purposes. For instance, carbon nanotubes are subject to intensive study in areas such as drug delivery and cancer-cell targeting.[17-18, 25] Carbon

nanoparticles, such as carbon dots[20-21] and nanodiamonds[22], have found applications in biosensing, bioimaging and theranostics. Additionally, the high specific surface area and the small pore size of porous carbons contribute to their great performance as cellular delivery and imaging agents.[23-24]

Carbon coatings are also of current interest as materials for biological applications: pyrolytic carbon,[26-28] diamond-like carbon (DLC),[29-38] and nanoporous carbon[39] have been used in the form of thin films integrated into catheters, stents, joint replacements, sensors and contact lenses.[33, 40-42] Pyrolytic carbon, also known as pyrocarbon, is perhaps the most well studied type of carbon coating, with more than 40 years usage in orthopaedic and cardiovascular fields.[27, 43-44] With its isotropic form, pyrocarbon has demonstrated excellent biocompatibility and anti-thrombogenic behaviour.[25]

However, *in vivo* long-term studies on the adoption of pyrocarbon as a coating for stents, revealed that pyrolytic carbon did not exhibit a significant improvement on the stent performance.[45] Pyrolytic carbons have also been correlated with poor biocompatibility of heart valves and with the promotion of thrombogenic effects at the bioimplanted surface (Figure 1.1).[44] Likewise, studies on the usage of pyrolytic carbon as a coating in the cardiovascular field reported that for long time *in vivo* exposure, as in the case of pacemakers, heart valves and stents, pyrocarbon coatings show susceptibility to crack growth and propagation, resulting in a defected coating.[15, 44] Therefore, there is an urgent need for new carbon coatings that not only display excellent performances as biocompatible and hemocompatible materials, but also improve wear properties and resistance towards defects and corrosion processes.

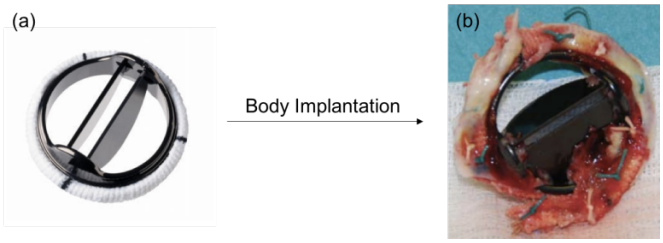


Figure 1.1. Example of a pyrocarbon-based mechanical heart valve **(a)** prior and **(b)** after implantation in the body, where thrombus formation is clearly visible.[46]

Recent developments in the field of biomedical coatings has suggested the use of DLC to improve, or even replace, pyrolytic carbon as coatings for carbon-based devices.[41]

DLC has proved to be a material which combines an exceptional range of properties, which are suitable for its usage as a coating in the cardiovascular and orthopaedic fields.[16, 33, 41, 47] Many of the DLC applications *in vivo* rely on the careful control of its interfacial properties in order to modulate chemical/electrochemical reactivity and/or biological responses. The next section includes a detailed review on the DLC fabrication methods, properties and applications on the biomedical field.

1.1.1. Diamond-Like Carbon (DLC)

Diamond-like carbon (DLC) is the term used to describe a broad range of amorphous carbon coatings and it consists of a dense metastable form of carbon which is commonly specified as an amorphous carbon network with crystalline regions.[13, 40, 48] In the early 1950's, Schmellenmeier[49] described for the first time hydrogen doped hard amorphous carbon (a-C:H), and only two decades later the term "diamond-like carbon" was first used by Aisenberg and Chabot,[50] who defined DLC as amorphous carbon films prepared by ion beam deposition.[13] Nowadays the term DLC is used to described a wider variety of carbon-based thin films in which their properties can be tailored by tuning the crystalline and amorphous carbon phases and the concentrations of molecular hydrogen.[13, 16, 32] Jacob and Moller were the first to propose a schematic organisation of this family of disordered carbon films in a ternary phase diagram (Figure 1.2); the bottom left corner of the diagram corresponds to graphitic carbon, the top corner to crystalline carbon and the bottom right to C-H alloys.[51]

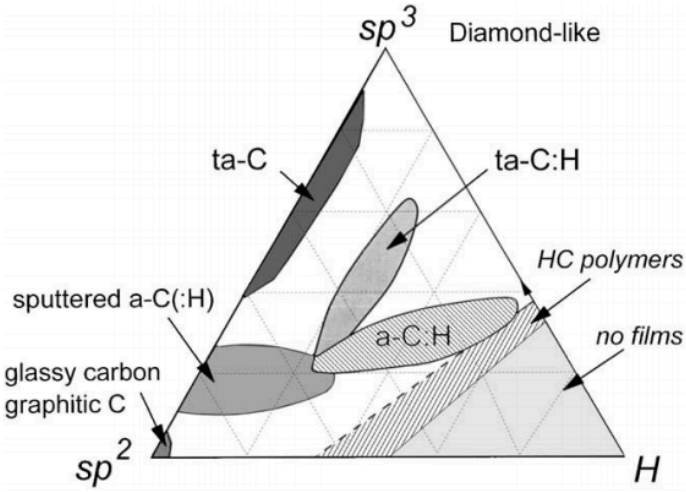


Figure 1.2. Ternary phase diagram of bonding in amorphous carbon-hydrogen alloys.[48]

The crystalline phase corresponds to a diamond-like structure, in which carbon atoms adopt a tetrahedral coordination with strong σ bonds, commonly referred to as sp^3 hybridisation. Diamond displays extreme physical properties, such as a wide bandgap of 5.5 eV, a high atomic density and thermal conductivity, a result derived from diamond's strong σ bonds (Table 1.1). In the graphite-like sp^2 bonding configuration, each atom is trigonally coordinated to three other atoms through σ bonds.[52] Due to the π orbitals orientated parallel to the σ bonding plane, each graphite layer behaves as a zero-bandgap semiconductor and in three dimensions assumes the properties of an anisotropic metal, a result of weak Van der Waals bonding between the layers.[48]

DLC combines properties of diamond and graphite in an isotropic disordered film. The sp^3 bonding offers properties of diamond-like films such as wide bandgap, high hardness and electrical resistivity, excellent thermal conductivity and chemical inertness (Table 1.1). Concurrently, the sp^2 hybridization carbon bond confers high wear rate and low coefficient of friction to DLC films, a desirable characteristic of biomaterials to be use in the orthopaedic field.[13, 16, 25, 48, 52]

DLC films assume different classifications depending on the ratio of sp^2/sp^3 centres present in the film and also on the amount of hydrogen incorporated.[32] Tetrahedral amorphous carbon (ta-C), amorphous carbon (a-C), hydrogen-doped carbon (a-C:H) and hydrogenated tetrahedral amorphous carbon (ta-C:H) are few examples of DLC films

designation with varied crystalline, amorphous phases and hydrogen content (Figure 1.2). According to McKenzie, films rich in sp^3 bonding (> 80 %) are defined as ta-C whereas films produced through carbon sputtering are designated as a-C and possess high graphitic content.[53] Hydrogenation of ta-C and a-C films results in ta-C:H and a-C:H films, respectively, and they possess chemical bonds that are significantly modified when compared with the starting DLC film (Figure 1.2).

Table 1.1. Comparison of major physico-chemical properties of DLC with those of reference, *i.e.* diamond and graphite (adapted from [13, 48]).

	sp^3 (%)	H (%)	Density ($g.cm^{-1}$)	Bandgap (eV)	Hardness (GPa)	Resistivity (Ω cm)
Diamond	100	0	3.515	5.5	100	10^{18}
Graphite	0	0	2.267	0	-	$10^{-6} – 10^{-2}$
ta-C	80 – 88	0	3.1	2.5	80	$10^{6} – 10^{10}$
a-C	5	0	2.2	0.5	-	-
ta-C:H	70	30	2.4	2.0 – 2.5	50	-
a-C:H	40 – 60	30 – 50	1.2 – 16	1 – 4	< 20	$10^{4} – 10^{12}$

Industry has developed several deposition methods to produce DLC films with physico-chemical properties adjusted to the application that they are design for.[13, 32, 54] The most common methods to deposit DLC films, from a variety of carbonaceuous percursors, are physical vapour deposition (PVD), *i.e.* sputtering or arc evaporation, and plasma-enhanced chemical vapour deposition (PECVD).[13, 32, 40, 48, 55] Of particular interest, magnetron sputtering is commonly used in industrial processes to produce DLC films, due to its versatility, widespread use with many materials and its easy scalability.[35, 55] In this work, magnetron sputtering was chosen to produce a-C films and the experimental details and carbon physico-chemical properties are described in Chapters II and III, respectively.

More complex coatings can also be produced using different strategies for DLC surface and bulk modifications. Varying parameters during DLC production (*e.g.* temperature, pressure and bias), changing the coating architecture with multi-layer films and introducing additional elements in the coating (*e.g.* Si, N, O, F, Ti) are common approaches used to tailor physico-chemical properties of DLC films.[16, 52, 56] In this work,

particular attention is dedicated to the modification and control over the interfacial properties of DLC films by introducing oxidised groups through an oxidative treatment. UV/ozone oxidation is a widely used method for the modification of carbons, including nanotubes,[5, 57] fullerenes,[58] and nanodiamonds,[59] and for the modulation of cell adhesion at diamond and amorphous carbon surfaces.[60-62] Also, DLC has shown growth suppression of cortical neurons in areas where the film was oxidized through UV radiation.[52, 63] All of these different approaches to fabricate and modify DLC films have been used to optimise its functional performance in different sectors, particularly in the biomedical field where the enhancement of DLC performance is still an issue.

1.1.2. DLC Coatings: Biomedical Applications

The host response towards a material implanted in the human body is a critical governing factor for the success of a biomaterial *in vivo*. Therefore, engineering biomaterials, which promote favourable biological reactions, is one of the most challenging areas of research.[16] Once exposed to biological fluids and tissues, the implanted material is susceptible to extreme environmental conditions such as a wide range of pHs, interaction with biological molecules and innumerable chemical interactions at the solid/liquid interface.[64-65] An implantable biomaterial is expected to not only endure all the aforementioned environmental conditions but also to re-establish biological and mechanical functions of the natural organ/tissue.[31] Depending on the biomedical application that the material is designed for, the biomaterial can enhance, in the case of stents and cardiovascular valves, or even replace, *e.g.* orthopaedic applications, biological function of the organ/tissue.[26, 31, 66]

Despite the fact that the number of implantable biomaterials has increased in recent years, a material that has the ability to enhance or/and replace the functionalities of human organs and tissues and at the same time displays good biocompatibility remains elusive and is still the subject of intense research.[26, 66] The success of a material's biocompatibility is attributed to a combination of bio-activity, chemical and biochemical inertness to the biological environment, wear and corrosion resistance, and more importantly to its resistance to millions of cycles of load stress without leaching any

toxic elements into the human body.[41, 64, 67] Stainless steels, titanium, cobalt and platinum alloys are the most common metals used for joint replacement, stents and pacemakers due to their high fatigue and corrosion resistance.[64] Also, zirconia and alumina ceramics are utilised for articular prosthesis due to their dense, hard and chemically stable nature.[64] Likewise, biodegradable and biostable polymers, such as ultra-high molecular weight polyethylene (UHMWPE), polymethyl methacrylate (PMMA) and polyvinyl chloride (PVC) have been used as staples, sutures and membranes for tissue regeneration.[26, 66]

Nevertheless, the long-term biocompatibility of the implantable material remains a critical limitation on any device's functionality; metals are known to release metallic ions due to corrosion resulting in platelet activation, cell damage and blood clot formation.[64] Also, manufacturing ceramics as biomaterials is limited to pre-determined forms and they can minimize bone in-growth. Furthermore, biopolymers undergo thermal degradation, which represents an advantage but also a disadvantage since it leads to polymer leaching and wear.[26, 66] These results suggest that despite the great physico-chemical properties of the aforementioned materials, their prolonged inflammatory response and other adverse side effects constrain their usage as biomimetic materials.[30, 64, 68]

Biocompatibility and physico-chemical interactions at the biomaterial interface can be optimised through the introduction of a protective coating that meets the application requirement.[31, 40] Surface coatings have been bioengineered to not only be biocompatible and bio inert but also wear, corrosion and friction resistant.[30] Due to the versatility and wide range of tunable physico-chemical properties, DLC films have been extensively investigated and widely reported in the open literature as coatings to carbon-based biodevices.[13, 16, 30-33, 39-41, 44, 52, 56]

Nowadays, DLC films are mostly applied to cardiovascular and orthopaedic fields, but they can also be found as coatings for contact lenses and chirurgical tools.[30-31, 40] DLC coatings have been used on orthopaedic implants due to their reduced wear, corrosion and debris formation (Figure 1.3).[39, 69] For instance, articular joint prostheses made of UHMWPE have been coated with DLC to reduce the formation of wear debris.[40, 64] Moreover, DLC-coated stainless steel roads have promoted osteoblast and fibroblast

cells adhesion at the bioimplant interface. *In vivo* tests involving DLC-coated rods implanted in rats have also showed no adverse effects towards the carbon-based coating.[25]

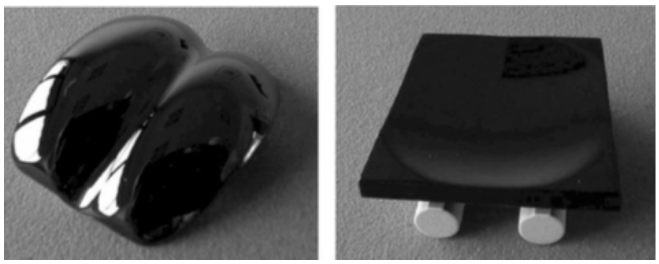


Figure 1.3. Example of a talar (left) and tibial (right) components of an ankle joint replacement coated with DLC films (adapted from [31]).

The ability of carbon to promote hemocompatibility by minimizing thrombosis and platelet activation at the biomaterial's interface allows the usage of carbon thin films on cardiovascular stents, guidewires and pacemakers (Figure 1.4).[16, 64] DLC has been utilised as a protective coating on metallic implants for the purpose of limiting the release of metallic ions, such as chromium, nickel, molybdenum, and manganese, a critical factor in thrombus formation.[64] Also, thromboembolic incidences happening at mechanical heart valves interface have been reduced after DLC surface modification, preventing long-term anticoagulation.[70] Furthermore, DLC films have been combined with cytotoxic elements (*e.g*. silver, copper, vanadium, *etc*) for applications where cell or bacterial adhesion is not desired.[31]

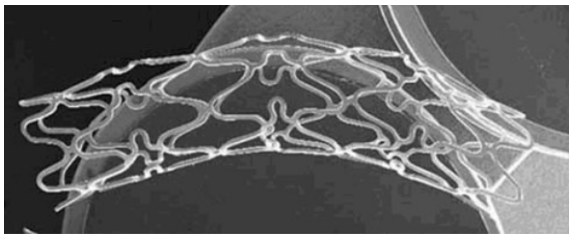


Figure 1.4. SEM image of a ~14 mm length biodiamond stent produced by Plasmachem (adapted from [41]).

DLC may find use in other medical applications, such as contact lenses[64, 67] and retinal prosthesis[39], where DLC coatings were found to improve lenses' index of refraction and UV protection and restore the sight of blind patients. DLC was also found to be neurocompatible and has been used as a coating in neuronal microprobes[33, 52, 67] and

nanoporous electrodes[39]. Finally, carbon coatings have demonstrated antifungal performances, which is key for all implanted biomaterials and chirurgical tools.[71]

All of the aforementioned applications of DLC coatings in the biomedical field have shown the tremendous potential of DLC films as protective coatings for optimisation of biodevice performances *in vivo*. Several literature studies and reviews have reported how DLC's bioinertness, biocompatibility and hemocompatibility stimulate an improved bioresponse, when compared with other types of biomaterials.[33, 64, 67] However, the origin of the outstanding bioresponse towards DLC coatings is not yet fully understood, and there is currently great interest in understanding what role carbon surface chemistry might play in determining DLC's performance as a biomaterial.[16, 30-31, 35, 37, 40, 72-74]

A small number of *in vivo* tests have been conducted on DLC coatings and have shown that adapting the *in vitro* results to the extreme environmental conditions that DLC coatings are exposed to *in vivo* is rather challenging and may result in the failure of the implantable biodevice.[25, 31] Also, biological interactions are known to be extremely sensitive to DLC surface physico-chemical properties.[52, 60, 62] Increasing interest has been generated in understanding DLC atomic structure and physico-chemical composition in order to predict its performance *in vivo*.[30, 52] This thesis aims at contributing to the understanding of carbon interfacial interactions with biological media and predicting how these interactions may impact on the bioresponse towards carbon materials. The next section provides an overview of interactions that are important at the biomaterial interface, with special emphasis on carbon/biological fluids interactions.

2. Biointeractions at Materials Interface

When a material is implanted in the human body, biointeractions are established within seconds after implantation; the outcome of such interactions is thought to

ultimately determine the long-term bioresponse towards the biomaterial.[16] Once in the body, time-dependent events are established at the biomaterial's surface, starting with a water layer coverage followed by the biomaterial's interaction with solvated ions.[26, 30, 66, 75] In the early stages after implantation, a dynamic competition for surface sites is initiated between small biomolecules, which are present in biological fluids and tissues and transport fast to the surface. The most abundant biomolecules found in common fluids (*e.g.* plasma, serum, synovial fluid, tears) are proteins and lipids and their adsorption at the biomaterial interface is known to form a conditioning layer which determines the outcome of more complex phenomena that occur over longer timescales, such as cellular binding interactions, adhesion or enzyme function (Figure 1.5).[26, 76-79] Hence, the long-term physiological response is attributed to the adsorbed lipid/protein conditioning layer, rather than the biomaterial surface itself.[26, 66]

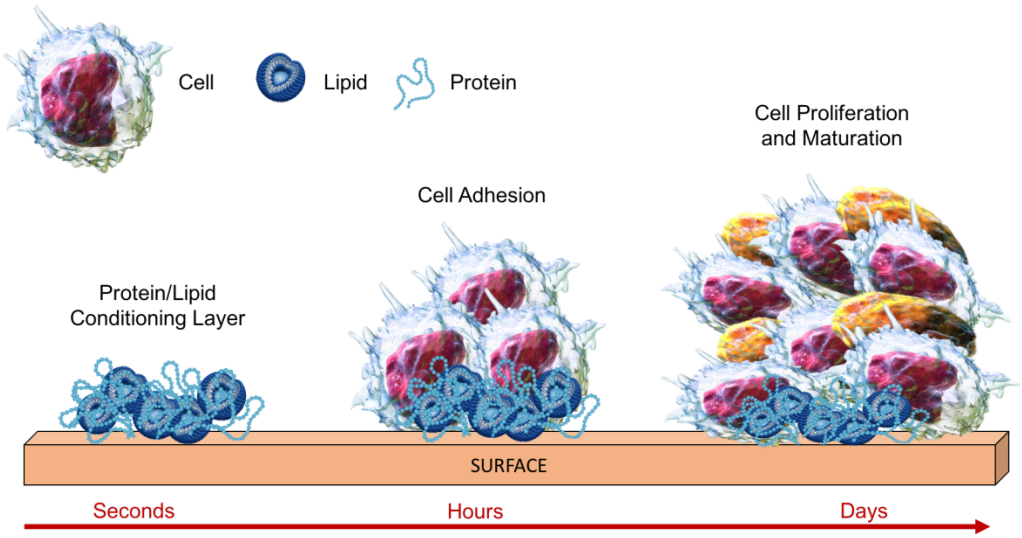


Figure 1.5. Diagram of biofilm formation at biomaterials surface.

Therefore, considerable attention has been dedicated to investigate biomolecule interactions with biomaterials and to develop novel methods for promoting or preventing their adsorption at the biomaterial interface.[26] Several studies have been focused on understanding how to tune and modulate host/protein interaction since, from the cellular point of view, proteins are known to define the structure and composition of the foreign biomaterial surface.[16, 30, 75] In particular, studies on carbons

bioresponse have attributed carbon's good biocompatibility to the formation of a protein layer at the interface.[80] Proteins, however, do not seem to be the solely contributors to the host material bioresponse and there is still a great controversy regarding the structure and dynamics of protein-layer formation at the interface and its role in the material's biocompatibility.[80]

As a direct correlation between the protein-biomaterial interface and the long-term bioresponse has not been established to date, other interfacial interactions at the biomaterial surface should also be taken into consideration.[81] Even though the literature is comparatively sparse regarding lipid/biomaterial interactions, the importance of including lipids in investigations of material bioresponses has been emphasized by several researchers.[26, 82-83] Early studies by Baier and Dutton[84] had in fact demonstrated that significant amounts of lipids co-adsorb with proteins at early times after a material comes in contact with blood. Lipids are present in biological fluids in concentrations that are similar to those of proteins and the composition of the adsorbed lipid layer is a key mediation of long-term biocompatibility towards the biomaterial.[85-86] Moreover, lipids are also known to modulate surface-protein interactions and critically determine the performance of biomaterials *in vivo*.[87-89]

The next section includes a description of lipids present in biological fluids, with special emphasis on phospholipids. Additionally, the role of lipids on the bioresponse towards implanted materials is addressed. In particular, lipid-carbon interaction is reviewed in relation to carbon surface properties and biological media composition. Finally, the impact of lipid/carbon interactions on the long-term bioresponse towards carbon, such as cell adhesion and platelet activation, is examined.

2.1. Phospholipids in Biological Media

Lipids are a heterogeneous group of biomolecules that display poor solubility in water and high solubility in organic solvents of low polarity.[90] Lipids are known to play diverse roles in biological media, from acting as a structural component of cell membranes, participating in signalling pathways and serving as energy storage sources.[91] The wide range of lipid functions in biological media is directly related to their remarkable structural diversity, driven by biochemical transformations and modifications.[91] More than 200,000 lipid structures have been identified to date and efforts towards categorising such structures have been developed.

The need to establish a comprehensive classification, nomenclature and chemical representation system of lipid structures has been recently addressed by LIPID MAPS (Lipid Metabolites and Pathways Strategy). According to LIPID MAPS, lipids are classified based on two fundamental building blocks: (i) ketoacyl and (ii) isoprene groups, as shown in Figure 1.6.[91] Hence, lipids are defined as amphiphilic molecules that may originate either by (i) carbanion-based condensations of thioesters and/or (ii) by carbocation-based condensations of isoprene units.[91]

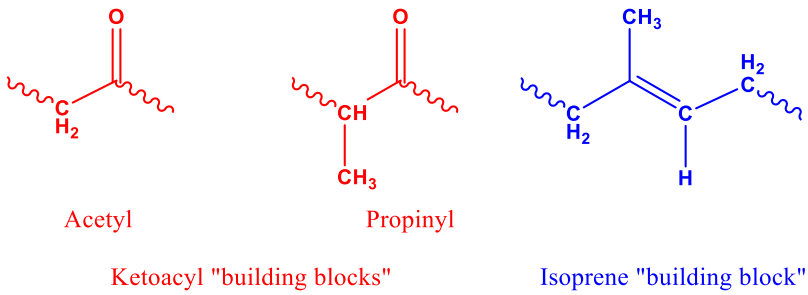


Figure 1.6. Fundamental two building blocks of lipids, according to LIPID MAPS classification: ketoacyl and isoprene groups; adapted from [91].

Based on the LIPID MAPS classification, lipids have been divided into eight categories according to their ketoacyl or isopropene subunits, as shown in Figure 1.7. Lipids such as fatty acyls, glycerolipids, glycerophospholipids, sphingolipids, saccharolipids and polyketides, which derived from condensation of ketoacyl subunits are represented in red whereas sterol and prenol lipids, derived from condensation of isoprene subunits, are shown in blue.[91]

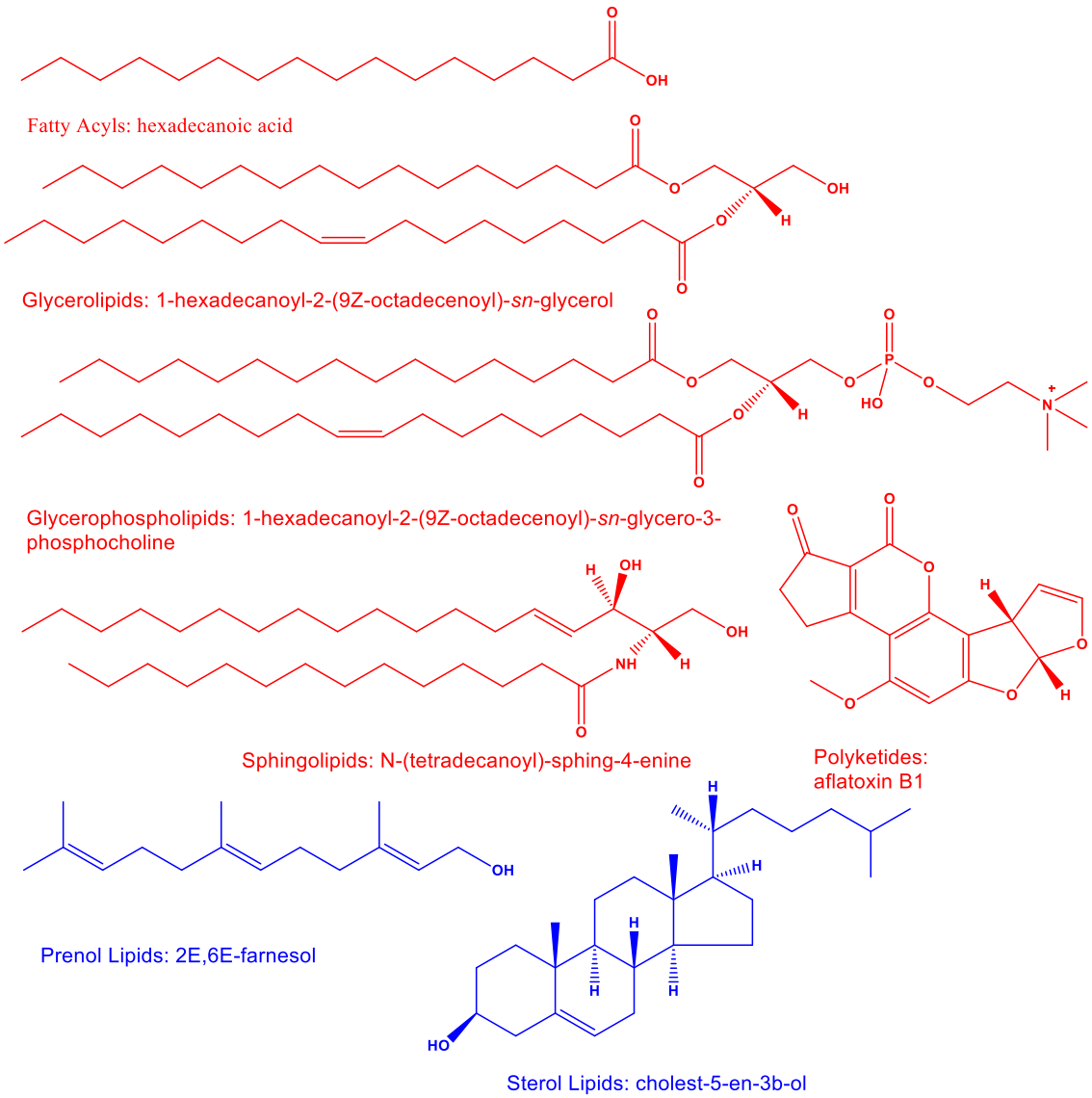


Figure 1.7. Representative structures of lipids, according to LIPID MAPS classification. In red are shown examples of lipids derived from condensation of ketoacyl subunits and in blue lipids derived from condensation of isoprene subunits; adapted from [91].

Glycerophospholipids, also referred to as phospholipids, are an important subclass of lipids that play a role as structural components in membranes[92-93] and in aggregates for the transport of other lipids such as triacylglycerols.[94-95] Their amphiphilic nature comprises a hydrophilic head group, which includes glycerol as the backbone and a phosphorus-containing molecule, in combination with two hydrophobic, nonpolar and uncharged hydrocarbon chains (Figure 1.8).[96] The phosphate group is further esterified with an additional alcohol, the most common one being choline, serine and ethanolamine in the case of phosphatidylcholine (PC), phosphatidylserine (PS) and

phosphatidylethanolamine (PE), respectively.[97] Not only the head group defines the nature of phospholipid, but also the non-polar moieties influence on the phospholipids physico-chemical properties. For instance, the two long hydrocarbon chains can vary in length and degree of saturation thus defining important phospholipid properties, such as melting point, fluidity and water solubility.[97]

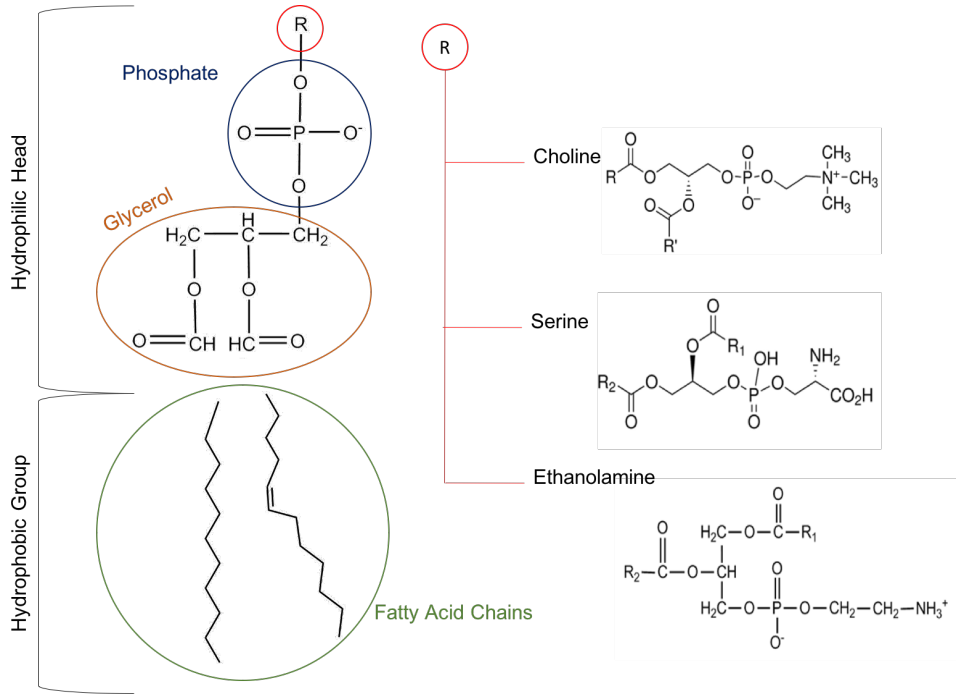


Figure 1.8. Glycerophospholipid structure: hydrophobic group, which includes two fatty acid chains and hydrophilic head group, which includes glycerol, phosphate and R groups. R group corresponds to choline, serine and ethanolamine in the case of phosphatidylcholine (PC), phosphatidylserine (PS) and phosphatidylethanolamine (PE), respectively.

Glycerophospholipids are the main components, and the structural building blocks of biological membranes, acting as a selective barrier between the intra- and extra-cellular environments.[92-93] Stabilised by non-covalent forces, the phospholipid bilayer is a two-dimensional structure built of amphipathic molecules, which consist of two adjacent layers of phospholipids with associated proteins and carbohydrates.[98] The variety of phospholipids present in natural biological membranes strongly depends on the type of membrane (*e.g.* cell or virus) and on its function (*e.g.* blood cells or neurons).[97] For instance, typical plasma membranes contain an asymmetric distribution of hundreds of

different phospholipids, such as phosphatidylcholine (PC), sphingomyelin (SM), gangliosides (GM), phosphatidylethanolamine (PE) and phosphatidylserine (PS).[99-100] Anionic phospholipids, *e.g.* PS, are preferentially distributed in the inner leaflet of the plasma membrane,[101-102] while neutral and zwitterionic lipids, such as PC, are found in the outer leaflet, facing the extra cellular medium.[100, 102]

Besides the functional role of phospholipids in biological membranes, phospholipids also act as boundary lubricant molecules in natural synovial joints.[103] Surface active phospholipids (SAPL) are present in synovial fluids as aggregates, which consist of almost 50 % PC in addition with small % of other phospholipids, such as PS and PE.[104] SAPLs are known to act as an efficient boundary lubrication system which remarkably decreases friction and wear corrosion associated with natural cartilage degeneration, such as osteoarthritis.[103, 105-106] Moreover, synthetic vascular prostheses have shown the formation of atherosclerotic plaques at the bioimplant walls, a process which has been attributed to lipid adsorption at the interface.[107]

Several studies have been dedicated to produce phospholipid membranes *in vitro*, either to mimic the physico-chemical properties comparable to those of biological membranes or/and to understand and modulate the aforementioned bioresponse towards implanted biomaterials.[108] Biological membranes, however, represent a complex system and their anisotropic structure and specific composition are challenging to reproduce.[108] One of the simplest model lipid aggregates used to mimic biological membranes is called liposome, which consists of a vesicle containing a water core enclosed by at least one phospholipid bilayer.[109-110]

2.2. Phospholipid Liposomes

Lipid vesicles, also called liposomes, are used to mimic the behaviour of biological membranes *in vitro* in a broad range of applications, such as drug delivery,[111] gene therapies[110, 112], protein support[113] and as platforms to understand the interaction of biological fluids with implanted materials.[114] Due to the amphipathic nature of phospholipids, liposome formation results from a thermodynamically stable molecular structure which is spontaneously formed in water; phospholipids in the liposome

arrange so that their hydrophilic head groups are exposed to water, while their hydrophobic tails form the inside of the bilayer.[111, 115]

Liposomes are commonly defined according to their (i) composition (ii) structure and (iii) preparation method.[110-111] Liposome features are strictly related with the nature and type of phospholipids used in the liposome formulation. They can include natural or synthetic phospholipids which show moderate biocompatibility and biodegradability.[110, 116] Advantages on the usage of natural phospholipids, over the synthetic choice, comprise their wide availability in nature, being derived from renewable sources and produced in more ecological friendly processes[97] As previously seen on the previous section, examples of the most common natural phospholipids are PC, PS and PE.

On the other hand, liposomes containing synthetic phospholipids permit control over the chemical specifics, such as head group charge and saturation/length of fatty acid chains. However, their poor availability and biocompatibility, when compared with liposomes-containing natural phospholipids, affect their usage in biological applications.[97] Thus, the advantages of using natural phospholipids, over the synthetic ones, must be taken into account when the aim is to reproduce, as closely as possible, the biological phospholipid bilayer, *e.g.* interaction of biological membranes with biomaterials. In this work, liposome suspensions were prepared using natural phospholipids, *i.e.* PC and PS, in a ratio which is found in natural cell membranes.

Regarding structure, liposomes present diameters (d) that can vary from 20 nm to several micrometers, as reported in Figure 1.9.[110, 116] Liposomes that comprise a single phospholipid bilayer enclosing the aqueous solution are classified as unilamellar liposomes and include small (SUV, $d < 100$ nm), large (LUV, $d > 100$ nm) and giant (GUV, $d > 1000$ nm) unilamellar vesicles. Liposomes with more than one layer of phospholipids are classified as oligolamellar vesicles (OLV, $100 < d < 500$ nm) and multilamellar vesicles (MLV, $d > 500$ nm).[110, 116]

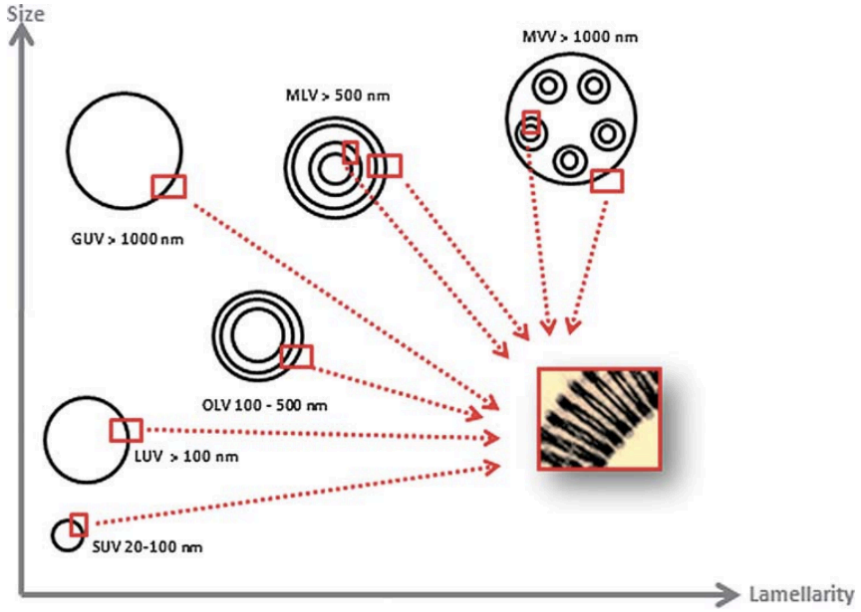


Figure 1.9. Size and structure of liposomes defined as small unilamellar vesicles (SUV) d < 100 nm, large unilamellar vesicles (LUV) d > 100 nm, giant unilamellar vesicles (GUV) d > 1000 nm, oligolamellar vesicles (OLV) 100 < d < 500 nm or multilamellar vesicles (MLV) d > 500 nm (adapted from [116]).

Liposome physico-chemical properties, in particular size and lamellarity, can be regulated through the appropriate formulation methodology.[96] Several liposome preparation methods have been developed, the most common ones being the Reverse-Phase Evaporation (REV)[115] and Bangham[116-117] methods. REV method consists on the preparation of a lipidic film by organic solvent evaporation. Subsequently, the phospholipids are re-suspended in another organic solvent under an inert atmosphere. Due to the amphiphilic nature of phospholipids, LUV and OLV are spontaneously formed once an aqueous buffer is added.[116] Following the removal of the organic solvent, the phospholipid vesicles can be further extruded through polymeric filter, resulting in homogeneous suspension of LUV/GUV.[116, 118]

One of the most widely used techniques for liposome formulation is the Bangham method,[116-117] which is the method extensively used in this report. Briefly, a selected organic solvent, which contains a dispersion of phospholipids, is evaporated thus resulting on a lipidic thin film. Afterwards, the lipidic film is hydrated with an aqueous buffer solution, added to the system under agitation at a temperature above the lipid transition temperature. This method yields MLV suspended in the aqueous buffer, which can go through subsequent sonication and extrusion cycles thus resulting in SUV or LUV

with a high homogeneity on size distribution.[116] In this thesis, liposome suspensions, prepared according to the Bangham method, were utilised to understand the interaction of biological lipid aggregates and membranes with host materials. The following section includes a discussion on the factors influencing liposome/host interaction, as well as a review on liposome's response to macroscopic surfaces, with special emphasis on carbon/liposome interactions.

2.3. Interactions of Liposomes with Macroscopic Surfaces

The interaction between liposomes and macroscopic surfaces is known to depend on a wide range of parameters; the formation of multiple lipidic structures at the interface can be achieved by varying surface chemistry, liposome formulation and/or buffer composition. McConnell *et al*.[119] were the first to study the interaction between liposomes in suspension with macroscopic surfaces and since then, many groups have studied liposome/surface interactions with applications in biosensors, cell-signalling and as a platform for protein studies.[98, 108, 120-124] However, there is limited information on phospholipid adsorption at carbon coatings,[107, 114, 121, 125-127] and no information is available on the mechanism of adsorption and its relation to carbon surface chemistry. This section comprises an overview of (i) factors influencing liposome/surface interaction, (ii) liposome/macroscopic surfaces interaction and (iii) liposome interaction with carbon surfaces.

2.3.1. Factors Influencing Liposome/Surface Interactions

When approaching solid surfaces, liposomes can adopt different adsorption structures or be repelled by the surface, as shown in Figure 1.10. When adsorbed, liposomes can maintain their spherical shape and adsorb as supported vesicle layers (SVL). Additionally, liposomes can abandon their spherical structure, spontaneously rupturing and spreading, thus producing a planar supported lipid bilayer (SLB).[128-130] Besides, SVL and SLB structures, a supported lipid monolayer (SLM) can also be obtained.

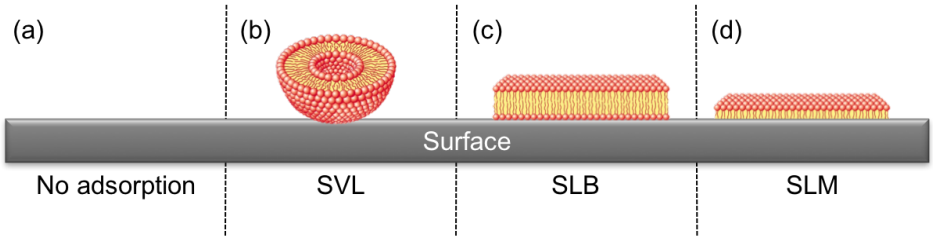


Figure 1.10. Schematic representation of liposome interaction with macroscopic surfaces. **(a)** Inhibited adsorption, **(b)** intact vesicle adsorption (SVL), **(c)** formation of a supported lipid bilayer (SLB) and **(d)** formation of a supported lipid monolayer (SLM).

Several studies have been focused on understanding the driving forces involved in determining the outcome of liposome adsorption at solid surfaces.[131-132] The outcome is thought to be influenced by electrostatic interactions, hydrogen bonding and hydrophobic interactions.[128, 133-134] The balance between the aforementioned interactions is direct related with the outcome structure of liposomes at the solid surface and it is known to strongly depend on buffer, liposome and surface physico-chemical properties, as discussed in the following sections.[114]

2.3.1.1. Influence of Buffer

Previous works have been focused on the effects of buffer temperature,[135-136] pH,[135, 137] ionic strength,[120, 135, 138] and valency,[137], *i.e.* mono- and divalent ions,[122, 132, 135, 138-143] on the interaction between liposomes and macroscopic surfaces. Lipid phase transitions are known to be strongly dependent on the temperature of the medium.[135-136] Liposome fusion and SLB formation is related to the fluidity of the bilayer, which is controlled by the phase transition temperature of the phospholipids present at the liposome. Additionally, the formation of a SLB at macroscopic surfaces, through the vesicle fusion method, is known to be temperature dependent. For a high critical vesicle coverage, a low temperature is required for vesicle rupture and SLB formation.[135-136]

As previously discussed, the interactions between liposomes and macroscopic surfaces are related to electrostatic interactions. Such interactions can be tuned by controlling the buffers pH and ionic strength, which influences the degree of ionisation of both surfaces and liposomes.[135] Macroscopic surfaces possess charged groups that

undergo ionization at different pH values, which in turn may affect the electrostatic interaction with liposomes of different charges.[135] For instance, PS has a negatively charged head groups for pH > 4, while in the case of the zwitterionic phospholipid PC, its charge is neutral for any pH above 4 and positive for pH < 4. Thus, the outcome between PC/PS liposome and macroscopic surface interactions can be modulate by varying the pH and consequently the charge of both liposome and surface charged groups, promoting or inhibiting adsorption at the interface.

Additionally, ionic strength is known to play an essential role in the modulation of surface and liposome electrostatic interactions, specifically by affecting both surface and liposome ζ-potentials, which significantly affects the outcome of liposome adsorption at the interface.[135] The interaction of surfaces and liposomes with similar charge are expected to be dominated by repulsive interactions, and little to no adsorption is observed at low ionic strength. Increase of ionic strength can lead to a switch on liposome and/or surface ζ-potential resulting in liposome adsorption and fusion at the macroscopic surface.[144-145]

Ionic valence is also a critical factor for determining the outcome of liposome/surface interaction, especially on liposomes containing phospholipids with charged head groups.[135] Various experimental methods have been applied in the past to understand the conformational changes in the phospholipid polar head groups when a dication, such as calcium (Ca^{2+}) and magnesium (Mg^{2+}), is added to the medium.[140-141, 143, 146] For instance, Ca^{2+} ion is known to greatly decrease the electrostatic repulsion between negative charged liposomes and negative charged surfaces, thus promoting liposome fusion and SLB/SVL formation at the macroscopic surface.[122, 132-133, 135] The dication binds to the phosphate group present on the phospholipids hydrophilic head, thus bridging two adjacent lipid molecules and neutralizing the overall net charge of liposomes.[135] This effect has extensive implications on the interaction of liposomes with solid surfaces which exhibit the same net charge; concentrations of Ca^{2+} ion as low as 25 μM[147] up to 2-100 mM[122, 132, 137] are known to promote liposome rupture and SLB formation.

2.3.1.2. Influence of Lipid Composition

Considerable attention has been dedicated to the influence of liposome size,[120, 138, 148-150] composition[128, 134] and charge[129, 132] on the interaction of model lipid aggregates with macroscopic surfaces. Seifert *et al.*[148] predicted that, for a given surface, large liposomes would deform more and spontaneously rupture at the surface, while for liposomes a few nanometres in radius, no adsorption at the macroscopic surface is observed. Later, Reviakine *et al.*[138] also estimated that the interaction of isolated liposomes with macroscopic surfaces is strongly dependent on the liposomes radius and there is indeed a critical adsorption radius, below which no liposome adsorption is observed. Recently, Dimitrievski and Kasemo[150] report computational modelling on the liposome/surface interaction and showed that liposomes with a radius $r > 150$ nm fuse at the surface, forming a SLB, and liposomes with a radius $r < 25$ nm do not interact with the surface and no adsorption was observed.

Similarly, Dimitrievski and Kasemo[128, 134] have also developed computational modelling on different liposome compositions interacting with macroscopic surfaces, reporting that, for a given charged surface, liposome deformation depends on the type and charge of phospholipids present on the liposome. For instance, neutral liposomes may interact with a macroscopic surface without undergoing a significant deformation and resulting in a SVL at the interface. They also estimated that liposomes that contain more than 40% positively charged phospholipids, being the remaining percentage made of zwitterionic phospholipids, would rupture spontaneously at a negatively charged surface. On the other hand, vesicles with more than 67% negatively charged phospholipids, such as PS, would not adsorb at macroscopic surfaces with the same charge.[128, 134] These results were also confirmed through experimental procedures which showed a strong correlation between liposome charge and its electrostatic attraction/repulsion towards macroscopic surfaces.[120, 129, 132] Nevertheless, for a given vesicle composition, the degree of liposome deformation at the interface, and the formation of multiple lipidic structures, *i.e.* SVL, SLB and SLM, are also strongly correlated with the surface physico-chemical properties.

2.3.1.3. Influence of Surface Physico-Chemical Properties

The influence of surface chemistry,[77, 117, 122, 126, 151-153] wettability,[151, 154-155] charge density[147, 156] and roughness[151, 157] on lipid/surface interactions has been investigated for decades. Several studies have focused on the interaction of lipid aggregates with model solid surfaces, such as SiO_2,[122] TiO_2,[114] and mica[129] and showed that the wettability of solid surfaces is a critical factor that affects the mechanism of liposome adsorption at the solid/liquid interface.[114, 151, 154-155, 158] It has been reported that liposome adsorption on hydrophobic surfaces results in the formation of a SLM while for hydrophilic surfaces either SVL or SLB can be observed.[120, 153, 159-160] Tero *et al*.[114] reviewed the influence of hydrophilicity on the liposome/surface interaction and also showed that the presence of –OH groups at the solid substrate increases the hydrophilicity of the substrates and ultimately the way of liposome adsorption. Hydrophilic surfaces usually possess a higher density of –OH groups that results in hydrogen-bonding with water molecules. The increase of hydration repulsion forces between the stable layer of water molecules attached to the phospholipid head groups and the water bound to the solid substrate act as a barrier to the adsorption of liposomes at solid surfaces, thus resulting in different lipidic structures at the interface.[154]

Control over surface wettability is a prerequisite condition for liposome fusion and adsorption at the interface, but not always a sufficient condition.[114, 156] Surface charge is also key on determining the rate and yield of surface reactions at macroscopic surfaces. As previously discussed (section 2.3.1), electrostatic interactions are known to critically determine the interaction of liposomes with macroscopic surfaces, in which surface modification can be effectively used to modulate surface charge density and ultimately define the degree of electrostatic interactions.[156] Cha *et al.*[156] reported liposome interactions with standard self-assembled monolayers (SAMs) with varied surface charge density, from positively ($–NH_3^+$) to negatively ($–COO^-$) charged. They have showed that, for a given liposome charge, there is a critical surface charge density of ~75%, for both positive and negative charged surface, above which liposomes would fuse and form a SLB.[156]

Table 1.2 summarises relevant examples for this work on the outcome of liposome interaction with standard macroscopic surfaces, such as SiO_2, TiO_2 and mica. As previously discussed, different conformations of liposome adsorption at macroscopic

surfaces strongly depend, but are not limited, on liposomes charge and surface chemistry. An example of the effect of different contributions on liposome conformation at macroscopic surfaces is the interaction of negatively charged liposomes with SiO_2 (Table 1.2.). For the same surface chemistry and liposome net charge, the outcome of such interaction can vary from SLB to SVL or no adsorption at all. Hence, all the aforementioned factors, such as buffer ionic strength and temperature, liposome type and size must also be taken into consideration for liposome interactions at macroscopic surfaces.

Table 1.2. Outcomes of the interaction between liposomes and standard macroscopic surfaces; possible outcomes are: no liposome adsorption, supported lipid monolayer (SLM), bilayer (SLB) or vesicle layer (SVL).

Liposome Charge	Surface	Outcome	Ref
Negative	Pt	SLM	142
	TiO_2	No adsorption	161
		SVL	122
	SiO_2	SLB	134, 161
		SVL	134
		No adsorption	132, 134
Positive	SiO_2	SLB	134 132
	glass	SLB	147
	(–OH^-) SAMs	SLB	156
	(–NH_3^+) SAMs	No adsorption	156
Neutral	TiO_2	SVL	134, 153
	SiO_2	SLB	77, 117, 122, 132, 134, 142, 151, 153-155
		SLM	154-155
	mica	SVL/SLB	138
		SLM	126
	(–OH) SAMs	SVL	156
	(–NH_3^+) SAMs	SLB	156
	glass	SLB	147
	polydopamine	SLB	152
	Pt	SVL	153
	Au	SVL	77, 120, 153
	Si_3N_4	SLB	153

2.3.2. Liposome Interactions with Carbon Surfaces

Carbon/lipid interfacial interactions have grown in importance for studying carbon nanomaterials in the areas of drug delivery and toxicity as lipid-nanoparticle interactions are known to affect the nano-bio interface.[162] Recently, Liu[163] reviewed the interaction of model lipid aggregates with carbon nanomaterials such as graphene, carbon nanotubes (CNT) and nanodiamonds (NDs) and their applications as drug delivery agents and biosensors for specific biomolecular interactions.[164] Additionally, lipid-carbon interfacial interactions that occur in the lung have been found to play an important role in determining the uptake of carbon nanomaterials via inhalation and, consequently, their effects on human health. Experimental studies with lung surfactants show that nanosized carbon particles are rapidly coated by lung phospholipids, which in turn affect protein adsorption by forming a tightly bound lipid corona.[165-166] Lipid formulations are also used to disperse nanosized carbon particles and to facilitate their cellular uptake and/or transport.[24] In particular, graphene has been intercalated in lipid membranes and its efficiency as a biocompatible material has been demonstrated.[114, 121, 127, 133, 163, 167-170]

Recently, the potential of graphene coatings as bio- and chemical sensors has also been explored.[127, 164, 168, 171-172] Graphene has been interfaced with phospholipid membranes, and the efficiency of lipid/graphene interaction has been correlated to the ability to sense specific protein adsorption and biomembrane-associated interactions.[164] The interaction of graphene coatings with model lipid aggregates is thought to be regulated by similar parameters to those present on the interaction of lipids with standard macroscopic surfaces, such as surface wettability, charge density and chemical groups. Thus, hydrophobic graphene substrates preferentially adsorb intact vesicles (SVL) or SLM and hydrophilic substrates tend to form a SLB at the interface.[171-172] Additionally, molecular dynamic simulations of model lipid aggregates with graphene coatings have shown that distinct liposome architectures at the graphene interface are strictly correlated with the polarity of the graphene substrate.[168]

Nevertheless, research on the interaction of model lipid aggregates with DLC coatings is sparse when compared with other types of carbon coatings.[107, 125-126] As previously discussed, DLC films are used as coatings in bioimplanted materials which are in direct contact with biological fluids, more specifically with lipid aggregates. Understanding the interaction between DLC and model lipid aggregates is imperative for applications of

DLC coatings in cardiovascular and orthopaedic fields, where lipid adsorption must be elucidated.

In the cardiovascular field, the performance of a biomaterial *in vivo* has been improved by using DLC films as coatings, which are known to prevent platelet adhesion and thrombus formation. However, thrombogenic effects are related to the formation of a lipidic film at the bioimplant interface and understanding the interfacial interaction between lipid aggregates and DLC coatings may help in enhancing DLC's anti-thrombogenic behaviour. On the other hand, DLC films have been widely used in the orthopaedic field, in the form of coatings for articular joint prosthesis; however, DLC interaction with model lipid aggregates is underreported. The presence of surface active phospholipids (SAPL) at the bioimplanted material interface are known to act as boundary lubrication systems which enhance wear and corrosion resistance of the biomaterial. Thus, understanding their interaction with DLC coatings may help in optimising DLC's tribological properties.[103, 105-106]

To the best of the author's knowledge the interaction of model lipid aggregates with DLC films has only been reported by a few groups in the literature.[107, 126, 173] Cui and his co-workers[107, 173] reported on carbon nitride (CNx) films interacting with liposomes and showed that a reduced lipid coverage is observed for CNx-coated surface, when compared with a non-coated surface. It was also reported that a control over the amount of chemical groups present, such as N and O and sp^2/sp^3 fraction may play a significant role on the interaction of DLC coatings with lipid aggregates.[107, 125] Diociaiuti *et al.*[126] also reported on the mechanism of liposome fusion and adsorption at DLC's surface, and have attributed different lipidic architectures to DLC's physico-chemical properties.[126]

The role of DLC surface chemistry has been invoked to explain different lipidic conformations at DLC surfaces, however a controllable method to form well-defined lipid structures remains elusive. Additionally, no information is available on the mechanism of liposome adsorption at DLC surfaces and its relation to carbon surface chemistry. A section of this thesis aims to answer some key points that are still not clear and/or have not been addressed to date:

- How and why is the liposome rupture initiated at DLC surfaces?
- What is the role of surface physico-chemical properties, in particular DLC surface charge, on the conformation of liposome adsorption?
- How to design strategies based on molecular self-assembly and DLC surface chemistry to promote/prevent liposome adsorption at carbon surfaces?

Answering these questions will also help to elucidate the origin of the long-term bioresponse towards carbon materials, with the aim of improving DLC's performance *in vivo* by preventing undesirable bioresponses. The next section includes an overview on carbon's long-term interactions *in vivo*, in particular DLC's bio- and hemocompatibility.

2.4. DLCs Long-Term Bioresponse

The long-term bioresponse towards carbon materials, in particular DLC coatings, has been widely reported.[30, 35, 73] Several studies have been focused on understanding how to tune and modulate carbon's physico-chemical properties, such as surface free energy,[174-175] wettability,[32, 175] surface chemical groups[30, 174, 176] and charge[176] and roughness[174] in order to optimise carbon's bioresponse. The design of carbon surfaces whose physico-chemical properties allow simultaneous control of cellular response and also possess anti-thrombogenic and anti-fungal behaviours has been a challenge to date.

For instance, thrombogenic effects at the biomaterial interface are a major concern when designing a biomaterial which is in direct contact with blood.[28, 31] In particular, platelet adhesion, activation and aggregation at the foreign material are known to be crucial factors affecting the performance of the biomaterial as they are known to precede thrombus formation and embolization.[31, 44] Carbon-based coatings, such as DLC,[74] pyrolytic carbon,[28] and graphene[14, 177] have been a promising choice of material to control and reduce platelet adhesion and activation.[31] Varied research has reported the implications of wettability of carbon coatings on platelet adhesion and activation, and revealed that higher surface hydrophobicity implies a more satisfactory inhibition of thrombotic events.[31, 44, 74, 178-179] Similarly, studies on the interaction of carbon coatings with endothelial cells have shown that an increase of hydrophobicity of DLC films results on a better cellular adhesion and proliferation at the interface.[31, 74, 175, 180]

Additionally, the interaction of fibroblasts with carbon coatings has also been widely reported.[181-183] Fibroblasts are known to play a particularly important role in wound healing and inflammation, being responsible for driving the progression of tissue repair and functional recovery.[44] Thus, understanding and modulating the response of fibroblasts to an implantable biomaterial is key to ensure functionality and integration of the foreign material.[182-184] The influence of substrate wettability on the adhesion of fibroblasts has been previously reported for different carbon films.[181-183] For instance, Ryoo *et al.*[181] reported on fibroblast adhesion on carbon thin films and showed a higher fibroblast affinity for carbon-based surfaces than for glass, which was attributed to the wettability and roughness of DLC.[181]

Efforts towards a surface coating which is able to reduce the susceptibility of a medical device to biofilm formation have also been explored.[185-186] The development of surfaces that can inhibit microbial, *i.e.* fungal and bacterial, adhesion and colonization has been addressed as an emerging area of research.[187-188] Recent developments in anti-infective carbon-based biomaterials have provided novel approaches to prevent biofilm formation, caused by bacteria[185-186, 189-190] and fungi[191-192] agglomeration at the biomaterial interface.

However, the literature is contradictory with respect to the main reason for the excellent long-term bioresponse of carbon coatings.[31] Some research shows that higher hydrophobicity implies higher cellular and platelet adhesion and spreading, whilst others report that hydrophilicity is a key factor on preventing thrombus and fungi biofilm formation.[44, 74] A special effort is made in this thesis towards the understanding the influence of carbon's physico-chemical properties, in particular wettability, on the induced long-term bioresponse.

3. Aim of this Thesis

Due to their unique combination of physico-chemical properties, carbon materials have been used in a wide range of applications. In particular, DLC films have been extensively used as coatings for carbon-based biodevices and despite the outstanding bioresponse towards this class of materials being widely reported, the origin of DLC's performance *in vivo* has not been addressed to date. It has been proposed that the long-term bioresponse is attributed to the formation of a lipid/protein passivated layer at the DLC's interface formed immediately after implantation.

The main aim of this thesis is to contribute to a fundamental understanding of the influence of DLCs physico-chemical properties on the host bioresponse towards carbon, in particular how to modulate DLC's interaction with model lipid aggregates.

Firstly, the influence of DLC's physico-chemical properties, such as surface roughness, chemistry, wettability and charge density, in lipid/carbon interactions is expected to be elucidated. Additionally, this study aims at establishing a relation between liposome's preparation method, type and nature of phospholipids present on the liposome and liposomes properties in suspension.

Secondly, this thesis intents at monitoring *ex situ* and *in situ* the interactions of phospholipid liposomes with macroscopic carbon surfaces. It is expected that the amount and mode of liposome adsorption at carbon surfaces are correlated to variations on carbon surface chemistry and buffer composition.

The final objective of this thesis is to predict long-term induced bioresponse towards DLC coatings with regards to its bio- and hemocompatibility by measuring the antithrombogenic and antifungal behaviours of DLC coatings.

4. References

1.Lee, J.; Kim, J.; Hyeon, T., *Advanced Materials* **2006,** *18* (16), 2073.
2.An, L.; Fu, Q.; Lu, C.; Liu, J., *J. J. Am. Chem. Soc.* **2004,** *126*, 10520.
3.Baughman, R. H.; Zakhidov, A. A.; de Heer, W. A., *Science* **2002,** *297* (5582), 787.
4.Gooding, J. J., *Electrochimica Acta* **2005,** *50* (15), 3049.
5.Morales-Lara, F.; Pérez-Mendoza, M. J.; Altmajer-Vaz, D.; García-Román, M.; Melguizo, M.; López-Garzón, F. J.; Domingo-García, M., *The Journal of Physical Chemistry C* **2013,** *117* (22), 11647.
6.De Volder, M. F. L.; Tawfick, S. H.; Baughman, R. H.; Hart, A. J., *Science* **2013,** *339* (6119), 535.
7.Feng, L.; Xie, N.; Zhong, J., *Materials* **2014,** *7* (5), 3919.
8.Metz, K. M.; Colavita, P. E.; Tse, K. Y.; Hamers, R. J., *Journal of Power Sources* **2012,** *198*, 393.
9.Geim, A. K.; Novoselov, K. S., *Nat Mater* **2007,** *6* (3), 183.
10.Behan, J. A.; Stamatin, S. N.; Hoque, M. K.; Ciapetti, G.; Zen, F.; Esteban-Tejeda, L.; Colavita, P. E., *The Journal of Physical Chemistry C* **2017,** *121* (12), 6596.
11.Martinez-Martinez, D.; De Hosson, J. T. M., *Surface and Coatings Technology* **2014,** *258*, 677.
12.Shirakura, A.; Nakaya, M.; Koga, Y.; Kodama, H.; Hasebe, T.; Suzuki, T., *Thin Solid Films* **2006,** *494* (1-2), 84.
13.Bewilogua, K.; Hofmann, D., *Surface and Coatings Technology* **2014,** *242*, 214.
14.Kumar, S.; Chatterjee, K., *ACS Applied Materials & Interfaces* **2016,** *8* (40), 26431.
15.Zeng, H.; Jarvik, R.; Catausan, G.; Moldovan, N.; Carlisle, J., *Surface and Coatings Technology* **2016,** *302*, 420.
16.Love, C. A.; Cook, R. B.; Harvey, T. J.; Dearnley, P. A.; Wood, R. J. K., *Tribology International* **2013,** *63*, 141.
17.Liang, F.; Chen, B., *Curr Med Chem* **2010,** *17* (1), 10.
18.Vardharajula, S.; Ali, S. Z.; Tiwari, P. M.; Eroglu, E.; Vig, K.; Dennis, V. A.; Singh, S. R., *Int J Nanomedicine* **2012,** *7*, 5361.
19.Krishna, V.; Stevens, N.; Koopman, B.; Moudgil, B., *Nat Nano* **2010,** *5* (5), 330.
20.Wang, J.; Qiu, J., *Journal of Materials Science* **2016,** *51* (10), 4728.
21.Sun, Y.-P.; Zhou, B.; Lin, Y.; Wang, W.; Fernando, K. A. S.; Pathak, P.; Meziani, M. J.; Harruff, B. A.; Wang, X.; Wang, H.; Luo, P. G.; Yang, H.; Kose, M. E.; Chen, B.; Veca, L. M.; Xie, S.-Y., *Journal of the American Chemical Society* **2006,** *128* (24), 7756.
22.Faklaris, O.; Joshi, V.; Irinopoulou, T.; Tauc, P.; Sennour, M.; Girard, H.; Gesset, C.; Arnault, J.-C.; Thorel, A.; Boudou, J.-P.; Curmi, P. A.; Treussart, F., *ACS Nano* **2009,** *3* (12), 3955.
23.Fang, Y.; Gu, D.; Zou, Y.; Wu, Z.; Li, F.; Che, R.; Deng, Y.; Tu, B.; Zhao, D., *Angewandte Chemie International Edition* **2010,** *49* (43), 7987.
24.Duffy, P.; Magno, L. M.; Yadav, R. B.; Roberts, S. K.; Ward, A. D.; Botchway, S. W.; Colavita, P. E.; Quinn, S. J., *Journal of Materials Chemistry* **2012,** *22* (2), 432.
25.Smart, S. K.; Cassady, A. I.; Lu, G. Q.; Martin, D. J., *Carbon* **2006,** *44* (6), 1034.
26.Buddy D. Ratner; Allan S. Hoffman; Frederick J. Schoen; Jack E. Lemons, 2 ed.; Elsevier Academic Press: London, 2004.
27.Gott, V. L.; Alejo, D. E.; Cameron, D. E., *Annals of Thoracic Surgery* **2003,** *76* (6), S2230.
28.Goodman, S. L., *J Biomed Mater Res* **1999,** *45* (3), 240.
29.Linder, S.; Pinkowski, W.; Aepfelbacher, M., *Biomaterials* **2002,** *23* (3), 767.
30.Lackner, M. J.; Waldhauser, W., *BHM Berg- und Hüttenmännische Monatshefte* **2010,** *155* (11), 528.
31.Hauert, R., *Diamond and Related Materials* **2003,** *12* (3–7), 583.
32.Gotzmann, G.; Beckmann, J.; Wetzel, C.; Scholz, B.; Herrmann, U.; Neunzehn, J., *Surface and Coatings Technology* **2017,** *311*, 248.
33.Grill, A., *Diamond and Related Materials* **2003,** *12* (2), 166.
34.Allen, M.; Myer, B.; Rushton, N., *J Biomed Mater Res* **2001,** *58* (3), 319.

35.Bociąga, D.; Jakubowski, W.; Komorowski, P.; Sobczyk-Guzenda, A.; Jędrzejczak, A.; Batory, D.; Olejnik, A., *Materials Science and Engineering: C* **2016,** *63*, 462.
36.Castellino, M.; Stolojan, V.; Virga, A.; Rovere, M.; Cabiale, K.; Galloni, M. R.; Tagliaferro, A., *Anal Bioanal Chem* **2013,** *405* (1), 321.
37.Chai, F.; Mathis, N.; Blanchemain, N.; Meunier, C.; Hildebrand, H. F., *Acta Biomater* **2008,** *4* (5), 1369.
38.Liao, T. T.; Deng, Q. Y.; Li, S. S.; Li, X.; Ji, L.; Wang, Q.; Leng, Y. X.; Huang, N., *ACS Biomaterials Science & Engineering* **2017,** *3* (4), 530.
39.Aramesh, M.; Tong, W.; Fox, K.; Turnley, A.; Seo, D.; Prawer, S.; Ostrikov, K., *Materials* **2015,** *8* (8), 4992.
40.Dearnaley, G.; Arps, J. H., *Surface and Coatings Technology* **2005,** *200* (7), 2518.
41.Roy, R. K.; Lee, K. R., *J Biomed Mater Res B Appl Biomater* **2007,** *83* (1), 72.
42.Sydow-Plum, G.; Tabrizian, M., *Materials Science and Technology* **2008,** *24* (9), 1127.
43.Bokros, J. C., *Ceramics International* **1983,** *9* (1), 3.
44.Ali, N.; Kousa, Y.; Gracio, J.; Cabral, G.; Sousa, A.; Shokufar, T.; Titus, E.; Madaleno, J. C.; Ahmed, W.; Jackson, M. J., 2016; pp 303.
45.Sick, P. B.; Gelbrich, G.; Kalnins, U.; Erglis, A.; Bonan, R.; Aengevaeren, W.; Elsner, D.; Lauer, B.; Woinke, M.; Brosteanu, O.; Schuler, G., *Am J Cardiol* **2004,** *93* (11), 1351.
46.Wilke, A.; Wende, C. M.; Horst, M.; Steverding, D., *Cardiology Research* **2011,** *2* (6), 298.
47.Qureshi, A.; Gurbuz, Y.; Niazi, J. H., *Sensors and Actuators B: Chemical* **2012,** *171-172*, 62.
48.Robertson, J., *Materials Science and Engineering R* **2002,** *37* (4–6), 129.
49.Schmellenmeier, H., *Exp. Tech. Phys.* **1953,** (1), 49.
50.Aisenberg, S.; Chabot, R., *Journal of Applied Physics* **1971,** *42* (7), 2953.
51.Jacob, W.; Möller, W., *Applied Physics Letters* **1993,** *63* (13), 1771.
52.Vetter, J., *Surface and Coatings Technology* **2014,** *257*, 213.
53.McKenzie, D. R., *Reports on Progress in Physics* **1996,** *59* (12), 1611.
54.Zahid, R.; Masjuki, H. H.; Varman, M.; Kalam, M. A.; Mufti, R. A.; Mohd Zulkifli, N. W. B.; Gulzar, M.; Nor Azman, S. S. B., *Journal of Materials Research* **2016,** *31* (13), 1814.
55.Wiatrowski, A.; Kijaszek, W.; Posadowski, W. M.; Oleszkiewicz, W.; Jadczak, J.; Kunicki, P., *Diamond and Related Materials* **2017,** *72*, 71.
56.Bruinink, A.; Bitar, M.; Pleskova, M.; Wick, P.; Krug, H. F.; Maniura-Weber, K., *Journal of Biomedical Materials Research Part A* **2014,** *102* (1), 275.
57.Simmons, J. M.; Nichols, B. M.; Baker, S. E.; Marcus, M. S.; Castellini, O. M.; Lee, C. S.; Hamers, R. J.; Eriksson, M. A., *The Journal of Physical Chemistry B* **2006,** *110* (14), 7113.
58.Heymann, D.; Bachilo, S. M.; Weisman, R. B.; Cataldo, F.; Fokkens, R. H.; Nibbering, N. M. M.; Vis, R. D.; Chibante, L. P. F., *Journal of the American Chemical Society* **2000,** *122* (46), 11473.
59.Mochalin, V. N.; Shenderova, O.; Ho, D.; Gogotsi, Y., *Nat Nano* **2012,** *7* (1), 11.
60.May, P. W.; Regan, E. M.; Taylor, A.; Uney, J.; Dick, A. D.; McGeehan, J., *Diamond and Related Materials* **2012,** *23*, 100.
61.Nistor, P. A.; May, P. W.; Tamagnini, F.; Randall, A. D.; Caldwell, M. A., *Biomaterials* **2015,** *61*, 139.
62.Regan, E. M.; Taylor, A.; Uney, J. B.; Dick, A. D.; May, P. W.; McGeehan, J., *IEEE Journal on Emerging and Selected Topics in Circuits and Systems* **2011,** *1* (4), 557.
63.Kelly, S.; Regan, E. M.; Uney, J. B.; Dick, A. D.; McGeehan, J. P.; Mayer, E. J.; Claeyssens, F., *Biomaterials* **2008,** *29* (17), 2573.
64.Ducheyne, P., Elsevier: 2011; p ii.
65.Pacelli, S.; Manoharan, V.; Desalvo, A.; Lomis, N.; Jodha, K. S.; Prakash, S.; Paul, A., *Journal of Materials Chemistry B* **2016,** *4* (9), 1586.
66.Barbucci, R., KLUWER ACADEMIC PUBLISHERS: 2002.
67.Grill, A., *Diamond and Related Materials* **1999,** *8* (2–5), 428.

68.Onuki, Y.; Bhardwaj, U.; Papadimitrakopoulos, F.; Burgess, D. J., *Journal of Diabetes Science and Technology* **2008,** *2* (6), 1003.
69.Moore, B.; Asadi, E.; Lewis, G., *Advances in Materials Science and Engineering* **2017,** *2017*.
70.Tran, H. S.; Puc, M. M.; Hewitt, C. W.; Soll, D. B.; Marra, S. W.; Simonetti, V. A.; Cilley, J. H.; DelRossi, A. J., *J Invest Surg* **1999,** *12* (3), 133.
71.Szczesna-Antczak, M.; Kaczorowska, A.; Kaczorowski, W.; Antczak, T., *International Biodeterioration & Biodegradation* **2014,** *88*, 106.
72.Ma, W. J.; Ruys, A. J.; Mason, R. S.; Martin, P. J.; Bendavid, A.; Liu, Z.; Ionescu, M.; Zreiqat, H., *Biomaterials* **2007,** *28* (9), 1620.
73.Ohgoe, Y.; Hirakuri, K. K.; Saitoh, H.; Nakahigashi, T.; Ohtake, N.; Hirata, A.; Kanda, K.; Hiratsuka, M.; Fukui, Y., *Surface and Coatings Technology* **2012,** *207*, 350.
74.Bociaga, D.; Kaminska, M.; Sobczyk-Guzenda, A.; Jastrzebski, K.; Swiatek, L.; Olejnik, A., *Diamond and Related Materials* **2016,** *67*, 41.
75.Wilson, C. J.; Clegg, R. E.; Leavesley, D. I.; Pearcy, M. J., *Tissue Eng* **2005,** *11* (1-2), 1.
76.Kasemo, B., *Current Opinion in Solid State and Materials Science* **1998,** *3* (5), 451.
77.Reimhult, E.; Zäch, M.; Höök, F.; Kasemo, B., *Langmuir* **2006,** *22* (7), 3313.
78.Parhami, F.; Garfinkel, A.; Demer, L. L., *Arteriosclerosis, Thrombosis, and Vascular Biology* **2000,** *20* (11), 2346.
79.Schwartz, Z.; Boyan, B. D., *J Cell Biochem* **1994,** *56* (3), 340.
80.Feng, L.; Andrade, J. D., *Biomaterials* **1994,** *15* (5), 323.
81.Thevenot, P.; Hu, W.; Tang, L., *Current Topics in Medicinal Chemistry* **2008,** *8* (4), 270.
82.Griesser, H. J.; Kingshott, P.; McArthur, S. L.; McLean, K. M.; Kinsel, G. R.; Timmons, R. B., *Biomaterials* **2004,** *25* (20), 4861.
83.Hellstrand, E.; Lynch, I.; Andersson, A.; Drakenberg, T.; Dahlbäck, B.; Dawson, K. A.; Linse, S.; Cedervall, T., *FEBS Journal* **2009,** *276* (12), 3372.
84.Baier, R. E.; Dutton, R. C., *Journal of Biomedical Materials Research* **1969,** *3* (1), 191.
85.Kratz, A.; Ferraro, M.; Sluss, P. M.; Lewandrowski, K. B., *New England Journal of Medicine* **2004,** *351* (15), 1548.
86.Quehenberger, O.; Armando, A. M.; Brown, A. H.; Milne, S. B.; Myers, D. S.; Merrill, A. H.; Bandyopadhyay, S.; Jones, K. N.; Kelly, S.; Shaner, R. L.; Sullards, C. M.; Wang, E.; Murphy, R. C.; Barkley, R. M.; Leiker, T. J.; Raetz, C. R. H.; Guan, Z.; Laird, G. M.; Six, D. A.; Russell, D. W.; McDonald, J. G.; Subramaniam, S.; Fahy, E.; Dennis, E. A., *Journal of Lipid Research* **2010,** *51* (11), 3299.
87.Malmsten, M.; Lassen, B., *Colloids and Surfaces B: Biointerfaces* **1995,** *4* (3), 173.
88.Lorentz, H.; Jones, L., *Optom Vis Sci* **2007,** *84* (4), 286.
89.McHenry, M. M.; Smeloff, E. A.; Fong, W. Y.; Miller, G. E., Jr.; Ryan, P. M., *J Thorac Cardiovasc Surg* **1970,** *59* (3), 413.
90.Morrison, R. T.; Boyd, R. N., 6th ed.; Boston: Allyn and Bacon: 1983.
91.Fahy, E.; Cotter, D.; Sud, M.; Subramaniam, S., *Biochim Biophys Acta* **2011,** *1811* (11), 637.
92.Yeagle, P. L., CRC Press: 2011; pp 1.
93.Lombard, J., *Biol Direct* **2014,** *9*, 32.
94.Hussain, M. M., *Atherosclerosis* **2000,** *148*, 1.
95.Kurt W. Miller; Donald M. Smalls, *The Journal of Biological Chemistry* **1983,** *258* (22), 13772.
96.Li, J.; Wang, X.; Zhang, T.; Wang, C.; Huang, Z.; Luo, X.; Deng, Y., *Asian Journal of Pharmaceutical Sciences* **2015,** *10* (2), 81.
97.van Hoogevest, P.; Wendel, A., *European Journal of Lipid Science and Technology* **2014,** *116* (9), 1088.
98.Castellana, E. T.; Cremer, P. S., *Surface Science Reports* **2006,** *61* (10), 429.
99.Ingólfsson, H. I.; Melo, M. N.; van Eerden, F. J.; Arnarez, C.; Lopez, C. A.; Wassenaar, T. A.; Periole, X.; de Vries, A. H.; Tieleman, D. P.; Marrink, S. J., *Journal of the American Chemical Society* **2014,** *136* (41), 14554.

100.Ingolfsson, H. I.; Arnarez, C.; Periole, X.; Marrink, S. J., *J Cell Sci* **2016,** *129* (2), 257.
101.Leventis, P. A.; Grinstein, S., *Annu Rev Biophys* **2010,** *39*, 407.
102.Siegenthaler, P. A.; Murata, N., 2004.
103.Daniel, M., *Wien Med Wochenschr* **2014,** *164* (5-6), 88.
104.Verberne, G.; Schroeder, A.; Halperin, G.; Barenholz, Y.; Etsion, I., *Wear* **2010,** *268* (7), 1037.
105.Hills, B. A.; Crawford, R. W., *The Journal of Arthroplasty* **2003,** *18* (4), 499.
106.Pawlak, Z.; Urbaniak, W.; Hagner-Derengowska, M.; Hagner, W., *Cell Biochem Biophys* **2015,** *71* (3), 1615.
107.Yang, W.; Cui, F. Z.; Qing, X., *Current Applied Physics* **2006,** *6* (5), 827.
108.Saeui, C. T.; Mathew, M. P.; Liu, L.; Urias, E.; Yarema, K. J., *J Funct Biomater* **2015,** *6* (2), 454.
109.Sessa, G.; Weissmann, G., *J Lipid Res* **1968,** *9* (3), 310.
110.Akbarzadeh, A.; Rezaei-Sadabady, R.; Davaran, S.; Joo, S.; Zarghami, N.; Hanifehpour, Y.; Samiei, M.; Kouhi, M.; Nejati-Koshki, K., *Nanoscale Research Letters* **2013,** *8* (1), 1.
111.Bozzuto, G.; Molinari, A., *Int J Nanomedicine* **2015,** *10*, 975.
112.Lasic, D. D., Lipowsky, R.; Sackmann, E., Eds. Elsevier Science B.V.: 1995; Vol. 1.
113.Khan, M. S.; Dosoky, N. S.; Williams, J. D., *Int J Mol Sci* **2013,** *14* (11), 21561.
114.Tero, R., *Materials* **2012,** *5* (12), 2658.
115.Wagner, A.; Vorauer-Uhl, K., *Journal of Drug Delivery* **2011,** *2011*.
116.Laouini, A.; Jaafar-Maalej, C.; Limayem-Blouza, I.; Sfar, S.; Charcosset, C.; Fessi, H., *Journal of Colloid Science and Biotechnology* **2012,** *1* (2), 147.
117.Reimhult, E.; Kasemo, B.; Höök, F., *International journal of molecular sciences* **2009,** *10* (4), 1683.
118.Szoka, F.; Olson, F.; Heath, T.; Vail, W.; Mayhew, E.; Papahadjopoulos, D., *Biochimica et Biophysica Acta (BBA) - Biomembranes* **1980,** *601*, 559.
119.McConnell, H. M.; Watts, T. H.; Weis, R. M.; Brian, A. A., *Biochim Biophys Acta* **1986,** *864* (1), 95.
120.Towns, E. N.; Parikh, A. N.; Land, D. P., *The Journal of Physical Chemistry C* **2015**, 150126074752006.
121.Okamoto, Y.; Tsuzuki, K.; Iwasa, S.; Ishikawa, R.; Sandhu, A.; Tero, R., *Journal of Physics: Conference Series* **2012,** *352*, 012017.
122.Cho, N.-J.; Frank, C. W.; Kasemo, B.; Hook, F., *Nat. Protocols* **2010,** *5* (6), 1096.
123.Scarano, S.; Mascini, M.; Turner, A. P. F.; Minunni, M., *Biosensors and Bioelectronics* **2010,** *25* (5), 957.
124.Limaj, O.; Etezadi, D.; Wittenberg, N. J.; Rodrigo, D.; Yoo, D.; Oh, S. H.; Altug, H., *Nano Lett* **2016,** *16* (2), 1502.
125.Cui, F. Z.; Qing, X. L.; Li, D. J.; Zhao, J., *Surface and Coatings Technology* **2005,** *200* (1â€“4), 1009.
126.Marco Diociaiuti; Agnese Molinari; Irene Ruspantini; Maria Cristina Gaudiano; Rodolfo Ippoliti; Eugenio Lendaro; Federico Bordi; Pietro Chistolini; Giuseppe Arancia, *Biochimica et Biophysica Acta* **2002,** *1559*, 21.
127.Tsuzuki, K.; Okamoto, Y.; Iwasa, S.; Ishikawa, R.; Sandhu, A.; Tero, R., *Journal of Physics: Conference Series* **2012,** *352*, 012016.
128.Dimitrievski, K.; Kasemo, B., *Langmuir* **2009,** *25* (16), 8865.
129.Richter, R. P.; Brisson, A. R., *Biophysical Journal* **2005,** *88* (5), 3422.
130.Kunze, A.; Svedhem, S.; Kasemo, B., *Langmuir* **2009,** *25* (9), 5146.
131.Reimhult, E.; Kasemo, B.; Hook, F., *Int J Mol Sci* **2009,** *10* (4), 1683.
132.Richter, R.; Mukhopadhyay, A.; Brisson, A., **2003**.
133.Wu, L.; Zeng, L.; Jiang, X., *J Am Chem Soc* **2015,** *137* (32), 10052.
134.Dimitrievski, K.; Kasemo, B., *Langmuir* **2008,** *24* (8), 4077.
135.Hardy, G. J.; Nayak, R.; Zauscher, S., *Current opinion in colloid & interface science* **2013,** *18* (5), 448.

136.Reimhult, E.; Höök, F.; Kasemo, B., *Physical Review E* **2002,** *66* (5), 051905.
137.Seantier, B.; Kasemo, B., *Langmuir* **2009,** *25* (10), 5767.
138.Reviakine, I.; Brisson, A., *Langmuir* **2000,** *16* (4), 1806.
139.Böckmann, R. A.; Hac, A.; Heimburg, T.; Grubmüller, H., *Biophysical Journal* **2003,** *85* (3), 1647.
140.Böckmann, R. A.; Grubmüller, H., *Angewandte Chemie International Edition* **2004,** *43* (8), 1021.
141.Sovago, M.; Wurpel, G. W. H.; Smits, M.; Müller, M.; Bonn, M., *Journal of the American Chemical Society* **2007,** *129* (36), 11079.
142.Puu, G.; Gustafson, I., *Biochimica et Biophysica Acta (BBA) - Biomembranes* **1997,** *1327* (2), 149.
143.Melcrova, A.; Pokorna, S.; Pullanchery, S.; Kohagen, M.; Jurkiewicz, P.; Hof, M.; Jungwirth, P.; Cremer, P. S.; Cwiklik, L., *Sci Rep* **2016,** *6*, 38035.
144.Garcia-Manyes, S.; Oncins, G.; Sanz, F., *Biophysical Journal* **2005,** *89* (3), 1812.
145.Makino, K.; Shibata, A., Liu, A. L., Ed. Academic Press: 2006; Vol. Volume 4, pp 49.
146.Martín-Molina, A.; Rodríguez-Beas, C.; Faraudo, J., *Biophysical Journal* **2012,** *102* (9), 2095.
147.Cremer, P. S.; Boxer, S. G., *The Journal of Physical Chemistry B* **1999,** *103* (13), 2554.
148.Seifert, U., *Advances in Physics* **1997,** *46* (1), 13.
149.Reimhult, E.; Höök, F.; Kasemo, B., *The Journal of Chemical Physics* **2002,** *117* (16), 7401.
150.Dimitrievski, K., *Langmuir* **2010,** *26* (5), 3008.
151.Jurak, M.; Chibowski, E., *Langmuir* **2007,** *23* (20), 10156.
152.Nirasay, S.; Badia, A.; Leclair, G.; Claverie, J.; Marcotte, I., *Materials* **2012,** *5* (12), 2621.
153.Reimhult, E.; Hook, F.; Kasemo, B., *Langmuir* **2003,** *19*, 1681.
154.Isono, T.; Tanaka, H.; Ogino, T., *e-Journal of Surface Science and Nanotechnology* **2007,** *5*, 99.
155.Alexandrova, L.; Karakashev, S. I.; Grigorov, L.; Phan, C. M.; Smoukov, S. K., *Advances in Colloid and Interface Science* **2015,** *220*, 1.
156.Cha, T.; Guo, A.; Zhu, X. Y., *Biophysical Journal* **2006,** *90* (4), 1270.
157.Pfeiffer, I.; Petronis, S.; Köper, I.; Kasemo, B.; Zäch, M., *The Journal of Physical Chemistry B* **2010,** *114* (13), 4623.
158.Er, Y.; Prestidge, C. A.; Fornasiero, D., *Colloids and Surfaces B: Biointerfaces* **2004,** *36* (3–4), 147.
159.Hernandez, M. R.; Towns, E. N.; Ng, T. C.; Walsh, B. C.; Osibanjo, R.; Parikh, A. N.; Land, D. P., *Appl Opt* **2012,** *51* (15), 2842.
160.Keller, C. A.; Kasemo, B., **1998**.
161.Rossetti, F. F.; Bally, M.; Michel, R.; Textor, M.; Reviakine, I., *Langmuir* **2005,** *21* (14), 6443.
162.Nel, A. E.; Madler, L.; Velegol, D.; Xia, T.; Hoek, E. M. V.; Somasundaran, P.; Klaessig, F.; Castranova, V.; Thompson, M., *Nature Materials* **2009,** *8* (7), 543.
163.Liu, J., *Langmuir* **2016,** *32* (18), 4393.
164.Tabaei, S. R.; Ng, W. B.; Cho, S.-J.; Cho, N.-J., *ACS Applied Materials & Interfaces* **2016,** *8* (18), 11875.
165.Gasser, M.; Rothen-Rutishauser, B.; Krug, H.; Gehr, P.; Nelle, M.; Yan, B.; Wick, P., *Journal of Nanobiotechnology* **2010,** *8* (1), 31.
166.Kendall, M.; Brown, L.; Trought, K., *Inhalation Toxicology* **2004,** *16* (s1), 99.
167.Frost, R.; Jönsson, G. E.; Chakarov, D.; Svedhem, S.; Kasemo, B., *Nano Letters* **2012,** *12* (7), 3356.
168.Willems, N.; Urtizberea, A.; Verre, A. F.; Iliut, M.; Lelimousin, M.; Hirtz, M.; Vijayaraghavan, A.; Sansom, M. S. P., *ACS Nano* **2017,** *11* (2), 1613.
169.Liu, X.; Chen, K. L., *Langmuir* **2015,** *31* (44), 12076.
170.Wang, F.; Liu, J., *Nanoscale* **2013,** *5* (24), 12375.

171.Ang, P. K.; Jaiswal, M.; Lim, C. H.; Wang, Y.; Sankaran, J.; Li, A.; Lim, C. T.; Wohland, T.; Barbaros, O.; Loh, K. P., *ACS Nano* **2010,** *4* (12), 7387.
172.Li, W.; Chung, J. K.; Lee, Y. K.; Groves, J. T., *Nano Letters* **2016,** *16* (8), 5022.
173.Cui, F. Z.; Li, D. J., *Surface and Coatings Technology* **2000,** *131* (1–3), 481.
174.Miksovsky, J.; Voss, A.; Kozarova, R.; Kocourek, T.; Pisarik, P.; Ceccone, G.; Kulisch, W.; Jelinek, M.; Apostolova, M. D.; Reithmaier, J. P.; Popov, C., *Applied Surface Science* **2014,** *297*, 95.
175.Ogwu, A. A.; Okpalugo, T. I.; Ali, N.; Maguire, P. D.; McLaughlin, J. A., *J Biomed Mater Res B Appl Biomater* **2008,** *85* (1), 105.
176.Jelínek, M.; Smetana, K.; Kocourek, T.; Dvořánková, B.; Zemek, J.; Remsa, J.; Luxbacher, T., *Materials Science and Engineering: B* **2010,** *169* (1–3), 89.
177.Liu, X.; Cao, Y.; Zhao, M.; Deng, J.; Li, X.; Li, D., *Nanoscale Research Letters* **2015,** *10* (1), 14.
178.H. S. Tran, M. M. P. C. W. H. D. B. S. S. W. M. V. A. S. J. H. C. A. J., *Journal of Investigative Surgery* **1999,** *12* (3), 133.
179.Thampi, S.; Nandkumar, A. M.; Muthuvijayan, V.; Parameswaran, R., *ACS Applied Materials & Interfaces* **2017,** *9* (5), 4498.
180.Patelis, N.; Moris, D.; Matheiken, S.; Klonaris, C., *BioMed Research International* **2016,** *2016*.
181.Ryoo, S.-R.; Kim, Y.-K.; Kim, M.-H.; Min, D.-H., *ACS Nano* **2010,** *4* (11), 6587.
182.Wachesk, C. C.; Pires, C. A. F.; Ramos, B. C.; Trava-Airoldi, V. J.; Lobo, A. O.; Pacheco-Soares, C.; Marciano, F. R.; Da-Silva, N. S., *Applied Surface Science* **2013,** *266*, 176.
183.Almeida, C. N.; Ramos, B. C.; Da-Silva, N. S.; Pacheco-Soares, C.; Trava-Airoldi, V. J.; Lobo, A. O.; Marciano, F. R., *Applied Surface Science* **2013,** *275*, 258.
184.Hannan, R. T.; Peirce, S. M.; Barker, T. H., *ACS Biomaterials Science & Engineering* **2017**.
185.Campoccia, D.; Montanaro, L.; Arciola, C. R., *Biomaterials* **2013,** *34* (34), 8533.
186.Myllymaa, K.; Levon, J.; Tiainen, V. M.; Myllymaa, S.; Soininen, A.; Korhonen, H.; Kaivosoja, E.; Lappalainen, R.; Konttinen, Y. T., *Colloids Surf B Biointerfaces* **2013,** *101*, 290.
187.Pierce, C. G.; Srinivasan, A.; Ramasubramanian, A. K.; López-Ribot, J. L., *Microbiology Spectrum* **2015,** *3* (3).
188.Coad, B. R.; Kidd, S. E.; Ellis, D. H.; Griesser, H. J., *Biotechnology Advances* **2014,** *32* (2), 296.
189.Qi, X.; Poernomo, G.; Wang, K.; Chen, Y.; Chan-Park, M. B.; Xu, R.; Chang, M. W., *Nanoscale* **2011,** *3* (4), 1874.
190.Aslan, S.; Loebick, C. Z.; Kang, S.; Elimelech, M.; Pfefferle, L. D.; Van Tassel, P. R., *Nanoscale* **2010,** *2* (9), 1789.
191.Benincasa, M.; Pacor, S.; Wu, W.; Prato, M.; Bianco, A.; Gennaro, R., *ACS Nano* **2011,** *5* (1), 199.
192.Queiroz, J. R. C.; Fissmer, S. F.; Koga-Ito, C. Y.; Salvia, A. C. R. D.; Massi, M.; Sobrinho, A. S. d. S.; Júnior, L. N., *Journal of Prosthodontics* **2013,** *22* (6), 451.

Chapter II

Experimental Techniques

The theory and background of the techniques used throughout this thesis are described in this chapter. Firstly, the sputtering method used for carbon films deposition is presented. Secondly, liposomes characterisation through dynamic light scattering (DLS) and ζ-potential techniques is described. *Characterisation of carbon films is performed via surface* ζ-potential *(SZP). The interaction of liposomes with carbon macroscopic surfaces is studied through a combination of spectroscopic and microscopic techniques: infrared reflection absorption spectroscopy (IRRAS), fluorescence and atomic force microscopy (AFM) are utilised to measure the amount and mode of liposome adsorption at carbon surfaces. Finally, scanning electron microscopy (SEM) is used to image cell, platelets and fungi interactions with carbon films.*

1. Carbon Film Deposition

Physical vapour deposition (PVD) is a common technique utilised to produce thin films through the formation of a condensable vapour and subsequent deposition on a substrate.[1] Amorphous carbon (a-C) films are commonly produced by a type of PVD performed under moderate to low vacuum, which is called sputtering deposition. In sputtering deposition, a DC power supply generates Ar^+ ions which are accelerated towards a target (cathode) promoting an atomic collision cascade between Ar^+ and the atoms present at the cathode. The atoms are thus sputtered away from the target and deposit on the substrate as a thin film.[1-2] Moreover, the use of a permanent magnet, placed behind the target, is frequently utilised to increase the deposition rates. Magnetron sputtering allies the electric field to the ability of the magnetic field to confine the plasma to the proximity of the target surface to enhance the degree of plasma ionization and consequently sputtering rates.[1-2]

Production of a-C films through the sputtering deposition method is preformed using a graphite target as the cathode. The physico-chemical properties of a-C films can be tuned by changing plasma power, gas composition and pressure. For instance, graphitic films are obtained at high plasma power whereas carbon films rich in sp^3 carbon centres are achieved by applying a substrate bias voltage. Additionally, the incorporation of other gases on the sputtering chamber, such as nitrogen and hydrogen, results on carbon films with distinct physico-chemical properties.[2]

In this thesis, a DC-magnetron sputtering chamber (Torr International, Inc.) is used to deposit a-C films, as shown in Figure 2.1. The two sputtering guns generate ions that collide with titanium (left) and carbon (right) sputtering targets. Samples are placed at a rotating stage to assure a uniform deposition on the substrates. The deposition of bare a-C is carried out at a base pressure of $\leq 2 \times 10^{-6}$ mbar and a deposition Ar pressure of 7×10^{-3} mbar, as previously described.[3] Hydrogen doped amorphous carbon (a-C:H) films are produced by using H_2/Ar gas mixture (10 % H_2 content) in the deposition chamber. Additionally, the deposition of Ti films is also performed on the same DC-magnetron sputtering chamber, under similar conditions of a-C films production.

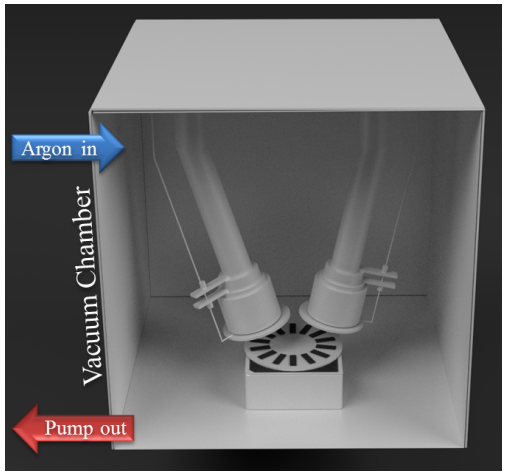


Figure 2.1. Schematic diagram of the vacuum chamber used on this thesis for thin film deposition. The sputtering guns accelerate ions to collide against titanium (left) and carbon (right) targets.

2. Liposome Characterisation

2.1. Dynamic Light Scattering (DLS)

Dynamic Light Scattering (DLS) or Photon Correlation Spectroscopy is an experimental technique used to obtain the size distribution of colloidal dispersions. DLS measures the Brownian motion of particles, *i.e.* the ability of particles to diffuse in a medium with known viscosity at a given temperature; larger particles diffuse slower in the medium while smaller particles show a faster motion profile. For a constant temperature and a medium of known viscosity at that temperature, the hydrodynamic diameter of a particle in suspension can be extrapolated from the diffusion coefficient D using the Stokes-Einstein equation (eq. 2.1):

$$\mathbf{d(H) = \frac{k_B T}{3\pi\eta D}} \qquad \boldsymbol{eq.\,2.1}$$

where $\mathrm{d(H)}$ is the hydrodynamic diameter, k_B is the Boltzmann's constant, T is the absolute temperature and η is the viscosity of the medium at a given temperature. The dynamic motion of the particle can be fitted in a second order correlation of the scattered intensity fluctuation over time. The normalised auto-correlation function of the scattered intensity $\mathrm{g}^{(2)}(\tau)$ is obtained according to eq. 2.2:

$$g^{(2)}(\tau) = \frac{I(t)I(t+\tau)}{I(t)^2} \qquad eq.2.2$$

where $I(t)$ is the scattered intensity at time t and $I(t+\tau)$ represents the intensity of the scattered light at a delay time τ. An example of an experimental auto-correlation function is shown in Figure 2.2. For small delays τ, a high correlation of the scattered signal at time t and delay τ is observed due to the slight particle movement from its initial position. For longer delays τ, the particle exhibits distinct scatter signals, when compared to the initial position, thus the correlation coefficient decays exponentially.

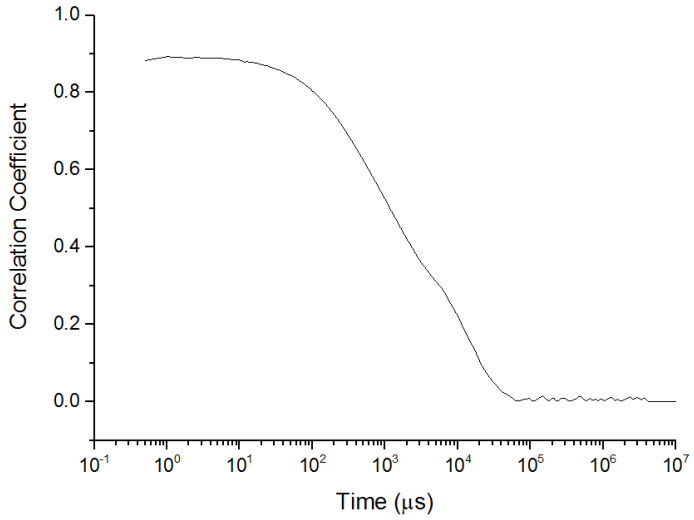


Figure 2.2. Example of an experimental correlation function against delay time **τ**.

For monodisperse particles in Brownian motion, the auto-correlation function can be fitted to an exponential decay according to eq. 2.3:

$$g^{(2)}(\tau) = B + \beta e^{-2\Gamma\tau} \qquad eq.2.3$$

where B is the correlation function baseline at infinite delay, β is the correlation function amplitude at $\tau = 0$, and Γ is the decay rate. The diffusion coefficient D can be derived from the decay constant Γ according to:

$$\Gamma = D\left(\left(\frac{4\pi n}{\lambda_0}\right)\sin\left(\frac{\theta}{2}\right)\right)^2 \qquad eq\ 2.4$$

where λ_0 is the laser's wavelength, θ is the angle at which the light is detected and n is the refractive index of the medium. Therefore, the hydrodynamic diameter $d(H)$ can be determined from the diffusion coefficient D (eq. 2.4) in equation 2.1.

Figure 2.3 shows the typical set up used on this thesis to measure the dynamic light scattering of particles and liposomes in suspension. A monochromatic and coherent light passes through a polarizer and reaches the cell where the particles are suspended in a medium with a given refractive index. The light is scattered by particles in suspension and collected in a photomultiplier detector positioned at a fixed angle θ. In this work, DLS measurements are carried out on a Malvern Zetasizer Nano-ZS, equipped with a λ_0 633 nm He-Ne laser and a 173° backscattering detector.

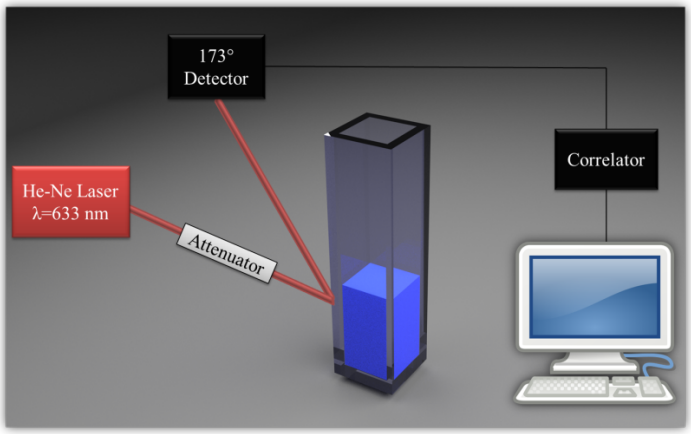


Figure 2.3. Optical configuration for dynamic light scattering measurements.

2.2. Particles ζ-Potential

When in contact with polar solvents, solid surfaces acquire a non-uniform distribution of electric charge at the interface. The electroneutrality of the system is achieved by the formation of an electric double layer (EDL) with a λ_D thickness, which exhibits excess of counterions of the opposite charge of the surface, as shown in Figure 2.4.[4] For a given negatively charged surface, a layer of anionic species is adsorbed at the interface, thus recruiting counterions to adsorb at the surface. The EDL structure shown in Figure 2.4 incorporates the following planes: the Inner Helmholtz plane (IHP), which includes the adsorbed anions and the Outer Helmholtz plane (OHP) that comprises the first plane of adsorbed counterions.

Additionally, the EDL 'edge' is called the Shear plane (SP) and consists on the frontier to a diffuse region in which ions are less attracted to the solid surface. SP represents a notional frontier in the diffuse region which defines the volume where ions and the particle form a stable entity. The potential difference between SP and the bulk solution is known as ζ-potential, and is taken to be equivalent to the potential ψ_D at the OHP.[4-6]

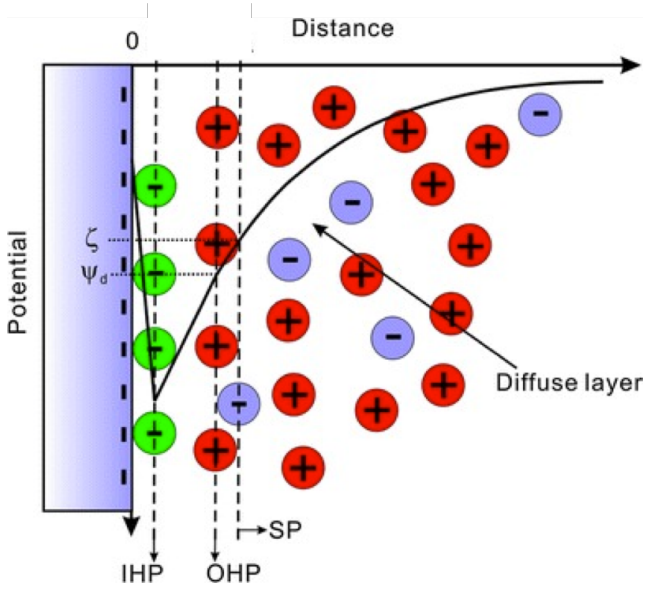


Figure 2.4. Electric double layer surrounding a negative charged particle.[4]

When an electric field is applied to a medium that contains particles with a charged surface, electrokinetic effects are observed. For a given surface charge, in the presence of an electric field, the particle is attracted to the electrolyte of opposite charge. At the same time a friction force will oppose the movement of the particle.[7] When in equilibrium, the balance of these two forces results on a constant particle velocity per unit field, called electrophoretic mobility. The electrophoretic mobility U_E is related to the ζ-potential of the particle by the Helmholtz–Smoluchowski equation (eq. 2.5):

$$U_E = \zeta \frac{\varepsilon_0 \varepsilon_r}{\eta} E_0 \qquad eq.2.5$$

where ε_0 is the electric permittivity of vacuum, ε_r the relative permittivity of the electrolyte solution, η the viscosity of the medium and E_0 the applied electric field. In this work, the ζ-potential of particles and liposomes in suspension is obtained using the Helmholtz–Smoluchowski model.[7]

Experimental ζ-potential measurements are performed on a Malvern Zetasizer Nano-ZS, with similar set up of the one presented on Figure 2.3. A monochromatic and coherent laser beam (He-Ne laser, $\lambda_0 = 633\ nm$) is split as a reference and an incident beam impinging on the sample. The incident beam is scattered and light is detected at 13°, with respect to the direction of incidence. When an electric field E_0 is applied, the particle electrophoretic mobility induces a fluctuation in the intensity of the light detected. The fluctuation frequency is proportional to the velocity of the particle and the shift between reference beam and incident beam is digitally processed and converted to particle ζ-potential using eq. 2.5.[7]

3. Carbon Surface Characterisation

3.1. Surface ζ-Potential

As for particles in suspension, macroscopic surfaces display different charges when exposed to different media. As previously discussed, ζ-potential measurements on particles or colloids rely on determinations of particle electrophoretic mobility in liquid suspensions and several instrumentation platforms are currently available to carry out these determinations. Surface ζ-potential (SZP) measurements on macroscopic surfaces, on the other hand, usually require specialised equipment that is not widely available. The preferred methods for macroscopic surfaces are based on determinations of streaming potential or electro osmotic mobility using microchannels that are coated with the surface under investigation.

An alternative to measurements on coated microchannels consists of measuring the mobility of tracer particles of known ζ-potential in close proximity to the surface that is the object of characterisation. Tracer particle methods were used by Yan *et al.*[8] in order to measure surface and particle ζ-potential simultaneously. Recently, Corbett *et al.*[9-11] developed a protocol based on tracer particles to determine the ζ-potential of macroscopic solid surfaces, which is described below. This method is advantageous as it allows for the measurement of ζ-potential of a macroscopic surface on the same

instrumentation platform used to measure ζ-potential of particles and bypasses many of the challenges of microchannel measurements.

The tracer particles method for SZP determinations has been previously described by Corbett *et al.*;[9] briefly, the velocity of the tracer particles under the effect of an AC field is measured via phase analysis light scattering after positioning the surface under characterisation at progressively greater distances from the probed volume (Figure 2.5). The velocity of the tracer particles at each position is the result of the sum of the particle electrophoretic migration, and of the electro osmotic flow in the proximity of the solid/liquid interface. As the probing volume is positioned further away from the surface, the effect of electro osmotic flow decreases until the observed mobility becomes only the result of electrophoretic migration.

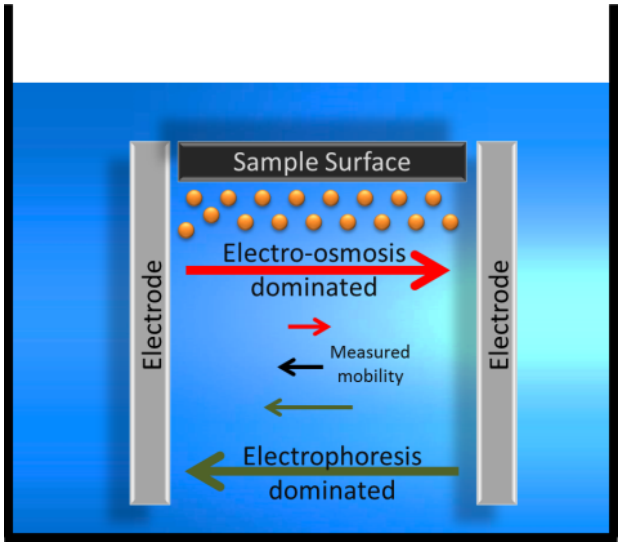


Figure 2.5. Schematic diagram of the measured mobility as a sum of electrophoresis and electro-osmosis.

The apparent ζ-potential is calculated from each mobility measurement using the following equation:

$$\zeta = \frac{\mu_{eo}\eta}{\varepsilon_r} \qquad eq.2.6$$

where μ_{eo} is the electroosmotic mobility, ε_r is the permittivity of the medium and η is the solution viscosity at a given temperature.[9] Values obtained are plotted *vs.* surface displacement and the SZP is obtained from extrapolation to zero-displacement (Figure

2.6); the contribution arising exclusively from the surface ($\zeta_{surface}$) is calculated from the intercept as in equation 2.7:

$$\zeta_{surface} = -intercept + \zeta_{particle} \qquad eq.2.7$$

Figure 2.6 shows an example of a surface ζ-potential determination on a standard polymeric surface.[12] The plot shows the reported ζ-potential - obtained from the measured mobility of the tracer particles as a function of surface displacement. The intercept (eq. 2.7) is obtained via linear extrapolation of the reported ζ-potential, excluding the value obtained at 1000 µm, for which the apparent ζ-potential matches that in bulk suspensions.[9]

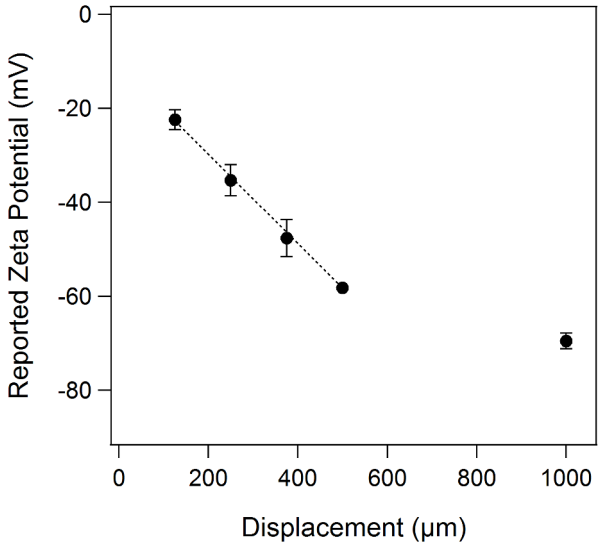


Figure 2.6. Plot of apparent ζ-potential as a function of surface displacement obtained for a standard polymer as a static surface using tracer particles with known ζ-potential of ~ -70 mV.

In this thesis, SZP measurements are carried out using a Malvern Zetasizer Nano-ZS with a similar setup to ζ-potential of particles in suspension (section 2.2) and equipped with a surface ζ-potential cell (Figure 2.7). Mobility determinations are conducted at 125, 250, 375, 500 and 1000 µm displacements from the sample surface. Carbon samples are included as 4 mm x 4 mm squares and placed on the sample holder of the surface ζ-potential cell.

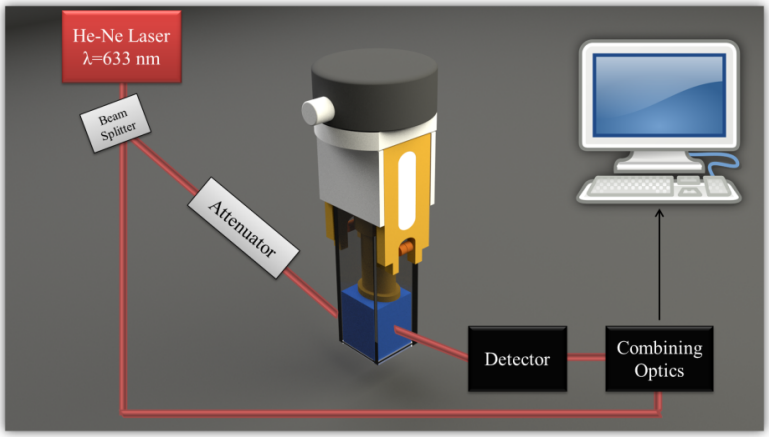


Figure 2.7. Optical configuration for surface ζ-potential measurements.

4. Carbon/Biomolecules Interaction

4.1. Infrared Reflectance Absorption Spectroscopy (IRRAS) *ex situ*

Infrared reflectance absorption spectroscopy (IRRAS) is a surface sensitive spectroscopic technique used to study the change in the reflectance spectrum when a thin film is deposited or adsorbed on a reflective substrates, typically metals.[13] Figure 2.8 shows an example of IRRAS measurement set-up; an electric field (red), polarized either parallel E_p (p-polarised) or perpendicular E_s (s-polarised) to the plane of incidence, reaches the surface at a well-defined angle. In order for molecules to absorb the incident light, the electric field vector of the sample must be orientated according to the polarization of the incident light;[14] to maximise the reflectance amplitude and the sensitivity of the IR measurement, p-polarized light is commonly used at grazing angles. For instance, for a given electric field reaching a metallic substrate, the amplitude of E_s vanishes near the surface whereas E_p is enhanced.

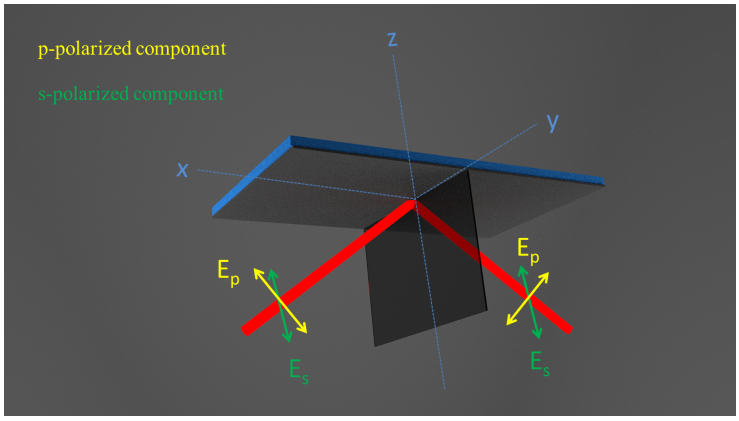


Figure 2.8. Incident and reflected electric field vectors and the correspondent plane polarisations: parallel (E_p) and perpendicular (E_s) polarisations with regards to the plane of incidence.

According to Fermi's golden rule, the intensity of an optical absorption is proportional to the intensity of the electric field and to the transition dipole projection along the direction of field polarization. Consequently, a molecule adsorbed at the surface will absorb radiation in resonance with a transition only if the molecule has a transition dipole projection along the direction of the electric field polarization.[15] This behaviour results in the metal surface selection rule (MSSR) that states that only vibrational modes with a transition dipole projection normal to the surface are excited and observed in the IRRAS spectra.

IRRAS spectra of thin films are generally presented as plots of reflectance-absorbance (RA) *vs* wavenumber. The RA spectrum is determined from the reflectance of the bare substrate (R_0) and the reflectance of the layer adsorbed on the substrate (R) according to equation 2.8:

$$\boldsymbol{RA = -log_{10}\left(\frac{R}{R_0}\right)} \qquad \boldsymbol{eq.2.8}$$

Thus, IRRAS sensitivity is enhanced for greatest changes of reflectivity RA, *i.e.* for a minimum in reflectance R_0. At high angles of incidence, the incident and reflected waves interfere constructively thus maximising IRRAS sensitivity. In the case of titanium (Ti), used in this thesis as an intermediate layer, the p-polarised reflectance (R_0) decreases considerably at grazing angles of incidence, resulting in an increase in the RA (Δ_{Rp}), as shown in Figure 2.9.[13] The maximum absorbance for a Ti substrate is approximately at

88° angle of incidence light polarised parallel to the plan of incidence (E_p). Below this angle, the normal components of the reflected beam become increasingly smaller so that the enhancement of the electric field decreases.

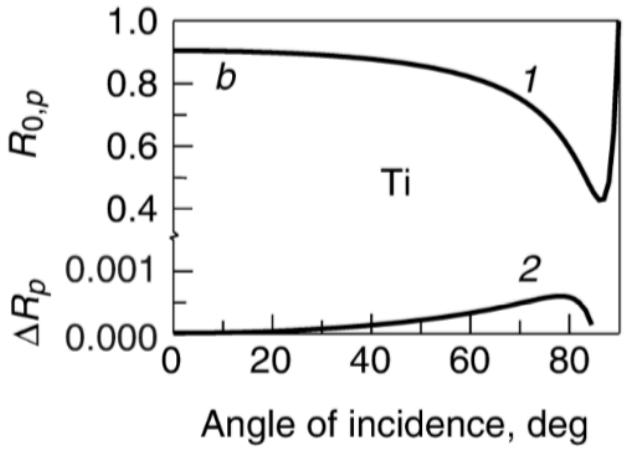


Figure 2.9. Dependence on angle of incidence of p-polarised light on (1) reflectance $R_{0,}$ corresponding to the bare substrate and (2) adsorption depth Δ_{Rp} for 1-nm layer at Ti substrate; reproduced from [13].

Due to the low sensitivity of IRRAS on non-metallic substrates, such as carbon films, a technique known as buried metal layer (BML) is adopted in this study. BML consists on a stack where the non-metallic layer is deposited on top of a metal substrate. The introduction of Ti in this study as metal substrate allows the surface to display a near-metallic behaviour provided that the thickness of the carbon layer is <100 nm. This combination of metal and non-metal film IRRAS induces an improvement on the limit of detection.[13]

In this thesis, IRRAS spectra are collected on a Fourier Transform Infrared (FTIR) spectrometer (Tensor 27, Bruker) equipped with a Mercury Cadmium Telluride (MCT) detector, a Zinc Selenide polarizer and a specular reflectance accessory (VeeMax II). 256 spectra are collected at 4 cm^{-1} resolution at > 80° incidence p-polarized light using a bare substrate as background unless otherwise noted.

4.2. Fluorescence Microscopy

The concept of fluorescence was first introduced in the 19th century by George Stokes, who noted that when a material is excited with a light of a given wavelength, the

fluorescence emission always occurs at a lower energy than that of the excitation light. This phenomenon is the principle used on fluorescence microscopy, which has become an essential tool in the fields of cell and molecular biology.

The excitation and emission processes are commonly described using a Jablonski diagram. Figure 2.10 shows an example of a Jablonski diagram of the fluorophore fluorescein isothiocyanate (FITC). During the excitation process, the energy absorbed by a fluorophore causes the molecule to transit from the ground state S_0 to the second singlet S_2 excited state (blue arrow). Once excited, the molecule uses different pathways to lose the absorbed energy and return to the ground state. Internal conversation and vibrational relaxation occurs within picoseconds, followed by fluorescence emission within nanoseconds. Due to the vibrational energy lost, the emission spectrum of a fluorophore is shifted to lower energy when compared to the excitation light, an effect known as Stokes' shift.

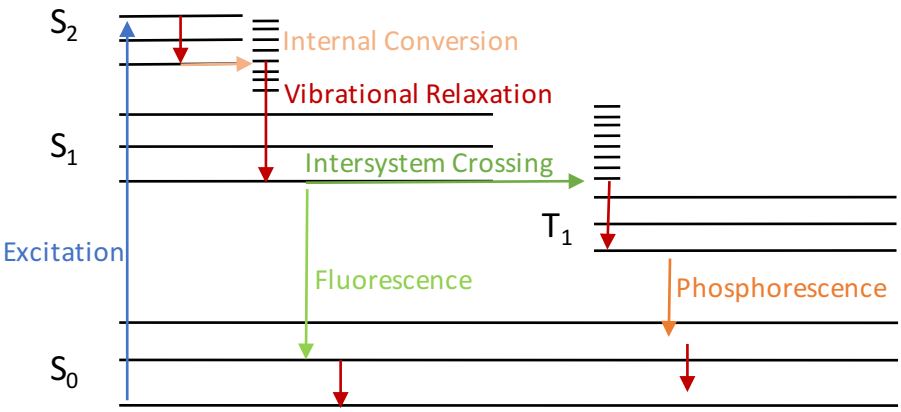


Figure 2.10. Jablonski diagram on the excitation and emission process of a common fluorophore FITC.

The properties of the fluorophores are determined by the efficiency of the emissive decay and the wavelength of excitation and emission. Depending on the fluorophore utilised, the excitation light can be adjusted in terms of wavelength and intensity, resulting in a higher signal to noise ratio. This particularity of fluorescence microscopy, when compared with other optic setups, presents numerous advantages for imaging different molecules simultaneously, as shown in Figure 2.11. Three different fluorophores, excited at three distinct wavelengths, result in distinct emission spectra at different energies. Hence, when imaging the three fluorophores simultaneously, as in

the case of fibroblast cells (Figure 2.11b), the fluorescence image of the sample is a combination of the three individual emission spectrum of the fluorophores.

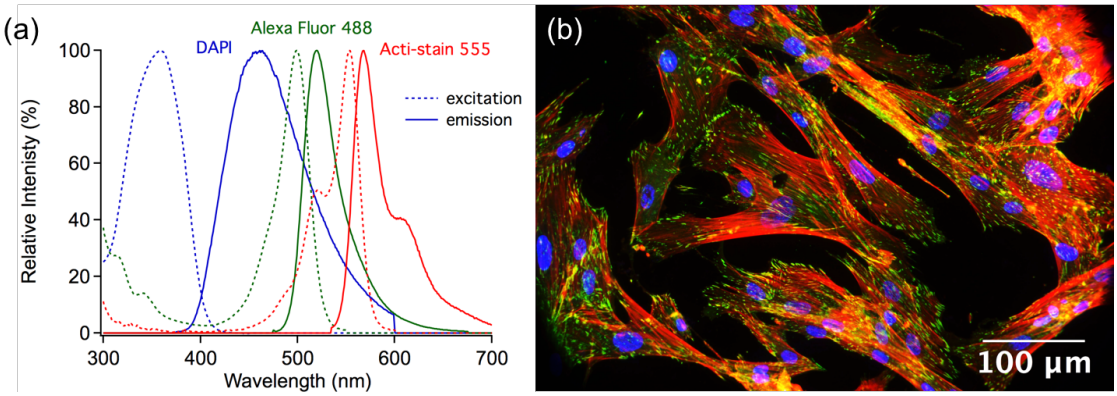


Figure 2.11. (a) Excitation (dot line) and emission (full line) spectra of DAPI (blue), alexa fluor 488 (green) and acti-stain 555 (red). **(b)** Fluorescence image of HFFF2 cells adherent to Si surface with nucleus stained using DAPI (blue), primary antibody (pAb) stained against vinculin with Alexa Fluor 488 as the fluorophore (green) and F-actin stained using phalloidin (red).

In a fluorescence microscope, a source of visible light emits a light beam that passes through a filter where the exciting wavelength that matches the fluorophore is selected (Figure 2.12). As the excitation and emission lights overlap in the light path, a dichroic beamsplitter mirror is used to transmit the longer wavelengths of the emitted fluorescence and reflect shorter wavelength light originated from the light source. Additionally, an emission filter is placed in front of the detector to prevent the passage of shorter wavelengths, coming from the excitation light, which results in only the emission light reaching the detector.

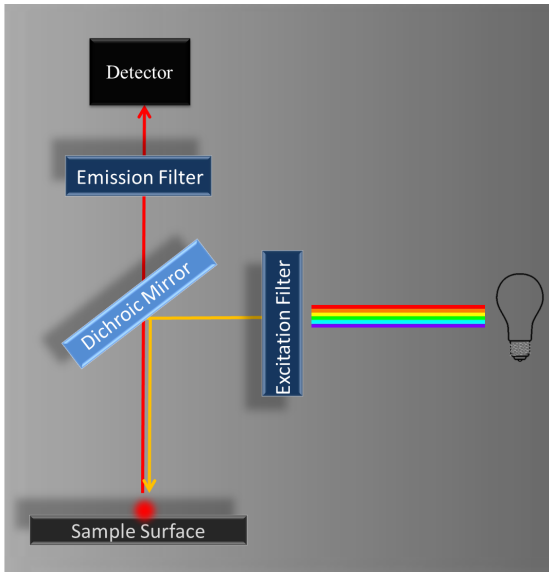


Figure 2.12. Optical setup for fluorescence microscopy measurements.

In this work, Texas Red 1,2-Dihexadecanoyl-sn-Glycero-3-Phosphoethanolamine, Triethylammonium Salt (Texas Red DHPE, ex/em ~595/615 nm) is utilised as the fluorophore in the liposome study. Fluorescence images are obtained with an Olympus BX51 upright microscope, using a DP73 camera and a CoolLed light source; the filter set consisted of excitation bandpass at 530-550 nm, dichroic mirror at 570 nm and emission filter at 573-648 nm. With regards to immunostaining measurements, DAPI ex/em ~358/461 nm, Alexa Fluor 488 (ex/em ~495/518 nm) and Acti-stain 555 (ex/em ~540/565 nm) staining are used as fluorophores and are excited in the UV (360 nm), 480 nm and 540 nm regions, respectively. Fluorescence imaging is performed in a Nikon TiS with epifluorescence attachment.

4.3. Fluorescence Recovery after Photobleaching (FRAP)

The diffusion of macromolecules in biological systems has been exploited by a technique known as fluorescence recovery after photobleaching (FRAP).[17] In particular, diffusion of lipids present on the cell membrane plays an important role in many cellular processes such as cell adhesion and signalling. FRAP has been used to understand lipid fluidity and to quantify the two dimensional lateral diffusion of lipids.[18]

FRAP relies on the ability of fluorophores to undergo bleaching when exposed to intense light of a given wavelength. Briefly, a high-powered focused laser beam irreversibly photobleaches fluorescent molecules in a confined area.[17] After bleaching, fluorescence is recovered by the diffusion of the neighbouring non-bleached molecules into the bleached area.[17, 19] The fluorescence recovery at the bleached area is related to the mobility of the fluorophore by the diffusion coefficient D, according to the equation 2.9:[18]

$$\boldsymbol{D = \frac{w^2}{4\tau_D}} \qquad \boldsymbol{eq.2.9}$$

where $\boldsymbol{\tau_D}$ is the diffusion time and $\boldsymbol{w}$ the radius of the bleached area. The diffusion coefficient gives insights on the mobility of a fluorophore within a biomolecule under study. For instance, fluorophores present on a fluid lipid bilayer would diffuse fast, resulting in fluorescence recovery in the bleached area within seconds. On the other hand, fluorophores on intact lipid vesicles possess low to no mobility resulting in no fluorescence recovery after photobleaching.[20]

In this work, FRAP measurements on lipid model aggregates are performed on a confocal microscope (Leica SP8) equipped with a krypton/argon laser (ex. 552 nm). Samples are incubated in suspensions of fluorescently labelled liposomes, then rinsed with water and imaged while wet before, during and after photobleaching, following published protocols.[20] A 25×25 μm^2 area is photobleached for 10 s, three times, with the high-powered focused laser beam; then, 250×250 μm^2 images are obtained every minute at low-power excitation to monitor fluorescence recovery.

4.4. Atomic Force Microscopy (AFM)

Atomic force microscopy (AFM) is a high-resolution type of scanning probe microscopy which has become a well-established technique for nanoscale structural characterisation. AFM has been utilised in a wide range of fields, such as electronics, semiconductors and biomaterials, as a powerful tool to measure simultaneously height profiles with sub-nanometre resolution and forces between the sample and the probe.[21]

In particular, AFM has been used for imaging the adsorption of lipid bilayers at solid surfaces, with vertical resolution that can be up to 0.1 nm.[22]

Figure 2.13 shows a schematic representation of the AFM system, which consists of a flexible cantilever probe with an AFM tip that scans over the sample and records the local interaction with the surface and the sample's morphology at the sub-nanometre scale. A piezoelectric (PZT) actuator is coupled to the cantilever and its vertical and lateral deflections imposed by the sample are collected by a position sensitive photo detector that provides feedback on the laser beam deflection intensity.[23] The feedback mechanisms on the photodetector enables the tip to scan at a constant force or constant height above the sample surface.[23]

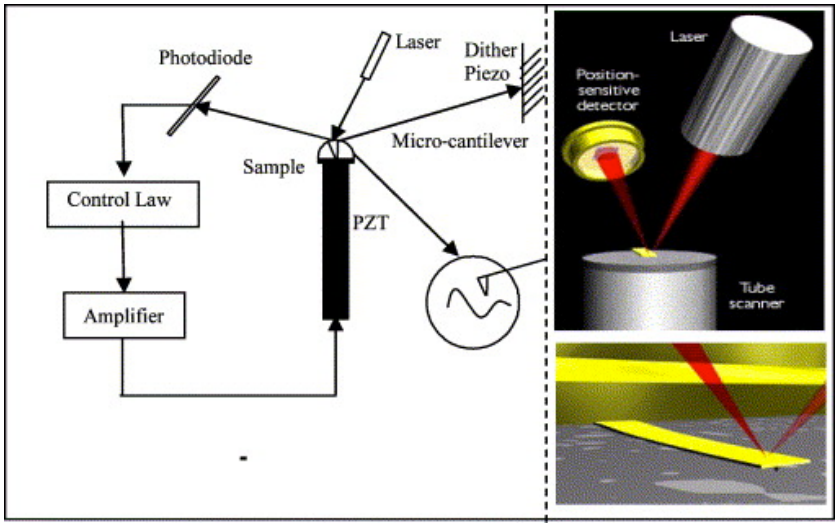


Figure 2.13. Schematic of AFM configuration reproduced from Jalili *et al*.[21].

AFM imaging can be performed through non-contact, contact and tapping modes. Non-contact mode consists on scanning the sample with the cantilever oscillating near its resonance frequency slightly away from the surface. This mode is typically used to probe electric, magnetic and atomic forces within the sample under examination. Alternatively, the contact mode imaging results on dragging the tip across the sample, creating a topographical mapping of the surface.

An advance on AFM systems is the usage of tapping mode AFM (TAFM) which allows high resolution topographic imaging on samples that cannot be probed by AFM (non) contact mode, either due to low adhesion to the substrate or by being easily damaged,

e.g. lipid bilayers. In the TAFM mode, the cantilever is oscillated at or near its natural resonant frequency using a PZT actuator. Prior contact with the surface, the PZT actuator causes the cantilever to oscillate at high amplitudes, typically above 20 nm. The oscillating cantilever slowly approaches the surface until light contact between sample and tip is achieved (Figure 2.14). TAFM overcomes limitation related to contact and non-contact modes of AFM, such as surface and tip damage, friction and image artefacts.[21]

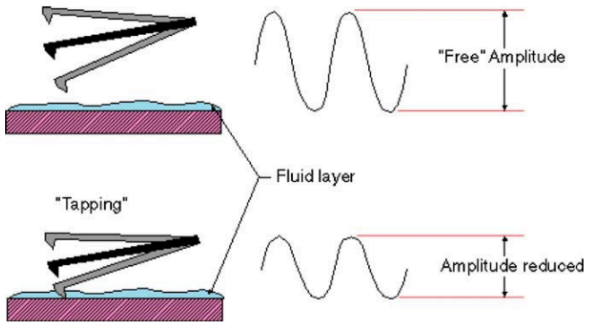


Figure 2.14. Schematic of tapping mode AFM operation; reproduced from Jalili *et al.*[21].

During scanning, the tip alternately contacts the surface and lifts off frequencies of about 50–500 cycles/second. The intermittent contact between tip and sample causes variations in oscillation amplitude, which is directly related to the topographical nature of the sample under examination; bumps on the sample results in a reduction of amplitude, while a depression on the surface promotes the increase of the tip oscillation amplitude. Similarly to contact and non-contact AFM modes, the change in oscillation amplitude is detected by the photodiode detector and feedback mechanisms allow to adjust scan height and amplitude.[21]

In this thesis, AFM imaging is performed in tapping mode on an Asylum Research (1 Hz, 512 scan lines) using Au-coated silicon cantilevers (NT-MDT, 1.45-15.1 N m^{-1} spring constant).

4.5. Scanning Electron Microscopy (SEM)

Scanning electron microscopy (SEM) uses a focused beam of electrons to obtain a topographical image of a sample under examination. The interaction of the electron beam with atoms at various depths within the sample, results in the loss of energy by repeated random scattering and absorption at the surface. The electrons produced from such interaction are scattered from the sample in the form of elastic and inelastic scattering; electromagnetic radiation can also result from interactions with the electron beam.[24]

The set-up for a typical SEM instrument can be observed in Figure 2.15. A beam of electrons is produced by applying a potential at the electron gun. Subsequently, high voltage is utilised to accelerate the electron beam through a vertical path. The high energy beam is focused onto the sample surface by using electromagnetic field and lenses. Once the incident electron beam reaches the sample surface, a range of electrons and X-rays are scattered and emitted in all directions. In particular, backscattered electrons (BSE) and secondary electrons (SE) are collected in specific detectors, in which the SEM signal is converted to a sample image.

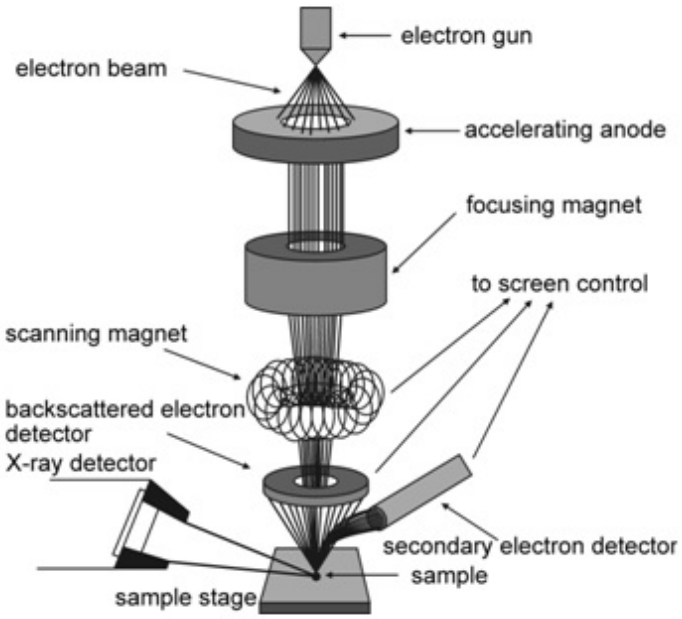


Figure 2.15. Set-up of a scanning electron microscope (SEM).[25]

BSEs consist of high-energy electrons that are back-scattered out of the sample by elastic interactions with the nuclei of the sample atoms. Hence, elements with heavier

atomic mass numbers, backscatter electrons more strongly than elements with lower atomic number, thus appearing brighter on BSE image. The final BSE image is a result of species with different atomic density and chemical composition. On the other hand, SE images are a result of inelastic collisions between the incident electron beam and electrons present in the sample atoms. SEs are ejected at low-energy, typical < 50eV, approximately at 10-100 nm deep in the sample surface. Finally, X-rays are also created on SEM measurements and collected in a third detector, which uses the emitted X-rays for elemental analysis and mapping across the sample surface.

Commonly, SEM is utilised on dry samples that can go under high vacuum without getting damages or/and losing their morphological features. Due to the high content of water on living cells and tissues, biological samples require chemical fixation to preserve and maintain their morphology in high vacuum. Thus, imaging biological samples using SEM is frequently preceded by the usage of a fixation solution that dehydrated the sample without impacting on its morphological features.

In this thesis, SEM is performed using a Karl Zeiss Ultra Field Emission at a working distance of ~4 mm and at an accelerating voltage between 2-5 kV. Prior to SEM imaging, the samples are fixated and covered with 4 nm gold film to prevent sample charging and increase signal to noise ratio.

5. References

1.Robertson, J., *Materials Science and Engineering R* **2002,** *37* (4–6), 129.

2.Mahan, J. E., *Wiley-VCH* **2000**, 336.

3.Cullen, R. J.; Jayasundara, D. R.; Soldi, L.; Cheng, J. J.; Dufaure, G.; Colavita, P. E., *Chemistry of Materials* **2012,** *24* (6), 1031.

4.Zhao, C.; Yang, C., *Microfluidics and Nanofluidics* **2012,** *13* (2), 179.

5.Kirby, B. J.; Hasselbrink, E. F., Jr., *Electrophoresis* **2004,** *25* (2), 203.

6.Hunter, R. J., Academic Press Limited: 1988.

7.Delgado, A. V.; Gonzalez-Caballero, F.; Hunter, R. J.; Koopal, L. K.; Lyklema, J.; International Union of, P.; Applied Chemistry, P.; Biophysical Chemistry Division, I. T. R., *J Colloid Interface Sci* **2007,** *309* (2), 194.

8.Sun, Y.-P.; Zhou, B.; Lin, Y.; Wang, W.; Fernando, K. A. S.; Pathak, P.; Meziani, M. J.; Harruff, B. A.; Wang, X.; Wang, H.; Luo, P. G.; Yang, H.; Kose, M. E.; Chen, B.; Veca, L. M.; Xie, S.-Y., *Journal of the American Chemical Society* **2006,** *128* (24), 7756.

9.Corbett, J. C. W.; McNeil-Watson, F.; Jack, R. O.; Howarth, M., *Colloids Surf., A* **2012,** *396*, 169.

10.Corbett, J.; Mcneil-Watson, F.; Jack, R. Surface charge measurement. WO2012172330 A1, 2012.

11.Tucker, I. M.; Corbett, J. C. W.; Fatkin, J.; Jack, R. O.; Kaszuba, M.; MacCreath, B.; McNeil-Watson, F., *Curr. Opin. Colloid Interface Sci.* **2015,** *20* (4), 215.

12.Vasconcelos, J. M.; Zen, F.; Stamatin, S. N.; Behan, J. A.; Colavita, P. E., *Surface and Interface Analysis* **2017**, n/a.

13.Tolstoy, V. P.; Chernyshova, I.; Skryshevsky, V. A., *Wiley* **2003**.

14.Mendelsohn, R.; Mao, G.; Flach, C. R., *Biochimica et Biophysica Acta (BBA) - Biomembranes* **2010,** *1798* (4), 788.

15.Greenler, R. G., *The Journal of Chemical Physics* **1966,** *44* (1), 310.

16.Lichtman, J. W.; Conchello, J. A., *Nat Methods* **2005,** *2* (12), 910.

17.Rayan, G.; Guet, J.-E.; Taulier, N.; Pincet, F.; Urbach, W., *Sensors (Basel, Switzerland)* **2010,** *10* (6), 5927.

18.Seu, K. J.; Cambrea, L. R.; Everly, R. M.; Hovis, J. S., *Biophysical Journal* **2006,** *91* (10), 3727.

19.Reits, E. A. J.; Neefjes, J. J., *Nat Cell Biol* **2001,** *3* (6), E145.

20.Cha, T.; Guo, A.; Zhu, X. Y., *Biophysical Journal* **2006,** *90* (4), 1270.

21.Jalili, N.; Laxminarayana, K., *Mechatronics* **2004,** *14* (8), 907.

22.Canale, C.; Jacono, M.; Diaspro, A.; Dante, S., *Microsc Res Tech* **2010,** *73* (10), 965.

23.Maver, U.; Velnar, T.; Gaberšček, M.; Planinšek, O.; Finšgar, M., *TrAC Trends in Analytical Chemistry* **2016,** *80*, 96.

24.Reichelt, R., Hawkes, P. W.; Spence, J. C. H., Eds. Springer New York: New York, NY, 2007; pp 133.

25.Havancsák, K. High-Resolution Scanning Electron Microscopy.

Chapter III

Carbon and Carbon-Modified Thin Films

Many carbon film applications and coatings rely on the ability to control carbon interfacial properties, in particular, surface charge density. Herein, the physicochemical characterisation of carbon and carbon-modified thin films, with special emphasis on surface ζ-potential determinations, is reported.

The data presented on this chapter is part of the following publications:

1. Vasconcelos, J. M.; Zen, F.; Stamatin, S. N.; Behan, J. A.; Colavita, P. E., *Surface and Interface Analysis* **2017**, 49, 781
2. Zen, F.; Angione, M. D.; Behan, J. A.; Cullen, R. J.; Duff, T.; Vasconcelos, J. M.; Scanlan, E. M.; Colavita, P. E., *Scientific Reports* **2016,** *6*, 24840.

Co-author contributions to this Chapter are as follow: J.A.B. carried out ellipsometric determinations; F.Z. contributed with XPS and contact angle measurements and SFE determinations.

1. Introduction

Carbon in the form of coatings and thin-films has gained great attention in the medical field, specifically in the biosensing, orthopaedic and cardiovascular sectors.[1-2] Many of the aforementioned applications rely on careful control of carbon interfacial properties in order to modulate chemical/electrochemical reactivity and/or a biological response. Surface charge is one of the key properties that can determine the yield and strength of interactions that take place at carbon interfaces.

Surface ζ-potential (SZP) measurements are a common method of monitoring the effect of chemical treatments and surface modifications on surface electrostatic charge,[3-4] isoelectric point and, indirectly, density of surface ionisable groups (*e.g.* –COOH, $–NH_2$). Recent SZP measurement protocols consist of measuring the mobility of tracer particles in suspension, of known ζ-potential, in close proximity of the surface that is the object of characterisation. Recently, Corbett *et al.*[5-7] developed a protocol based on tracer particles to determine the ζ-potential of macroscopic solid surfaces, which is described in detail in the Experimental Chapter.

In this Chapter, a detailed physico-chemical characterisation of carbon thin films is presented. To understand the influence of carbon surface functional groups on carbon interfacial properties, a combination of spectroscopic and microscopic techniques was utilised. Special emphasis is given to the development of a protocol for the application of the tracer particle method to the determination of SZP and isoelectric point of carbon surfaces as a function of pH, in which the use of sulfonated (SL) and amine-terminated (AL) latex bead as tracer particles was investigated. The use of these particle suspensions was validated using standard polymeric surfaces followed by the demonstration of their application to the determination of SZP and isoelectric point of macroscopic carbon surfaces. The method was found to be sensitive to chemical changes at the carbon surface and was effective at establishing isoelectric points, an important requirement for understanding the behaviour of macroscopic carbon surfaces in aqueous media.

2. Results and Discussion

Amorphous carbon (a-C) thin films used in this chapter were firstly prepared in a DC-magnetron sputtering chamber and were further subject to various surface modifications, such as oxidation, as described in the experimental section. The amorphous carbon films produced were labelled as a-C, for the as-deposited amorphous carbon, a-C:O for the oxidised amorphous carbon and as a-C:H for the hydrogen doped amorphous carbon thin films. The physico-chemical properties of these films were determined using a combination of spectroscopic and microscopic techniques, as described below.

2.1. Physico-Chemical Characterisation of Amorphous Carbon Thin Films

Morphological characterisation was carried out by Scanning Electron Microscopy (SEM) on a sputtered a-C film and no obvious morphological features were detected, as shown in Figure 3.1. Literature reports on amorphous carbon thin films deposited via sputtering techniques show that a-C films are relatively smooth and featureless.[8-10] Bociaga *et al.*[10] studied the topography of DLC films, similar to the ones prepared on this chapter, and reported as well homogeneous coatings, with no visible relevant defects. Therefore, in order to evaluate the microscopic topography of a-C films, atomic force microscopy was utilised (Figure 3.2).

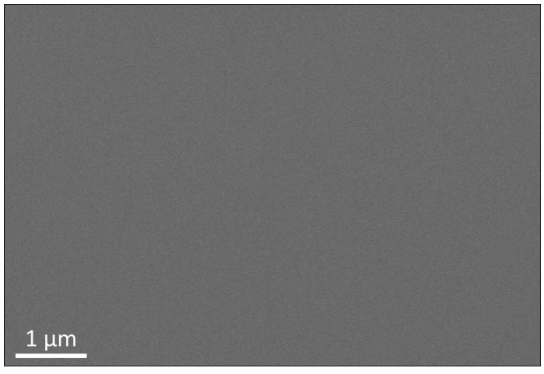


Figure 3.1. SEM image of a a-C film deposited on a Si substrate.

Atomic force microscopy (AFM) analysis (Figure 3.2) yielded root mean square (rms) roughness values for a-C, a-C:H and a-C:O thin films of (0.94 ± 0.03) nm, (1.16 ± 0.08) nm and (0.86 ± 0.07) nm, respectively, in good agreement with previous measurements on sputtered carbon films.[8-9] For instance, Peng *et al.*[27] reported a relation between surface roughness of DLC films and the preparation technique of those films. The authors reported rms roughness values between 0.04 and 1.6 nm for DLC films deposited via magnetron sputtering technique at room temperature.[27]

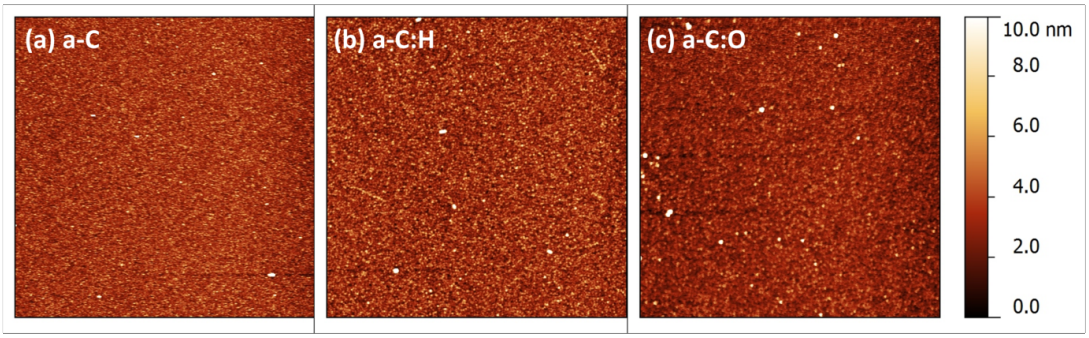


Figure 3.2. 10 × 10 µm AFM topographic images of (a) a-C, (b) a-C:H and (c) a-C:O surfaces. All surfaces roughness values were obtained from height profile determinations.

The surface chemistry of the three carbon surfaces was characterised *via* X-ray photoelectron spectroscopy (XPS), Figures 3.3 and 3.4. The XPS survey of a-C, a-C:H and a-C:O surfaces showing the characteristic peaks associated to C 1s and O 1s core levels can be observed in Figure 3.3. The surface O/C atomic percentage (%) was determined by high resolution spectra analysis on the C 1s (Figure 3.4) and O 1s regions.

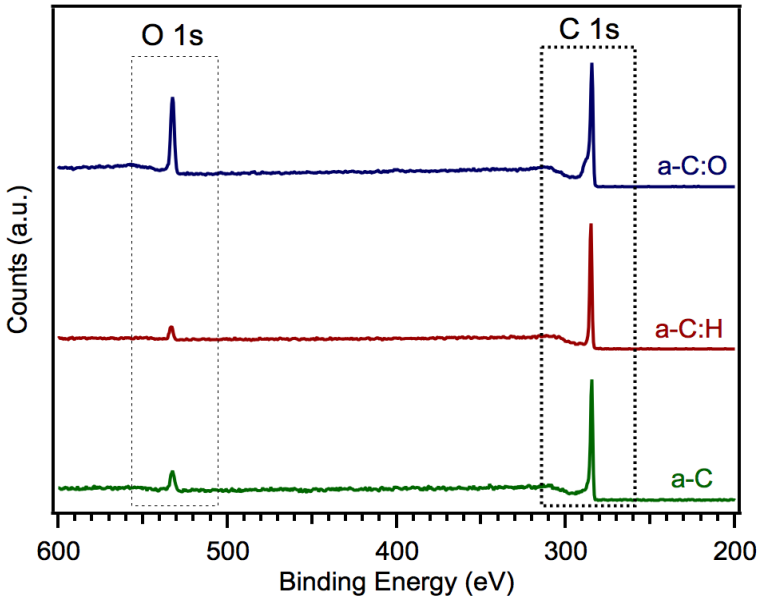


Figure 3.3. Survey XPS spectra on the region 600-200 eV of a-C, a-C:H and a-C:O surfaces showing C 1s and O 1s core level peaks.

Figure 3.4 shows the C 1s spectra of a-C, a-C:H and a-C:O surfaces; all three surfaces display a main asymmetric peak characteristic of amorphous carbon. The main C 1s peak of a-C and a-C:O was satisfactorily fitted with two main contributions at 284.4 eV and 285.1 eV attributed to trigonally (sp^2) and tetrahedrally (sp^3) bonded carbon (C—C), respectively. Only the sp^3 contribution was necessary to obtain a satisfactory fit for a-C:H surfaces, thus confirming that this surface is rich in sp^3 carbon centres.

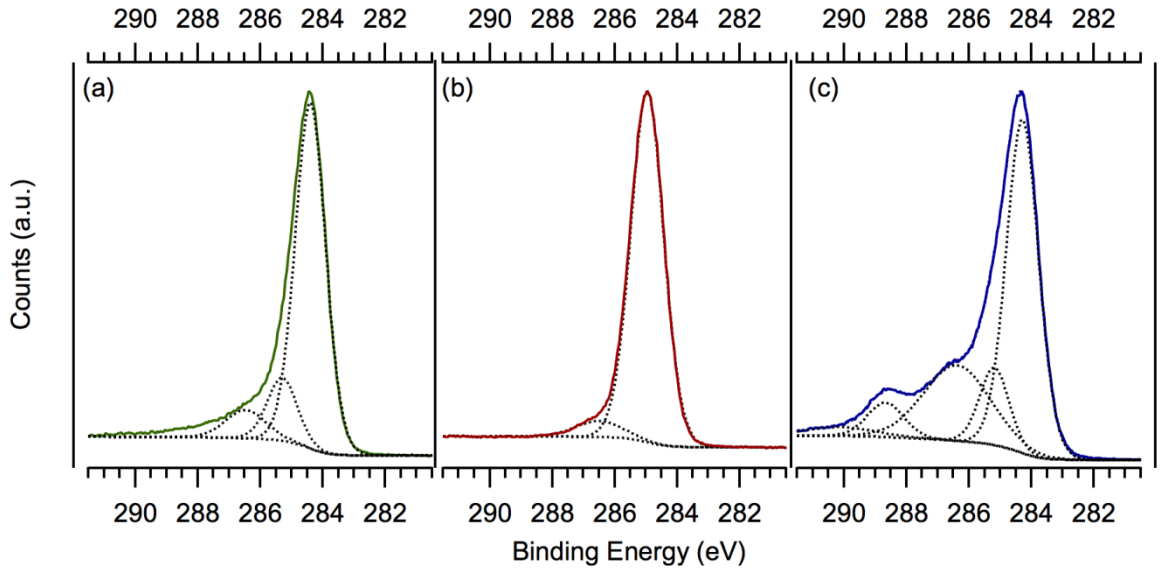


Figure 3.4. XPS spectra of (a) a-C, (b) a-C:H and (c) a-C:O surfaces in the C 1s region; Shirley background and individual contributions are shown under each curve.

This finding is consistent with literature work, which had shown that the introduction of hydrogen in the carbon scaffold occurs mainly via formation of C—H bonds.[11] Cullen *et al.*[11] reported infrared studies on a-C:H surfaces and showed that a-C:H displays a broad peak at ~2900 cm^{-1}, which is assigned to sp^2 and sp^3 C—H stretching modes, while above 3000 cm^{-1} no peaks associated with the aromatic C—H stretching modes were observed.[11-12] The presence of the C—H stretching absorption peak at ~2900 cm^{-1} confirms that the great number of hydrogen atoms are bonded to sp^2 and sp^3 carbon centres in the a-C:H film.[11]

The fraction of graphitic carbon on the carbon surfaces was estimated from the $A_{284}/A_{285+284}$ area ratios to be 85%, 82% and 0% for a-C, a-C:O and a-C:H, respectively. The a-C, and to a greater extent a-C:O, also show contributions at high binding energy (286-288 eV) that arise from the presence of oxidised groups (C—O, C=O). In the case of a-C:O, a contribution at 288.7 eV indicates the presence of carboxyl groups as a result of the oxidation process.[13] The oxygen content of the three carbon materials was obtained from fits of the O 1s peak at 532 eV (Figure 3.3). The peak area ratio A_{O1s}/A_{C1s} corrected by relative sensitivity factors yielded O/C at% contents of 5%, 8% and 20% for a-C:H, a-C and a-C:O, respectively. The high O/C content observed for a-C:O is consistent with the sample having undergone oxidative treatment.

The electronic properties of these films were obtained via spectroscopic ellipsometry (courtesy of James A. Behan); optical constants were used to calculate the absorption coefficient and subsequently determine the Tauc gap (E_T) of the amorphous carbon films. In the case of a-C films, the resulting data was fitted using a 3-layer model which takes into account the Si substrate, a native SiO_2 layer of fixed thickness (1.9 nm) and the a-C layer, as previously reported by our group.[14] A B-spline model was used to extract the complex refractive index of the a-C layer. In the case of a-C:H films, the best fits were obtained with a similar 3-layer modelling procedure using the Tauc-Lorentz (TL) model to describe the a-C:H layer. The TL model is an empirical model which has been successfully applied by other groups to describe the optical properties of a-C films with a high degree of sp^3 bonding.[15 16]

In order to obtain the Tauc gap (E_T) of deposited films, the imaginary part of the refractive index was used to calculate the absorption coefficient as a function of wavelength according to the expression:

$$\alpha = \frac{4\pi k}{\lambda}.$$

A Tauc plot of $(\alpha h\nu)^{1/2}$ *vs.* photon energy ($h\nu$) was used to carry out a fit of the linear region to the equation:[17-18]

$$(\alpha h\nu)^{1/2} = B(h\nu - E_T)$$

The intercept on the x-axis yields the E_T value which relates to the metallic/semiconducting nature of the amorphous carbon material. Typical Tauc plots for a-C and a-C:H films are shown in Figure 3.5, where the intercept on the x-axis yields the E_T value, related to the metallic/semiconducting nature of the amorphous carbon material.[17-18] The average E_T values calculated over 9 samples were found to be (0.66 ± 0.01) eV and (1.77 ± 0.01) eV for a-C and a-C:H, respectively (95% C.I.), thus confirming that a-C has a greater metallic character than a-C:H, in agreement with similarly prepared films from our group.[11]

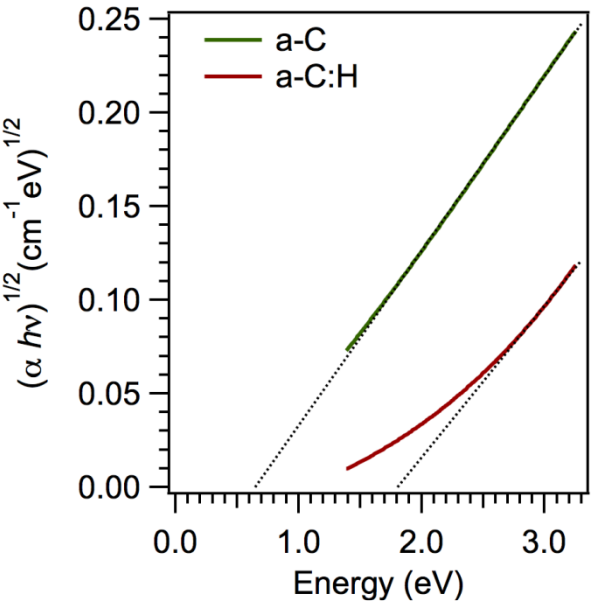


Figure 3.5. Tauc plots for a-C (red) and a-C:H (blue) films. Extrapolation of the linear fit (dot line) to the X-axis results in Tauc Gap values for both carbon surfaces (courtesy of James A. Behan).

The UV/ozone oxidation of a-C films is a surface treatment that yields a graphitic surface with an overlayer of oxidised material. In order to determine the thickness of the oxide layer, spectroscopic ellipsometry was also used (courtesy of James A. Behan); the model used consisted of a Si substrate, a native SiO_2 layer of fixed thickness (1.9 nm), an a-C layer with optical constants as determined for as deposited films, and an oxidised surface overlayer modelled as a transparent Cauchy layer.[19] The thickness of both the a-C and the oxidised overlayer were allowed to vary yielding a thickness for the oxidised overlayer of 2.8 ± 0.2 nm after 2h UV treatment.

The observed differences in carbon surface chemistry resulted in a varied wetting behaviour (Figure 3.6, Table 3.1). Static water contact angle (wCA) measurements were carried out on a-C, a-C:H and a-C:O films (Figure 3.6) yielding values of (35.2 ± 2.9)°,[20-21] (46.6 ± 2.6)° [21] and (3.2 ± 0.4)° [21], respectively (courtesy of Federico Zen). These values obtained for a-C and a-C:H surfaces are in good agreement with previous wCA determinations on similar carbon thin films.[22-24] Ostrovskaya *et al.*[24] reported on wettability measurements of DLC films and obtained values of wCA 35° and ~50° to a-C and hydrogen treated a-C films, respectively. They attributed the increase on hydrophobicity on a-C:H films to the strong C—H bonds at the carbon film.[24-25] Also, Leezenberg *et al.*[22-23] described a detailed study on wCa and SFE measurements on a-C:H films and reported values of wCa 40-50° for a-C:H films deposited with a similar H_2 flow rate as the one used on this study.

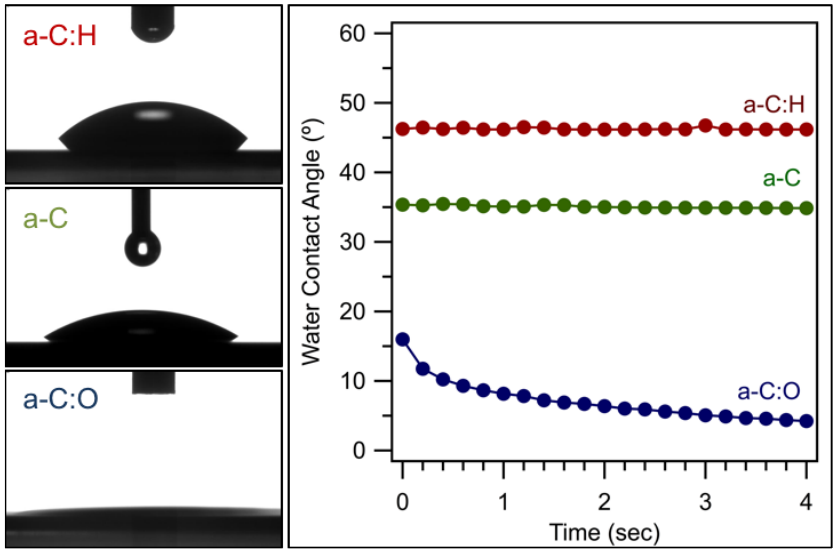


Figure 3.6. Representative images (left) of water contact angle (wCA) measurements and correspondent wCA plots (right) of a-C:H, a-C and a-C:O thin films.

Another interesting observation from the wCA measurements is the relation between wettability and oxygen content at the carbon films. a-C:O films display a wCA lower than 5°, a result from the doubling of the oxygen content on a-C:O, when compared with a-C, as observed from the XPS data (see Figure 3.4). Literature reports on induced oxidation of DLC and amorphous carbon films, attributed the increased wettability of carbon films to the introduction of oxygen containing species at the carbon interface.[26-27] Anil *et al.*[26] reported wCA of 67° ± 1.2° for DLC surface that was further reduced to 9.2° ± 2.1° after oxygen plasma treatment. Recently, Kozbial *et al.*[28] studied the hydrophobicity of graphitic surfaces and showed how after only 5 min oxidative treatment, graphitic surfaces decrease their wCA from 64° to ~ 30°.

Table 3.1. Water contact angle ($\boldsymbol{\theta_w}$) and total SFE ($\boldsymbol{\Upsilon^{tot}}$), its dispersive ($\boldsymbol{\Upsilon^{LW}}$), acid ($\boldsymbol{\Upsilon^{+}}$) and base ($\boldsymbol{\Upsilon^{-}}$) components for a-C, a-C:H and a-C:O thin films (courtesy of Federico Zen).

Surface	**Contact Angle (°)**	**Surface Free Energy (mJ m^{-2})**			
	θ_w	Υ^{LW}	Υ^{+}	Υ^{-}	Υ^{tot}

a-C	35.3 ± 1.4	49.7	1.79	27.4	63.7
a-C:H	46.6 ± 2.6	50.7	0.83	21.8	59.2
a-C:O	< 5	48.1	1.34	46.7	64

Surface free energy is known to play a role in the interfacial properties of carbon thin films and in their performance as biomaterials.[23, 25, 29-30] Table 3.1 shows a summary of total SFE (Υ^{tot}), its dispersive (Υ^{LW}), acid (Υ^{+}) and base (Υ^{-}) components for carbon thin films (courtesy of Federico Zen); both a-C and a-C:O display a similar SFE of $\Upsilon^{tot} = 64\ mJ\ m^{-2}$, while a-C:H displays a slightly lower SFE of $\Upsilon^{tot} = 59.2\ mJ\ m^{-2}$. These results are consistent with literature SFE values on amorphous carbon thin films that show that neither oxidation nor hydrogenation of carbon films induces a significant change on the total SFE.[23, 25, 29-30] For instance, Zebda *et al.*[23] reported on the surface free energies of amorphous carbon sputtered films with $A_{285}/A_{285+284}$ area ratios similar to the ones presented on this chapter (see Figure 3.4). They observed that the incorporation of hydrogen in the carbon film does not modify significantly the total SFE component of a-C:H when compared with a-C.[23]

In order to evaluate the influence of hybridisation and oxidation on the SFE components for the three carbon surfaces herein presented, SFE acid (Υ^{+}) and base (Υ^{-}) components were further analysed (Figure 3.7). The three surfaces display a similar SFE acid component of 0.83, 1.34 and $1.79\ mJ\ m^{-2}$ in the order a-C:H < a-C < a-C:O, showing that introduction of hydrogen and oxygen in the carbon film does not significant change on the SFE acid component (Υ^{+}). On the other hand, a-C:O displays a substantial increase on the SFE basic component of $\Upsilon^{-} = 46.7\ mJ\ m^{-2}$, when compared with a-C with a $\Upsilon^{-} = 27.4\ mJ\ m^{-2}$. In the case of the sp^3-rich carbon surface, a-C:H displays a lower SFE basic component of $\Upsilon^{-} = 21.8\ mJ\ m^{-2}$. These results are consistent with previous work on SFE measurements on hydrogenation[233124] and oxidation[24, 26-28] of carbon films. Ostrovskaya *et al.*[24] related the SFE polar component with the wettability of carbon surfaces and reported that near hydrophilic surfaces, as in

the case of a-C:O, dipoles of water are found to be mainly oriented normal to the surface, resulting in an enhanced SFE polar component.

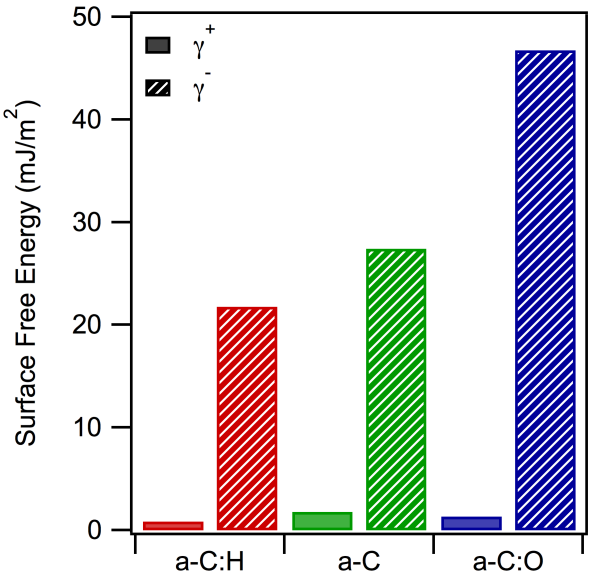


Figure 3.7. SFE acid (Υ^+) and base (Υ^-) components of a-C:H (red), a-C (green) and a-C:O (blue) thin films.

To assess the role of surface physico-chemical properties on the charge present at the carbon interface, surface ζ-potential (SZP) measurements were performed. Next sub-chapter describes in detail surface ζ-potential measurements using the tracer particles method.

2.2. Surface ζ-Potential Determinations

2.2.1. Characterisation of Particle Suspensions

The tracer particle method was used to investigate the surface ζ-potential of thin films as a function of pH. Two different tracer particle suspensions were utilised for this purpose, sulfate latex (SL) and aliphatic amine latex (AL) beads, which are terminated with $–SO_3H$ and $–NH_2$ groups, respectively.

Figure 3.8a shows the hydrodynamic size of SL and AL beads as a function of pH, obtained from DLS measurements. The hydrodynamic size of SL beads remains constant as a function of pH and the average value was found to be 582 ± 3 nm, indicating that the average hydrodynamic size is only marginally higher than the nominal diameter under the experimental conditions. AL beads also exhibit an approximately constant hydrodynamic diameter with average value of 553 ± 11 nm. These results indicate that both SL and AL bead suspensions are stable and do not aggregate or sediment over the pH range of 4.5-8.5.

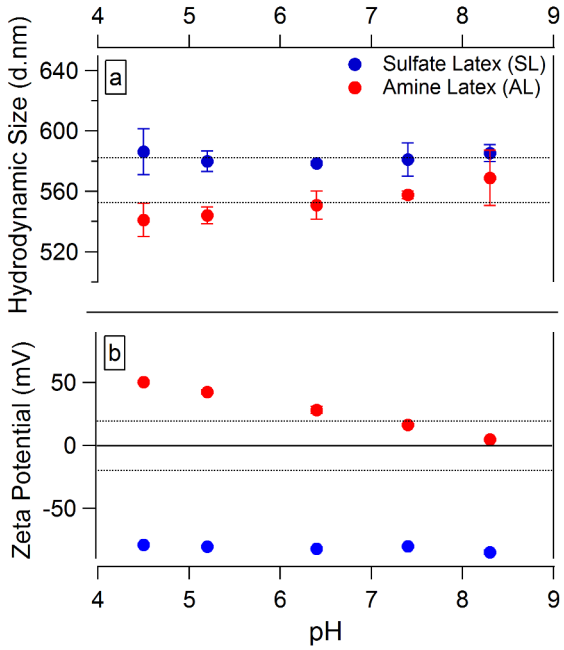


Figure 3.8. (a) Hydrodynamic size and **(b)** ζ-potential of sulfate latex (SL) and amine latex (AL) beads used as tracer particles for surface ζ-potential measurements. SL and AL beads were suspended in 100 µM PBS buffer (1.37 mM NaCl and 27 µM KCl) with total ionic strength of 1.80 ± 0.15 mM for all pH values studied.

Figure 3.8b shows the SZP of SL and AL particles as a function of pH, at a constant total ionic strength of 1.80 mM. The ζ-potential of SL beads remains at approximately -80 mV at all pH values, which is consistent with the presence of $–SO_3H$ groups at the particle surface which are acidic, with $pK_a < 2$. The results for SL particles are in agreement with those reported by Thielbeer *et al.*[31] who compared the ζ-potential of microparticles with different surface functional groups and reported a SZP of -65 mV for sulfonic acid terminated particles. AL beads display positive ζ-potential values, which range from a maximum value of 50.5 ± 1.0 mV at pH 4.5 to approximately 5 mV at pH

8.3; a linear extrapolation of the results to the pH-axis yields an estimate of pH_{iso} of 8.8. Cros *et al.* showed ζ-potential measurements of aminated ($-NH_2$) latex particles (10 mM NaCl) as a function of pH, and found that for acidic pH the particles show a stable ζ-potential of 60 mV that decreases to 0 mV at pH ~ 9.[32] The results presented here are in good agreement with the above study, and indicate that AL beads are stable in acidic media and that they possess an isoelectric point of 8.8.

2.2.2. Characterisation of Nylon and PTFE Surfaces using Tracer Particles

To confirm that the tracer particle suspensions could be applied to SZP determinations as a function of pH, the performance of latex bead suspensions in the determination of the SZP of two standard polymeric surfaces, Nylon 6,6 and polytetrafluoroethylene (PTFE), was investigated. Figure 3.9 displays the SZP ($\zeta_{surface}$) of PTFE and Nylon 6,6 obtained using SL beads as tracers, over the pH range 4-7; SZP values normalised by counterion concentration (pC) are also reported on the right-hand axis to facilitate comparison with literature data. PTFE and Nylon 6,6 show similar SZP at all pH values that compare well to those reported in literature;[33-34] values were found to decrease from approximately -20 mV at pH 4.4 to less than -50 mV for pH 6.7. Extrapolation to the x-axis yielded an estimate of pH_{iso} of 3.7 and 3.4 for Nylon and PTFE, respectively.

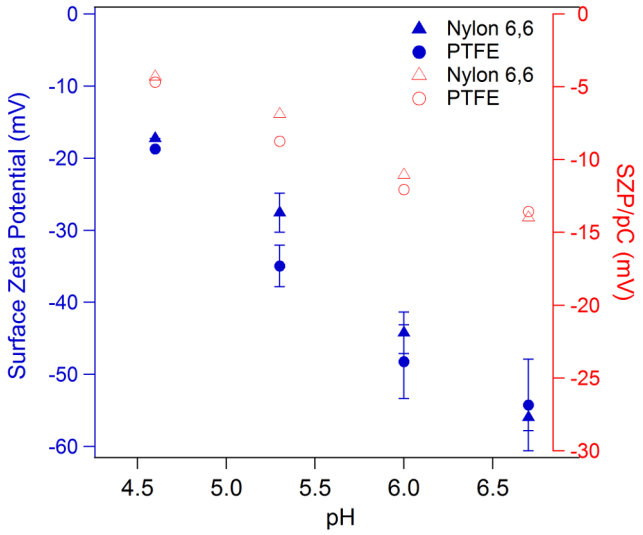


Figure 3.9. Surface ζ-potential measurements of Nylon 6,6 and PTFE surfaces (blue data points) using SL beads as tracer particles. SL beads were suspended in 100 µM PBS

buffer (1.37 mM NaCl and 27 µM KCl) and the ionic strength remained at 1.80 ± 0.15 mM for all pH studied (pC = 2.82). Surface ζ-potential values were normalized by the counterion concentration (pC) for both polymers (red data points).

Results obtained with SL tracer particles are similar to reports in the literature of ζ-potential for Nylon and PTFE obtained via streaming potential determinations.[33] Kirby *et al.*[33] published a review of SZP determinations for common polymeric substrates using microchannel methods at various pH and ionic strength values, which allows for a comparison with tracer particle SZP determinations. This review includes work from Rendall *et al.*[33-34] which reported SZP for pC = 2.0 – 4.0 in the pH range of this current study. Also, Werner *et al.*[3] studied the influence of pC on the SZP of flat solid surfaces and reported SZP/pC ratios for PTFE substrates, which comparable to the results shown in Figure 3.9. Therefore, the tracer particle method in combination with latex bead suspensions appears to offer a satisfactory protocol for the determination of SZP of macroscopic surfaces.

2.2.3. Determination of Carbon SZP using Tracer Particles

The SZP of the three carbon surfaces was determined via mobility determinations of tracer particles. In order to understand whether tracer particle chemistry can potentially affect the observed SZP, pH-dependent studies were carried out using both SL and AL particles, which possess ionisable groups with different acid-base chemistry. Figure 3.10 shows a summary of SZP values for a-C, a-C:H and a-C:O surfaces obtained with SL and AL particles as a function of pH. The most graphitic surface, a-C, displays SZP values of -51 ± 2 mV and -63 ± 5 mV at pH 7.4 using SL and AL suspensions, respectively; the SZP value increases with decreasing pH to -25 mV at pH 4.4. Extrapolation to the pH-axis yielded an estimate of pH_{iso} for a-C of 3.0 and 3.7 when SL and AL beads were used, respectively.

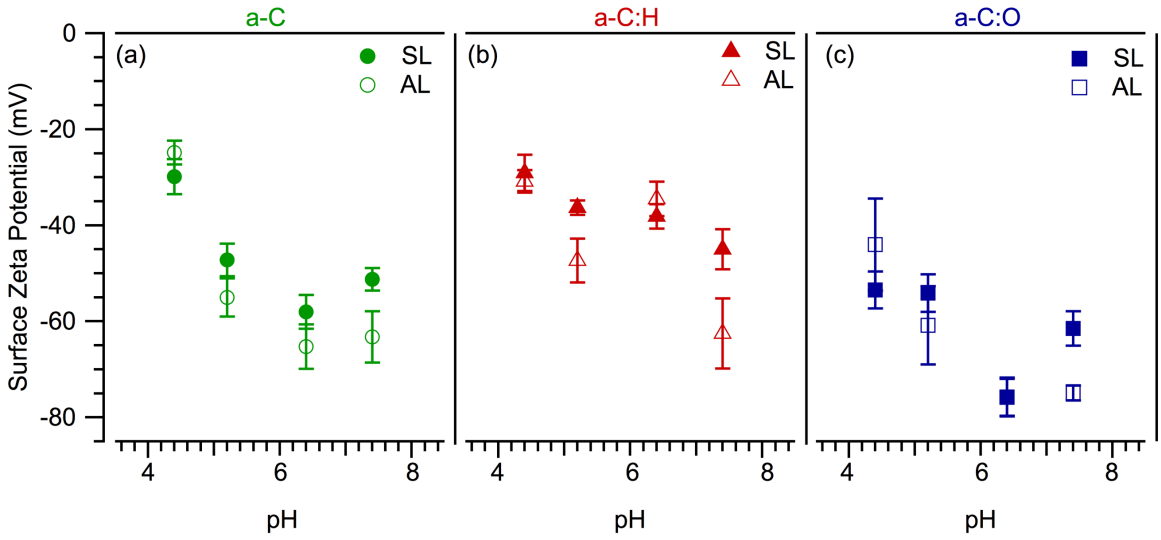


Figure 3.10. Surface ζ-Potential of a-C, a-C:H and a-C:O surfaces obtained using SL (full) and AL (empty) beads as tracer particles, suspended in 100 µM PBS buffer, 1.80 ± 0.15 mM ionic strength, for all pH values studied.

In the case of a-C:H surfaces, it becomes difficult to identify a clear trend in SZP *vs.* pH, therefore a determination of isoelectric points was not attempted for this surface. SZP values for a-C:H were found to be generally more positive than those observed for a-C under the same conditions; for instance, the SZP of a-C:H was found to be 45 ± 4 mV at pH 7.4 compared to -63 ± 5 mV for the a-C surface. Finally, surface modification with UV treatment led to more negative SZP values at all pH's, when compared with the pristine a-C surface; for instance, at pH 7.4, a-C:O surfaces yielded SZP values of -61 ± 4

mV and -75 ± 2 mV with SL and AL beads, respectively. Even at acidic pH, a-C:O surfaces were found to have the most negative SZP values among the three surfaces examined; an extrapolation to the pH-axis yielded a pH_{iso} < 1.5, which is consistent with the presence of acidic groups at the surface, as previously determined via XPS.

3. Discussion

a-C and a-C:H were found to display negative SZP at all pH values studied, despite these carbon surfaces having a negligible amount of ionisable groups observable via XPS; moreover, in the case of a-C it was possible to determine pH_{iso} in the range 3.0-3.7. There are no available published values for SZP of sputtered a-C and a-C:H as a function of pH to which the previous results can be directly compared. However, the experimental values of SZP on carbon films are in excellent agreement with published SZP determinations of other carbon surfaces with similar properties obtained using microchannel methods. Jelínek *et al*.[35] studied DLC thin films and observed a similar SZP as that of a-C in Figure 3.10 and pH_{iso} =3.7, which is identical to that obtained in this work using the tracer particle method. Nitta *et al.*[36] reported negative SZP for DLC thin films independently of the degree of oxidation. Finally, Voss *et al*.[37] also observed negative SZP for a diamond/a-C composite film at pH > 4, in agreement with the observations presented on this chapter.

Negative SZP values are often ascribed to the presence of negatively charged surface groups, however, this is not the only potential mechanism of charge build-up at the solid-aqueous interface. Although it is not possible to exclude the presence of a small amount of amphoteric –OH groups at a-C or a-C:H surfaces, these groups are not likely to give rise to negative SZP values over the pH range explored. The observations of (a) pH_{iso} between 3 and 4 for a-C surfaces, (b) a relatively hydrophobic character for a-C and a-C:H surfaces and (c) the absence of a significant surface density of acidic groups, suggest that the negative SZP is instead attributable to asymmetric adsorption of hydroxide and hydronium ions at the solid-electrolyte interface. It is now well established that for hydrophobic surfaces, even in the absence of ionisable groups, the SZP in aqueous solutions is usually negative at pH > 4.[38-39] This observation has a long

history in the literature of electrokinetic measurements (19th century),[38-39] however it is only relatively recently that a physical model has emerged to explain this behaviour. Negative SZP at hydrophobic surfaces is attributed to the preferential adsorption of hydroxide ions at the solid surface. Hydroxide adsorption has been confirmed via simulations[40-42] and experimental determinations, for instance at polymer surfaces,[38, 43] at hydrophobic self-assembled monolayers,[44] and at diamond surfaces.[37, 45-46] In the specific case of hydrophobic carbon materials, several recent reports have confirmed hydroxide adsorption. Härtl *et al.*[46] reported streaming potential measurements of H-terminated diamond, yielding a pH_{iso} in the range 3-4; complementary surface conductivity measurements and simulations demonstrated that this can be attributed to the asymmetric adsorption of OH^- and H_3O^+ ions. These results on a-C and a-C:H suggest that hydroxide ion adsorption is likely to be the dominant effect, given the absence of acidic groups at theses surfaces, thus yielding negative SZP, and pH_{iso} values similar to those observed at other carbon hydrophobic interfaces under similar conditions.

SZP results for a-C:O, the oxidised form of a-C, indicate that oxidation leads to more negative SZP values at all pH and to a decrease in isoelectric point. This is consistent with XPS results which indicate that a-C:O possesses carboxylic groups which are expected to impart greater surface acidity and increase the density of negative charges when deprotonated. These results for a-C:O are also in good agreement with SZP and pH_{iso} values previously reported for oxidised carbon particles.[47-48] Moreno-Castilla *et al.*[48] studied the effect of surface treatments on the SZP of carbon particles; they reported pH_{iso} in the range 3-4 after activation and $pH_{iso} < 2$ after oxidative treatments. Previous literature on SZP of carbon coatings is also in agreement with the results presented in this work. Nitta *et al.*[36] showed a decrease in SZP for DLC films, reporting SZP values of -26 mV for a-C *vs.* -50 mV for a-C:O at pH 5.8. Härtl *et al.*[46] reported a $pH_{iso} < 1.5$ at O-terminated diamond surfaces, in good agreement with the pH_{iso} of a-C:O surfaces presented in this work. Finally, Chakrapani *et al.*[45] showed how oxidation of diamond surfaces results in $pH_{iso} = 1$. In all cases the SZP trends were attributed to the dominant effect of acidic O-containing surface groups that are created via oxidative processes.

SZP values obtained with SL and AL were found to display similar trends *vs.* pH and only small differences at each of the pH values examined. This indicates that

repulsive/attractive electrostatic interactions or acid/base interactions between the static surface and the tracer particles do not affect SZP determinations under the conditions used in this study. Interestingly, the greatest divergence between SL and AL SZP values is observed at pH 7.4. This effect could be due to the fact that AL particles possess a ζ-potential at pH 7.4 at the margin of colloidal stability, thus suggesting that this is a limiting pH for the application of AL suspensions as tracers. Beyond colloidal stability, it is worth mentioning that AL beads are chemically less stable than SL beads as amine groups oxidise when exposed to air. AL beads were found to yield more negative particle SZP values than those reported in Figure 3.8b when measured after 30 days of storage. However, SZP determinations of carbon surfaces remained similar to those obtained with fresh AL suspensions, as long as the value chosen for SZP determinations was the value obtained at 1000 μm displacement.

4. Conclusions

In this Chapter, the physico-chemical properties of amorphous carbon thin films were investigated using a combination of spectroscopic, microscopic and light scattering techniques. Table 3.2 summarises the results obtained on this chapter which will be utilised for the following chapters.

Table 3.2. Summary of composition and properties of carbon thin films.

Surface	AFM	XPS		CA		SZP	
	Roughness (rms, nm)	$A_{284}/A_{285+284}$	O/C at.%	CA_{H2O} (°)	SFE_{total} (mJ m^{-2})	ζ-potential pH 7.4 (mV)	pH_{iso}
a-C	0.94 ± 0.03	85	8	35.2 ± 1.4	63.7	51 ± 2	3.0
a-C:H	1.16 ± 0.08	0	5	46.6 ± 2.6	59.2	-45 ± 4	-
a-C:O	0.86 ± 0.07	82	20	< 5	63.9	62 ± 4	<1.5

In summary, SEM and AFM data showed that the three carbon surfaces presented on this chapter are smooth and featureless, with no significant change on the roughness

values after hydrogenation/oxidation of the carbon film. XPS results indicate that the three carbon surfaces chosen for this study display significantly different properties, in particular the materials were found to have increasing graphitic content in the order a-C:H < a-C:O < a-C. They were also found to have increasing density of oxidised groups in the order a-C:H < a-C < a-C:O. wCA measurements show that the oxidation treatment of a-C, results in a high hydrophilic surface for a-C:O and in a significant increase on its SFE polar component. In the case of the sp^3-rich surface, a-C:H shows a similar wettability and SFE values, when compared with a-C.

A special focus was directed on establishing, first, whether pH-dependent surface ζ-potential determinations using the tracer particle method in combination with commercially available particle suspensions are comparable to those obtained with traditional streaming potential methods. This objective was tackled by measuring ζ-potential and isoelectric points of standard polymeric substrates and, indeed, found that results were comparable to reference values reported in the literature, thus confirming the applicability of the protocol.

Second, the tracer particle method for the carbon surfaces characterisation was investigated. Carbon coatings such as the ones under study in this work, are of relevance for applications in biomaterials, diagnostics and biosensing, and ζ-potential determinations are essential to understand their interactions with biomolecules, cells and organisms. The results presented on this chapter are the first determinations of pH-dependent ζ-potential and isoelectric points for sputtered carbon films; It was presented results for carbon with three different types of surface termination/chemistry: graphitic, hydrogenated and oxidised. It was shown that the two most hydrophobic surfaces display negative ζ-potential values over the range pH = 4-7; in the case of graphitic surfaces the isoelectric point could be determined to be at pH < 4. These results are consistent with the ζ-potential being dominated by the asymmetric adsorption of hydroxide ions, a common finding for hydrophobic surfaces that is consistent with prior electrokinetic results obtained on diamond materials. In the case of oxidation, it was found that the presence of acidic ionisable groups leads to a significant lowering, with respect to the non-oxidised surface, of both the ζ-potential and the isoelectric point.

Finally, to the best of the author's knowledge, there is no information currently in the literature on whether the tracer particle chemistry might affect ζ-potential and isoelectric point determinations. This is an important issue in the case of carbon materials, as these can display a wide range of chemical groups and acid/base behaviour. In this work, this problem was tackled by carrying out measurements using suspensions of tracer particles that possess terminal groups at the two extremes of the basicity/acidity spectrum: strong acid ($-SO_3H$) and basic ($-NH_2$). Furthermore, measurements with carbon materials bearing both hydrophobic and acidic groups were carried out. Results obtained with the two types of tracer particles were found to be similar in trends and values, thus indicating that SZP determinations are not affected by the acid-base chemistry or the electrostatic interactions between the solid surface and the particle surface under the aforementioned experimental conditions. However, sulfonic acid groups are more stable towards ambient oxidation than amine groups and the corresponding suspensions possess greater SZP stability over time.

5. Experimental

5.1. Chemicals and Materials

Hydrochloric acid (37%), sodium hydroxide, isopropyl alcohol, sulfuric acid (95-97%), hydrogen peroxide (30%), diiodomethane (99%), glycerol (≥99.5%), acetonitrile (HPLC grade), methanol (semiconductor grade) and phosphate buffer saline (PBS) were purchased from Sigma Aldrich; all were used without further purification. Millipore water (> 18 MΩ) was used for all experiments. Si wafers (MicroChemicals), polyester transparency films (3M), Nylon 6,6 sheets (Goodfellow) and PTFE sheets were sonicated in isopropyl alcohol for 10 min prior to further use as substrate materials. Standard Ø 300 nm latex tracer particles suspensions, 1 mM NaCl, pH 9.2 were purchased from Malvern (DTS1235). Sulfate latex beads (8% w/v, Ø 0.5 μm) and aliphatic amine latex beads (2% w/v, Ø 0.4 μm) were purchased from Life Technologies.

5.2. Preparation of Tracer Particle Suspensions

Suspensions of sulfonated latex beads (50×10^{-6} v/v) and amine-terminated latex

beads (50 × 10^{-6} v/v) were prepared in 100 µM PBS solution containing 1.37 mM NaCl and 27 µM KCl. A range of solutions with pH 4.5-8.5 were prepared for studies of ζ-potential as a function of pH; HCl and NaOH were used to adjust the pH of the PBS buffer to the desired value. The ionic strength remained at 1.80 ± 0.15 mM for all studies where pH was monitored.

5.3. Preparation of carbon thin films

A DC-magnetron sputtering chamber (Torr International, Inc.) was used to deposit amorphous carbon (a-C) films at a base pressure of ≤ 2 × 10^{-6} mbar and a deposition Ar pressure of 7 × 10^{-3} mbar, according to a literature procedure.[49] Hydrogenated amorphous carbon (a-C:H) films were prepared using a H_2/Ar gas mixture (10% H_2, 90% Ar) as previously described.[11] Oxidised amorphous carbon (a-C:O) was prepared by oxidation of a-C surfaces under a UV lamp for 2 h in air, a well-established oxidation method for carbon coatings and nanomaterials.[50-51]

5.4. Characterisation Methods

XPS characterisation was performed in a Omicron ultrahigh vacuum system (1 × 10^{-10} mbar base pressure) equipped with a monochromated Al Kα source (1486.6 eV) and a multichannel array detector. Spectra were recorded at 45° take-off angle. Peaks were fitted to Voigt functions after Shirley background correction using Casa XPS software; atomic ratios were obtained from area ratios using relative sensitivity factors (C = 1.00; O = 2.93). Scanning electron microscopy (SEM) was performed using a Karl Zeiss Ultra Field Emission at a working distance of ~4 mm and at an accelerating voltage between 2-5 kV. AFM (Asylum Research) imaging was performed in tapping mode (1 Hz and 512 scan lines) using Au-coated silicon cantilevers with nominal spring constant in the range 1.45-15.1 N m^{-1} (NT-MDT). Spectroscopic ellipsometry (SE) measurements of amorphous carbon surfaces were performed using a J.A. Woolam Co. Inc. alpha-SETM ellipsometer; data were modelled using CompleteEASE™ software as discussed in the Supporting Information.[52] Static contact angles (CA) were measured on a CA analyser (FTA) using 20µL droplets under ambient conditions of temperature and humidity;[23] samples were

rinsed in methanol immediately prior to CA characterisation and a minimum of three CA measurements were obtained for each surface. Surface Free Energy (SFE) determinations were obtained by multi-solvent analysis, utilising water, glycerol and diiodomethane as solvents. SFE data was modelled using the van OSS model, as previously described in literature.[20] This model considers that the total surface tension is a result of its polar (γ^{AB}) and apolar (γ^{LW}) contributions, where γ^{AB} comprehends electron donor (γ^{-}) and acceptor (γ^{+}) interactions.[20]

Dynamic light scattering (DLS) and ζ-potential measurements were carried out using a Malvern Zetasizer Nano-ZS, λ = 633 nm He-Ne laser; the signal was detected at 173° and 13° for DLS and ζ-potential measurements, respectively. Hydrodynamic size was determined using a refractive index n = 1.59 for latex.[53] Particle ζ-potential was obtained using the same instrument which determines particle velocity and mobility via phase analysis light scattering (PALS);[5] solution conditions were optimized as described in the experimental section.

5.5. Surface ζ-Potential Determinations

Surface ζ-potential measurements were performed using a surface ζ-potential cell (Malvern Instruments). Mobility determinations were conducted at 125, 250, 375, 500 and 1000 μm displacements from the sample surface. Thin film samples were prepared with the dimensions of 4 × 4 mm to fit the cell sample holder. SL and AL beads were used as tracer particles in suspensions containing 100 μM PBS buffer (1.37 mM NaCl and 27 μM KCl) of total ionic strength 1.80 ± 0.15 mM at all pH values studied. A buffered suspension at pH = 7.4 was prepared first and pH was varied via addition of HCl or NaOH as appropriate; the error bar for the ionic strength reflects the range of variation introduced by the pH adjustment process. The conductivity of the suspension was optimized for values in the range 200-300 μS/cm; values above this range were found to lead to electrochemical degradation of cell electrodes or of the beads, and were found to result in large deviations in calculated SZPs. Error bars indicate standard deviations calculated from three measurements on each sample.

5. References

1.Roy, R. K.; Lee, K. R., *J. Biomed. Mater. Res., Part B* **2007,** *83* (1), 72.
2.Stüber, M.; Niederberger, L.; Danneil, F.; Leiste, H.; Ulrich, S.; Welle, A.; Marin, M.; Fischer, H., *Advanced Engineering Materials* **2007,** *9* (12), 1114.
3.Werner, C.; Körber, H.; Zimmermann, R.; Dukhin, S.; Jacobasch, H.-J., *Journal of Colloid and Interface Science* **1998,** *208* (1), 329.
4.Werner, C.; Jacobasch, H. J., *Int. J. Artif. Organs* **1999,** *22* (3), 160.
5.Corbett, J. C. W.; McNeil-Watson, F.; Jack, R. O.; Howarth, M., *Colloids Surf., A* **2012,** *396*, 169.
6.Corbett, J.; Mcneil-Watson, F.; Jack, R. Surface charge measurement. WO2012172330 A1, 2012.
7.Tucker, I. M.; Corbett, J. C. W.; Fatkin, J.; Jack, R. O.; Kaszuba, M.; MacCreath, B.; McNeil-Watson, F., *Curr. Opin. Colloid Interface Sci.* **2015,** *20* (4), 215.
8.Peng, X. L.; Barber, Z. H.; Clyne, T. W., *Surface and Coatings Technology* **2001,** *138* (1), 23.
9.Dearnaley, G.; Arps, J. H., *Surface and Coatings Technology* **2005,** *200* (7), 2518.
10.Bociaga, D.; Kaminska, M.; Sobczyk-Guzenda, A.; Jastrzebski, K.; Swiatek, L.; Olejnik, A., *Diamond and Related Materials* **2016,** *67*, 41.
11.Cullen, R. J.; Jayasundara, D. R.; Soldi, L.; Cheng, J. J.; Dufaure, G.; Colavita, P. E., *Chemistry of Materials* **2012,** *24* (6), 1031.
12.Pierson, H. O., William Andrew Publishing: Oxford, 1993; pp 337.
13.Johansson, E.; Nyborg, L., *Surface and Interface Analysis* **2003,** *35*, 375.
14.Zen, F.; Angione, M. D.; Behan, J. A.; Cullen, R. J.; Duff, T.; Vasconcelos, J. M.; Scanlan, E. M.; Colavita, P. E., *Sci. Rep.* **2016**, 24840.
15.Jellison Jr, G. E.; Merkulov, V. I.; Puretzky, A. A.; Geohegan, D. B.; Eres, G.; Lowndes, D. H.; Caughman, J. B., *Thin Solid Films* **2000,** *377–378* (0), 68.
16.Logothetidis, S., *Diamond and Related Materials* **2003,** *12* (2), 141.
17.Silva, S. R. P., *Properties of amorphous carbon*. 1st ed.; INSPEC, Inc. The Institution of Electrical Engineers: London, 2003.
18.Tauc, J., *Amorphous and liquid semiconductors*. 1st ed.; Plenum Press: London and New York, 1974.
19.Franquet, A.; De Laet, J.; Schram, T.; Terryn, H.; Subramanian, V.; van Ooij, W. J.; Vereecken, J., *Thin Solid Films* **2001,** *384* (1), 37.
20.Zen, F.; Angione, M. D.; Behan, J. A.; Cullen, R. J.; Duff, T.; Vasconcelos, J. M.; Scanlan, E. M.; Colavita, P. E., *Scientific Reports* **2016,** *6*, 24840.
21.Vasconcelos, J. M.; Zen, F.; Stamatin, S. N.; Behan, J. A.; Colavita, P. E., *Surface and Interface Analysis* **2017,** (49), 781.
22.Leezenberg, P. B.; Johnston, W. H.; Tyndall, G. W., *J. Appl. Phys.* **2001,** *89* (6), 3498.
23.Zebda, A.; Sabbah, H.; Ababou-Girard, S.; Solal, F.; Godet, C., *Appl. Surf. Sci.* **2008,** *254* (16), 4980.
24.Ostrovskaya, L.; Perevertailo, V.; Ralchenko, V.; Dementjev, A.; Loginova, O., *Diamond and Related Materials* **2002,** *11* (3), 845.
25.Hansen, J. O.; Copperthwaite, R. G.; Derry, T. E.; Pratt, J. M., *Journal of Colloid and Interface Science* **1989,** *130* (2), 347.
26.Anil, M.; Ahmed, S. F.; Yi, J. W.; Moon, M.-W.; Lee, K.-R.; Kim, Y. c.; Seok, H. K.; Han, S. H., *Diamond and Related Materials* **2010,** *19* (4), 300.
27.Roy, R. K.; Choi, H.-W.; Park, S.-J.; Lee, K.-R., *Diamond and Related Materials* **2007,** *16* (9), 1732.
28.Kozbial, A.; Zhou, F.; Li, Z.; Liu, H.; Li, L., *Accounts of Chemical Research* **2016,** *49* (12), 2765.
29.Buddy D. Ratner; Allan S. Hoffman; Frederick J. Schoen; Jack E. Lemons, 2 ed.; Elsevier Academic Press: London, 2004.

30.Ostrovskaya, L.; Perevertailo, V.; Ralchenko, V.; Dementjev, A.; Loginova, O., *Diamond and Related Materials* **2002,** *11* (3–6), 845.
31.Thielbeer, F.; Donaldson, K.; Bradley, M., *Bioconjugate chemistry* **2011,** *22* (2), 144.
32.Ganachaud, F.; Elaïssari, A.; Pichot, C.; Laayoun, A.; Cros, P., *Langmuir* **1997,** *13* (4), 701.
33.Kirby, B. J.; Hasselbrink, E. F., Jr., *Electrophoresis* **2004,** *25* (2), 203.
34.Rendall, H. M.; Smith, A. L., *J. Chem. Soc., Faraday Trans.* **1978,** (74), 1179.
35.Jelínek, M.; Smetana, K.; Kocourek, T.; Dvořánková, B.; Zemek, J.; Remsa, J.; Luxbacher, T., *Materials Science and Engineering: B* **2010,** *169* (1–3), 89.
36.Nitta, Y.; Okamoto, K.; Nakatani, T.; Hoshi, H.; Homma, A.; Tatsumi, E.; Taenaka, Y., *Diamond and Related Materials* **2008,** *17* (11), 1972.
37.Voss, A.; Wei, H.; Müller, C.; Popov, C.; Kulisch, W.; Ceccone, G.; Ziegler, C.; Stengl, M.; Reithmaier, J. P., *Diamond Relat. Mater.* **2012,** *26*, 60.
38.Beattie, J. K., *Lab Chip* **2006,** *6* (11), 1409.
39.McCarty, L. S.; Whitesides, G. M., *Angew Chem Int Ed Engl* **2008,** *47* (12), 2188.
40.Kreuzer, H. J.; Wang, R. L. C.; Grunze, M., *J. Am. Chem. Soc.* **2003,** *125* (27), 8384.
41.Kudin, K. N.; Car, R., *J. AM. CHEM. SOC.* **2008,** *130* (12), 3915.
42.Zangi, R.; Engberts, J. B. F. N., *J. Am. Chem. Soc.* **2005,** *127* (7), 2272.
43.Zimmermann, R.; Dukhin, S.; Werner, C., *J. Phys. Chem. B* **2001,** *105* (36), 8544.
44.Dicke, C.; Hähner, G., *J. Am. Chem. Soc.* **2002,** *124* (42), 12619.
45.Chakrapani, V.; Angus, J. C.; Anderson, A. B.; Wolter, S. D.; Stoner, B. R.; Sumanasekera, G. U., *Science* **2007,** *318* (5855), 1424.
46.Hartl, A.; Garrido, J. A.; Nowy, S.; Zimmermann, R.; Werner, C.; Horinek, D.; Netz, R.; Stutzmann, M., *J. Am. Chem. Soc.* **2007,** *129* (5), 1287.
47.Duffy, P.; Magno, L. M.; Yadav, R. B.; Roberts, S. K.; Ward, A. D.; Botchway, S. W.; Colavita, P. E.; Quinn, S. J., *Journal of Materials Chemistry* **2012,** *22* (2), 432.
48.Moreno-Castilla, C.; Ferro-Garcia, M. A.; Joly, J. P.; Bautista-Toledo, I.; Carrasco-Marin, F.; Rivera-Utrilla, J., *Langmuir* **1995,** *11* (11), 4386.
49.Murphy, D. M.; Cullen, R. J.; Jayasundara, D. R.; Scanlan, E. M.; Colavita, P. E., *RSC Advances* **2012,** *2* (16), 6527.
50.Simmons, J. M.; Nichols, B. M.; Baker, S. E.; Marcus, M. S.; Castellini, O. M.; Lee, C. S.; Hamers, R. J.; Eriksson, M. A., *The Journal of Physical Chemistry B* **2006,** *110* (14), 7113.
51.Colavita, P. E.; Sun, B.; Wang, X.; Hamers, R. J., *Journal of Physical Chemistry C* **2009,** *113* (4), 1526.
52.Bruinink, A.; Bitar, M.; Pleskova, M.; Wick, P.; Krug, H. F.; Maniura-Weber, K., *Journal of Biomedical Materials Research - Part A* **2014,** *102* (1), 275.
53.Gittings, M. R.; Saville, D. A., *Colloids and Surfaces A: Physicochemical and Engineering Aspects* **1998,** *141* (1), 111.

Chapter IV

Physico-Chemical Characterisation of Phospholipid Liposomes

Phospholipids are found in vivo in the form of aggregates and as the main constituents of cell membranes. In vitro, phospholipids are often combined in liposomes and used to mimic the interaction of biomaterials with biological fluids. Herein, the influence of nature, type and preparation methods of phospholipid liposomes on their size and electrostatic stability is reported.

1. Introduction

Lipids are defined as a large family of biomolecules which are not soluble in water but soluble in organic solvents.[1] In solution, lipids are mostly transported as part of aggregates, whether self-assembled into layer structures or as lipoprotein aggregates. Phospholipids are an important sub-class of lipids that play various roles in many biological systems including the building blocks of eukaryotic plasma membranes,[2] and aggregates for the transport of other lipids such as triacylglycerols.[3-4]

One of the simplest model lipid aggregates is called liposome, which consists of a vesicle containing a water core enclosed by at least one phospholipid layer.[5-7] Liposomes have been used to mimic the interaction of liposomes with biomaterials, in particular as biosensors, cell-signaling and as a platform for protein studies.[2, 8-12 13] Moreover, liposomes have also been used to mimic plasma membrane *in vitro* and as efficient drug delivery systems.[6, 14]

Liposomes are commonly defined according to their composition, structure and preparation method.[6, 15] The physico-chemical properties of liposomes in solution is strongly dependent on the combination of phospholipids present in the liposome[16], such as phosphatidylcholine (PC) and phosphatidylserine (PS), and on buffer's temperature,[17-18] pH[17, 19] and ionic composition.[7, 18, 20-23]

In this chapter, the physico-chemical properties of PC and PS phospholipids is studied using FT-IR. Subsequently, PC and PS are combined in a liposome, in a 80/20 ratio, which is commonly used to mimic biological membranes.[7, 24] Firstly, the influence of liposome preparation method is studied. Additionally, the effect caused by varying the type of phospholipid, PC and PS, on the liposome's size, electrostatic stability and morphology is reported. Finally, the influence of buffer pH and ionic composition on the size and charge of PC/PS liposomes is investigated.

2. Results and Discussion

2.1. Characterisation of Phosphatidylcholine (PC) and 3-sn-Phosphatidyl-L-serine (PS)

Over the last few decades, IR spectroscopy has been utilised as a major technique to characterise phospholipids. Various studies in literature use IR spectroscopy to determine the IR band assignments of phospholipids with regards to lipid alkyl chains and head groups[25-26] and buffer ion composition[26-27] and temperature[25, 28]. Table 4.1 shows a summary of the major phospholipids IR bands that are present in literature for phospholipids;[25, 29-30] specific IR bands present on the phospholipids used in this work are discussed below.

Table 4.1. Assignment of major IR bands present on phospholipid groups.[25, 29-30]

Phospholipid group	Wavenumber (cm^{-1})	Assignment
Fatty acids	2957	CH_3 antisymmetric stretching
	2921	CH_2 antisymmetric stretching
	2870	CH_3 symmetric stretching
	2851	CH_2 symmetric stretching
	1735	$C = O$ stretching
Glycerol / Fatty	1470-1420	CH_2 scissor/bending
Phosphate	1223	PO_2^- antisymmetric stretching
	1088	PO_2^- symmetric stretching
Glycerol	1173	$C - O - C$ antisymmetric stretching
	1068	$C - O - C$ symmetric stretching
Choline/Serine	1400-1395	$N^+ - \ CH_3$ symmetric stretching
	970	$N^+ - \ CH_3$ antisymmetric stretching

Figure 4.1 shows a FT-IR spectrum of PC (blue) and PS (red) phospholipids used in this chapter, characterised individually prior to liposome production; R1 and R2 represent fatty acid residues present on the phospholipids. In IR, PC and PS phospholipids possess common bands of alkyl chains and phosphate/glycerol groups which are present on the

fatty acid chains and head groups, respectively (Table 4.1).[29] Bands at $2800 - 3000\ cm^{-1}$ are attributed to the symmetric and antisymmetric stretching modes of $C - H$ groups; CH_2 exhibits two peaks at $2924\ cm^{-1}$ and $2852\ cm^{-1}$ correspondent to the antisymmetric and symmetric stretching, respectively.[29] Peaks at $2957\ cm^{-1}$ and $2874\ cm^{-1}$ are assigned to antisymmetric and symmetric CH_3 stretching modes, respectively.[25, 30] These bands of $C - H$ groups are highly sensitive to the degree of order/disorder transition of the alkyl chains and their IR frequency can greatly shift as a result of an increase/decrease of gauche/trans conformers in the fatty acid chains.[26, 28, 31] In the case of natural phospholipids, used in this work, the control over gauche/trans conformers in the lipids chains is rather difficult.[32] In fact, in Figure 4.1 the IR absorption band attributed to CH_2 mode is shifted to higher wavenumbers, suggesting an higher density of gauche conformers in the lipid chain.[25]

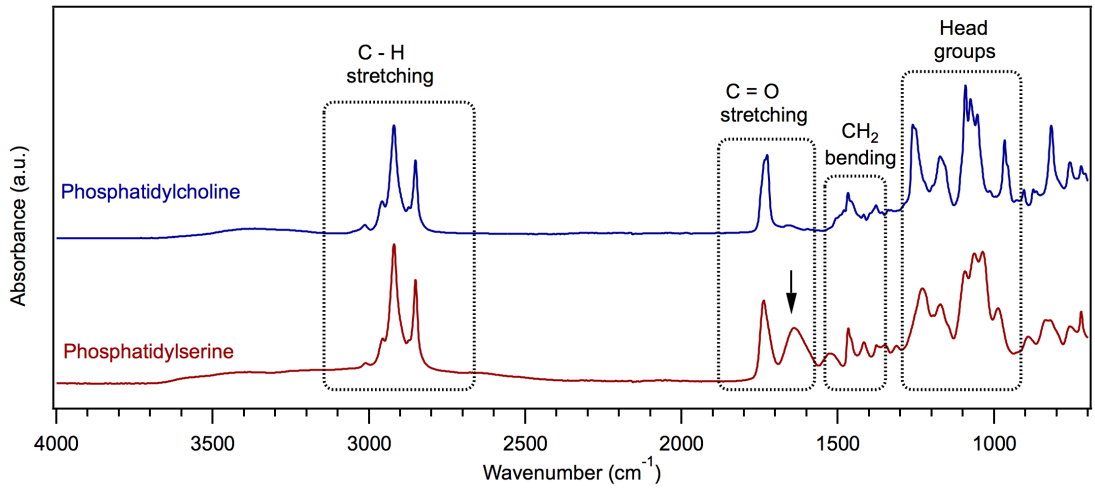


Figure 4.1. FT-IR spectra on the 4000 – 1000 cm^{-1} region of phosphatidylcholine (**PC**) and phosphatidylserine (**PS**); phospholipid main groups are assigned on the spectra.

With regards to the phospholipid polar component, both PC and PS phospholipids display peaks at 1735 cm^{-1} and between 1220–1240 cm^{-1}, corresponding to $C = O$ stretching and PO_2^- antisymmetric double bond stretching bands, respectively.[25, 30] PS phospholipid possesses a specific peak at 1620 cm^{-1} (denoted by the arrow in Fig. 1), that is not observed for the PC phospholipid, and it is attributed to the COO^- asymmetric stretch on PS head group.[27]

2.2.Characterisation of Phospholipid Liposomes

In this study, the fabrication and characterisation of liposomes containing PC and PS phospholipids were performed. To determine if the size and electrostatic stability of the liposomes used in this study are dependent on the preparation method, the nature and the type of phospholipids, the following questions were considered:

(i) Is the size and stability of PC liposomes dependent on the preparation method?

(ii) How does PS influence on the size and electrostatic stability of PC liposomes?

(iii) Does pH influence on PC/PS liposome size and stability?

(iv) How does the ionic composition of the buffer affect PC/PS liposome electrostatic stability?

2.2.1. Morrisey *vs* Freeze-Thaw Protocols for Preparation of PC Liposome: Size and Stability Study

Scanning Electron Microscopy (SEM) was performed on PC-based liposomes suspended in PBS buffer at pH 7.4, prepared according to the Morrisey protocol (see experimental section). Distribution of liposome diameters, after extrusion through a Ø450 nm porous filter, were found to be 102 ± 17 nm, excluding the presence of some aggregates with diameter > 400 nm, as shown in Figure 4.2.

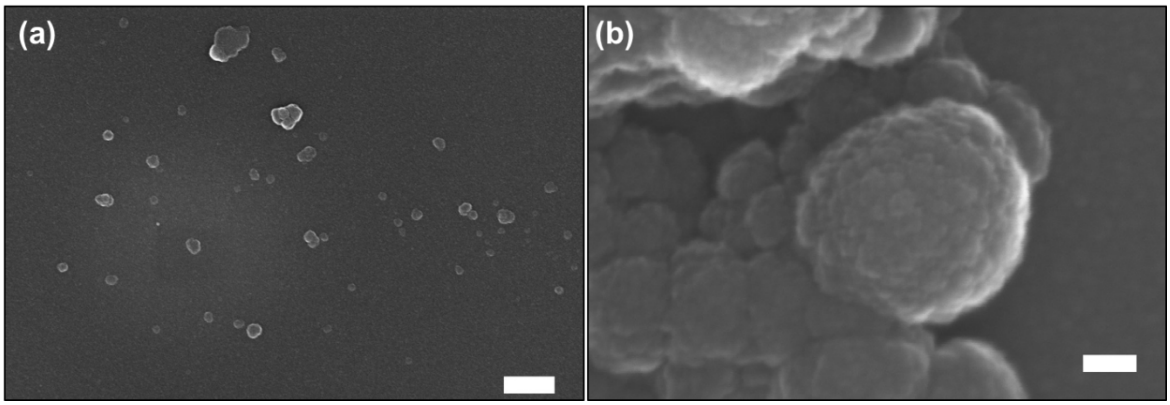


Figure 4.2. SEM images of PC liposomes deposited on a Si substrate; white bars correspond to **(a)** 500 nm and **(b)** 50 nm.

Dynamic Light Scattering (DLS) experiments were performed to compare liposomes produced through two similar protocols: the Morrisey and Freeze-thaw protocols, both described in the experimental section.[33-35] The hydrodynamic size distribution results of the obtained PC liposome suspensions measured via DLS can be observed in Figure 4.3. Figure 4.3a shows an example of a DLS measurement, at neutral pH, after extrusion through a Ø100 nm porous filter on a suspension of PC liposomes using the Freeze-thaw (blue) and Morrisey (red) protocols. For both preparation protocols, the presence of a singular peak at ~ 100 nm reveals that the liposome size is monodisperse, and no agglomeration/sedimentation of liposomes in solution is observed. Literature values on hydrodynamic size of liposomes show that liposomes with hydrodynamic diameter in the range of 50-200 nm are associated with Large Unilamellar Vesicles (LUV), *i.e.* one single bilayer of liposomes.[6]

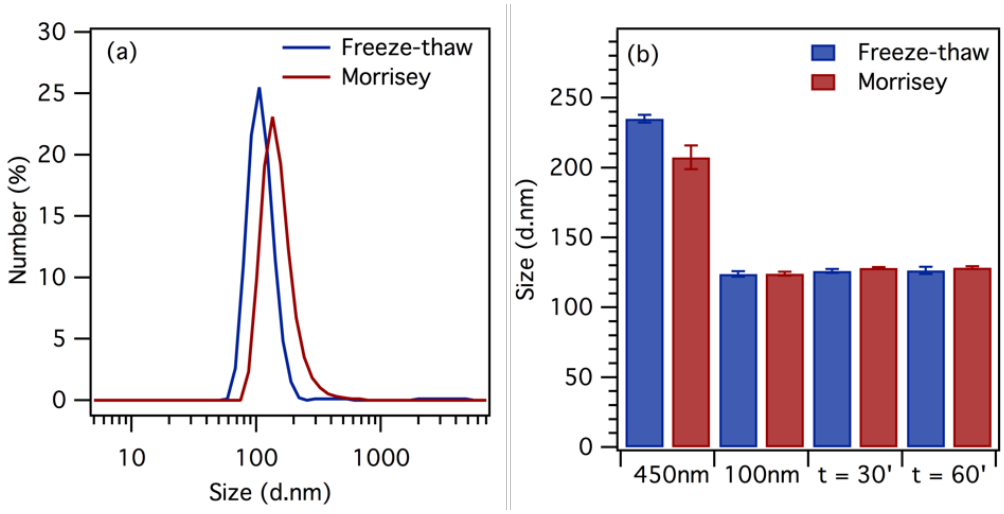


Figure 4.3. (a) Example of a measurement on the PC liposome hydrodynamic size (d.nm) using the Freeze-thaw (**blue**) and Morrisey (**red**) protocols after extrusion through a Ø100 nm filter. **(b)** Hydrodynamic size of PC liposomes for Freeze-thaw protocol (**red**) and for Morrisey protocol (**blue**). Liposomes were extruded through a nylon membrane (450 nm pore diameter) followed by a second extrusion through another nylon membrane (100 nm pore diameter). The hydrodynamic size was measured immediately after extrusion, for t=30 min and for t=60 min.

The homogeneity of liposomes in suspension represents a key factor on liposomes efficiency as drug carriers, and as mimic lipid aggregates.[36-37] Poly-Dispersive Index (PDI) values are commonly utilised as a quality parameter for DLS measurements on

nanoparticles, and it is use to describe the variation on particles size: values close to 1 are correlated to high dispersity of particles size, while values close to 0 represent a population of particles that is monodisperse.[36] The PDI for the PC liposomes hydrodynamic size was determined to be < 0.4 for both the Freeze-thaw and Morrisey protocols. PDI range obtained for PC liposomes prepared using both preparation protocols, is consistent with literature values for a suspension of monodisperse liposomes using natural phospholipids[16-17, 36-38] For example, Jacquot *et al.*[38] studied the morphology of natural-phospholipids based biomembranes through the analysis of their electrophoretic mobility. They reported PDI values of ~0.1 for synthetic-phospholipids based liposomes, which was further increased to PDI ~0.3 when a natural phospholipid was added to the liposome. Additionally, Tefas *et al.*[36] reported PDI values from 0.083 to 0.3 for increased % of natural PC phospholipids included on the liposome. Finally, Silva Malheiros *et al.*[37] characterised the electrostatic stability of PC liposomes and reported hydrodynamic sizes in the range of 150-200 nm with a correspondent PDI of 0.3-04.

Figure 4.3b shows DLS measurements of liposomes suspended in a buffer at pH 7.4, prepared through two different methods. For both methods, liposome suspensions were extruded through Ø450 nm and Ø100 nm pore size nylon membranes (reported in the graph as 450 nm and 100 nm, respectively) after preparation of the liposome suspension in PBS. After the liposome suspension is extruded through the 450 nm pore size nylon membrane, the measured hydrodynamic mean diameter is $d_{(450nm)}$ = 235 ± 23 nm for the Morrisey protocol and $d_{(450nm)}$ = 207 ± 9 nm for the Freeze-thaw protocol. A second extrusion through 100 nm pore size nylon membranes, reduces the liposome mean diameter to $d_{(100nm)}$ = 124 ± 2 nm and $d_{(100nm)}$ = 124 ± 1 nm for the Morrisey and Freeze-thaw methods, respectively. Therefore, considering the DLS diameter values obtained after the second extrusion, there were no significant differences in hydrodynamic size for liposomes obtained using both methods. These results are consistent with literature studies on liposomes size made of PC, using similar preparation protocols.[37] For instance, Silva Malheiros *et al.*[37] reported liposomes hydrodynamic diameter of ~ 150 nm for PC liposomes prepared through a film hydration protocol. Additionally, Jacquot *et al.*[38] used the vesicle fusion method for the preparation of PC-based liposomes and reported hydrodynamic sizes of ~ 125 nm for natural-based PC membranes.

The stability of liposomes in suspension is a key factor in the determination of the performance of liposomes *in vivo*.[37] The liposome hydrodynamic size was measured as a function of time after filtered through the Ø100 nm nylon membrane; liposomes hydrodynamic size was measured at 3 different intervals: time = 0 min, when the liposome preparation is initiated, for time = 30 min, half-time after preparation and for time = 60 min, as shown in Figure 4.2b. With regards to the Morrisey protocol, the liposome hydrodynamic diameter was found to be $d_{(t=30\ min)}$ = 126 ± 1 nm and $d_{(t=60\ min)}$ = 126 ± 3 nm, whereas for the Freeze-thaw protocol, $d_{(t=30\ min)}$ = 128 ± 1 nm and $d_{(t=60\ min)}$ = 129 ± 1 nm. These results indicate that PC liposomes, produced either using the Freeze-thaw or the Morrisey protocols, show a great homogeneity and stability of their hydrodynamic sizes over 1 h in suspension. Silva Malheiros *et al.*[37] studied the stability of PC liposomes in solution over a course of 24 days and reported a similar homogeneity on liposomes size and stable PDI for that time range. Given that no significant differences were observed on the liposomes size prepared using the two methods, the Morrissey protocol was chosen to be used from now on due to its simplicity when compared with the Freeze-thaw protocol.

2.2.2. Influence of PS on the Electrostatic Stability of PC-containing Liposomes

In general, lipid membranes present in biological media are made of more than one type of phospholipid, and the combination of different types of phospholipids results in different degrees of liposome stability in solution.[39-40] To tackle the second question proposed on this work, the influence of PS on PC-containing liposomes was investigated. These two phospholipids, PC and PS, were combined in a liposome, in a ratio of 80/20 PC/PS, according to the procedure described in the experimental section.[33, 35]

In Table 4.2, the hydrodynamic size, PDI and ζ-potential values for the PC and PC/PS liposomes are shown. PC-based liposomes display a hydrodynamic diameter of 210 ± 1 nm and a ζ-potential of - 0.1 ± 2.0 mV. When PS is added to the PC liposome suspension, the average hydrodynamic size and ζ-potential decrease to 148 ± 2 nm and – 84.6 ± 0.8 mV, respectively. It is well known that the introduction of PS on PC-containing liposomes results in a drastic decrease of ζ-potential for a wide range of buffer conditions.[40] This

behaviour is a result of the strong negatively charged carboxyl group present on the PS head group, which is known to stabilize liposomes containing different phospholipids.[40]

Table 4.2. Hydrodynamic size, PDI and ζ-potential of PC (100) and PC/PS (80:20) liposomes.

Liposome	Hydrodynamic size (nm)	PDI	ζ-potential (mV)
PC	210 ± 1	0.31	- 0.1 ± 2.0
PC/PS	148 ± 2	0.25	- 84.6 ± 0.8

In this current work, the decrease of the liposome hydrodynamic size and ζ-potential, when PS is added to PC-based liposomes, is related to the enhanced electrostatic stability of liposomes in suspension.[40-41] As mentioned before, PS is known to contribute to a higher electrostatic stability to PC-based liposomes, resulting in a decrease of ζ-potential values and in a decrease of hydrodynamic size. For instance, Roy *et al.*[40] reported ζ-potential values in the range of - 5 to - 10 mV for liposomes containing PC only. When PS was added to the PC liposome suspension, ζ-potential values reached the electrostatic stability range, displaying ζ-potential of - 73.9 mV. Consequently, liposomes formed by PC/PS resulted in a lower hydrodynamic size when compared to PC liposomes, due to the increase on the electrostatic stability of the liposomes in suspension.[40] *Roy et al.*[41] also studied the distribution of PS on mainly choline constituted liposomes and showed that serine is responsible for stabilising the zwitterionic behaviour of choline, resulting in a remarkable decrease in the liposome size.[41]

2.2.3. Influence of pH on the Electrostatic Stability of PC/PS Liposomes

Phospholipid liposomes are commonly used as drug carriers and the control over drug encapsulation and stability in solution are greatly dependent on the pH of the medium.[17, 19] The pH gradient stablished between the liposomes core and the aqueous medium ultimately defines the liposome efficiency as drug carrier and its stability while

in circulation in the body.[19] Additionally, the pH of the aqueous medium influences the interaction of liposomes with macroscopic surfaces and dictates the conformation of liposomes adsorption at the solid-liquid interface.[42-43] To understand how the pH effects the stability of PC/PS liposomes used in this work, light scattering measurements were performed on liposomes at pH range of 4.5-9.5 and hydrodynamic size and ζ-potential were analysed.

Figure 4.4 shows the hydrodynamic diameter of PC/PS liposome regarding pH (blue) and its respective PDI (red). The PC/PS liposome diameter reaches a minimum of 76 ± 1 nm at pH 8.5, increasing for 108 ± 2 nm and 241 ± 2 nm for basic (pH 9.5) and acidic (pH 4.5) pHs, respectively. Similar results were reported by Sabin *et al.*[44] that showed a change in liposome sizes when the concentration of ions changed in the buffer solution. At high ion concentration, the electric interactions between the ions adsorbed onto the phospholipids head group initiates an alteration in the bilayer curvature and therefore in the change in the liposome sizes. For all sizes, the liposome PDI is within the range of 0.22-0.39, consistent with PDI values for liposomes containing natural phospholipids.[16-17, 36-38]

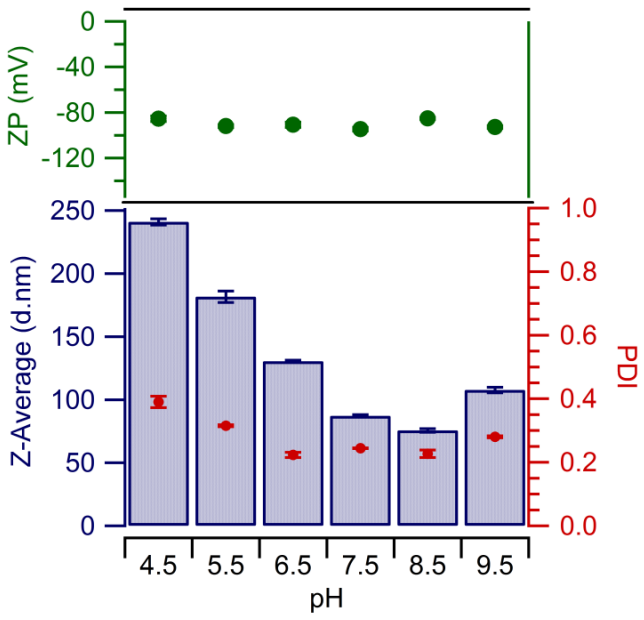


Figure 4.4. Hydrodynamic diameter (**blue**) and ζ-potential (**green**) values of PC/PS liposomes regarding pH and its respective polidispersity index (PDI-**red**).

Moreover, ζ-potential of PC/PS liposomes for a pH range of 4.5-9.5 are displayed is Figure 4.4. For all pH intervals, the PC/PS liposomes possess a ζ-potential of – 85.1 ± 0.9 mV, a much lower ζ-potential when compared with the PC-based liposomes ($\zeta_{potential}$ ~ 0 mV). As seen before (Table 4.2), the introduction of PS to the PC-based liposomes, confers a significantly higher stability to the liposome suspension, bringing the ζ-potential of the PC/PS liposomes suspension to the stability range for all pH values analysed.[40-41]

2.2.4. Influence of Ionic Composition on the Electrostatic Stability of PC/PS Liposomes

Understanding the interactions of lipid membranes with various cations, which can be found in the body, is of great importance considering their role in processes occurring at the molecular level in the cell membrane. Emphasis is given in literature on the importance of calcium based processes happening at the membrane interface, which include protein binding, cell signaling and cell activation.[7] In this work, the effect of calcium on the size and electrostatic stability of PC/PS liposome was studied. PC/PS liposome suspensions were prepared in a PBS buffer with 10 mM $CaCl_2$ at a constant ionic strength of ~164 mM.

Figure 4.5 displays the average hydrodynamic sizes and corresponding PDIs of PC/PS liposomes suspended in PBS solution with and without Ca^{2+} added. The introduction of Ca^{2+} di-cation, at a 10 mM concentration, results in a slight decrease in the hydrodynamic size of PC/PS liposomes from 148 ± 2 nm (PDI 0.4) to 128 ± 3 nm (PDI 0.3). Liposomes size was stable over a range of 1 h for both PBS and PBS.$CaCl_2$ buffers. The slight decrease in liposome diameter is consistent with reported effects of divalent cations on the curvature of phospholipid vesicles and membranes.[20, 22, 23, 45-47] It is well stablished that a stronger interaction occurs between lipid molecules and Ca^{2+} ions when compared to Na^{+} ions and lipid molecules. The stronger interaction for lipid/Ca^{2+} ion combination results in a significant change in the lipid membrane conformation.[7, 21, 48] It is also well known that the introduction of Ca^{2+} results in a lower degree of hydration, higher molecular packing and higher degree of fatty acid chain order.[7, 48]

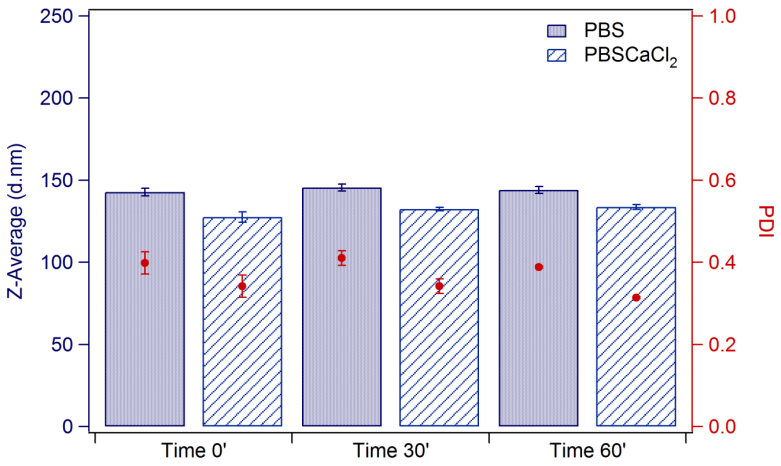


Figure 4.5. Hydrodynamic size (**blue**) of PC/PS liposomes in the absence and presence of 10 mM $CaCl_2$ and its respective polidispersity index (PDI-**red**). Liposomes were extruded through a nylon membrane (450 nm pore diameter). The hydrodynamic size was measured immediately after extrusion, for t=30 min and for t=60 min.

To understand the effect of Ca^{2+} on the electrostatic stability of the liposomes, ζ-potential measurements were performed on PC and PC/PS liposomes, Figure 4.6. As previously observed, the PC liposomes suspended in a PBS solution exhibit a ζ-potential of ~ 0 mV which is dramatically decreased to - 85 ± 1 mV when PS is added to the liposome, Table 4.2. The introduction of Ca^{2+} in the PBS buffer does not seem to interfere with the ζ-potential of PC liposomes that remain close to 0 mV, Figure 4.6. Interestingly, PC/PS liposomes have their ζ-potential increased to – 44 ± 1 mV, suggesting that the ζ-potential of the negatively charged liposome is significantly affected by the di-cation.

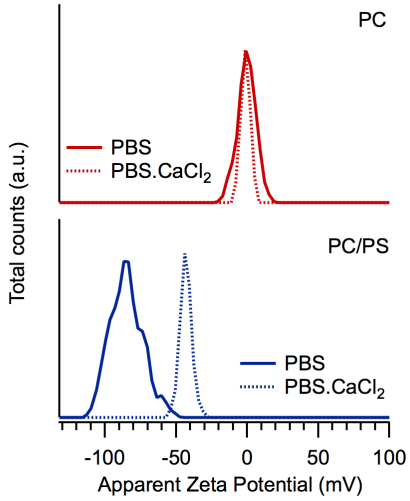


Figure 4.6. Apparent ζ-potential values of PC (**red**) and PC/PS (**blue**) liposomes in the absence (solid line) and presence (dot line) of $CaCl_2$ in the PBS solution.

Recently, Melcrova *et al.*[7] reported on the interaction of Ca^{2+} with PC/PS membranes and suggested three possible binding sites for Ca^{2+} on the phospholipid membrane: (i) carboxyl groups of PS, (ii) phosphate groups of PC and PS, and (iii) carbonyl groups of PC and PS.[7] Literature studies on the Ca^{2+} and phospholipid membranes have shown that Ca^{2+} binds primarily to the phosphate group of all phospholipids, including PC.[47] Also, the binding of Ca^{2+} to the carboxyl group of PS have been studied by molecular dynamics simulation.[47-48] It was shown that in the presence of PS, the Ca^{2+} binds both at the phosphate groups of PC and PS but also to the carboxyl group of PS.[48]

3. Conclusions

In this chapter, the physico-chemical properties of phospholipids liposomes were studied. Firstly, the FT-IR spectra of PC and PS phospholipids was analysed. Subsequently, PC and PS were combined in a liposome and their electrostatic stability in solution was examined regarding liposome preparation method, type and nature of phospholipids present in the liposome and buffer pH and ionic composition.

PC-containing liposomes prepared through the Morrisey protocol exhibit similar diameter when comparing with the Freeze-thaw procedure. The stability of the PC liposomes in solution was observed for both preparation protocols; the Morrisey

protocol was used due to its easy and simple protocol when compared with the Freeze-thaw.

The influence of PS on PC-based liposomes was analysed and it was found that the introduction of PS in a PC-containing liposome results in a smaller hydrodynamic size. Additionally, the PC/PS liposomes exhibit a significantly higher electrostatic stability in solution when compared with PC liposomes, displaying ζ-potential values in the stability range (< -20 mV), while PC liposomes display ζ-potential values close to 0 mV.

The influence of pH on PC/PS electrostatic stability was also studied. ζ-potential measurements on the PC/PS liposomes suspended in PBS buffer in a pH range of 4.5-9.5 showed that buffer pH does not affect significantly the ζ-potential of PC/PS liposomes in suspension. With regards to the hydrodynamic size, PC/PS liposomes hydrodynamic diameter reaches a minimum at pH 8.5 and was found to increase when PC/PS liposomes were suspended in more acidic and basic conditions.

Finally, the influence of buffer ionic composition was examined and showed that the introduction of Ca^{2+} in the PBS solution has a great influence on the ζ-potential of PC/PS liposomes. Ca^{2+} is known to bind to the PC and PS phosphate groups and also to the PS carboxylic group, resulting in an increase of ζ-potential values for PC/PS liposomes.

The study presented in this chapter clarifies the physico-chemical properties of PC/PS liposomes in suspension. The results in this chapter on the PC/PS liposomes will be utilised in the following chapter. In subsequent chapters, the PC/PS liposomes will be incubated with carbon surfaces and their interaction will be examined with regards to buffer ionic composition and pH and amorphous carbon physico-chemical properties.

4. Experimental

4.1. Chemicals and Materials

Phosphatidylcholine from egg yolk 99.9% (PC) and 3-sn-Phosphatidyl-L-serine from bovine brain 95% (PS) were purchased from Sigma Aldrich as a lyophilized powder. Phosphate buffer saline solution (PBS 0.01 M, 0.0027 M KCl and 0.137 M NaCl pH 7.4)

was prepared by dilution of ready to use tablets (Sigma). Chloroform (HPLC grade) and calcium chloride were purchased from Sigma Aldrich, and were used without further purification. All water used for experiments was obtained from a Millipore purification system.

4.2. Liposome Preparation

Phosphate buffer (PBS) and PBS with 10 mM calcium chloride (PBS.$CaCl_2$) were prepared and kept at pH 7.4 and constant ionic strength of 164 mM. Liposomes were prepared according to previously published protocols.[33-35] Briefly, stock solutions of 10 mg mL^{-1} of PC and PS in chloroform were prepared and kept in the freezer. Before use, 2.6 µmol of phospholipids (80:20 molar ratio PC/PS) were dispensed in a glass vial and the mixture of phospholipids was dried under argon gas and left under vacuum for two hours at room temperature. 2.6 mL of previously prepared buffer were added to the mixture of PL and vortexed until a milky suspension was obtained. The suspension was further sonicated for 30 min until the liquid appeared clear thus yielding a 1 mM suspension of liposomes in buffer. The suspension was filtered (0.45 µm) and the filtrate stored in the fridge at 4°C.

An alternative procedure, called Freeze-thaw protocol,[49] was utilised to compare the hydrodynamic size of liposomes produced through the Morrisey's protocol. Freeze-thaw procedure shares the first steps of liposomes preparation with Morrisey's protocol. Phospholipids were placed in the freezer on a stock solution of 10 mg/mL PC and PS in chloroform. Following Morrisey's protocol, 1mM suspension of phospholipids in buffer solution (pH 7.4) was obtained. The liposome suspension was further frozen for 20 min, thawed by sonication for 5 min and extruded through a nylon membrane (Ø450 µm). The cycle of freeze-thaw-extrusion was repeated at least 10 times.

4.3.Characterisation Methods

Dynamic light scattering (DLS) and ζ-potential measurements were carried out using a Malvern Zetasizer Nano-ZS, λ = 633 nm He-Ne laser. The signal was detected at 173° and 13° for DLS and ζ-potential measurements, respectively. Fourier transform infrared spectroscopy (FT-IR) measurements were carried out using a PerkinElmer Spectrum 100

FT-IR Spectrometer with PerkinElmer Universal ATR Sampling Accessory. Scan electron microscopy (SEM) was performed on a Karl Zeiss Ultra Field Emission SEM at an accelerating voltage of 10 kV at a working distance of ~ 5 mm. The samples were coated with 4 mm layer of gold before SEM imaging.

5. References

1.Morrison, R. T.; Boyd, R. N., 6th ed.; Boston: Allyn and Bacon: 1983.
2.Castellana, E. T.; Cremer, P. S., *Surface Science Reports* **2006,** *61* (10), 429.
3.Hussain, M. M., *Atherosclerosis* **2000,** *148*, 1.
4.Kurt W. Miller; Donald M. Smalls, *The Journal of Biological Chemistry* **1983,** *258* (22), 13772.
5.Sessa, G.; Weissmann, G., *Journal of lipid research* **1968,** *9* (3), 310.
6.Akbarzadeh, A.; Rezaei-Sadabady, R.; Davaran, S.; Joo, S.; Zarghami, N.; Hanifehpour, Y.; Samiei, M.; Kouhi, M.; Nejati-Koshki, K., *Nanoscale Res Lett* **2013,** *8* (1), 1.
7.Melcrova, A.; Pokorna, S.; Pullanchery, S.; Kohagen, M.; Jurkiewicz, P.; Hof, M.; Jungwirth, P.; Cremer, P. S.; Cwiklik, L., *Sci Rep* **2016,** *6*, 38035.
8.Towns, E. N.; Parikh, A. N.; Land, D. P., *The Journal of Physical Chemistry C* **2015**, 150126074752006.
9.Okamoto, Y.; Tsuzuki, K.; Iwasa, S.; Ishikawa, R.; Sandhu, A.; Tero, R., *Journal of Physics: Conference Series* **2012,** *352*, 012017.
10.Cho, N.-J.; Frank, C. W.; Kasemo, B.; Hook, F., *Nat. Protocols* **2010,** *5* (6), 1096.
11.Scarano, S.; Mascini, M.; Turner, A. P. F.; Minunni, M., *Biosensors and Bioelectronics* **2010,** *25* (5), 957.
12.Limaj, O.; Etezadi, D.; Wittenberg, N. J.; Rodrigo, D.; Yoo, D.; Oh, S. H.; Altug, H., *Nano Lett* **2016,** *16* (2), 1502.
13.Saeui, C. T.; Mathew, M. P.; Liu, L.; Urias, E.; Yarema, K. J., *J Funct Biomater* **2015,** *6* (2), 454.
14.Sovago, M.; Wurpel, G. W. H.; Smits, M.; Müller, M.; Bonn, M., *Journal of the American Chemical Society* **2007,** *129* (36), 11079.
15.Bozzuto, G.; Molinari, A., *Int J Nanomedicine* **2015,** *10*, 975.
16.Yandrapati, R. K. 2012.
17.Sułkowski, W. W.; Pentak, D.; Nowak, K.; Sułkowska, A., *Journal of Molecular Structure* **2005,** *744-747*, 737.
18.Morini, M. A.; Sierra, M. B.; Pedroni, V. I.; Alarcon, L. M.; Appignanesi, G. A.; Disalvo, E. A., *Colloids and Surfaces B: Biointerfaces* **2015,** *131*, 54.
19.Drummond, D. C.; Zignani, M.; Leroux, J.-C., *Progress in Lipid Research* **2000,** *39* (5), 409.
20.Mashaghi, A.; Mashaghi, S.; Reviakine, I.; Heeren, R. M.; Sandoghdar, V.; Bonn, M., *Chemical Society reviews* **2014,** *43* (3), 887.
21.Ruso, J. M.; Besada, L.; Martinez-Landeira, P.; Seoane, L.; Prieto, G.; Sarmiento, F., *J Liposome Res* **2003,** *13* (2), 131.
22.Roux, M.; Bloom, M., *Biochemistry* **1990,** *29* (30), 7077.
23.Claessens, M. M. A. E.; van Oort, B. F.; Leermakers, F. A. M.; Hoekstra, F. A.; Cohen Stuart, M. A., *Biophysical journal* **2004,** *87* (6), 3882.
24.Weinstein, D. B.; Marsh, J. B.; Glick, M. C.; Warren, L., *The Journal of Biological Chemistry* **1969,** *244* (13), 4103.
25.Popova, A. V.; Hincha, D. K., *Biophysical journal* **2003,** *85* (3), 1682.
26.Casal, H.; Mantsch, H.; Hauser, H., *Biochemistry* **1987,** *26* (14), 4408.
27.Dluhy, R.; Cameron, D. G.; Mantsch, H. H.; Mendelsohn, R., *Biochemistry* **1983,** *22* (26), 6318.
28.Brumfeld, V.; Bach, D.; Miller, I. R., *Eur Biophys J* **1991,** *19*, 287.
29.Chen, C.; Tripp, C. P., *Biochimica et biophysica acta* **2008,** *1778* (10), 2266.
30.Toyran, N.; Severcan, F., *Spectroscopy* **2002,** *16*, 399.
31.Ouyang, H.; Moore, D. J.; Sills, R. H.; Mendelsohn, R., *Spectroscopy* **2004,** *18* (3), 407.
32.Ingólfsson, H. I.; Melo, M. N.; van Eerden, F. J.; Arnarez, C.; Lopez, C. A.; Wassenaar, T. A.; Periole, X.; de Vries, A. H.; Tieleman, D. P.; Marrink, S. J., *Journal of the American Chemical Society* **2014,** *136* (41), 14554.

33.Morrissey, J. H. Morrissey laboratory protocol for preparing phospholipid vesicles (SUV) by sonication. (accessed 04.10.2016).
34.Liu, S.; Pu, Q.; Byun, C. K.; Wang, S.; Lu, J.; Xiong, Y., *The Journal of Physical Chemistry C* **2007,** *111* (29), 10818.
35.Silva-Lopez, E. I.; Edens, L. E.; Barden, A. O.; Keller, D. J.; Brozik, J. A., *Chem Phys Lipids* **2014,** *183*, 91.
36.Tefas, L. R.; Muntean, D.; Vlase, L.; Porfire, A. S.; Achim, M.; Tomuta, I., *Farmacia* **2015,** *63* (1).
37.Silva Malheiros, P.; Micheletto, Y. M. S.; Silveira, N. P. d.; Brandelli, A., *Food Research International* **2010,** *43* (4), 1198.
38.Jacquot, A.; Francius, G.; Razafitianamaharavo, A.; Dehghani, F.; Tamayol, A.; Linder, M.; Arab-Tehrany, E., *PLoS ONE* **2014,** *9* (9), e107435.
39.Li, J.; Wang, X.; Zhang, T.; Wang, C.; Huang, Z.; Luo, X.; Deng, Y., *Asian Journal of Pharmaceutical Sciences* **2015,** *10* (2), 81.
40.Roy, M. T.; Gallardo, M.; Estelrich, J., *J Colloid Interface Sci* **1998,** *206* (2), 512.
41.Roy, M. T.; Gallardo, M.; Estelrich, J., *Bioconjugate Chemistry* **1997,** *8* (6), 941.
42.Hautala, J. T.; Wiedmer, S. K.; Riekkola, M. L., *Electrophoresis* **2005,** *26* (1), 176.
43.Rapaport, D.; Hague, G. R.; Pouny, Y.; Shai, Y., *Biochemistry* **1993,** *32* (13), 3291.
44.Sabin, J.; Prieto, G.; Ruso, J. M.; Hidalgo-Alvarez, R.; Sarmiento, F., *The European physical journal. E, Soft matter* **2006,** *20* (4), 401.
45.Boettcher, J. M.; Davis-Harrison, R. L.; Clay, M. C.; Nieuwkoop, A. J.; Ohkubo, Y. Z.; Tajkhorshid, E.; Morrissey, J. H.; Rienstra, C. M., *Biochemistry* **2011,** *50* (12), 2264.
46.Seantier, B.; Kasemo, B., *Langmuir* **2009,** *25* (10), 5767.
47.Martín-Molina, A.; Rodríguez-Beas, C.; Faraudo, J., *Biophysical journal* **2012,** *102* (9), 2095.
48.Pedersen, U. R.; Leidy, C.; Westh, P.; Peters, G. H., *Biochimica et Biophysica Acta (BBA) - Biomembranes* **2006,** *1758* (5), 573.
49.Claessens, M. M. A. E.; van Oort, B. F.; Leermakers, F. A. M.; Hoekstra, F. A.; Cohen Stuart, M. A., *Biophysical journal 87* (6), 3882.

Chapter V

Interaction of Carbon Thin Films and Phospholipid Liposomes

Carbon bioresponse has been related with the composition/structure of an initially adsorbed lipid layer, however, there is still a great controversy regarding the structure of the adsorbed layer and the role of this layer in terms of the resulting bioresponse. Herein, a study on carbon/lipid interfacial interactions regarding buffer pH and composition and carbon surface terminal groups is reported.

The data presented on this chapter is part of the following publications:

1. Vasconcelos, J. M.; Zen, F.; Stamatin, S. N.; Behan, J. A.; Colavita, P. E., *Surface and Interface Analysis* **2017**, 49, 781
2. *Joana M. Vasconcelos, Federico Zen, M. Daniela Angione, Ronan J. Cullen, Maria J. Santos-Martinez, and Paula E. Colavita,* (Under Review)

1. Introduction

Carbon materials are extensively used in biological applications, both in the form of coatings or thin films,[1-6] or as nanostructured forms of carbon, *e.g.* nanotubes[7], fullerenes[8], nanodiamonds[9-10] and porous carbons[11-12]. Altough carbon-based materials offer a wide range of desirable properties[5-6, 13-14] for their application in the medical sector, the origin of carbon bioresponse is not yet fully understood, and there is currently great interest in understanding what role carbon surface chemistry might play in determining its properties as a biomaterial.[4, 15-22]

It is believed that during the early stages after implantation, small biomolecules found in biological fluids and tissues transport fast to the surface and condition the physiological response to the implanted solid, thus determining the outcome of more complex phenomena that occur over longer timescales.[1, 23-25] The most abundant biomolecules found in common fluids (*e.g.* plasma, serum, synovial fluid, tears) are proteins and lipids. Considerable attention has been dedicated to the study of protein/carbon interactions and of novel methods for promoting or preventing their adsorption,[26] however the literature is comparatively sparse as regards lipid/carbon interactions.

In this chapter, lipid-carbon interaction is studied in relation to carbon surface properties and buffer composition. Firstly, the influence of carbon surface termination on the adsorption of phosphatidylcholine (PC) / phosphatidylserine (PS) at carbon surfaces is investigated; adsorption was studied at a high graphitic amorphous carbon surface (a-C) and at the same surface after an oxidative treatment. Secondly, the effect that pH and ionic composition have on the amount and mode of adsorption of liposomes on carbon surfaces is addressed by using a combination of surface spectroscopy, fluorescence imaging, quartz crystal microbalance with dissipation technology and atomic force microscopy. Finally, a relation between surface chemistry, buffer composition and liposome adsorption on carbon surfaces is established. Results demonstrate that adsorption and adsorbate structure of PC/PS liposomes onto carbon surfaces is highly dependent on both carbon chemistry and buffer composition.

2. Results

2.1. Influence of Surface Chemistry

Infrared Reflection-Absorption Spectroscopy (IRRAS) *ex situ* was performed to examine the adsorption of phospholipids onto amorphous carbon surfaces. Phospholipid adsorption onto surfaces yields characteristic peaks of alkyl chains and phosphate groups which are present in the hydrophobic tails and head groups, respectively (see Chapter IV).[27-30] Methyl groups present on phospholipids alkyl chains yield characteristic absorption band in the C—H stretching region ~ 2900 cm^{-1}. More specifically, peaks at 2957 cm^{-1} and 2874 cm^{-1} are assigned to the antisymmetric and symmetric -CH_3 stretching modes; peaks at 2924 cm^{-1} and 2852 cm^{-1} are assigned to the -CH_2 antisymmetric and symmetric stretching modes, respectively. At lower wavenumber, on the C=O stretching mode region ~ 1728 - 1743 cm^{-1}, another peak is observed and is assigned to ester carbonyl groups present in the phospholipid heads.[27-30]

Figure 5.1 shows IRRAS spectra in the region of 3200 - 1500 cm^{-1} of a-C, a-C:H and a-C:O surfaces after 1 h incubation of 1 mM PC/PS liposome at pH 7.4. IRRAS spectra of a-C and a-C:H exhibit characteristic absorption bands of phospholipids, on the C—H stretching mode ~ 2900 cm^{-1} and C=O stretching mode ~ 1734 cm^{-1} regions. At the graphitic (a-C) and hydrogen doped surfaces (a-C:H), two strong absorbance bands are seen in the C—H stretching regions, which are located at 2921 cm^{-1} and 2853 cm^{-1} (-CH_2 stretching modes), and a small shoulder is also observed at 2965 cm^{-1} (-CH_3 stretching modes). At lower wavenumbers it is also present a C=O stretching peak at 1736 cm^{-1}, observed for both a-C and a-C:H surfaces.

Regarding a-C:O surface, no absorption is seen on the C-H stretching mode ~ 2900 cm^{-1} nor on the C=O stretching mode ~ 1734 cm^{-1} regions. The absence of absorption bands on methyl and ester carbonyl groups regions indicate that phospholipids are not present on a-C:O surfaces. However, the region of ester carbonyl groups, present in the phospholipid head group, overlaps with C=O absorbances of a-C:O, thus making this region of limited use for monitoring lipid adsorption in the case of oxidised carbons.

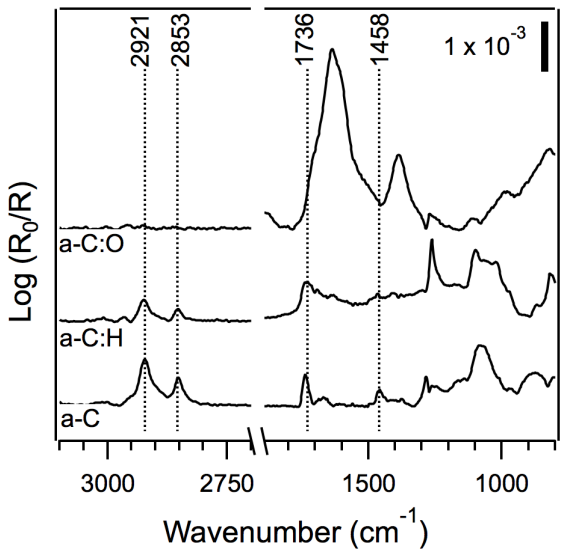


Figure 5.1. IRRAS spectra on the 3200 – 800 cm^{-1} region of a-C, a-C:H and a-C:O surfaces after 1 h incubation of 1 mM PC/PS liposome in PBS at pH 7.4.

To understand whether differences observed in Figure 5.1 are only observed *ex situ*, and to determine the mode of adsorption of PC/PS liposomes at carbon surfaces, fluorescence recovery after pohtobleaching (FRAP) experiments were carried out. Surfaces were incubated at pH 7.4 in PC/PS suspensions prepared with 0.02% mol Texas Red DHPE, a phospholipid with a fluorescently labelled head group, then rinsed in water and measured while wet.

Figure 5.2 shows fluorescence images collected before (t = 0 min), during (t = 1 min) and after (t = 2 - 5 min) photobleaching of the adsorbed lipids. A comparison of the three surfaces in the pre-bleached images shows a much higher fluorescence emission for a-C and a-C:H when compared with a-C:O, thus indicating higher lipid adsorption at a-C/a-C:H *vs.* a-C:O and in agreement with IRRAS results (Figure 5.1). The effect of photobleaching is evident in the case of a-C and a-C:H (t = 1 min), since the intensity of fluorescence was reduced, followed by a recovery of < 5% and < 10% within the bleached area (t = 2 -5 min), respectively. This result suggests that liposomes are present in the form of intact vesicles at the graphitic and hydrogen doped carbon surfaces, as near complete fluorescence recovery would be expected in the case of supported lipid layer formed via vesicle rupture.[31-32] In the case of a-C:O, no photobleaching was

observed as expected based on the absence of lipid adsorption evident from pre-bleaching images (Figure 5.2) and IRRAS (Figure 5.1) results.

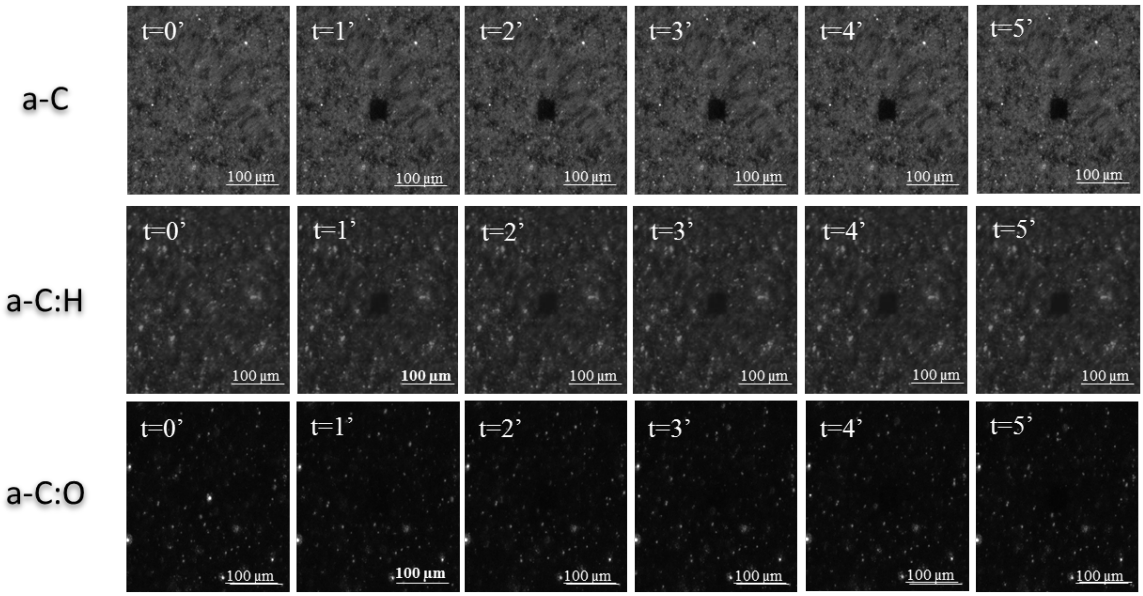


Figure 5.2. FRAP images obtained after incubation of PC/PS liposomes onto a-C, a-C:H and a-C:O surfaces. Each image is 250 µm x 250 µm and the photobleached area is 25 µm x 25 µm. After photobleaching at t=0', images are taken at one minute time intervals. (scale bar corresponds to 100 µm).

In situ quartz crystal microbalance with dissipation (QCM-D) measurements provided further insight on the mode of liposome adsorption. Figure 5.3 shows changes in frequency and dissipation at a-C (top) and a-C:O (bottom) coated sensors; at time zero the crystal is stabilized in PBS, while the PC/PS liposome suspension is injected as indicated by the arrows. In the case of a-C there is a sharp decrease in frequency (Δf = 52 Hz) with a concomitant increase in dissipation ($\Delta D = 9.5\times10^{-6}$). Liposome adsorption at a-C leads to formation of a viscoelastic film with relatively large dissipation. However, in the case of oxidised carbon no change in frequency or dissipation is observed, indicating that no adsorption takes place at oxidised surfaces. Under the experimental condition used on this work, it was not possible to observe vesicle rupture over the course of approximately 50 min, which would have been evidenced by a collapse in the dissipation after the initial adsorption.[33-34] Therefore, results are consistent with adsorption via formation of supported vesicular layers at these graphitic surfaces, while surface oxidation prevents liposome adsorption entirely.[33]

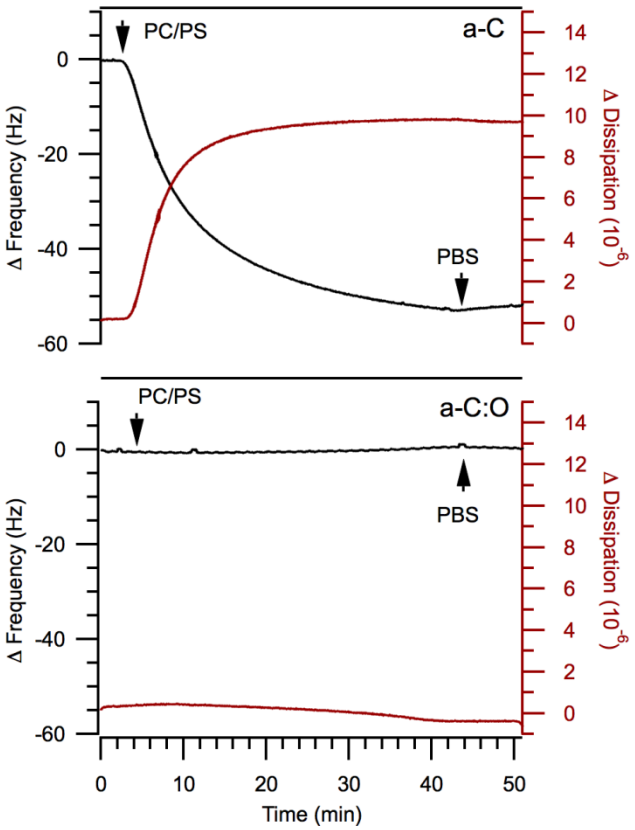


Figure 5.3. QCM-D monitoring of PC/PS liposome adsorption at a-C (top) and a-C:O (bottom) surfaces. After PBS injection, the PC/PS solution (0.40 mg/mL) was injected at 10 min and the interaction of PC/PS liposomes with a-C and a-C:O surfaces was monitored during 30 min; the surface was further rinsed with PBS. All frequencies (left) and dissipations (right) are presented in the third overtone and measured in the range of 0 to -60 Hz and 0 - 12 x 10^{-6}, respectively.

2.2. Influence of Buffer pH

In order to access the influence of pH in the mode of liposome adsorption at carbon surfaces, IRRAS *ex situ* was performed in a-C and a-C:O after 1 h incubation of 1 mM PC/PS suspended in PBS at different pHs. Figure 5.4 shows IRRAS spectra obtained for a-C (left) and a-C:O (right) surfaces in the C—H stretching region after immersion in PC/PS suspensions over the 4.5 - 9.5 pH range. As previously observed in Figure 5.1, peaks at 2924 cm^{-1} and 2853 cm^{-1} are assigned to -CH_2 antisymmetric and symmetric stretching modes, while the shoulder at 2965 cm^{-1} is assigned to -CH_3 stretching modes. IRRAS spectra of a-C surfaces display strong absorbances associated to the phospholipid alkyl tails at all pH values examined, however in the case of a-C:O it was not possible to detect any peaks, independently of pH.

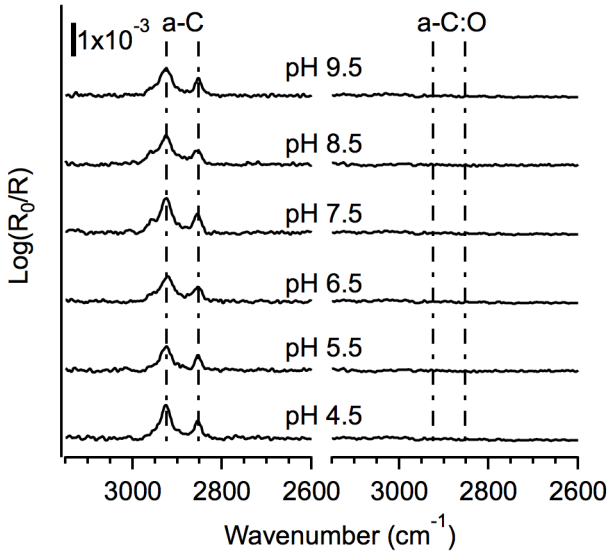
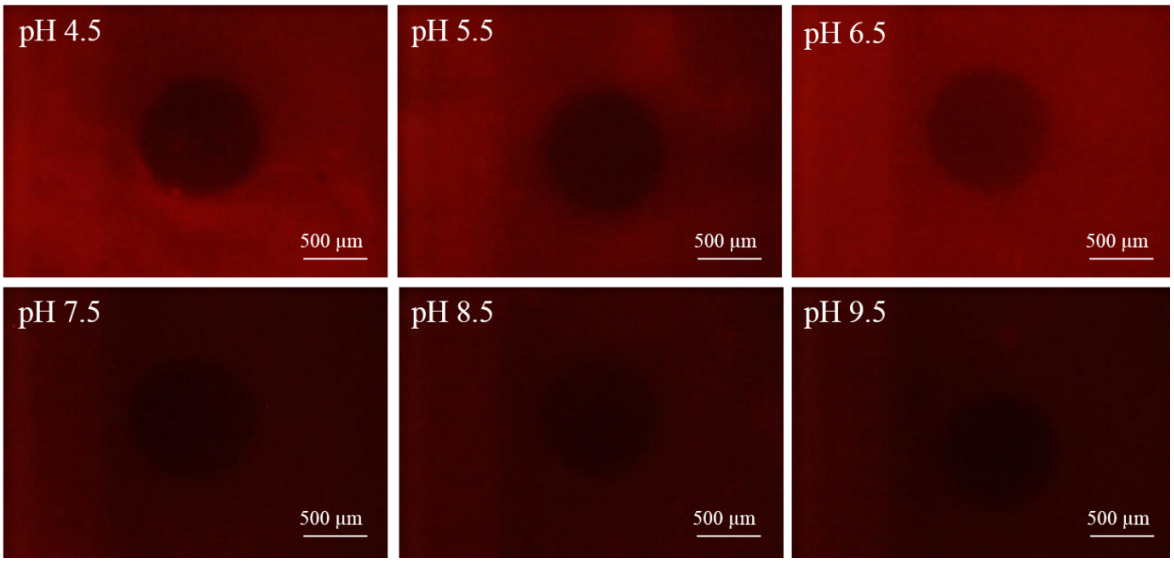


Figure 5.4. IRRAS spectra in the 3000-2600 cm^{-1} region of a-C and a-C:O surfaces after 1 h incubation of PC/PS liposomes suspended in PBS buffer at different pH. The position of CH_2 stretching bands is indicated with dot lines.

Fluorescence measurements were carried out at carbon surfaces after incubation on PC/PS liposome suspensions prepared with 0.02% mol Texas Red DHPE at different pHs. Figure 5.5 shows a-C surfaces with a circular area of oxidised carbon (a-C:O) (see experimental section) after 1 h incubation of PC/PS liposome suspensions, with Texas Red DHPE, in PBS at different pHs. For all pH values, the fluorescence signal emitted by the phospholipid labelled in the head group with the fluorescence dye (Texas Red DHPE) is more intense over a-C than over a-C:O regions, meaning higher liposome adsorption at the graphitic surface, confirming previous results.



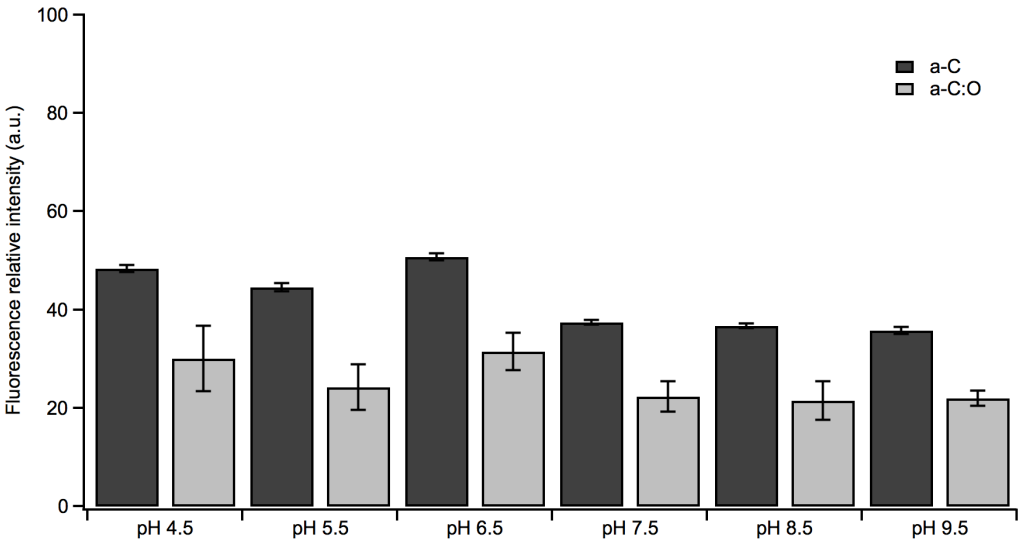


Figure 5.5. (Top) Fluorescence measurements of a-C/a-C:O pattern for different pH. a-C:O is the darker area in the picture while a-C is the outer of that area. **(Bottom)** Table of relative fluorescence intensities emitted from the adsorption of PC/PS liposomes at a-C and a-C:O surfaces.

The relative fluorescence intensity emitted from liposome adsorption at a-C and a-C:O surfaces was measured and displayed in Figure 5.5 (bottom). In general, the average fluorescence intensity ratio $I_{a\text{-}C:O/(a\text{-}C:O + a\text{-}C)}$ was found to be 36 ± 6 for all pH on this study, confirming previous results with IRRAS (Figure 5.4). Thus, results on IRRAS and fluorescence microscopy show that pH has little influence on liposome adsorption at carbon films, displaying a constant adsorption of PC/PS liposomes at a-C surfaces and no to little adsorption observed in the case of a-C:O surfaces for all pH studied.

2.3. Influence of Buffer Ionic Composition

Previous work on liposome interactions at inorganic oxides and model monolayers on Au[35] has shown that substrate wetting properties and surface charge can affect the outcome of liposome/solid interactions. For hydrophilic and/or charged surfaces specifically, the presence of di-cations can promote liposome adsorption and rupture.[35-37] To assess the effect of di-cations in the case of graphitic and oxidised carbon surfaces exposed to natural PC/PS, 10 mM $CaCl_2$ was added to the phosphate buffer while keeping the ionic strength constant at 164 mM.

Figure 5.6a shows IRRAS spectra in the C—H stretching region for a-C and a-C:O surfaces after 1 h incubation of PC/PS liposomes in PBS, and in PBS with 10 mM $CaCl_2$ buffers. Spectra of a-C surfaces exhibits the characteristic peaks of adsorbed lipid tails independently of whether the di-cation is present in solution. a-C:O surfaces, on the other hand, show a dramatic increase in C—H absorbances upon introduction of Ca^{2+} in solution, indicating that di-cations clearly have a switching effect on PC/PS adsorption at the oxidised surface. A comparison of -CH_2 net absorbances at a-C suggests that Ca^{2+} binding might also enhance lipid adsorption at this more graphitic surface (~20% increase in intensity), however it is not possible to exclude that chain reorientation might be responsible for the observed enhancement.

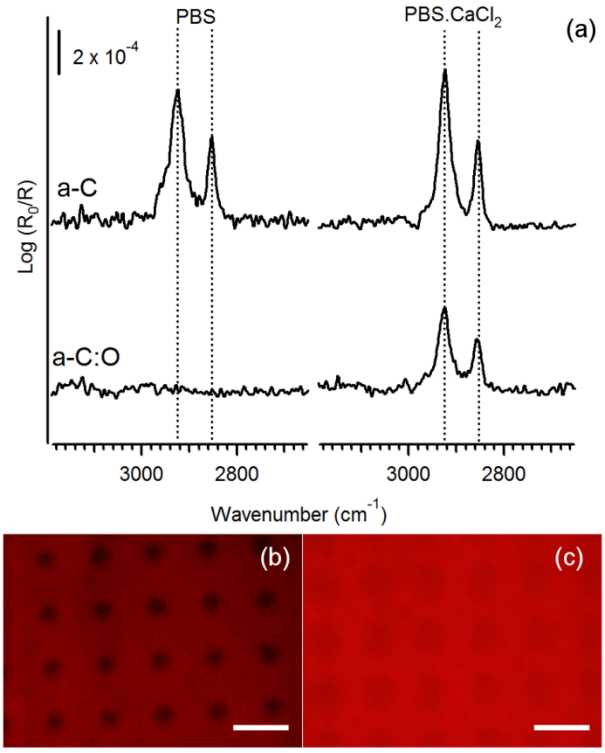


Figure 5.6. (a) IRRAS spectra in the region 3200-2650 cm^{-1} of a-C and a-C:O surfaces after 1 h incubation of liposomes suspended in PBS and PBS with 10 mM $CaCl_2$ at pH 7.4. The position of -CH_2 stretching bands is indicated with dotted lines. Fluorescence images of a-C:O patterned over the a-C surface after incubation in suspensions of fluorescently labelled PC/PS liposomes (1 mM PC/PS, 1 h) in PBS **(b)** and in PBS with 10 mM $CaCl_2$ **(c)** at pH 7.4; scale bar = 500 µm.

Methylene and methyl stretching peak intensities in IRRAS spectra are strongly dependent on the orientation of adsorbed alkyl chains at the surface in addition to surface coverage.[30, 38] To confirm that changes in peak intensity are not exclusively the result of chain reorientation, complementary fluorescence imaging experiments were carried out using PC/PS liposomes labeled with Texas Red DHPE. Carbon surfaces were oxidised via UV/ozone through a shadow mask, thus creating a-C surfaces with oxidised circular regions in a regular array (see experimental section); these samples were then exposed to the PC/PS suspensions for 1 h.

Figures 5.6b and 5.6c show fluorescence images obtained in the absence and presence, respectively, of Ca^{2+} in the PBS solution. In the absence of Ca^{2+}, the emission intensity was found to be approximately 40% higher in the a-C (non-oxidised) compared to a-C:O regions, and the chemical contrast created via oxidation translated into spatial control over lipid surface density. The intensity contrast was found to be negligible in the presence of Ca^{2+}, which effectively overwhelms the substrate chemistry leading to increased adsorption over the entire surface. These results confirmed that differences in peak intensities in IRRAS reflect indeed differences in amount of liposme adsorption at the interface. The introduction of Ca^{2+} enhances adsorption at both a-C and a-C:O surfaces effectively nullifying the chemical contrast created via patterned oxidation.

2.4. Study of liposome rupture

To investigate whether the carbon surface chemistry influenced liposome adsorbate structures upon vesicle rupture, we carried out atomic force microscopy (AFM) characterisation studies at surfaces decorated with ruptured vesicles. Graphitic a-C and oxidised a-C:O surfaces were exposed to a small volume of liposome suspension in PBS solution (20 μL), then rinsed and used for *ex situ* AFM imaging. Figure 5.7a shows the topography of a-C samples after liposome adsorption (left); images display adsorbates in the form of smooth “islands” that are consistent with the presence of supported lipid layers obtained after rupture.[37, 39] The step edge of these layers yielded an average height of 1.13 ± 0.04 nm, which strongly suggests that the preferred mode of adsorption involves the formation of a lipid monolayer.[40] Similar results were obtained in the case of samples incubated under identical conditions but in the presence of Ca^{2+}, as shown in

Figure 5.7b (left). The thickness of the supported layer was found to be 1.1 ± 0.1 nm which again indicates formation of monolayers after rupture.

Equivalent imaging experiments on oxidised surfaces are shown in Figures 5.7a and 5.7b (right). In the absence of Ca^{2+} (Figure 5.7a - right), the liposome incubation process at a-C:O surface did not yield any adsorbates, in agreement with IRRAS and fluorescence images. The introduction of the di-cation resulted in the formation of a defective supported layer (Figure 7b - right) whose average height was found to be 3.5 ± 0.2 nm, a value that matches the Luzzati thickness of a PC bilayer.[40] These results indicate that the introduction of a di-cation can be used to promote liposome adsorption at oxidised carbon surfaces, however the resulting supported lipids consist of bilayers and differ from the monolayer adsorbates formed via vesicle rupture at graphitic surfaces (a-C).

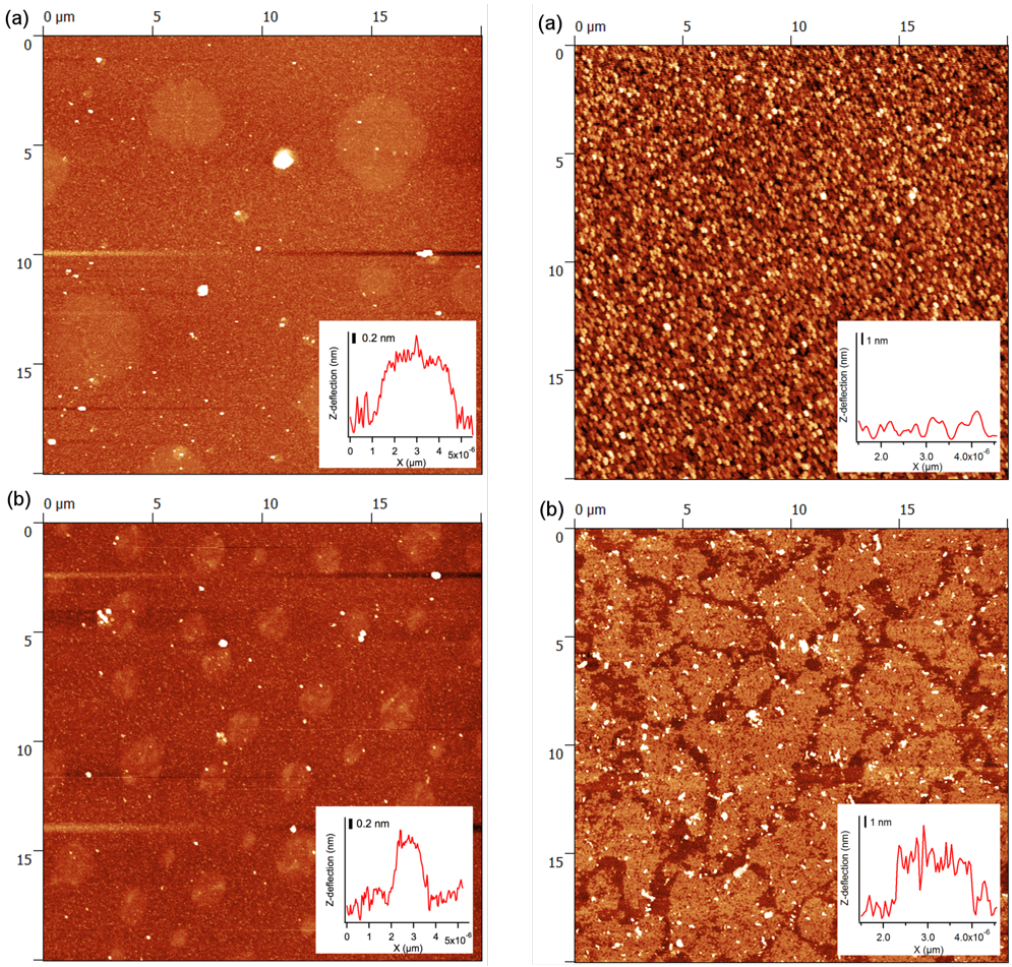


Figure 5.7. AFM images of a-C (left) and a-C:O (right) surfaces after incubation in 20 µL of 1 mM PC/PS suspensions in **(a)** PBS and **(b)** PBS with 10 mM $CaCl_2$ at pH 7.4. Height profiles (inset) show step edges of average 1.1 nm thickness in either absence or presence of Ca^{2+} (z-scale = 20 nm).

3. Discussion

The results present on this chapter show that there are marked differences in the amount and structure of lipid adsorbates on carbon surfaces with different surface chemistry. A combination of spectroscopic, nanogravimetric and fluorescence studies indicates that adsorption at graphitic surfaces occurs predominantly in the form of supported intact vesicles; however, under conditions that promote rupture, adsorbates appear to consist of supported lipid monolayers, based on the experimentally determined height profiles (Figure 7). All *in situ* and *ex situ* experiments showed that carbon oxidation results in liposome rejection when compared with graphitic surfaces, such as a-C.

The introduction of a di-cation (Ca^{2+}) in the buffer was found to promote liposome adsorption, with the most remarkable changes observed in the case of oxidised surfaces. Interestingly, after vesicle rupture, the adsorbate thickness is much larger than that observed on graphitic surfaces and consistent with the presence of supported lipid bilayer (Figure 5.7b). Therefore, our results indicate that the specific carbon surface termination/modification can dictate both density and type of lipid adsorption either in the presence or absence of the di-cation, a result that has important implications for applications of carbon coatings or nanocarbons as biomaterials.

In the following paragraphs, the effect of (i) carbon surface chemistry and wettability and (ii) buffer ionic valence, on the outcome of liposome/carbon interactions is discussed.

3.1. Surface Chemistry Effects

Several studies have reported the interaction of lipid aggregates with model solid surfaces, such as SiO_2,[33] TiO_2,[35] and mica[37] and showed that the wettability of solid surfaces is a critical factor that defines the mechanism of liposome adsorption at the solid/liquid interface.[28, 35, 41-43] Literature agrees on the effect of surface hydrophilicity on the adsorbed lipidic structure at the interface: at hydrophobic surfaces, liposomes adsorb preferentially as supported vesicle layers (SVL) or supported lipid bilayer (SLB),

whereas at hydrophilic surfaces a supported lipid monolayer (SLM) can be observed. This behaviour was reviewed by Tero *et al*.[35] which attributed the liposomes structure at hydrophilic surfaces to the higher density of –OH groups, which correlate to the increase of hydration repulsion forces between the stable layer of water molecules attached to the phospholipid head groups and the water bound to the solid substrate.

The effect of surface wettability on the structure of liposome adsorption at the interface has been recently extended to carbon coatings, more specifically graphene bio- and chemical sensors.[44-48] Similarly to the aforementioned macroscopic surfaces, the adsorbed structure of lipids at graphene surfaces was shown to be regulated by surface wettability; hydrophobic graphene preferentially adsorb intact vesicles (SVL) or SLM and hydrophilic substrates tend to form a SLB at the interface.[45-46] Nevertheless, research on the interaction of liposomes with a-C macroscopic surfaces is comparatively sparse; the role of carbon surface chemistry and wettability on the structure of liposome has been poorly reported, and a controllable method of liposome adsorption at a-C surface, with defined surface physico-chemical properties, has not been presented to date.[49-51]

In this work, a-C surfaces, which displays a WCA of 35.25 ± 2.86°, were incubated in PC/PS liposomes and *in situ* QCM-D and FRAP experiments revealed the presence of SVL at the interface. Interestingly, after incubation in PC/PS suspension in PBS, oxidised carbon (a-C:O), an extremely hydrophilic surface with a WCA <5°, no liposomes adsorption at the interface was observed. Complete lack of liposome adsorption at macroscopic surfaces is rare or perhaps underreported, suggesting that in this work the control over surface wettability is not a sufficient condition to promote liposome fusion and adsorption at the interface.[31, 35]

In addition to a substantial decrease in wettability, carbon surface oxidation results in a significant change in the density of ionisable groups at the surface, which also plays a critical role on liposome/surface interactions and adsorbate structures. Results presented in Chapter III, on the surface ζ-potential of amorphous carbon surfaces, showed that at neutral pH, a-C and a-C:O surfaces display a SZP of – 51.3 ± 2.4 mV and – 61.5 ± 3.6 mV, respectively.[52] The additional negative electrostatic charge arising from acid groups in a-C:O surfaces indicates that a contribution from surface charges absent in the case of a-C, might contribute to prevent liposome rupture.[53] The outcome of this

additional electrostatic contribution is clearly repulsive under our experimental conditions.

The role of repulsive electrostatic interactions has been invoked to explain reduced/lack of liposome adsorption in various types of carbon materials, such as nanodiamond (ND), carbon nanotubes and graphene oxide.[53-55] Wang *et al.*[54] reported on the interaction of PC-containing liposomes with ND and explained the lack of liposome adsorption to electrostatic repulsions between ND and liposome headgroup. Recently, Frost *et al.*[53] observed complete repulsion between PC/PS liposome suspensions and graphene oxide surfaces, with an oxygen content of 20 % and a surface ζ-potential of −56 ± 1.1 mV at non-physiological pH (pH = 4). However, to the best of the author's knowledge, the work herein presented is the first report on lipid adsorption/repulsion at amorphous carbon macroscopic surfaces, with controllable surface wettability and charge density.

As previously discussed, *ex situ* and *in situ* measurements used on this study strongly indicate that not only surface chemistry and wettability play a role on liposome adsorption but also the buffer ionic valence should be taken into consideration. Literature suggests that the introduction of a di-cation is a pre-requisite for bilayer adsorption at solid surfaces.[31, 56-57] Next section includes the influence of Ca^{2+} on zwitterionic/anionic liposomes adsorption at amorphous carbon surfaces.

3.2. Buffer Composition Effects

Previous reports in literature[31, 36, 56-65] have been focused on the effects of buffer composition, *i.e.* charge, ionic strength and ion nature, on the interaction between liposome and solid surface. Cha *et al*.[31] described a relation between liposome conformation at solid surfaces and the nature of the ions present in the buffer. For phosphate buffers, molecular anions such as HPO_4^{2-} and $H_2PO_4^-$ stay at the solid/liquid interface and decrease the interaction between liposomes and solid surfaces.[36] For a zwitterionic liposome, *e.g.* PC, the positively charged choline group present on the phospholipid head group, interacts with a negatively charged solid surface, *e.g.* amorphous carbon, through ion-dipole interactions.[36] When this attractive interaction is

strong, it causes an unbalance in the hydration repulsive forces and induces vesicle adsorption at the solid surface; for sufficiently high attraction between charged liposome and surface, the vesicle undergoes rupture and form a supported lipid (bi)layer.[31] As so, the counterions present in the medium, *e.g.* Na^+ and Ca^{2+}, are squeezed between liposome and surface when these interfaces come together.[66] This is the well-known entropic repulsion which is strongly dependent on the nature and charge density of the counterion; higher the charge density, higher the entropic repulsion and liposome adsorption is impeded.[31, 36]

In this work, the effect of Ca^{2+} in PC/PS liposome adsorption is observed for both carbon surfaces. The graphitic surface displays a slight enhancement of PC/PS liposome adsorption when Ca^{2+} is added to the buffer, however it is on the oxidised surface that the introduction of the dication has a significant impact on liposome adsorption. Prior to Ca^{2+} inclusion in the buffer no liposome adsorption is observed at a-C:O surfaces, whereas dication addiction led to SVL formation at the interface.

Zwitterionic/anionic liposomes are known to interact with solid surfaces either with the positively charged choline group or the negatively charged phosphate group present on the phospholipid headgroups. Due to the negative charge of amorphous carbon surfaces and PC/PS liposomes at neutral pH, it is believed that the presence of Ca^{2+} ions at the solid/liquid interface results in a bound between negatively charged a-C and the negatively charged phosphate groups present on the phospholipid head group.

Studies of artificial cell membranes interacting with solid surfaces, have indeed assigned the formation of SLB at the solid surface, to the introduction of a di-cation in the aqueous medium.[56-57] More specifically, the interaction of zwitterionic/anionic liposomes with negatively charged surfaces is known to be promoted by the introduction of Ca^{2+} ions added to the liposome suspension.[36, 56, 64] The enhanced interaction between liposome and charged surface is known to be a result of the ability of Ca^{2+} to act as a “bridge” between the negatively charged phosphate groups at liposomes head groups and the negatively charged solid surface. [36, 64-65]

4. Conclusions

In this work, the interaction of PC/PS liposomes with amorphous carbon surfaces was studied with regards to buffer composition and carbon surface chemistry and wettability. The amount and mode of liposome adsorption at a-C and a-C:O surfaces were investigated by using a combination of spectroscopic, nanogravimetric and microscopic techniques. IRRAS experiments on carbon surfaces after exposure to PC/PS liposome suspensions in PBS showed liposome adsorption exclusive at a-C surfaces for all pH investigated; QCM-D and FRAP measurements revealed that PC/PS liposomes adsorb at a-C surfaces as supported intact vesicles. The lack of liposome adsorption at the oxidised surface is attributed to the significantly higher hydrophilicity and density of charged groups, which results in an increase of electrostatic repulsion between liposome and a-C:O surfaces.

The introduction of the dication Ca^{2+} in the buffer solution led to PC/PS liposome adsorption at a-C:O and a slightly increased adsorption at a-C surfaces. Fluorescence results were in good agreement with IRRAS measurements, indicating a lower a-C:O/a-C fluoresence intensity ratio when the dication was added to the phosphate buffer. Finally, AFM measurements gave insights about the conformational adsorption of liposomes at amorphous carbon surface. Under conditions that promote liposome rupture, it was found that for bare a-C, PC/PS liposomes adsorb as a monolayer while for a-C:O the adsorption of a bilayer is only observed when the dication is added.

The research herein presented represents a novel method on the interaction of liposomes with amorphous carbon macroscopic surfaces, with controllable carbon surface chemistry and wettability. These results have implications on applications of amorphous carbon films in the biomedical field, where the mode and amount of model lipid aggregate adsorption at the interface is key in defining the long-term bioresponse towards carbon-based biodevices.

5. Experimental

5.1. Materials and Compounds

Phosphatidylcholine from egg yolk 99.9% (PC) and 3-sn-Phosphatidyl-L-serine from bovine brain 95% (PS) lyophilized powders, phosphate buffer saline (PBS 0.01 M, 0.0027 M KCl and 0.137 M NaCl pH 7.4) tablets, sulfuric acid (95-97%), hydrogen peroxide (30%), methanol (semiconductor grade), chloroform (HPLC grade) and calcium chloride were purchased from Sigma Aldrich. Texas Red 1,2-Dihexadecanoyl-*sn*-Glycero-3-Phosphoethanolamine, Triethylammonium Salt (Texas Red DHPE, ex/em ~595/615 nm) was purchased from Life Technologies as a lyophilized powder. All water was obtained from a Millipore purification system.

5.2. Liposome Preparation

Liposomes were prepared according to previously described protocols in Chapter IV. Briefly, stock solutions of 10 mg mL^{-1} of PC and PS in chloroform were prepared and stored in the freezer; 2.6 µmol in 80:20 PC/PS molar ratio were dispensed in a glass vial and dried under Ar and vacuum until dry. 2.6 mL of buffer were added to the mixture and vortexed until a milky suspension was obtained, which was further sonicated for 30 min until the liquid appeared clear, thus yielding a 1.0 mM (0.79 mg/mL) suspension in buffer. Liposomes were extruded through 0.45 µm and 0.10 µm nylon membranes, unless otherwise noted; the filtrate was stored at 4°C prior to use. For all fluorescence measurements, 0.02% by mol of Texas Red DHPE was added to the 1.0 mM (0.79 mg/mL) liposome suspension. Unless otherwise noted, 1.0 mM suspensions were used for adsorption experiments.

5.3. Substrate Preparation

A DC-magnetron sputtering chamber (Torr International, Inc.) was used to deposit amorphous carbon (a-C) films at a base pressure ≤ 2×10^{-6} mbar and a deposition Ar pressure of 7×10^{-3} mbar, as previously described in chapter III.[67] For IRRAS measuements, Si substrates were coated with an optically thick 449 ± 29 nm (C.I. 95%) Ti layer via DC magnetron sputtering prior to a-C deposition. Oxidized carbon films (a-C:O)

were prepared via exposure of a-C to a UV grid-lamp (UVP, 5.9 mW cm^{-2} of 254 nm emission at sample distance) in air, as previously described.[68-69] Patterned oxidation was obtained using a stainless steel shadow mask (courtesy of Prof. Duesberg) with 80 µm diameter holes in a square array. The mask was placed in contact with a-C surfaces resulting in a pattern of circular regions of a-C:O on a-C.

5.4. Adsorption Experiments

Substrates were rinsed with methanol, dried under Ar and immediately afterwards immersed in 1 mM PC/PS suspensions for 1 h, following published protocols.[35, 70] Substrates were rinsed and dried in Ar prior to characterization. For atomic force microscopy (AFM) measurements, 20 µL of the PC/PS suspensions were dispensed over surfaces, left for 1 h in a humid chamber, then rinsed and dried prior to imaging. For *in-situ* measurements, PC/PS solution (0.40 mg/mL) was injected and the interaction of PC/PS liposomes with a-C and a-C:O surfaces was monitored during 30 min; the surface was further rinsed with PBS.

5.5. Characterisation Methods

IRRAS spectra were collected on a Fourier Transform Infrared (FTIR) spectrometer (Tensor 27, Bruker) equipped with a Mercury Cadmium Telluride (MCT) detector, a Zinc Selenide polarizer and a specular reflectance accessory (VeeMax II). 256 spectra were collected at 4 cm^{-1} resolution at 80° incidence p-polarized light using a bare substrate as background unless otherwise noted; spectra were baseline corrected using FTIR software (WinFIRST). Fluorescence images were obtained with an Olympus BX51 upright microscope, using a DP73 camera and a CoolLed light source; the filter set consisted of excitation bandpass at 530-550 nm, dichroic mirror at 570 nm and emission filter at 573-648 nm. Fluorescence recovery after photobleaching (FRAP) measurements were performed on a confocal microscope (Leica SP8) equipped with a krypton/argon laser (exc. 552 nm). Samples were incubated in suspensions of fluorescently labelled liposomes, then rinsed with water and imaged while wet before, during and after photobleaching, following published protocols.[31] A 25×25 μm^2 area was photobleached for 10 s, three times, with the high-powered focused laser beam; then, 250×250 μm^2

images were obtained every minute at low-power excitation to monitor recovery. Only brightness and contrast were adjusted in all images presented. Atomic force microscopy (AFM, Asylum Research) was performed in tapping mode (1 Hz, 512 scan lines) using Au-coated silicon cantilevers (NT-MDT, 1.45-15.1 N m^{-1} spring constant). Quartz crystal microbalance with dissipation (QCM-D, Q-Sense E4) was carried using 5 MHz Au sensors coated with 10 nm a-C films; studies on oxidized surfaces used a-C coated sensors exposed for 5 min to the UV lamp. All measurements were carried out at 150 µL min^{-1} with the sensor module thermostated at 20 °C.[33]

6. References

1.Buddy D. Ratner; Allan S. Hoffman; Frederick J. Schoen; Jack E. Lemons, 2 ed.; Elsevier Academic Press: London, 2004.
2.Gott, V. L.; Alejo, D. E.; Cameron, D. E., *Annals of Thoracic Surgery* **2003,** *76* (6), S2230.
3.Grill, A., *Diamond and Related Materials* **2003,** *12* (2), 166.
4.Dearnaley, G.; Arps, J. H., *Surface and Coatings Technology* **2005,** *200* (7), 2518.
5.Roy, R. K.; Lee, K. R., *Journal of biomedical materials research. Part B, Applied biomaterials* **2007,** *83* (1), 72.
6.Sydow-Plum, G.; Tabrizian, M., *Mater. Sci. Technol.* **2008,** *24* (9), 1127.
7.Liang, F.; Chen, B., *Curr Med Chem* **2010,** *17* (1), 10.
8.Krishna, V.; Stevens, N.; Koopman, B.; Moudgil, B., *Nat Nano* **2010,** *5* (5), 330.
9.Chen, M.; Pierstorff, E. D.; Lam, R.; Li, S.-Y.; Huang, H.; Osawa, E.; Ho, D., *ACS Nano* **2009,** *3* (7), 2016.
10.Faklaris, O.; Joshi, V.; Irinopoulou, T.; Tauc, P.; Sennour, M.; Girard, H.; Gesset, C.; Arnault, J.-C.; Thorel, A.; Boudou, J.-P.; Curmi, P. A.; Treussart, F., *ACS Nano* **2009,** *3* (12), 3955.
11.Fang, Y.; Gu, D.; Zou, Y.; Wu, Z.; Li, F.; Che, R.; Deng, Y.; Tu, B.; Zhao, D., *Angewandte Chemie International Edition* **2010,** *49* (43), 7987.
12.Duffy, P.; Magno, L. M.; Yadav, R. B.; Roberts, S. K.; Ward, A. D.; Botchway, S. W.; Colavita, P. E.; Quinn, S. J., *Journal of Materials Chemistry* **2012,** *22* (2), 432.
13.Robertson, J., *Materials Science and Engineering R* **2002,** *37* (4–6), 129.
14.Gutensohn, K.; Beythien, C.; Bau, J.; Fenner, T.; Grewe, P.; Koester, R.; Padmanaban, K.; Kuehnl, P., *Thrombosis Research* **2000,** *99* (6), 577.
15.Hauert, R., *Diamond and Related Materials* **2003,** *12* (3–7), 583.
16.Ma, W. J.; Ruys, A. J.; Mason, R. S.; Martin, P. J.; Bendavid, A.; Liu, Z.; Ionescu, M.; Zreiqat, H., *Biomaterials* **2007,** *28* (9), 1620.
17.Ohgoe, Y.; Hirakuri, K. K.; Saitoh, H.; Nakahigashi, T.; Ohtake, N.; Hirata, A.; Kanda, K.; Hiratsuka, M.; Fukui, Y., *Surface and Coatings Technology* **2012,** *207*, 350.
18.Lackner, M. J.; Waldhauser, W., *BHM Berg- und Hüttenmännische Monatshefte* **2010,** *155* (11), 528.
19.Love, C. A.; Cook, R. B.; Harvey, T. J.; Dearnley, P. A.; Wood, R. J. K., *Tribology International* **2013,** *63*, 141.
20.Chai, F.; Mathis, N.; Blanchemain, N.; Meunier, C.; Hildebrand, H. F., *Acta biomaterialia* **2008,** *4* (5), 1369.
21.Bociaga, D.; Kaminska, M.; Sobczyk-Guzenda, A.; Jastrzebski, K.; Swiatek, L.; Olejnik, A., *Diamond and Related Materials* **2016,** *67*, 41.

22.Bociąga, D.; Jakubowski, W.; Komorowski, P.; Sobczyk-Guzenda, A.; Jędrzejczak, A.; Batory, D.; Olejnik, A., *Materials Science and Engineering: C* **2016,** *63*, 462.
23.Kasemo, B., *Current Opinion in Solid State and Materials Science* **1998,** *3* (5), 451.
24.Schwartz, Z.; Boyan, B. D., *Journal of cellular biochemistry* **1994,** *56* (3), 340.
25.Thevenot, P.; Hu, W.; Tang, L., *Current Topics in Medicinal Chemistry* **2008,** *8* (4), 270.
26.Zen, F.; Angione, M. D.; Behan, J. A.; Cullen, R. J.; Duff, T.; Vasconcelos, J. M.; Scanlan, E. M.; Colavita, P. E., *Scientific Reports* **2016,** *6*, 24840.
27.Jiang, C.; Gamarnik, A.; Tripp, C. P., *The Journal of Physical Chemistry B* **2005,** *109* (10), 4539.
28.Er, Y.; Prestidge, C. A.; Fornasiero, D., *Colloids and Surfaces B: Biointerfaces* **2004,** *36* (3–4), 147.
29.Hernandez, M. R.; Towns, E. N.; Ng, T. C.; Walsh, B. C.; Osibanjo, R.; Parikh, A. N.; Land, D. P., *Appl Opt* **2012,** *51* (15), 2842.
30.Mashaghi, A.; Mashaghi, S.; Reviakine, I.; Heeren, R. M.; Sandoghdar, V.; Bonn, M., *Chem Soc Rev* **2014,** *43* (3), 887.
31.Cha, T.; Guo, A.; Zhu, X. Y., *Biophysical journal* **2006,** *90* (4), 1270.
32.Silva-Lopez, E. I.; Edens, L. E.; Barden, A. O.; Keller, D. J.; Brozik, J. A., *Chem Phys Lipids* **2014,** *183*, 91.
33.Cho, N.-J.; Frank, C. W.; Kasemo, B.; Hook, F., *Nat. Protocols* **2010,** *5* (6), 1096.
34.Reimhult, E.; Kasemo, B.; Hook, F., *International journal of molecular sciences* **2009,** *10* (4), 1683.
35.Tero, R., *Materials* **2012,** *5* (12), 2658.
36.Seantier, B.; Kasemo, B., *Langmuir* **2009,** *25* (10), 5767.
37.Richter, R. P.; Brisson, A. R., *Biophysical journal* **2005,** *88* (5), 3422.
38.Tolstoy, V. P.; Chernyshova, I.; Skryshevsky, V. A., *Wiley* **2003**.
39.Richter, R.; Mukhopadhyay, A.; Brisson, A., *Biophysical journal* **2003,** *85* (5), 3035.
40.Nagle, J. F.; Tristram-Nagle, S., *Current opinion in structural biology* **2000,** *10* (4), 474.
41.Alexandrova, L.; Karakashev, S. I.; Grigorov, L.; Phan, C. M.; Smoukov, S. K., *Advances in Colloid and Interface Science* **2015,** *220*, 1.
42.Jurak, M.; Chibowski, E., *Langmuir* **2007,** *23* (20), 10156.
43.Isono, T.; Tanaka, H.; Ogino, T., *e-Journal of Surface Science and Nanotechnology* **2007,** *5*, 99.
44.Tabaei, S. R.; Ng, W. B.; Cho, S.-J.; Cho, N.-J., *ACS Applied Materials & Interfaces* **2016,** *8* (18), 11875.
45.Ang, P. K.; Jaiswal, M.; Lim, C. H.; Wang, Y.; Sankaran, J.; Li, A.; Lim, C. T.; Wohland, T.; Barbaros, O.; Loh, K. P., *ACS Nano* **2010,** *4* (12), 7387.
46.Li, W.; Chung, J. K.; Lee, Y. K.; Groves, J. T., *Nano Letters* **2016,** *16* (8), 5022.
47.Tsuzuki, K.; Okamoto, Y.; Iwasa, S.; Ishikawa, R.; Sandhu, A.; Tero, R., *Journal of Physics: Conference Series* **2012,** *352*, 012016.
48.Willems, N.; Urtizberea, A.; Verre, A. F.; Iliut, M.; Lelimousin, M.; Hirtz, M.; Vijayaraghavan, A.; Sansom, M. S. P., *ACS Nano* **2017,** *11* (2), 1613.
49.Marco Diociaiuti; Agnese Molinari; Irene Ruspantini; Maria Cristina Gaudiano; Rodolfo Ippoliti; Eugenio Lendaro; Federico Bordi; Pietro Chistolini; Giuseppe Arancia, *Biochimica et Biophysica Acta* **2002,** *1559*, 21.
50.Cui, F. Z.; Qing, X. L.; Li, D. J.; Zhao, J., *Surface and Coatings Technology* **2005,** *200* (1â€“4), 1009.
51.Yang, W.; Cui, F. Z.; Qing, X., *Current Applied Physics* **2006,** *6* (5), 827.
52.Vasconcelos, J. M.; Zen, F.; Stamatin, S. N.; Behan, J. A.; Colavita, P. E., *Surface and Interface Analysis* **2017**, n/a.
53.Frost, R.; Jönsson, G. E.; Chakarov, D.; Svedhem, S.; Kasemo, B., *Nano Letters* **2012,** *12* (7), 3356.
54.Wang, F.; Liu, J., *Nanoscale* **2013,** *5* (24), 12375.
55.Liu, J., *Langmuir* **2016,** *32* (18), 4393.

56.Rossetti, F. F.; Bally, M.; Michel, R.; Textor, M.; Reviakine, I., *Langmuir* **2005,** *21* (14), 6443.
57.Reviakine, I.; Brisson, A., *Langmuir* **2000,** *16* (4), 1806.
58.Böckmann, R. A.; Grubmüller, H., *Angewandte Chemie International Edition* **2004,** *43* (8), 1021.
59.Sovago, M.; Wurpel, G. W. H.; Smits, M.; Müller, M.; Bonn, M., *Journal of the American Chemical Society* **2007,** *129* (36), 11079.
60.Puu, G.; Gustafson, I., *Biochimica et Biophysica Acta (BBA) - Biomembranes* **1997,** *1327* (2), 149.
61.Boettcher, J. M.; Davis-Harrison, R. L.; Clay, M. C.; Nieuwkoop, A. J.; Ohkubo, Y. Z.; Tajkhorshid, E.; Morrissey, J. H.; Rienstra, C. M., *Biochemistry* **2011,** *50* (12), 2264.
62.Hardy, G. J.; Nayak, R.; Zauscher, S., *Current opinion in colloid & interface science* **2013,** *18* (5), 448.
63.Fernanda F. Rossetti; Marcus Textor; Ilya Reviakine, *Langmuir* **2006,** *22*, 3467.
64.Richter, R.; Mukhopadhyay, A.; Brisson, A., **2003**.
65.Walker, G. M., *Magnesium research* **1999,** *12* (4), 303.
66.Nirasay, S.; Badia, A.; Leclair, G.; Claverie, J.; Marcotte, I., *Materials* **2012,** *5* (12), 2621.
67.Cullen, R. J.; Jayasundara, D. R.; Soldi, L.; Cheng, J. J.; Dufaure, G.; Colavita, P. E., *Chemistry of Materials* **2012,** *24* (6), 1031.
68.Cullen, R. J.; Jayasundara, D. R.; Baker, R. J.; O' Connell, G.; Donnelly, T.; Ballantine, K. E.; Lunney, J. G.; Colavita, P. E., *RSC Advances* **2016,** *6* (86), 82924.
69.Vasconcelos, J. M.; Zen, F.; Stamatin, S. N.; Behan, J. A.; Colavita, P. E., *Surface and Interface Analysis* **2017,** *49* (8), 781.
70.Okamoto, Y.; Tsuzuki, K.; Iwasa, S.; Ishikawa, R.; Sandhu, A.; Tero, R., *Journal of Physics: Conference Series* **2012,** *352*, 012017.

Chapter VI

In Vitro Bioresponse Towards Carbon Thin Films

Performance of carbon-based materials in biological media has been studied for decades and the desire of understanding the reasons for carbon's great biocompatibility is still present nowadays. Herein, the in vitro performance of carbon thin films is studied and surfaces that not only display great biocompatibility but also possess anti-thrombogenic and anti-fungal behaviours are shown.

1. Introduction

Carbon thin films have been used for the past decades as ubiquitous coatings in the biomedical field.[1] Diamond-like carbon (DLC),[2-11], graphene,[12] amorphous carbon (a-C),[13] pyrolytic carbon[14] and nanopourous carbon films,[15] have been used as coatings for implantable orthopaedic devices, bionic devices and dental, cardiovascular implants and chirurgical tools. The choice of carbon thin films for a wide range of biomedical applications, over other type of materials, is related to the versatility on tuning carbon surface properties.

The physico-chemical properties of carbon thin films are known to influence the *in vitro* interaction with cells and molecules, but also to modulate the *in vivo* bioresponse. Several studies have focused on understanding how to tune and modulate carbon/biological media interactions through the control of carbon surface free energy,[16-17] wettability,[5, 17] surface chemical groups[3, 16, 18], charge,[18] roughness[16]. However, the challenge of having a carbon thin film whose physico-chemical properties allow simultaneous control of cellular response and also possess anti-thrombogenic and anti-fungal behaviours has not been achieved to date.

Herein, a study on the *in vitro* interaction of a-C films with cells is reported. Firstly, surfaces were characterised in regard to their cytotoxic behaviour. Subsequently, the interaction of carbon thin films with endothelial and fibroblast cells is shown. In particular, cellular adhesion, proliferation, morphology and the establishment of focal adhesions (FAs) were quantified. Finally, the anti-thrombogenic and anti-fungal properties of a-C and a-C:O surfaces are presented. The results presented in this chapter provide new evidences of the direct effect of carbon surface oxidation on endothelial and fibroblastic cell response and give new insights on the potential of carbon thin films as anti-thrombogenic and anti-fungal coatings for carbon-based biodevices.

2. Results

The influence of carbon surface properties on the cytotoxicity, biocompatibility, thrombogenicity and fungal behaviour of carbon surfaces was studied. Using a combination of microscopic techniques, the interaction of carbon with *in vitro* model systems was analysed. Wettability of carbon surfaces used on this study was found to have a major role in carbon/ biological media interaction. Endothelial cells, fibroblasts, platelets and fungi adhesion at carbon surfaces was investigated in regard to surface chemistry. These results have a huge impact on the implementation of a-C films in carbon-based biodevices, since a great biocompatibility of a-C films is desired as much as non-thrombogenic and anti-fungal behaviours, all in the same surface.

2.1. Cytotoxicity

A fundamental characteristic of a reliable biomaterial to succeed in a biological environment is its non-toxicity. *In vitro* cytotoxicity tests are commonly used as a first examination to evaluate the biocompatibility of a material through the analysis of cell viability upon exposure to extracts that may contain cytotoxic compounds.[15] The cytotoxicity of a-C films used in this chapter was determined using the extract method described in ISO 10993-5 (see experimental section).

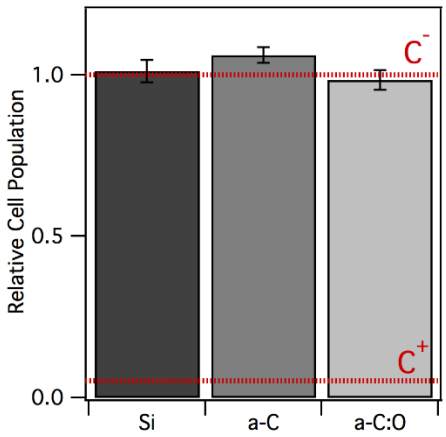


Figure 6.1. Results of the cytotoxicity test of Si substrate, a-C and a-C:O films deposited on Si; values given as mean ± stdev. Negative and positive controls are represented in red.

Figure 6.1 shows the cytotoxic profile of Si substrates and a-C and a-C:O films deposited on Si after 48 h incubation in DMEM; negative and positive controls are shown in red. The relative cell population for all three surfaces are comparable with the negative control, meaning that the two carbon films used in this chapter do not show any cytotoxic behaviour, neither does the Si substrate. These results were expected for this type of coatings, since carbon-related materials have a long history of usage in the biomaterials industry due to their absence of adverse effects on biological media.[6, 15, 18-19]

2.2. Endothelial Cells Culture

Carbon surface chemistry plays a major role on the interaction of carbon-based biodevices with biological fluids, in particular with blood.[20] Studies on the interaction of carbon coatings with endothelial cells have helped in elucidating the role of carbon surface chemistry on the *in vitro* biological response.[4] However there is still a great controversy regarding the effect of surface chemistry on carbon coatings performance *in vitro*.[20-21] The influence of surface wettability, SFE, charge and functional groups on the adhesion and proliferation of endothelial cells must be elucidated.

To address these challenges, a comprehensive investigation of *in vitro* bioactive effects on endothelial cells at both the multiple- (*i.e.* viability) and single-cell (*i.e.* spreading, morphology and focal adhesions) levels was carried out. In particular, cellular adhesion, proliferation and morphology were quantified, and an investigation on the establishment of focal adhesions (FAs) was performed. Figure 6.2 shows the relative population of endothelial cells adherent to a-C and a-C:O surfaces normalised against the control (C_{cell}) after 24 h of cell culture. The graphitic surface enables a satisfactory adhesion of endothelial cells, since the adhesion on a-C is comparable to the C_{cell}. In the case of a-C:O surfaces, the adhesion of endothelial cells is reduced by 20% relative to the C_{cell}, suggesting an effect of carbon surface oxidation on the adhesion of endothelial cells.

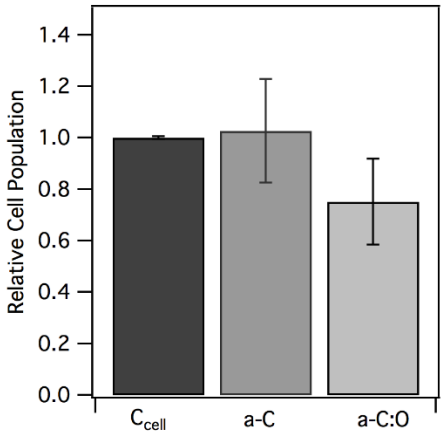


Figure 6.2. Relative population of endothelial cells adherent at a-C and a-C:O surfaces comparative to control (C_{cell}) after 24 h of cell culture; values given as mean ± stdev.

These results were validated through fluorescence microscopy imaging after 48 hours incubation of endothelial cells at a-C surfaces (Figure 6.3). The observation of adherent cell morphology was performed through staining of the nucleus and F-actin cytoskeleton using DAPI and phalloidin, respectively. Surface-dependent variation in cellular morphology was observed for carbon films; cells adhering onto a-C surfaces exhibit larger and more elongated cytoskeleton structure when compared with morphology of adherent cells onto a-C:O surface.

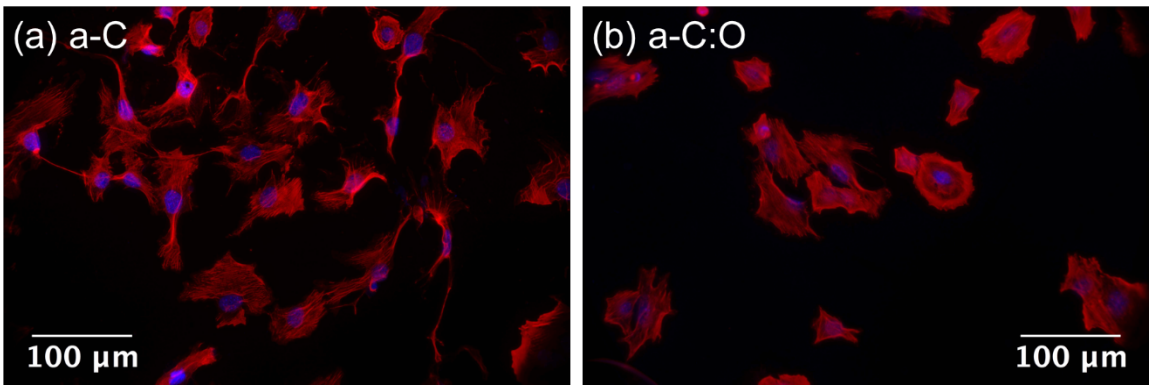


Figure 6.3. Fluorescence images of rat aortic endothelial cells adherent to **(a)** a-C and **(b)** a-C:O surfaces. The nucleus (blue) and the F-actin cytoskeleton (red) were stained using DAPI and phalloidin, respectively.

Furthermore, investigation on adherent cell morphology parameters, such as area and aspect ratio was performed. Surface area of cells adherent at a-C is ~33 % larger when compared with adhesion onto a-C:O (55007 μm^2 for a-C vs. 35730 μm^2 for a-C:O) ,

demonstrating an enhanced cellular spreading at a-C surface after 48 h of cell incubation.[22] The aspect ratio was also affected by the carbon surface chemistry. In fact, cells adherent onto a-C surface adopt a more elongated geometry, with a length/width aspect ratio of 2.7 ± 0.8, whereas cell adhesion onto a-C:O surface display an aspect ratio of 1.5 ± 0.2. The significant difference between cell morphology adherent onto the carbon films could be related to a better cell adhesion and proliferation onto a-C when compared to a-C:O surfaces.

The variations in cell morphology adherent on solid surfaces has been related with the development of focal adhesions (FAs).[22] FAs are membrane-associated protein complexes that are present near the plasma membrane where they form mechanical links between the actin fibres and the extracellular matrix. They can possess diameters in the range 0.5 - 5 µm, depending on the degree of maturation.[23] Numeric analysis of FAs is a good quantitative test to understand the affinity of cells for a substrate and predict further interaction of cell/substrate at the solid/liquid interface.[22]

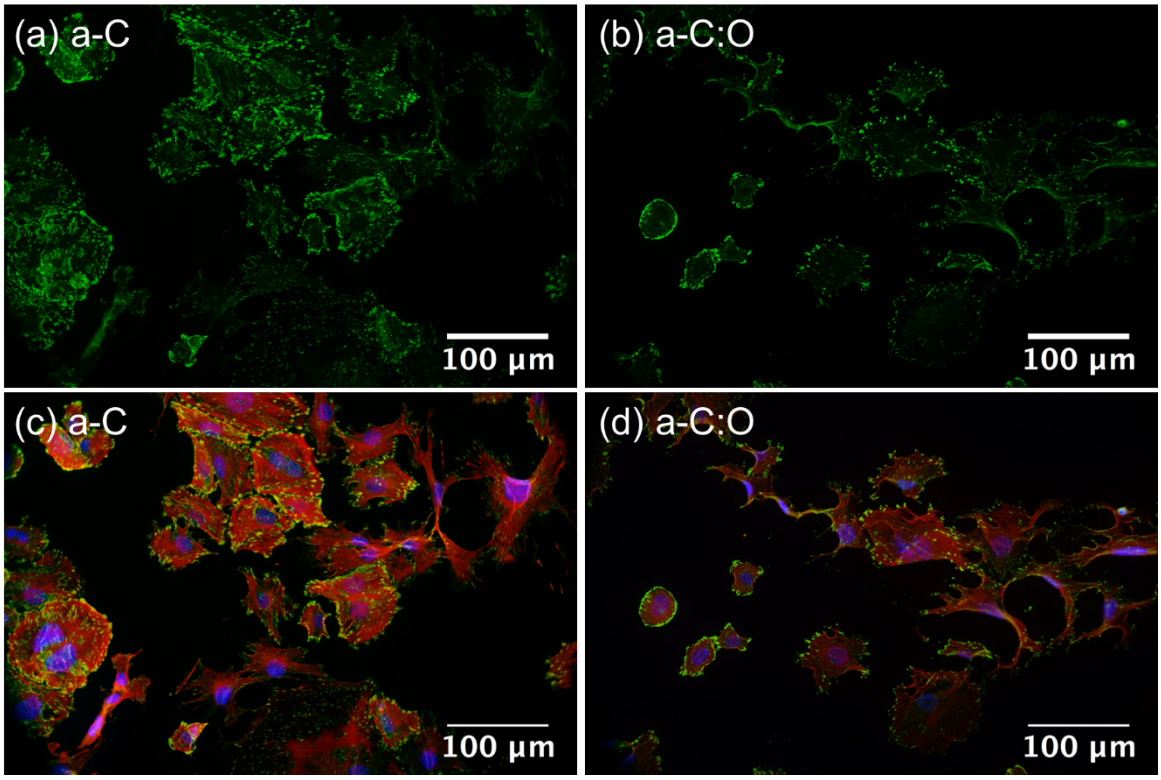


Figure 6.4. Fluorescence images of focal adhesions (FA) of endothelial cells adherent to **(a)** a-C and **(b)** a-C:O surfaces stained with an antibody (pAb) stained against vinculin (green). Overlap of fluorescence images of pAb, nucleus and F-actin cytoskeleton at **(c)** a-C and **(d)** a-C:O surfaces; nucleus (blue) and F-actin cytoskeleton (red) were stained using DAPI and phalloidin, respectively.

Figures 6.4a and 6.4b show immunofluorescence images of endothelial cells adherent to a-C and a-C:O surfaces stained against vinculin (green). Figures 6.4c and 6.4d display the overlap of fluorescence images of vinculin, nucleus and F-actin cytoskeleton of endothelial cells adherent onto a-C and a-C:O surfaces, respectively. Both surfaces show similar patterns of vinculin distribution on endothelial cells, with FAs identified at the edge of each cell adherent onto the substrate. Nevertheless, cells adhered on a-C surfaces showed abundant and mature, dash-like FAs, whereas a-C:O surfaces tended to show smaller round-like aggregations of vinculin that resembled early focal complexes. Numeric analysis on the FAs on a-C and a-C:O, normalised against number of cells, yielded values of 196 ± 24 and 85 ± 17, respectively. Complexes at a-C:O are significantly higher than on a-C surface, suggesting lower interaction of endothelial cells with a-C:O surfaces when compared with a-C.

Overall, FAs allowed to understand cell compatibility of carbon coatings used on this study and suggested that carbon films are not detrimental to cells with respect to adhesion and spreading. Analysis on FAs assembly and qualitative maturation helped to explain the higher cell adhesion on a-C in relation to a-C:O, indicating that there is a superior interaction between the graphitic substrate and endothelial cells.[23]

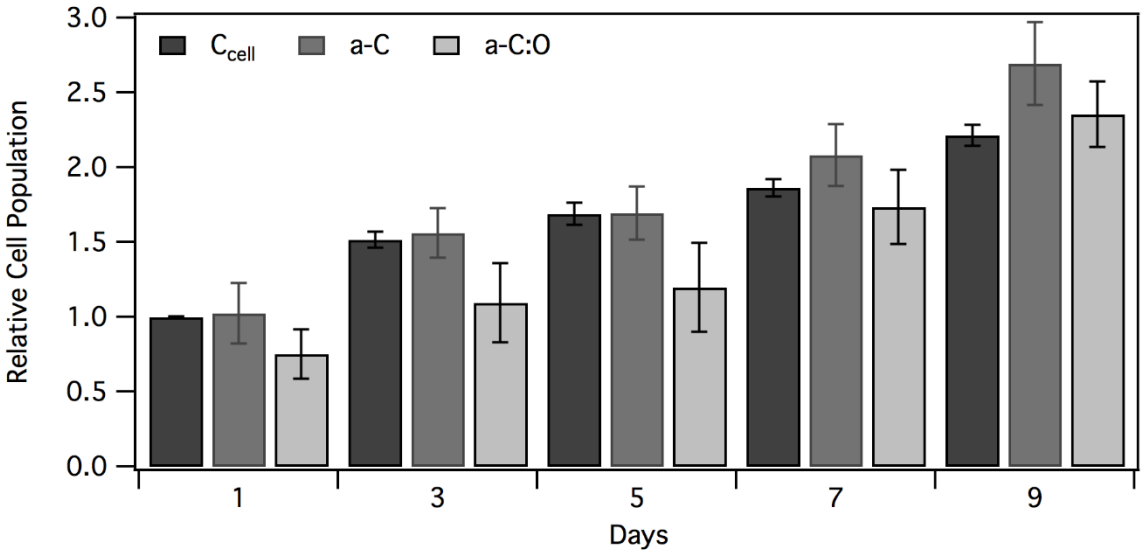


Figure 6.5. Relative population of endothelial cells. Adhesion (day 1) and proliferation (days 3-9) at a-C and a-C:O surfaces compared to control (C_{cell}); values given as mean ± stdev.

In order to understand if the initially enhanced endothelial cell adhesion at the a-C surface would be observed for an extended period of time, proliferation tests were performed. Figure 6.5 shows proliferation profiles of endothelial cells after 3, 5, 7 and 9 days incubation onto a-C and a-C:O surfaces; values were normalised against C_{cell} on day 1. Proliferation of endothelial cells at a-C and a-C:O surfaces was comparable with C_{cell}, displaying a regular increment in the relative cell population over 9 days. As seen for the adhesion of endothelial cells at a-C:O, the oxidation of the carbon film results in a slightly reduced cell population over the 9 days of cell proliferation.

2.3. *HFFF2* Fibroblasts Culture

As seen for endothelial cells, the long-term bioresponse towards an implanted biomaterial is strongly correlated on cellular adhesion and spreading at the material interface. Fibroblasts are known to play a key role in tissue and functional recovery after biomaterial implantation, hence understanding and tuning fibroblasts response to an implantable biomaterial is key to ensure complete integration of the foreign material.[2024-26] A biomaterial which is capable of minimizing deleterious consequences from fibrotic response, generated by recruitment of fibroblasts during wound healing, is desired.[22]

Investigation on the *in vitro* interaction of fibroblasts, from the *HFFF2* line, with amorphous carbon films was performed. As in the case of the EC study, interactions at multiple- and single-cell level between fibroblasts and a-C surfaces could be observed. Figure 6.6 shows relative population of *HFFF2* cells adherent to a-C and a-C:O surfaces and normalised against the control (C_{cell}) after 24 h of cell culture. Both surfaces display a satisfactory *HFFF2* cell viability after 24 h of incubation; bare a-C exhibits cell adhesion comparable with the C_{cell}, while oxidised carbon displays a reduction of ~48 % of adherent *HFFF2* cells when compared with C_{cell}. Surface wettability is known to play a major role in fibroblast adhesion at solid surfaces. Tamada *et al.*[27] reported on rat fibroblast adhesion at solid surfaces with different degrees of wettability and observed that for extreme hydrophilic surfaces, as the case of a-C:O (wCA < 5°), fibroblast adhesion is significantly reduced. Similarly to EC interaction with carbon thin films, the reduction on cell adhesion for a-C:O surfaces is attributed to a water interlayer at the cell/substrate interface that

impedes cell adherence at the oxidised surface.[17, 21, 28-30]

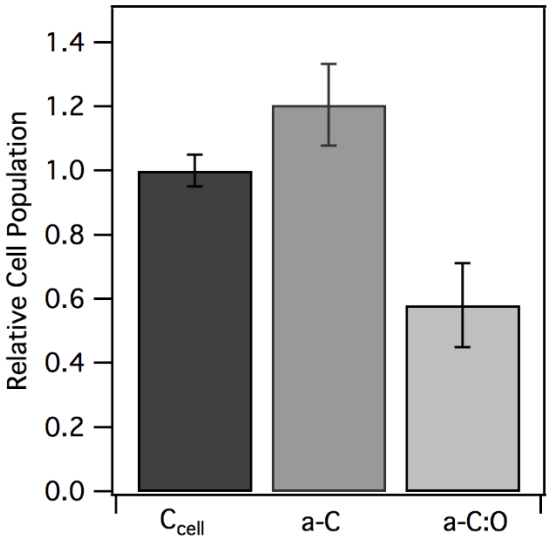


Figure 6.6. Relative population of *HFFF2* cells adherent at a-C and a-C:O surfaces comparative to control (C_{cell}) after 24 h of cell culture; values given as mean ± stdev.

Cell morphology was assessed by fluorescence microscopy as is shown in Figure 6.7; nucleus and F-actin cytoskeleton were stained using DAPI and phalloidin, respectively. *HFFF2* cells adhesion at carbon surfaces show elongated and flattened profiles, characteristic of a good adhesion at the solid surface. Surface-dependent variations on the adhesion of *HFFF2* cells were not observed, with both a-C and a-C:O surfaces displaying fibroblasts spread at the surface. To better quantify the adhesion of *HFFF2* cells at carbon surfaces, an analysis of FAs on both surfaces was performed.

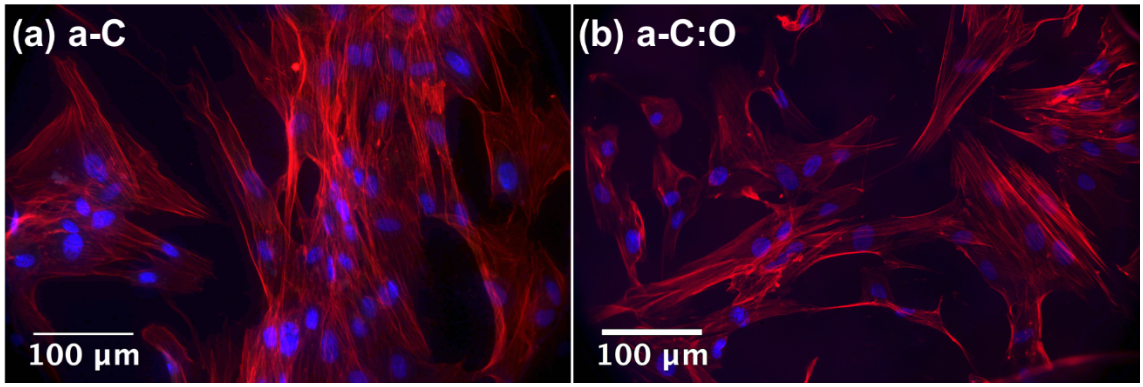


Figure 6.7. Fluorescence images of HFFF2 cells adherent to **(a)** a-C and **(b**) a-C:O surfaces. The nucleus (blue) and the F-actin cytoskeleton (red) were stained using DAPI and phalloidin, respectively.

Figures 6.8a and 6.8b show fluorescence images of *HFFF2* cells adherent to a-C and a-C:O surfaces stained with pAB against vinculin; Figures 6.8c and 6.8d show the overlap of fluorescence images of pAb, nucleus and F-actin cytoskeleton of *HFFF2* cells adherent onto a-C and a-C:O surfaces, respectively. FAs were identified at the edge of F-actin cytoskeleton, a result of cell adhesion at the carbon surfaces. Both surfaces possess dash-like FAs, a confirmation of good cell adhesion and spreading at these surfaces; numeric analysis on the FAs yielded values of 259 ± 34 and 205 ± 23 for a-C and a-C:O surfaces, respectively.

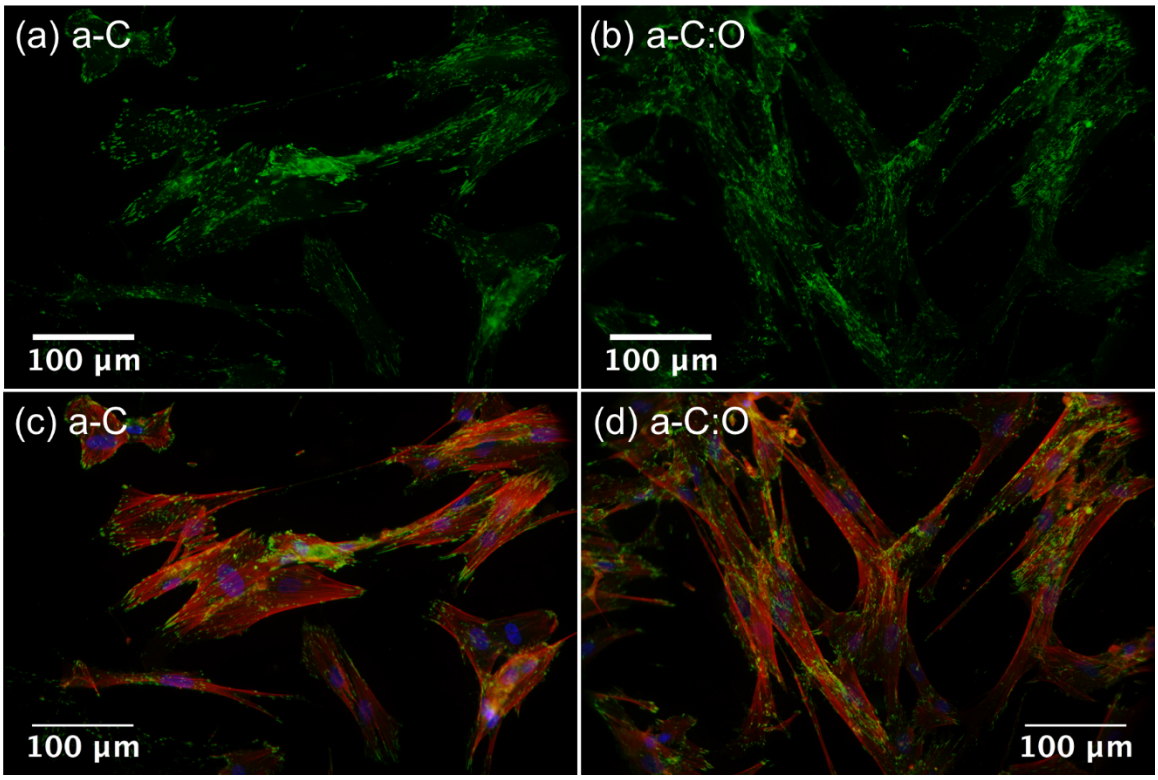


Figure 6.8. Fluorescence images of focal adhesions (FA) of HFFF2 cells adherent to **(a)** a-C and **(b)** a-C:O surfaces with primary antibody (pAb) stained against vinculin (green). Overlap of fluorescence images of pAb, nucleus and F-actin cytoskeleton at **(c)** a-C and **(d)** a-C:O surfaces; nucleus (blue) and F-actin cytoskeleton (red) were stained using DAPI and phalloidin, respectively.

The proliferation of *HFFF2* cells was also studied after 3, 5, 7 and 9 days of cell incubation on carbon films (Figure 6.9); values were normalised against C_{cell} on day 1. As previously discussed, the adhesion of *HFFF2* cells onto carbon films is roughly 50% higher on a-C than on a-C:O surfaces. However, both graphitic and oxidised carbon surfaces display a comparable proliferation profile of *HFFF2* cells over 9 days of incubation,

suggesting that carbon surface wettability does not significantly influence fibroblast cell proliferation.

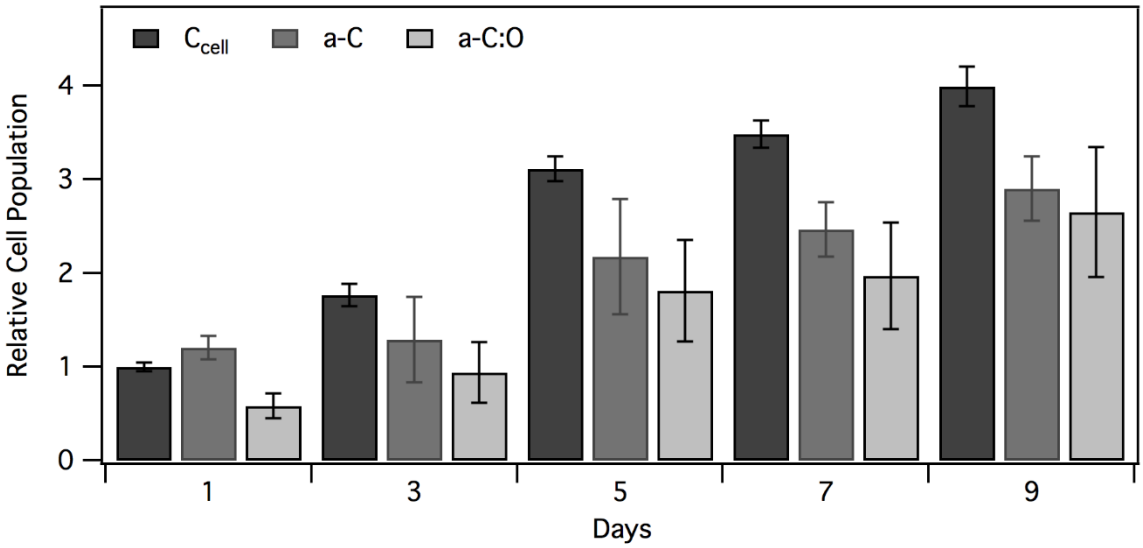


Figure 6.9. Relative population of fibroblasts, from the line HFFF2, adhesion (day 1) and proliferation (days 3-9) at a-C and a-C:O surfaces comparative to control (C_{cell}); values given as mean ± stdev.

2.4. Thrombogenicity

When designing a biomaterial that is expected to be in contact with blood, thrombogenic effects, which may occur after biomaterial implantation, are a major concern.[4, 14] Thrombus formation are known to be preceded by platelet adhesion, activation and aggregation at the biomaterial interface.[4, 20] The morphology of platelets at the biomaterial surface have been associated to the capability of the biomaterial to prevent undesirable bioresponses such as platelet-mediated thrombosis.[20]

In vitro studies with human platelets in a-C and a-C:O surfaces were performed and the adhesion of platelets was examined. According to Goodman's classification,[14] it is possible to categorize platelet shapes in different morphological forms and relate it with the degree of platelet activation. Figure 6.10 shows the morphology of human platelet adhesion at a-C and a-C:O surfaces: the dendritic (D) (Figure 6.10a) and the spread dendritic (SD) (Figure 6.10b) morphologies, which correspond to early and medium stages of activation, respectively.[14] These two types of platelet morphologies are related with an increased degree of platelet activation in the order of D < SD; surfaces with a higher

density of SD, when compared with D morphology, are more prone to platelet-mediated thrombosis.[14]

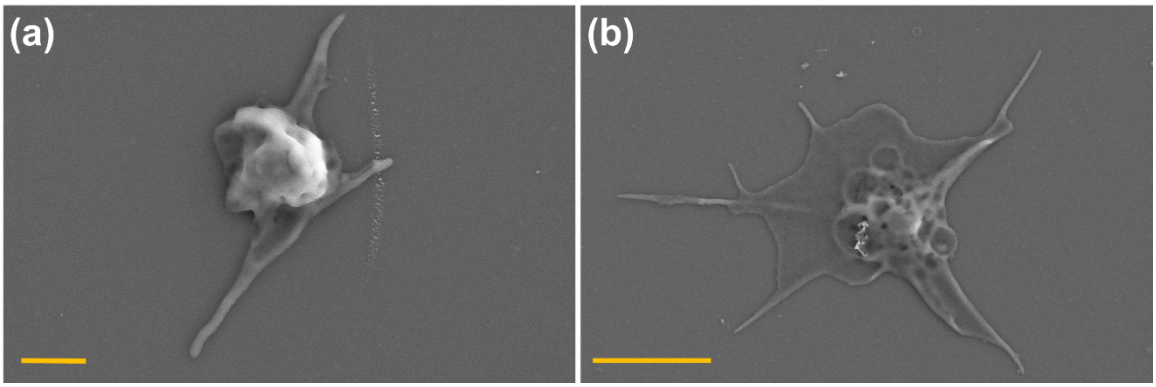


Figure 6.10. (a) Dendritic (D) and **(b)** spread dendritic (SD) morphologies of adherent platelets on a-C films imaged with SEM; scale bars correspond to 3 µm and 1 µm, respectively.

The propensity of platelet-mediated thrombus formation was evaluated considering three parameters: number of platelets in the (i) D morphology, (ii) SD morphology and by the number of focal centres, *i.e.* aggregates of three or more platelets. Figure 6.11 shows low magnification SEM images of platelet adhesion at a-C and a-C:O surfaces. Overall, platelet adhesion at a-C is substantially higher than on a-C:O surfaces. Also, D and SD morphologies of platelet adhesion can be identified both for a-C and a-C:O surfaces. Finally, platelet adhesion on a-C and a-C:O surfaces show similar low to no levels of focal centres.

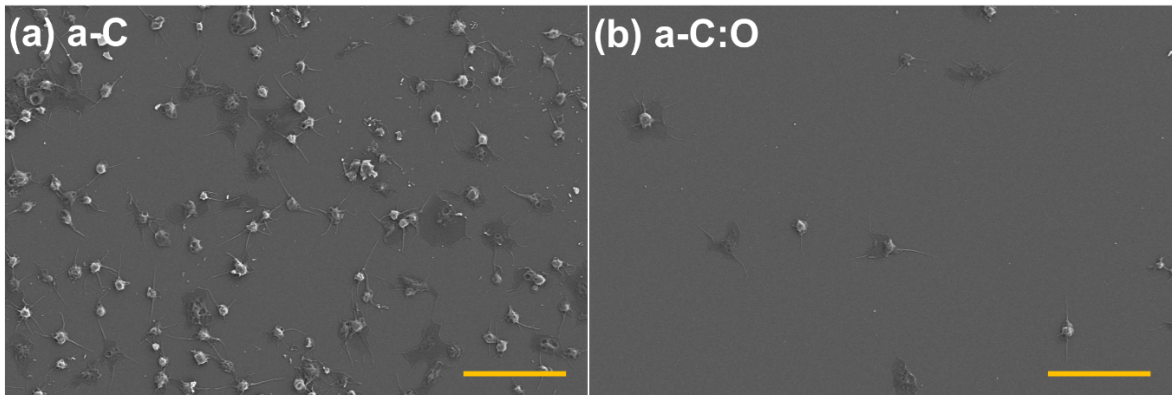


Figure 6.11. SEM image of *in vitro* human platelet adherent at **(a)** a-C and **(b)** a-C:O surfaces (scale bar = 20 µm).

These results were corroborated through numeric analysis of platelet adhesion at carbon surfaces, considering the aforementioned parameters (Figure 6.12). The number of platelets adherent at a-C is approximately 6x higher than on a-C:O. Adhesion of platelets with D morphology at a-C and a-C:O surfaces were found to be 66% and 56% of the total platelets adhered to the surface, respectively; the remaining % corresponds to platelets with SD morphology. As seen in Figure 6.11, the amount of focal centres was found to be insignificant, corresponding to <10% of the total platelet adhesion at a-C surfaces; at a-C:O surfaces no focal centres were observed.

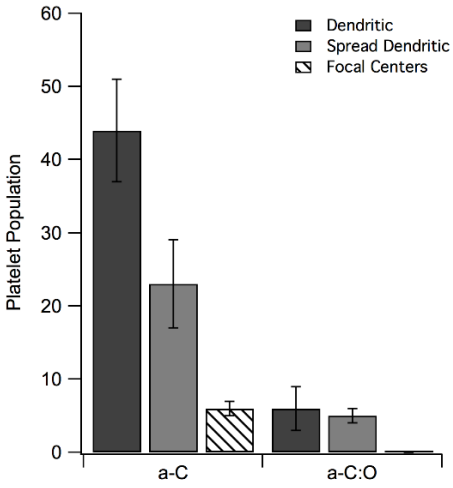


Figure 6.12. Platelet dendritic (D) and spread dendritic (SD) morphologies distribution and focal centres at a-C and a-C:O surfaces; each plot shows the platelet population in a 100×75 μm^2 area (mean ± stdev).

The morphology of platelets adherent at the a-C films are associated with low to medium degree of platelet activation, suggesting that a-C films produced in this work show an excellent ability to prevent platelet-mediated thrombus formation.[14] The absence of focal centres and the reduced number of platelets adherent at a-C:O surface, when compared with a-C, implies that oxidised carbon shows a great promise in inhibiting thrombotic events, which is strongly related with the increased wettability of a-C:O.[4, 20, 28, 31-32]

2.5. *Saccharomyces Cerevisiae* Biofilm Formation

For the last decades, efforts have been developed on surface coatings that prevent biofilm formation, *i.e.* fungal and bacterial, at the biomaterials interface.[33-34] Despite the progress seen for the last years associated with the development of materials with antifungal properties, yeasts are still known as one of the most common microorganisms responsible for catheter-related bloodstream infections.[35-36]

Due to the high demand of carbon-based materials in the biomedical field, the control over biofilm formation has been reported.[33-34, 37-40] Carbon surfaces have shown outstanding performances in preventing biofilm formation caused by bacteria[33-34, 39-40] and fungi[38, 41] agglomeration at the biomaterial interface. Research has suggested standard microbiological tests using suitable well-characterised fungi strains, such as yeast, as they are a good representation of biodegradation of carbon coatings through biofilm formation and are responsible for biomaterial-related infections.[37-38]

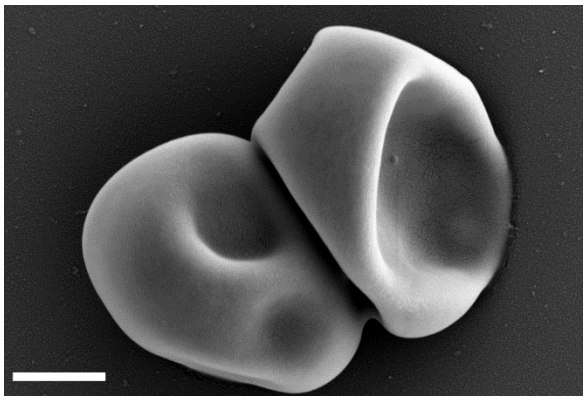


Figure 6.13. Example of *saccharomyces cerevisiae* (yeast) adsorption at carbon films; scale bar = 1 µm.

In vitro studies on the interaction of *saccharomyces cerevisiae*, a well-known yeast strain, and carbon films were performed (Figure 6.13-14). Fungal biofilm development is characterised as a complex process that occurs through multiple steps: (i) adhesion to the substrate, (ii) cell proliferation and (iii) biofilm maturation.[35] Figure 6.13 shows an example of yeast cells adherent to a carbon film, typical of an initial stage of fungal biofilm formation. Analysis on the diameter of yeast cells resulted in (3.6 ± 0.5) µm, a common diameter found for the fungal strain *saccharomyces cerevisiae*.[42-43]

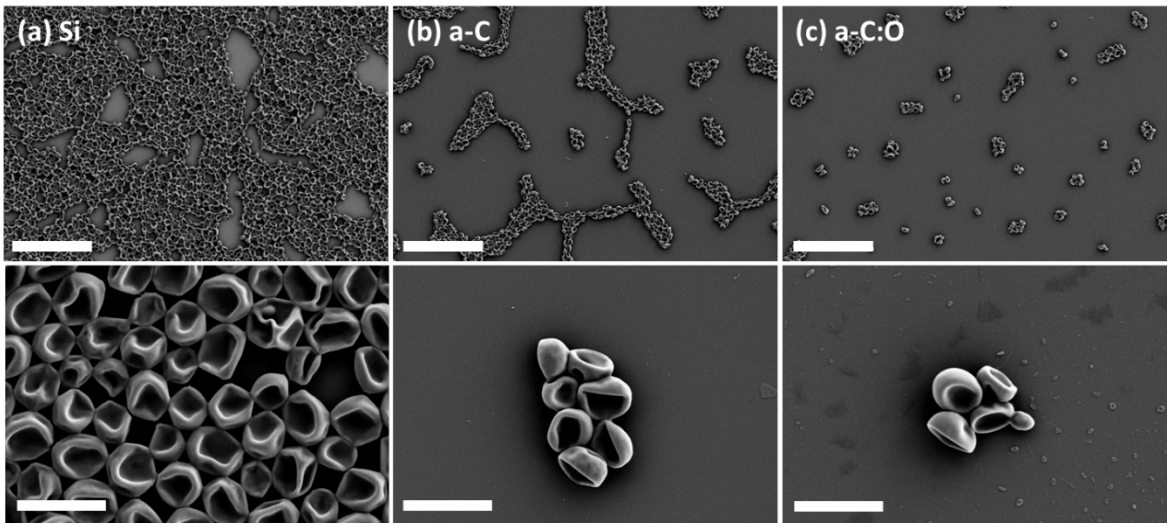


Figure 6.14. SEM images at low (top) and high (bottom) magnifications on the adhesion of yeast at **(a)** Si, **(b)** a-C and **(c)** a-C:O surfaces; scale bars corresponds to 40 μm (top) and 5 μm (bottom).

Figure 6.14 shows SEM images of Si, a-C and a-C:O surfaces after 7 days of yeast cell inoculation. In general, the three surfaces display yeast cells adherent to the surface in the first step of biofilm formation; no surfaces exhibited a matrix of self-produced polymeric material, which is characteristic of biofilm maturation.[35] The anti-infective behaviour of the three surfaces studied here was found to be enhanced in the order Si < a-C < a-C:O.

The % area occupied with yeast on Si, a-C and a-C:O surfaces was analysed (Figure 6.15). The Si substrate was found to have ~36 % occupied by yeast cells while a-C and a-C:O surfaces had only 25 % and 6 % of yeast coverage, respectively. The very low coverage of a-C and a-C:O films with yeast cells reveals that the carbon films used in this studied show a great promise as carbon-based biodevices. Also, as previously seen for platelets adhesion at carbon films, the oxidation of a-C results in a much more effective anti-fungal behaviour when compared with the bare a-C.

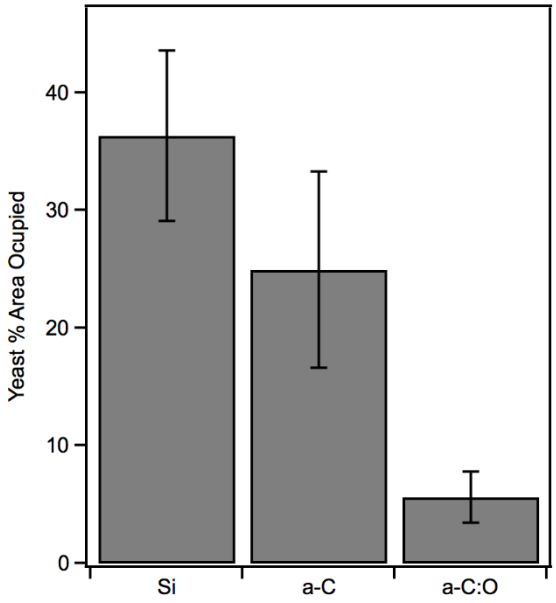


Figure 6.15. Percentage of covered surface (mean ± stdev) by collection of *saccharomyces cerevisiae* (yeast) on Si, a-C and a-C:O surfaces.

3. Discussion

In this chapter, the bioresponse of carbon thin films was evaluated, with emphasis on cellular adhesion, proliferation, morphology and establishment of FAs. Also, the thrombogenic and fungal behaviours of carbon thin films were assessed. Existing literature suggests that surface wettability significantly contributes to determining the bioresponse of carbon-based biodevices and it has been proposed that wettable surfaces are less prone to cell adhesion and proliferation.[17, 21, 28-30] In order to compare and discuss the influence of carbon surface wettability on the bioresponse of carbon films, the results obtained in this chapter are summarised in Figure 16; adhesion of endothelial and fibroblast cells are reported as relative cell population, platelets are reported as total population and yeast as % area occupied.

The bioresponse displayed for a-C surface is significantly different when compared with a-C:O, suggesting an effect of carbon surface physico-chemical properties on carbon *in vitro* interaction with cells and biomolecules. Previous analysis on the physico-chemical properties of both carbon films used in this work (Chapter III), yielded values of water contact angle (wCA) of (35.2 ± 1.4)° and < 5° for a-C and a-C:O surfaces, respectively. The

variation of wetting behaviour after surface oxidation was attributed to the increase of oxygen-containing groups on a-C:O, a conclusion obtained after the analysis of XPS C 1s peak and observation of the doubling of oxygen content at a-C:O (20 %), when comparing with a-C (8 %).

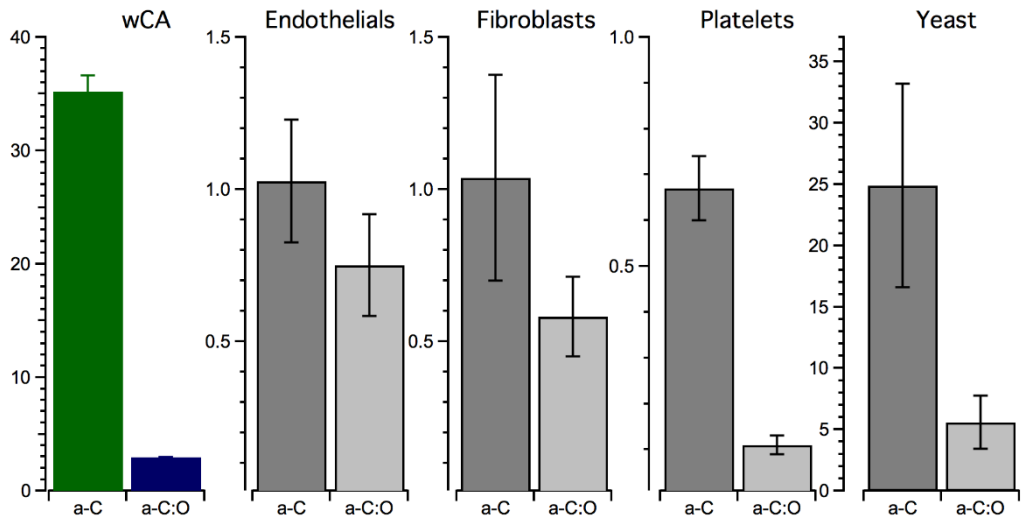


Figure 6.16. Water contact angles (wCAs) of a-C (green) and a-C:O (blue) surfaces and resume of results previously obtained in this chapter. Adhesion of endothelial and fibroblast cells are reported as relative cell population; platelets are reported as total platelet population and yeast as % area occupied.

Endothelial cell adhesion at a-C surface is slightly higher, ~20 %, when compared with a-C:O, suggesting a contribution of surface wettability on such interaction. Literature suggests that the interaction of carbon films with endothelial cells can be tuned by the control of surface wettability.[17, 21, 28-30] Similar to the results present in this study, Bociaga *et al.*[28] reported that an increase of hydrophobicity of DLC films would result in a better adhesion and proliferation of endothelial cells. Also, Ogwu *et al.*[17] showed that for hydrophobic surfaces, the interaction with water molecules is reduced and results in a more direct contact with the endothelial cells, rather than an interaction mediated by a water layer. Finally, Patelis *et al.*[12] showed how oxidation of graphene is able to reduce endothelial cell adhesion and proliferation.

Also, wettability influenced the interaction of carbon films with *HFFF2* fibroblasts; adhesion at a-C:O surface was significantly lower than at a-C. However, the long term

interaction of carbon films with fibroblasts did not seem affected by substrate wettability since both surfaces show similar proliferation profiles after 9 days of incubation. The influence of substrate wettability on the adhesion of fibroblasts has been previously reported for different carbon films.[22, 25-26] For instance, Ryoo *et al.*[22] reported on cell adhesion on carbon thin films, utilising FAs to understand the influence of surface chemistry on the interaction between the substrate and intracellular signalling. Analysis on the FAs allowed Ryoo *et al.* to conclude a higher fibroblasts affinity for carbon-based surfaces than for glass and attributed the difference observed to surface physico-chemical properties, such as wettability and roughness.[22]

Carbon coatings have also been a promising choice of material to control and reduce platelet adhesion and activation, the main cause of increased degree of thrombosis formation.[4, 14, 28, 44-45] In this work, a-C:O showed significant reduction of platelet adhesion when compared with a-C. Also, the absence of focal centres at the oxidised carbon indicates that a-C:O displays a better anti-thrombotic behaviour than a-C. These results confirm research on the implication of wettability of carbon coatings on platelet adhesion and activation, which revealed that higher surface hydrophilicity implies a more satisfactory inhibition of thrombotic events.[4, 20, 28, 31-32]

Furthermore, as previously seen for platelets adhesion at carbon films, the oxidation of a-C results in a much effective anti-fungal behaviour when compared with the bare a-C. In fact, the inhibition of *saccharomyces cerevisiae* biofilm formation on a-C:O is ~ 5x higher when compared with bare a-C. The hydrophilicity of a-C:O results in a particular interaction of this coating with biomolecules and cells: while the interaction with fibroblasts and endothelial cells does not seem significantly affected in terms of cell morphology and spreading, the platelet adhesion and fungi biofilm formation is remarkably reduced.

4. Conclusions

In summary, this study contributed to an understanding of the effects of surface properties on the cellular compatibility of carbon thin films. Endothelial cells and fibroblasts behaviour at carbon surfaces, *i.e.* cell adhesion, proliferation, morphology and establishment of FAs were investigated. Quantitative information was extracted from the analysis of cell morphology and FAs at carbon interface; a direct relation was established between the cell adhesion and FAs at both carbon surfaces. It was shown that cell adhesion is dependent on the substrate properties, most likely wettability reduces cells adhesion given the poor number of FA points established at early stages of cell/substrate interaction.

Additionally, the anti-thrombogenic and anti-fungal behaviours of carbon films were studied. Oxidised carbon shows a significant reduction in platelet adhesion and spreading when compared with a-C. Moreover, in the study of anti-fungal properties of carbon, the oxidation process of carbon films leads to a substantial decrease of *saccharomyces cerevisiae* biofilm formation. These results are attributed to the increase of wettability in a-C:O, which restrain surface/biomolecules interaction.

Research of carbon-based biodevices has been looking for carbon coatings whose physico-chemical properties allow satisfactory cell adhesion and spreading and also inhibit biofilm formation and thrombogenic events to happen at the interface. These results show the potential of carbon films for biomedical applications, which display a unique combination of high biocompatibility, anti-thrombogenic and anti-fungal behaviours.

5. Experimental

5.1. Materials and Chemicals

Fibroblasts from cell line *HFFF2* (*Human Caucasian foetal foreskin fibroblast)* were

purchased from the European Collection of Authenticated Cell Cultures (ECACC, Porton Down, UK). Vero cells (monkey kidney epithelial cells) were kindly supplied by Prof. Gabriela Rodrigues from the Department of Animal Biology, Faculty of Science, University of Lisbon, Portugal. Rat aortic endothelial cells were kindly supplied by Dr. Gabriel Martins from the Gulbenkian Science Institute, Oeiras, Portugal. Human plasma was obtained from the Portuguese Institute for Blood and Transplantation.

Dulbecco's Modified Eagle Medium (DMEM, cat# D5030) and primary antibody (Anti-Vinculin antibody, Mouse monoclonal, cat# V9264) were purchased from Sigma Aldrich. Fetal bovine serum (FBS), penicillin, streptomycin, secondary antibody (Goat anti-Mouse IgG Secondary Antibody, Alexa Fluor 488, cat# A11001) and 4',6-diamidino-2-phenylindole (DAPI) were purchased from ThermoFisher Scientific. Bovine serum albumin (BSA) and resazurin sodium salt were purchased from VWR. YEPD (1% (w/v) yeast extract, 2% (w/v) peptone, 2% (w/v) glucose) was purchased from Fisher.

Note: Carbon films were prepared according to previously described protocols in Chapters III. All substrates were sterilized with 70 % ethanol prior to *in vitro* tests.

5.2. *In vitro* tests

5.2.1. Cytotoxicity

Cytotoxicity tests were performed according to the ISO 10993-5 standard (biological evaluation of medical devices —Tests for *in vitro* cytotoxicity) and executed through the extract method. Samples were immersed in culture medium DMEM supplemented with penicillin (10000 U/mL) and streptomycin (10000 µg/mL) (P-S) for 48 h at 37 °C, 5% CO_2. The extracts were then collected, supplemented with 10 % FBS and used as culture medium for *Vero* cells (monkey kidney epithelial cells). Cells were pre-seeded using fresh DMEM supplemented with P-S and FBS at a density of 20k cells/cm^2 in a 96 multiwell plate 24 h before to allow cells to adapt to the new environment. Subsequently, the medium was substituted for the extract. Negative (C-) and positive (C+) controls were used as ideal and cytotoxic growing environments, respectively. For the positive control, 10 µL of DMSO were added to each well. 5 replicas were prepared for each experimental condition. After

incubating for 48 h, the extract was removed and 100 µL of a resazurin solution (10 % of a 0.2 mg/ml resazurin sodium salt solution in PBS + 90 % of complete fresh medium) was added to each well. After 3 h of incubation, the optical densities (OD) were measured at 570 nm and 600 nm. Cell viability for each experimental condition was calculated as the ratio of the corrected OD of the experimental wells and the negative control.

5.2.2. Fibroblasts and Endothelial Cells

Fibroblasts and endothelial cells were cultured in DMEM supplemented with penicillin (10000 U/mL) and streptomycin (10000 µg/mL) (P-S) for 48 h at 37 °C, 5% CO_2. Cells were seeded on the substrate at a density of 20k cells/cm^2 in a 24 multiwell plate; cell control (C_{cell}) was used as an ideal growing environment. 3 replicas were prepared for each experimental condition. Adhesion test was performed 24 h after cell seeding and proliferation tests were performed 3, 5, 7 and 9 days after cell seeding onto the substrate. For adhesion and proliferation tests, cells were exposed to 800 µL resazurin solution for 3 h and the OD were measured at 570 nm and 600 nm (see cytotoxicity protocol); data represents mean ± stdev of at least 3 replicas. Fluorescence measurements were performed 48 h after cell seeding on the substrate and the protocol of cell preparation for fluorescence imaging is described below in the immunostaining section.

5.2.3. Thrombogenicity

The thrombogenicity of a-C films was examined using human plasma rich in platelets (PRP) obtained by 10 min centrifugation of whole blood at low speed. The carbon films were incubated in PRP for 30 min at 37 °C with gentle, end to end mixing, following a procedure previously described.[14] Subsequently, the samples were rinsed 3 times with PBS and fixed with 2.5 % glutaraldehyde for 1 h at room temperature. Finally, the carbon samples were rinsed with PBS and left drying in air prior to microscope imaging.

5.2.4. *Saccharomyces Cerevisiae* Biofilm

The biofilm formation at carbon films was studied using the fungal strain *saccharomyces cerevisiae* BY4741 (yeast), grown overnight in YEPD broth prior to incubation. Subsequently, yeast was diluted 1:100 in fresh YEPD medium and 2 mL of

diluted yeast were added to each well containing the surfaces to be examined. The plate was covered with sterile adhesive lid and left incubating statically at 30 °C for 5-7 days. Afterwards, the medium was aspirated and each well was washed 3 times with 2 mL sterile distilled water and placed on the rocking plate for 5 min between washes. Water was aspirated and the plate was covered with sterile adhesive lid prior to microscope imaging. Biofilm formation at the carbon surfaces was expressed as the percentage of area covered with yeast; all tests were performed in duplicate. Numeric analysis on yeast diameter was performed using at least 100 individual yeast cells.

5.3. Characterisation methods

5.3.1. Spectrophotometer

Optical densities (OD) were obtained through absorbance measurements on a spectrophotometer Biotek ELx800UV at 570 and 600 nm.

5.3.2. Immunostaining

Fluorescence images of cells were obtained 48 h after cell seeding onto carbon surfaces. Prior to fluorescence imaging, the samples were rinsed 3 times with PBS and fixed with 3.7 % PFA for 10 min at room temperature, followed by rinsing with PBS. After fixation, cells were treated with 0.5 % Triton X-100 in PBS for permeabilization, followed by rinsing with PBS. 100 µL of primary anti-body (Anti-Vinculin antibody, Mouse monoclonal, Sigma-Aldrich V9264, diluted 1:100), suspended in 1% BSA in PBS, were added to each sample and left for 2 h at room temperature. After PBS rinsing, 100 µL of secondary antibody (Goat anti-Mouse IgG Secondary Antibody, Alexa Fluor 488, ThermoFisher Scientific, A11001, diluted 1:500), suspended in 1 % BSA in PBS, were added to each sample and left 2 h at room temperature protected from light. After PBS rinsing, 100 µL of 100 nM phalloidin (Acti-stain 555 Fluorescent Phalloidin, Cytoskeleton Inc, cat# PHDH1) for F-actin staining were added to each sample and left to incubate for 30 min at RT. Finally, 100 µL of DAPI was added to each sample and left for 5 minutes, followed by PBS rinsing.

Fluorescence imaging was performed in a Nikon TiS with epifluorescence attachment. Excitation in the UV (360 nm), 480 nm and 540 nm regions were utilised to image DAPI, Alexa Fluor 488 (secondary antibody) and Acti-stain 555 (phalloidin) staining, respectively. Samples were mounted in PBS on a microscope slide and observed using 10x and 40x objectives; statistical analysis was performed in at least 3 replicates of each sample.

5.3.3. Scanning electron microscopy (SEM)

Scanning electron microscopy (SEM) was utilised to analyse the morphology of platelets and *saccharomyces cerevisiae* (yeast) biofilm formation onto a-C films. SEM was performed using a Karl Zeiss Ultra Field Emission at a working distance of ~4 mm and at an accelerating voltage between 2-5 kV. Prior to SEM imaging, the samples were covered with 4 nm gold film. ImageJ software was used to characterise the % area, ratio and morphology of platelets and yeast at carbon films; at least 3 replicates of 100×75 μm^2 area (mean ± stdev) were utilised for each sample.

6. References

1.Love, C. A.; Cook, R. B.; Harvey, T. J.; Dearnley, P. A.; Wood, R. J. K., *Tribology International* **2013,** *63*, 141.
2.Linder, S.; Pinkowski, W.; Aepfelbacher, M., *Biomaterials* **2002,** *23* (3), 767.
3.Lackner, M. J.; Waldhauser, W., *BHM Berg- und Hüttenmännische Monatshefte* **2010,** *155* (11), 528.
4.Hauert, R., *Diamond and Related Materials* **2003,** *12* (3–7), 583.
5.Gotzmann, G.; Beckmann, J.; Wetzel, C.; Scholz, B.; Herrmann, U.; Neunzehn, J., *Surface and Coatings Technology* **2017,** *311*, 248.
6.Grill, A., *Diamond and Related Materials* **2003,** *12* (2), 166.
7.Allen, M.; Myer, B.; Rushton, N., *Journal of biomedical materials research* **2001,** *58* (3), 319.
8.Bociąga, D.; Jakubowski, W.; Komorowski, P.; Sobczyk-Guzenda, A.; Jędrzejczak, A.; Batory, D.; Olejnik, A., *Materials Science and Engineering: C* **2016,** *63*, 462.
9.Castellino, M.; Stolojan, V.; Virga, A.; Rovere, M.; Cabiale, K.; Galloni, M. R.; Tagliaferro, A., *Analytical and bioanalytical chemistry* **2013,** *405* (1), 321.
10.Chai, F.; Mathis, N.; Blanchemain, N.; Meunier, C.; Hildebrand, H. F., *Acta biomaterialia* **2008,** *4* (5), 1369.
11.Liao, T. T.; Deng, Q. Y.; Li, S. S.; Li, X.; Ji, L.; Wang, Q.; Leng, Y. X.; Huang, N., *ACS Biomaterials Science & Engineering* **2017,** *3* (4), 530.
12.Patelis, N.; Moris, D.; Matheiken, S.; Klonaris, C., *BioMed Research International* **2016,** *2016*.
13.Charitidis, C. A., *International Journal of Refractory Metals and Hard Materials* **2010,** *28* (1), 51.
14.Goodman, S. L., *Journal of biomedical materials research* **1999,** *45* (3), 240.
15.Aramesh, M.; Tong, W.; Fox, K.; Turnley, A.; Seo, D.; Prawer, S.; Ostrikov, K., *Materials* **2015,** *8* (8), 4992.
16.Miksovsky, J.; Voss, A.; Kozarova, R.; Kocourek, T.; Pisarik, P.; Ceccone, G.; Kulisch, W.; Jelinek, M.; Apostolova, M. D.; Reithmaier, J. P.; Popov, C., *Applied Surface Science* **2014,** *297*, 95.
17.Ogwu, A. A.; Okpalugo, T. I.; Ali, N.; Maguire, P. D.; McLaughlin, J. A., *Journal of biomedical materials research. Part B, Applied biomaterials* **2008,** *85* (1), 105.
18.Jelínek, M.; Smetana, K.; Kocourek, T.; Dvořánková, B.; Zemek, J.; Remsa, J.; Luxbacher, T., *Materials Science and Engineering: B* **2010,** *169* (1–3), 89.
19.Tang, L.; Tsai, C.; Gerberich, W. W.; Kruckeberg, L.; Kania, D. R., *Biomaterials* **1995,** *16* (6), 483.
20.Ali, N.; Kousa, Y.; Gracio, J.; Cabral, G.; Sousa, A.; Shokufar, T.; Titus, E.; Madaleno, J. C.; Ahmed, W.; Jackson, M. J., 2016; pp 303.
21.Okpalugo, T. I. T.; Ogwu, A. A.; Maguire, P. D.; McLaughlin, J. A. D.; Hirst, D. G., *Diamond and Related Materials* **2004,** *13* (4-8), 1088.
22.Ryoo, S.-R.; Kim, Y.-K.; Kim, M.-H.; Min, D.-H., *ACS Nano* **2010,** *4* (11), 6587.
23.Steeves, A. J.; Atwal, A.; Schock, S. C.; Variola, F., *Journal of Materials Chemistry B* **2016,** *4* (18), 3145.
24.Hannan, R. T.; Peirce, S. M.; Barker, T. H., *ACS Biomaterials Science & Engineering* **2017**.
25.Wachesk, C. C.; Pires, C. A. F.; Ramos, B. C.; Trava-Airoldi, V. J.; Lobo, A. O.; Pacheco-Soares, C.; Marciano, F. R.; Da-Silva, N. S., *Applied Surface Science* **2013,** *266*, 176.
26.Almeida, C. N.; Ramos, B. C.; Da-Silva, N. S.; Pacheco-Soares, C.; Trava-Airoldi, V. J.; Lobo, A. O.; Marciano, F. R., *Applied Surface Science* **2013,** *275*, 258.
27.Tamada, Y.; Ikada, Y., *Journal of biomedical materials research* **1994,** *28* (7), 783.
28.Bociaga, D.; Kaminska, M.; Sobczyk-Guzenda, A.; Jastrzebski, K.; Swiatek, L.; Olejnik, A., *Diamond and Related Materials* **2016,** *67*, 41.
29.Dearnaley, G.; Arps, J. H., *Surface and Coatings Technology* **2005,** *200* (7), 2518.
30.Grinnell, F., *International Review of Cytology* **1978,** *53*, 65.

31.H. S. Tran, M. M. P. C. W. H. D. B. S. S. W. M. V. A. S. J. H. C. A. J., *Journal of Investigative Surgery* **1999,** *12* (3), 133.
32.Thampi, S.; Nandkumar, A. M.; Muthuvijayan, V.; Parameswaran, R., *ACS Applied Materials & Interfaces* **2017,** *9* (5), 4498.
33.Campoccia, D.; Montanaro, L.; Arciola, C. R., *Biomaterials* **2013,** *34* (34), 8533.
34.Myllymaa, K.; Levon, J.; Tiainen, V. M.; Myllymaa, S.; Soininen, A.; Korhonen, H.; Kaivosoja, E.; Lappalainen, R.; Konttinen, Y. T., *Colloids and surfaces. B, Biointerfaces* **2013,** *101*, 290.
35.Pierce, C. G.; Srinivasan, A.; Ramasubramanian, A. K.; López-Ribot, J. L., *Microbiology Spectrum* **2015,** *3* (3).
36.Coad, B. R.; Kidd, S. E.; Ellis, D. H.; Griesser, H. J., *Biotechnology Advances* **2014,** *32* (2), 296.
37.Szczesna-Antczak, M.; Kaczorowska, A.; Kaczorowski, W.; Antczak, T., *International Biodeterioration & Biodegradation* **2014,** *88*, 106.
38.Benincasa, M.; Pacor, S.; Wu, W.; Prato, M.; Bianco, A.; Gennaro, R., *ACS Nano* **2011,** *5* (1), 199.
39.Qi, X.; Poernomo, G.; Wang, K.; Chen, Y.; Chan-Park, M. B.; Xu, R.; Chang, M. W., *Nanoscale* **2011,** *3* (4), 1874.
40.Aslan, S.; Loebick, C. Z.; Kang, S.; Elimelech, M.; Pfefferle, L. D.; Van Tassel, P. R., *Nanoscale* **2010,** *2* (9), 1789.
41.Queiroz, J. R. C.; Fissmer, S. F.; Koga-Ito, C. Y.; Salvia, A. C. R. D.; Massi, M.; Sobrinho, A. S. d. S.; Júnior, L. N., *Journal of Prosthodontics* **2013,** *22* (6), 451.
42.Tang, S.-Y.; Zhang, W.; Soffe, R.; Nahavandi, S.; Shukla, R.; Khoshmanesh, K., *PLOS ONE* **2014,** *9* (8), e104109.
43.Walker, K.; Skelton, H.; Smith, K., *Journal of Cutaneous Pathology* **2002,** *29* (10), 616.
44.Liu, X.; Cao, Y.; Zhao, M.; Deng, J.; Li, X.; Li, D., *Nanoscale Res Lett* **2015,** *10* (1), 14.
45.Kumar, S.; Chatterjee, K., *ACS Applied Materials & Interfaces* **2016,** *8* (40), 26431.

Chapter VII

Conclusions and Future Work

This chapter includes the main conclusions reached in this thesis and proposes work to be developed in the future on carbon surface interactions with lipid model aggregates. A brief overview on the in vitro bioresponse towards carbon thin films, previously passivated with a lipid bilayer, is reported.

1. Conclusions

The main aim of this thesis was to contribute to a fundamental understanding of the origin of the outstanding bioresponse to amorphous carbon (a-C) thin films. In particular, the influence of the physico-chemical properties of carbon on a-C films interactions with model lipid aggregates was addressed. Moreover, the long-term bioresponse of a-C films was discussed and the anti-thrombogenic and anti-fungal behaviours of a-C films were also evaluated.

Amorphous carbon (a-C) and hydrogen doped amorphous carbon (a-C:H) were produced using a DC-magnetron sputtering chamber. Oxidised amorphous carbon (a-C:O) was obtained by carbon surface modification through an oxidative treatment. The physico-chemical properties of the three carbon surfaces were evaluated and discussed with regards to surface roughness, chemistry, wettability and charge density. Bulk modification of a-C films resulted in a a-C:H film with low graphitic content. Additionally, carbon surface oxidation (a-C:O) results in hydrophilic films with high density of negatively charge groups. Additionally, model lipid aggregates were produced and characterised with regards to the preparation method, type and nature of phospholipids present in the liposome and the ionic species in the buffer. Phosphatidylcholine (PC) and phosphatidylserine (PS) phospholipids were combined in 80:20 PC/PS liposomes and found to be electrostatically stable and homogeneously dispersed at all buffer conditions utilised in this work.

Investigation of PC/PS liposome adsorption on a-C surfaces was carried out by using a combination of *ex situ* and *in situ* techniques. Both the amount and mode of liposome adsorption at carbon surfaces were found to strongly correlate with carbon surface wettability and charge and buffer composition. *Ex-situ* results indicated that liposomes adsorb at a-C surfaces independent of the buffer being used. Liposome adsorption at a-C:O surfaces, however, is only observed when Ca^{2+} is added to the buffer. Further *in-situ* measurements confirm *ex-situ* observation and suggest that liposome adsorption on both a-C and a-C:O surfaces is made through intact vesicle adsorption at the interface, unless under conditions that promote liposome rupture.

Finally, the long-term bioresponse of carbon films was investigated by analysing cellular compatibility using endothelial and fibroblast cells. Cellular adhesion was found to be slightly reduced on a-C:O, when compared to a-C surfaces. Additionally, the anti-thrombogenic and anti-fungal behaviours of carbon films were also studied. Oxidised carbon showed a significant decrease in platelet and fungi adhesion, and in spreading when compared with a-C, which is attributed to the high hydrophilicity of a-C:O.

Carbon surface modification was found to be a good strategy to modulate the interactions of lipids, cells, fungi and platelets with carbon surfaces. The unique combination of high biocompatibility, anti-thrombogenic and anti-fungal behaviours displayed by carbon films reinforce the potential of carbon-based devices for biomedical applications.

2. Future Work

The successful integration of an implantable carbon material in biological media is strongly dependent on cellular interactions at carbon's interface, with long-term effects on the implant function and tissue regeneration. Lipids present in biological media are known to form a lipid conditioning layer (LCL) at the biomaterial's interface thus influencing further bioresponse towards carbon, including cellular adhesion and proliferation. Hence, understanding and modulating the interactions of cells with model lipid aggregates is key to ensure functionality and integration of the foreign material.

Preliminary investigation on the *in vitro* interaction of fibroblasts, from the *HFFF2* line, with a passivated lipid layer was performed and compared with previous *in vitro* results obtained on fibroblasts interacting with a-C surfaces (Chapter VI). Carbon films were prepared and characterised according to the procedures described on Chapter III. A passivated lipid layer at carbon surfaces was prepared according to Chapter V. Briefly, carbon surfaces were exposed to PC/PS liposome suspensions in PBS.$CaCl_2$ buffer for 1 h followed by surface rinsing and drying. As shown in Chapter V, the outcome result of such interaction on a-C and a-C:O surfaces is the formation of a SLB and a SLM, respectively.

The complex carbon/lipid layer was exposed to fibroblasts, from the *HFFF2* line, and the cellular adhesion, proliferation and morphology were analysed. Figure 7.1. shows

relative cell population adherent to carbon surfaces in the absence (solid bars) and presence (light bars) of a PC/PS lipid passivated layer; results are normalised against the control (C_{cell}) after 24 h of cell culture. All surfaces display a satisfactory cell viability comparable to the C_{cell}; the presence of a LCL does not seem to affect cellular adhesion at the interface.

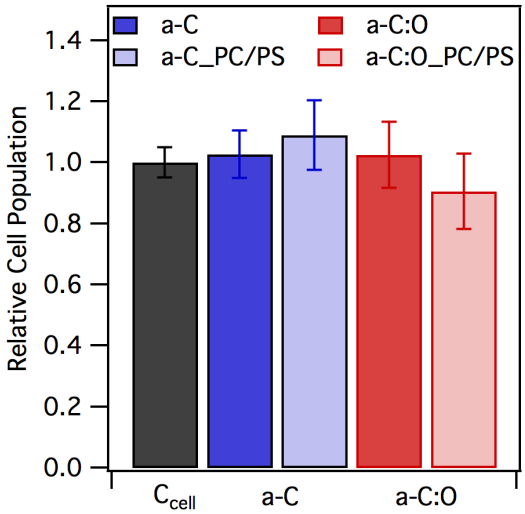


Figure 7.1. Relative population of *HFFF2* cells adherent at a-C and a-C:O surfaces, in the absence (solid bars) and presence (light bars) of a PC/PS lipid passivated layer. Results are shown comparative to control (C_{cell}) after 24 h of cell culture; values given as mean ± stdev.

Figure 7.2 shows the morphology of fibroblast cells adherent to carbon surfaces in the presence and absence of a PC/PS lipid passivated layer. Nucleus, F-actin cytoskeleton and primary antibody (pAB) were stained using DAPI, phalloidin and vinculin, respectively. As previously discussed in Chapter VI, the adhesion of *HFFF2* cells at a-C surfaces show elongated and flattened profiles, characteristic of a good adhesion at the solid surface. Interestingly, the complex carbon/lipid layer exhibit surface-dependent variations on the adhesion of *HFFF2* cells when compared to carbon surfaces. Similar to bare carbon surfaces, both carbon/LCL surfaces possess dash-like FAs confirming good cell adhesion and spreading at these surfaces. Nonetheless, numeric analysis on the FAs present on a-C/LCL and a-C:O/LCL surfaces yielded values ~5x and ~2x higher per unit cell, when comparing with a-C and a-C:O surfaces, respectively.

These results indicate that the cellular adhesion at carbon surfaces is similar to carbon/LCL complexes (Figure 7.1). However, the presence of a lipid passivated layer seems to promote the affinity of cells to carbon substrates, a result observed by the increase on the number of FAs at the surface. Further works will involve the investigation on the relation between liposome adsorption at carbon interfaces with the cellular long-term response, especially cellular viability and proliferation. A correlation of liposome adsorption and cellular response is expected to be stablished and extended to platelet, fungi and bacteria responses. Furthermore, the dynamics of liposome adsorption at carbon surfaces will be accessed by using *in-situ* QCM and used as a model for understanding the long-term cellular response and ultimately define the *in vivo* performance of carbon coatings.

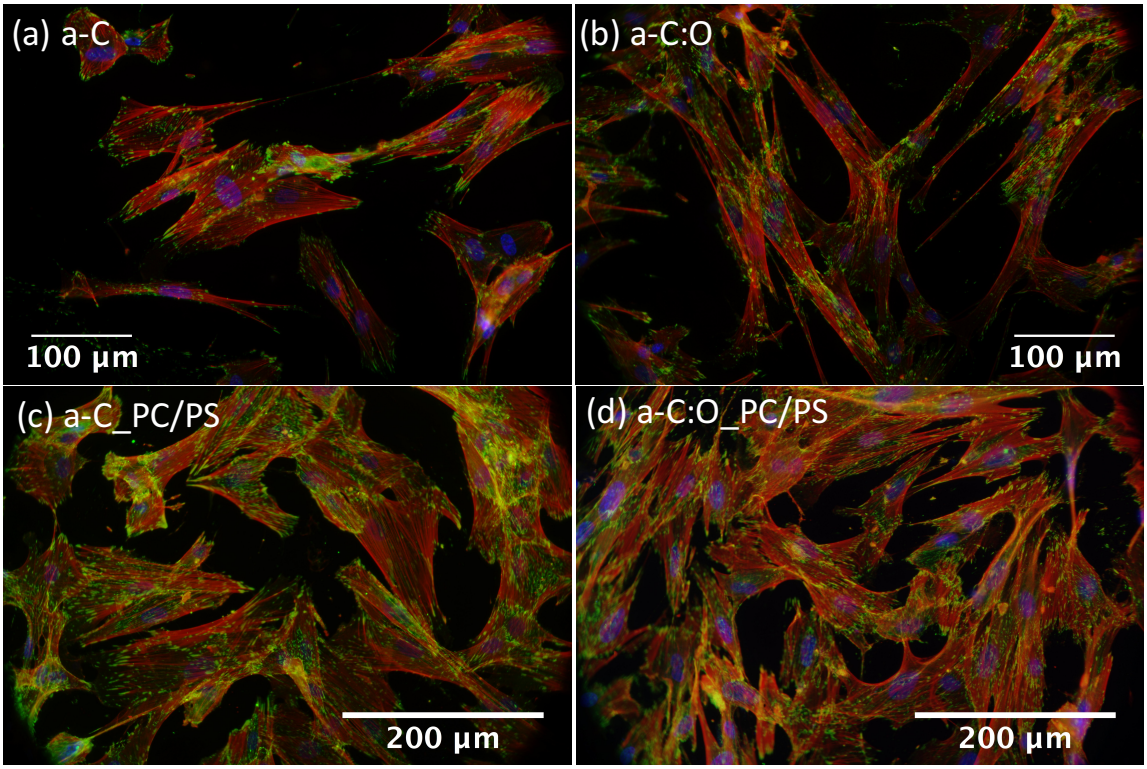


Figure 7.2. Overlap of fluorescence images of HFFF2 cells adherent to **(a)(c)** a-C and **(b)(d)** a-C:O surfaces without (a and b) and with (c and d) a PC/PS lipid passivated layer at carbon surfaces. Nucleus (blue) and F-actin cytoskeleton (red) were stained using DAPI and phalloidin, respectively. Primary antibody (pAb) is stained against vinculin (green).

Published Work

Research article

SURFACE and INTERFACE ANALYSIS

Received: 27 May 2016 Revised: 31 January 2017 Accepted: 14 February 2017 Published online in Wiley Online Library: 10 March 2017

(wileyonlinelibrary.com) DOI 10.1002/sia.6223

Determination of surface ζ-potential and isoelectric point of carbon surfaces using tracer particle suspensions

Joana M. Vasconcelos, Federico Zen, Serban N. Stamatin,† James A. Behan and Paula E. Colavita*

Carbon materials are widely used in a range of applications from biomaterials to sensing and electronics. Many of these applications rely on the ability to control carbon/water interfacial properties, in particular, surface charge density. This work reports a study of the electrokinetic properties of amorphous carbon thin films as a function of pH and surface chemistry. Surface ζ-potential (SZP) and isoelectric point were determined using the tracer particle method. Initially, the use of sulfonated and amine-terminated latex bead suspensions as tracer particles for the determination of SZP of reference polymer surfaces was validated. The tracer particle method was then applied to the determination of SZP and isoelectric point of macroscopic carbon surfaces with different surface chemistry. Highly graphitic and sp^3-rich hydrogenated carbon surfaces were found to display negative SZP, as expected for hydrophobic surfaces. The isoelectric point of the most highly graphitic surface was found to be pH_{iso} = 3.7. Surface oxidation of these films resulted in a decrease of SZP at all pH values and in a downshift of pH_{iso} to values lower than 1.5, consistently with the presence of surface acidic groups arising from oxidation. Results indicate that the specific choice of acid/base chemistry for the tracer particles does not significantly affect either SZP or pH_{iso} determinations. These results show that the tracer particle method in combination with widely available latex beads as tracers can be applied for the determination of carbon SZP as a function of pH. Copyright © 2017 John Wiley & Sons, Ltd.

Additional Supporting Information may be found online in the supporting information tab for this article.

Keywords: zeta potential; amorphous carbon; tracer particles; electro-osmosis; electrophoresis

Introduction

Carbon materials display a wide range of physicochemical, optical and electronic properties.[1,2] Nanomaterials such as nanodiamonds,[3,4] nanotubes,[5] graphene and C-dots[6] are the subject of intense study for vast number of applications such as biomaterials, sensing, electronics, therapeutics, catalysis, separation technologies and mechanical reinforcements.[7–9] Carbon in the form of coatings and thin-films has also gained great attention in the medical sector, specifically in biosensing, orthopaedic and cardiovascular fields[10,11] and in the electronics sector.[12–14] Many of the aforementioned applications rely on careful control of interfacial properties in order to modulate chemical/electrochemical reactivity or biological response.

Surface charge is one of the key properties that can determine rate and yield of surface reactions and the strength of interactions at carbon interfaces. Surface ζ-potential (SZP) measurements are common methods of monitoring the effect of chemical treatments and surface modifications on surface electrostatic charge,[15,16] isoelectric point and, indirectly, density of surface ionizable groups (e.g. –COOH, $–NH_2$). These measurements have a long history in the characterization of carbon nanomaterials and carbon particles, particularly because of the numerous applications of carbon particles as absorbers and carriers.[17–19] SZP measurements on particles or colloids rely on determinations of particle electrophoretic mobility in liquid suspensions, and several instrumentation platforms are currently available to carry out these determinations. SZP measurements on macroscopic surfaces, on the other hand, usually require specialized equipment that is not widely available. The preferred methods for macroscopic surfaces are based on determinations of streaming potential or electro-osmotic mobility using microchannels that are coated with the surface under investigation. In the first case, a pressure-driven flow through the micro channel leads to the establishment of a streaming potential that is proportional to SZP.[20] In the second case, an electric field is used to create an electro-osmotic flow in a coated microchannel, and the electro-osmotic mobility is then related to SZP. Kirby and Hasselbrink[21] have previously reviewed this family of electrokinetic methods with particular emphasis on polymeric materials for microfluidics. However, to the best of our knowledge, there are only few reports of the use of these techniques on amorphous carbon coatings in the scientific literature.[17,22–24]

* *Correspondence to: Paula E. Colavita, School of Chemistry, Centre for Research on Adaptive Nanostructures and Nanodevices (CRANN) and AMBER Research Centre, Trinity College Dublin, College Green, Dublin 2, Ireland. E-mail: colavitp@tcd.ie*

† *The present address of author Serban N Stamatin is Heyrovsky Institute of Physical Chemistry of the CAS, Prague, Czech Republic.*

School of Chemistry, Centre for Research on Adaptive Nanostructures and Nanodevices (CRANN) and AMBER Research Centre, Trinity College Dublin, College Green, Dublin 2, Ireland

Copyright © 2017 John Wiley & Sons, Ltd.

An alternative to measurements on coated microchannels consists of measuring the mobility of tracer particles of known ζ-potential in close proximity of the surface that is the object of characterization. Tracer particle methods were used by Yan *et al.*[25] in order to measure surface and particle ζ-potential simultaneously. Recently, Corbett *et al.*[26–28] developed a protocol based on tracer particles to determine the ζ-potential of macroscopic solid surfaces, which is briefly described in the experimental methods section. This method is advantageous as it allows for the measurement of ζ-potential of a macroscopic surface on the same instrumentation platform used to measure ζ-potential of particles and bypasses many of the challenges of microchannel measurements. However, despite its potential as a rapid and cost effective approach to ζ-potential determinations, there are few protocols that establish criteria for tracer particle selection and preparation. More specifically, there are no published protocols for the selection and preparation of tracer particles for pH-dependent measurements of SZP, which are necessary for the determination of surface isoelectric points. Finally, there is no information on whether particle surface chemistry influences measured values; this is important for surfaces such as carbon, which can display a wide range of chemical functionalities and/or chemisorption sites.

In this work, a protocol for the application of the tracer particle method to the determination of SZP and isoelectric point of carbon surfaces as a function of pH is reported. The use of sulfonated (SL) and amine-terminated (AL) latex bead as tracer particles was investigated. These particles possess colloidal stability over a wide pH range and are commercially available to all researchers interested in carrying out ζ-potential measurements with this method. Initially, the use of these particle suspensions was validated using standard polymeric surfaces, and then application to the determination of SZP and isoelectric point of macroscopic carbon surfaces was demonstrated. The method was found to be sensitive to chemical changes at the carbon surface and was effective at establishing isoelectric points, an important requirement for understanding the behaviour of macroscopic carbon surfaces in aqueous media.

Experimental methods

Chemicals and materials

Hydrochloric acid (37%), sodium hydroxide, isopropyl alcohol, sulfuric acid (95–97%), hydrogen peroxide (30%), methanol (semiconductor grade) and phosphate buffer saline (PBS) were purchased from Sigma Aldrich; all were used without further purification. Millipore water (>18 MΩ) was used for all experiments. Si wafers (MicroChemicals), polyester transparency films (3 M), nylon 6,6 sheets (Goodfellow) and polytetrafluoroethylene (PTFE) sheets were sonicated in isopropyl alcohol for 10 min prior to further use as substrate materials. Standard Ø 300 nm latex tracer particles suspensions, 1 mM NaCl, pH 9.2 were purchased from Malvern (DTS1235). Sulfate latex (SL) beads (8% *w/v*, Ø 0.5 μm) and aliphatic amine latex (AL) beads (2% *w/v*, Ø 0.4 μm) were purchased from Life Technologies.

Preparation of tracer particle suspensions

Suspensions of sulfonated latex beads (50×10^{-6} *v*/v) and amine-terminated latex beads (50×10^{-6} *v*/v) were prepared in 100 μM PBS solution containing 1.37 mM NaCl and 27 μM KCl. A range of solutions with pH 4.5–8.5 were prepared for studies of ζ-potential as a function of pH; HCl and NaOH were used to adjust the pH of the PBS buffer to the desired value. The ionic strength remained at 1.80 ± 0.15 mM for all studies where pH was monitored.

Surface preparation

A DC-magnetron sputtering chamber (Torr International, Inc.) was used to deposit amorphous carbon (a-C) films at a base pressure of $\leq 2 \times 10^{-6}$ mbar and a deposition Ar pressure of 7×10^{-3} mbar, as previously described.[29] Hydrogenated amorphous carbon (a-C:H) films were prepared using a H_2/Ar gas mixture (10% H_2, 90% Ar) as previously described. Oxidized amorphous carbon (a-C:O) was prepared by oxidation of a-C surfaces under a UV lamp for 2 h in air, a well-established oxidation method for carbon coatings and nanomaterials.[30,31]

Characterization methods

X-ray photoelectron spectroscopy (XPS) characterization was performed using an Omicron ultrahigh vacuum system (1×10^{-10} mbar base pressure) equipped with a monochromated Al Kα source (1486.6 eV) and a multichannel array detector. Spectra were recorded at 45° take-off angle. Peaks were fitted to Voigt functions after Shirley background correction using Casa XPS software; atomic ratios were obtained from area ratios using relative sensitivity factors (C = 1.00; O = 2.93). Atomic force microscopy (Asylum Research) imaging was performed in tapping mode (1 Hz and 512 scan lines) using Au-coated silicon cantilevers with nominal spring constant in the range 1.45–15.1 N m^{-1} (NT-MDT). Spectroscopic ellipsometry measurements of amorphous carbon surfaces were performed using a J.A. Woolam Co. Inc. alpha-SE™ ellipsometer; data were modelled using CompleteEASE™ software as discussed in the Supporting Information.[32] Dynamic light scattering (DLS) and ζ-potential measurements were carried out using a Malvern Zetasizer Nano-ZS, λ = 633 nm He–Ne laser; the signal was detected at 173° and 13° for DLS and ζ-potential measurements, respectively. Hydrodynamic size was determined using a refractive index n = 1.59 for latex.[33] Particle ζ-potential was obtained using the same instrument, which determines particle velocity and mobility via phase analysis light scattering[26]; solution conditions were optimized as described hereafter.

Tracer particle suspensions and determinations of Surface ζ-potential

The tracer particle method for measuring the SZP of a static macroscopic surface requires the use of a suspension of narrowly dispersed particles with well-defined SZP. This method has been previously described by Corbett *et al.*[26]; briefly, the velocity of the tracer particles under the effect of an AC field is measured via phase analysis light scattering after positioning the surface under characterization at progressively greater distances from the probed volume. The velocity of the tracer particles at each position is the result of the sum of the particle electrophoretic migration, and of the electro-osmotic flow in the proximity of the solid/liquid interface. As the probing volume is positioned further away from the surface, the effect of electro-osmotic flow decreases until the observed mobility becomes only the result of electrophoretic migration. The apparent ζ-potential is calculated from each mobility measurement using equation $\zeta = \mu_{eo}\eta/\varepsilon$, where μ_{eo} is the electroosmotic mobility, ε is the permittivity and η is the solution viscosity.[26] Values obtained are plotted *versus* surface displacement, and the SZP is obtained

Copyright © 2017 John Wiley & Sons, Ltd.

from extrapolation to zero-displacement; the contribution arising exclusively from the surface ($\zeta_{surface}$) is calculated from the intercept as in Eqn (1):

$$\zeta_{surface} = -\boldsymbol{intercept} + \zeta_{particle} \quad (1)$$

An example of this procedure is shown in Fig. 2.

Surface ζ-potential measurements were performed using a SZP cell (Malvern Instruments). Mobility determinations were conducted at 125, 250, 375, 500 and 1000 μm displacements from the sample surface. Thin film samples were prepared with the dimensions of 4 × 4 mm to fit the cell sample holder. SL and AL beads were used as tracer particles in suspensions containing 100 μM PBS buffer (1.37 mM NaCl and 27 μM KCl) of total ionic strength 1.80 ± 0.15 mM at all pH values studied. A buffered suspension at pH = 7.4 was prepared first, and pH was varied via addition of HCl or NaOH as appropriate; the error bar for the ionic strength reflects the range of variation introduced by the pH adjustment process. The conductivity of the suspension was optimized for values in the range 200–300 μS/cm; values above this range were found to lead to electrochemical degradation of cell electrodes or of the beads and were found to result in large deviations in calculated SZPs. Error bars indicate standard deviations calculated from three measurements on each sample.

Results

Characterization of particle suspensions

The tracer particle method was used to investigate the SZP of thin films as a function of pH. Two different tracer particle suspensions were used for this purpose, SL and aliphatic AL beads, which are terminated with $-SO_3H$ and $-NH_2$ groups, respectively.

Figure 1a shows the hydrodynamic size of SL and AL beads as a function of pH, obtained from DLS measurements. The hydrodynamic size of SL beads remains constant as a function of pH, and the average value was found to be 582 ± 3 nm, indicating that the average hydrodynamic size is only marginally higher than the nominal diameter under the experimental conditions. AL beads also exhibit an approximately constant hydrodynamic diameter with average value of 553 ± 11 nm. These results indicate that both SL and AL bead suspensions are stable and do not aggregate or sediment over the pH range of 4.5–8.5.

Figure 1b shows the SZP of SL and AL particles as a function of pH, at a constant total ionic strength of 1.80 mM. The ζ-potential of SL beads remains at approximately −80 mV at all pH values, which is consistent with the presence of $-SO_3H$ groups at the particle surface that are acidic with $pK_a < 2$. The results for SL particles are in agreement with those reported by Thielbeer *et al.*[34] who compared the ζ-potential of microparticles with different surface functional groups. AL beads display positive ζ-potential values, which range from a maximum value of 50.5 ± 1.0 mV at pH 4.5 to approximately 5 mV at pH 8.3; a linear extrapolation of the results to the pH-axis yields an estimate of pH_{iso} of 8.8. Cros *et al.* showed ζ-potential measurements of aminated ($-NH_2$) latex particles (10 mM NaCl) as a function of pH and found that for acidic pH the particles show a stable ζ-potential of 60 mV that decreases to 0 mV at pH ~ 9.[35] The results presented here are in good agreement with the aforementioned study and indicate that AL beads are stable in acidic media and that they possess an isoelectric point of 8.8.

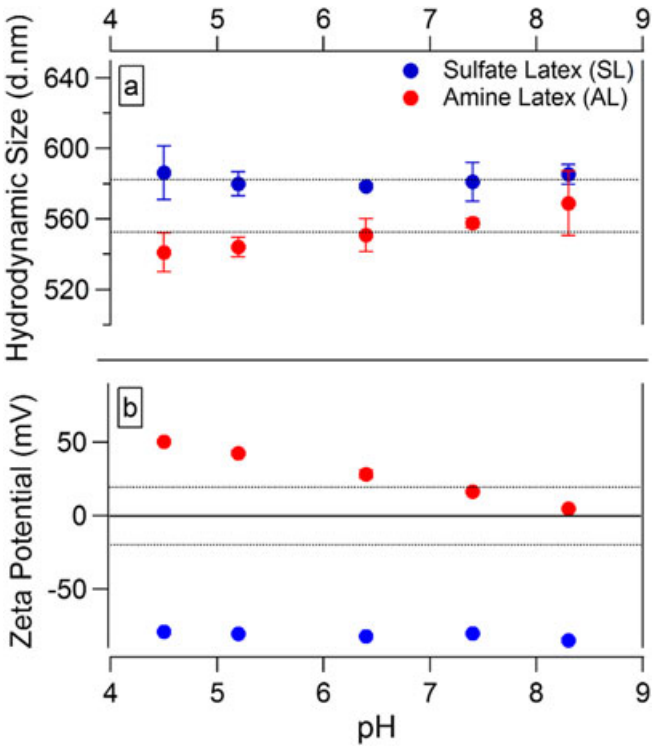


Figure 1. (a) Hydrodynamic size and (b) ζ-potential of sulfate latex (SL) and amine latex (AL) beads used as tracer particles for surface ζ-potential measurements. SL and AL beads were suspended in 100 μM phosphate buffer saline buffer (1.37 mM NaCl and 27 μM KCl) with total ionic strength of 1.80 ± 0.15 mM for all pH values studied. [Colour figure can be viewed at wileyonlinelibrary.com]

Characterization of nylon and polytetrafluoroethylene surfaces using tracer particles

To confirm that the tracer particle suspensions could be applied to SZP determinations as a function of pH, we investigated the performance of latex bead suspensions in the determination of the SZP of two standard polymeric surfaces: nylon 6,6 and PTFE. Figure 2 shows an example of a SZP measurement on nylon 6,6, using SL

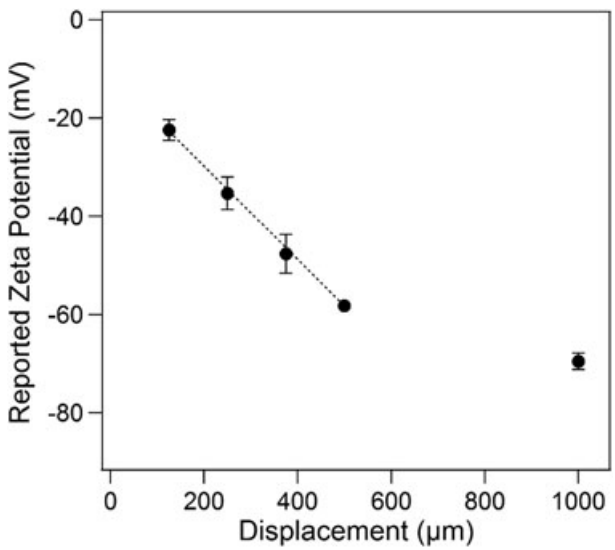


Figure 2. Plot of apparent ζ-potential as a function of surface displacement obtained for nylon 6,6 as a static surface using sulfate latex beads in 100 μM phosphate buffer saline buffer (pH 7.5) as tracer particles.

 Copyright © 2017 John Wiley & Sons, Ltd.

beads as tracer particles, suspended in a 100 μM PBS buffer at pH 7.5. The plot shows the reported ζ-potential – calculated from the measured mobility of the tracer particles – as a function of surface displacement. The intercept (Eq. 2) is obtained via linear extrapolation of the reported ζ-potential, excluding the value obtained at 1000 μm, for which the apparent ζ-potential matches that in bulk suspensions.[26]

Figure 3 displays the SZP ($\zeta_{surface}$) of PTFE and nylon 6,6 obtained using SL beads as tracers, over the pH range 4–7; SZP values normalized by counterion concentration (pC) are also reported on the right-hand axis to facilitate comparison with literature data. PTFE and nylon 6,6 show similar SZP at all pH values that compare well to those reported in literature (see below)[21,36]: Values were found to decrease from approximately −20 mV at pH 4.4 to less than −50 mV for pH 6.7. Extrapolation to the *x*-axis yielded an estimate of pH_{iso} of 3.7 and 3.4 for nylon and PTFE, respectively. Results obtained with SL tracer particles are similar to reports of ζ-potential for nylon and PTFE obtained via streaming potential determinations in the literature. Kirby *et al.*[21] published a review of SZP determinations for common polymeric substrates using microchannel methods at various pH and ionic strength values, which allows for a comparison with tracer particle SZP determinations. For instance, Rendall *et al.*[36] similar SZP for pC = 2.0–4.0 in the pH range of our study. Werner *et al.*[15] studied the influence of pC on the SZP of flat solid surfaces and reported SZP/pC ratios for PTFE substrates that are comparable with those shown in Fig. 3. Therefore, the tracer particle method in combination with latex bead suspensions appears to offer a satisfactory protocol for the determination of SZP of macroscopic surfaces.

Characterization of amorphous carbon films

Many of the applications of amorphous carbon films and coatings rely on the ability to control carbon interfacial properties and, in particular, surface charge density. SZP measurements using tracer particles were performed on three different amorphous carbon surfaces, a-C, a-C:H and a-C:O, all of which were fabricated in our lab as described in the experimental methods section.

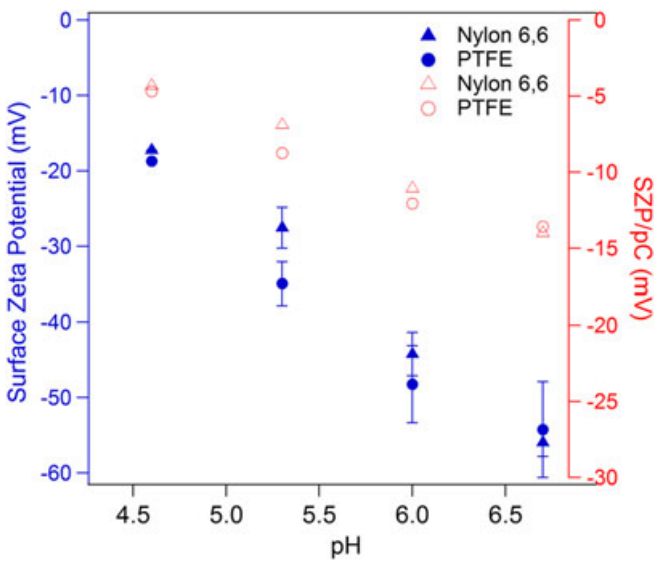


Figure 3. Surface ζ-potential measurements of nylon 6,6 and polytetrafluoroethylene (PTFE) surfaces (blue data points) using sulfate latex (SL) beads as tracer particles. SL beads were suspended in 100 μM phosphate buffer saline buffer (1.37 mM NaCl and 27 μM KCl), and the ionic strength remained at 1.80 ± 0.15 mM for all pH studied (pC = 2.82). Surface ζ-potential values were normalized by the counterion concentration (pC) for both polymers (red data points). [Colour figure can be viewed at wileyonlinelibrary.com]

Amorphous carbon films used for our experiments are relatively smooth and featureless, as shown by SEM imaging (Supporting Information). Atomic force microscopy measurements (Fig. 4) yielded root mean square roughness values for a-C, a-C:H and a-C:O of (0.94 ± 0.03) nm, (1.16 ± 0.08) nm and (0.86 ± 0.07) nm, respectively, in good agreement with previous determinations on sputtered carbon films.[37,38] The electronic properties of these films were characterized via spectroscopic ellipsometry as described in the Supporting Information. Optical constants determined from ellipsometry data for a-C and a-C:H films were used to calculate the absorption coefficient and subsequently determine the Tauc gap (E_T) of the amorphous carbon. Average E_T values were found to be 0.66 ± 0.01 eV and 1.77 ± 0.01 eV for a-C and a-C:H, respectively (95% CI), thus confirming that a-C has a greater metallic character than a-C:H. This indicates that a-C films possess a higher graphitic content, in agreement with materials deposited using similar protocols[29] and with XPS results in this work (see succeeding texts). a-C:O films are the result of a surface oxidation of a-C; therefore, spectroscopic ellipsometry was used to determine the thickness of the oxidized layer (Supporting Information), which was found to be 2.8 ± 0.2 nm.

The surface chemistry of these three carbon materials was studied via XPS characterization. Figure 5 shows the C 1 s spectra of a-C, a-C:H and a-C:O surfaces; all three display a main asymmetric peak characteristic of amorphous carbon. The main C 1s peak of a-C and a-C:O was satisfactorily fitted with two main contributions at 284.4 and 285.1 eV attributed to trigonally (sp^2) and tetrahedrally (sp^3) bonded carbon (C–C), respectively. Only the sp^3 contribution was necessary to obtain a satisfactory fit for a-C:H surfaces, thus confirming that this surface is rich in sp^3 centres. This finding is in agreement with previous work,[29] which had shown that the introduction of hydrogen in the carbon scaffold occurs mainly via formation of C–H bonds, as shown in greater detail in the Supporting Information. The fraction of graphitic carbon can be estimated from the $A_{284}/A_{285+284}$ area ratios to be 85%, 82% and 0% for a-C, a-C:O and a-C:H, respectively. a-C and, to a greater extent, a-C:O also show contributions at high binding energy (286–288 eV) that arise from the presence of oxidized groups (C–O, C=O). In the case of a-C:O, a contribution at 288.7 eV indicates the presence of carboxyl groups as a result of the oxidation process.[39] The oxygen content of the three carbon materials was obtained from fits of the O 1 s peak at 532 eV (data not shown). The peak area ratio A_{O1s}/A_{C1s} corrected by relative sensitivity factors yielded O/C at% contents of 5%, 8% and 20% for a-C:H, a-C and a-C:O, respectively. The high O/C content observed for a-C:O is consistent with the sample having undergone oxidative treatment. In summary, XPS results indicate that the three carbon surfaces chosen for our studies display significantly different properties, in particular the materials were found to have increasing graphitic content in the order a-C:H < a-C:O < a-C. They were also found to have increasing density of oxidized groups in the order a-C:H < a-C < a-C:O.

Differences in carbon surface chemistry also resulted in changes in wetting behaviour. Static water contact angle measurements were carried out on a-C, a-C:H and a-C:O surfaces yielding values of (35.2 ± 2.9)°,[32] (46.6 ± 2.6)° and (3.2 ± 0.4)°, respectively. Values obtained for a-C and a-C:H are in good agreement with previous determinations on similarly deposited carbon thin films.[40,41] The oxidation process increases surface hydrophilicity, as expected on the basis of the presence of oxidized groups as determined via XPS.

Copyright © 2017 John Wiley & Sons, Ltd.

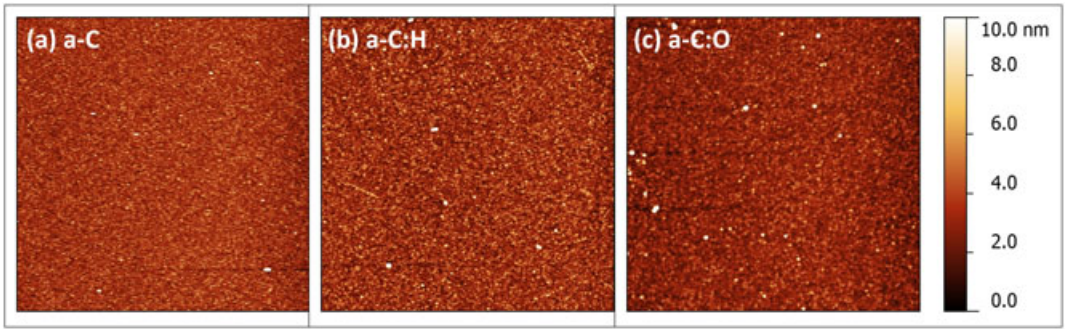


Figure 4. 10 × 10 μm atomic force microscopy topographic images of (a) a-C, (b) a-C:H and (c) a-C:O surfaces. Surfaces roughness values were obtained from height profile determinations. [Colour figure can be viewed at wileyonlinelibrary.com]

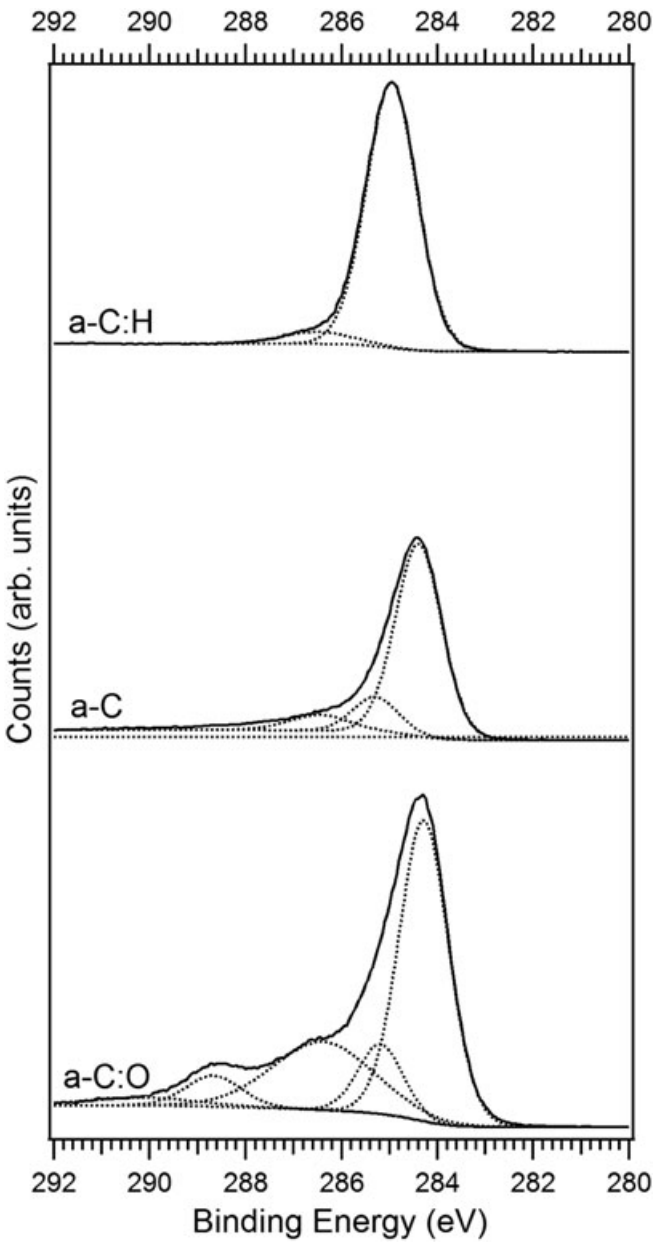


Figure 5. X-ray photoelectron spectroscopy spectra of a-C:H, a-C and a-C:O in the C 1s region; Shirley background and individual contributions are shown under each curve.

The SZP of the three carbon surfaces was determined via mobility determinations of tracer particles. In order to understand whether tracer particle chemistry can potentially affect the observed SZP, pH-dependent studies were carried out using both SL and AL particles, which possess ionizable groups with different acid–base chemistry. Figure 6 shows a summary of SZP values for a-C, a-C:H and a-C:O surfaces obtained with SL (blue) and AL (red) particles as a function of pH. The most graphitic surface, a-C, displays SZP values of −51 ± 2 and −63 ± 5 mV at pH 7.4 using SL and AL suspensions, respectively; the SZP value increases with decreasing pH to −25 mV at pH 4.4. Extrapolation to the pH-axis yielded an estimate of pH_{iso} for a-C of 3.0 and 3.7 when SL and AL beads were used, respectively. In the case of a-C:H surfaces, it appears more difficult to identify a clear trend in SZP *versus* pH, and a determination of isoelectric points was not attempted. SZP values for a-C:H were found to be in general more positive than those observed for a-C under the same conditions; for instance, the SZP of a-C:H was found to be −45 ± 4 mV at pH 7.4. Finally, surface modification with UV treatment led to more negative SZP values at all pH's when compared with the pristine a-C surface; for instance, at pH 7.4, a-C:O surfaces yielded SZP values of −61 ± 4 and −75 ± 2 mV with SL and AL beads, respectively. Even at acidic pH, a-C:O surfaces were found to have the most negative SZP values among the three surfaces examined; an extrapolation to the pH-axis yielded a $pH_{iso} < 1.5$, which is consistent with the presence of acidic groups at the surface determined via XPS.

a-C and a-C:H were found to display negative SZP at all pH values studied, despite these carbon surfaces having a negligible amount of ionizable groups observable via XPS; moreover, in the case of a-C, we were able to determine pH_{iso} in the range 3.0–3.7. There are no available published values for SZP of sputtered a-C and a-C:H as a function of pH to which our results can be directly compared. However, our experimental values are in excellent agreement with published SZP determinations of other carbon surfaces with similar properties obtained using microchannel methods. Jelínek *et al.*[23] studied diamond-like carbon (DLC) thin films and observed a similar SZP as that of a-C in Fig. 6 and $pH_{iso} = 3.7$, which is identical to that obtained in this work using the tracer particle method. Nitta *et al.*[17] reported negative SZP for DLC thin films independently of the degree of oxidation. Finally, Voss *et al.*[24] also observed negative SZP for a diamond/a-C composite film at pH > 4, in agreement with our observations.

Negative SZP values are often ascribed to the presence of negatively charged surface groups; however, this is not the only potential mechanism of charge build-up at the solid-aqueous interface. Although it is not possible to exclude the presence of a small

 Copyright © 2017 John Wiley & Sons, Ltd.

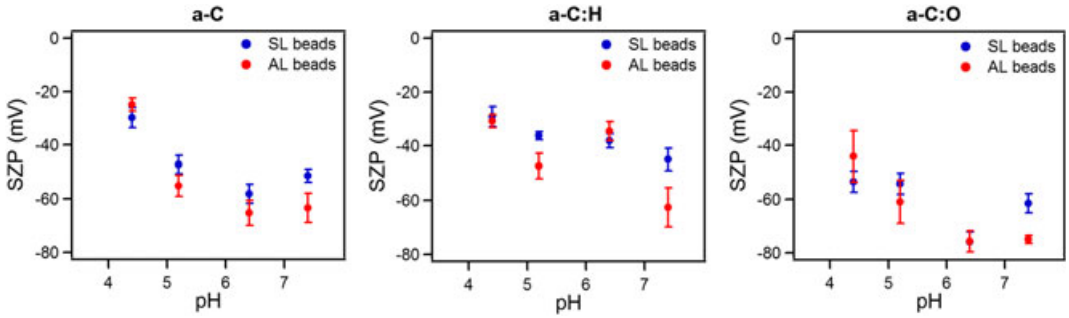


Figure 6. Surface ζ-Potential of a-C, a-C:H and a-C:O surfaces obtained using sulfate latex (SL) (blue) and amine latex (AL) (red) beads as tracer particles, suspended in 100 μM phosphate buffer saline buffer, 1.80 ± 0.15 mM ionic strength, for all pH values studied. [Colour figure can be viewed at wileyonlinelibrary.com]

amount of amphoteric –OH groups at a-C or a-C:H surfaces, these groups are not likely to give rise to negative SZP values over the pH range explored. The observations of (i) pH_{iso} between 3 and 4 for a-C surfaces, (ii) a relatively hydrophobic character for a-C and a-C:H surfaces and (iii) the absence of a significant surface density of acidic groups suggest that the negative SZP is instead attributable to asymmetric adsorption of hydroxide and hydronium ions at the solid-electrolyte interface. It is now well established that for hydrophobic surfaces, even in the absence of ionizable groups, the SZP in aqueous solutions is usually negative at pH > 4. This observation has a long history in the literature of electrokinetic measurements (19th century)[42,43]; however, it is only relatively recently that a physical model has emerged to explain this behaviour. Negative SZP at hydrophobic surfaces is attributed to the preferential adsorption of hydroxide ions at the solid surface. Hydroxide adsorption has been confirmed via simulations[44–46] and experimental determinations, for instance at polymer surfaces,[42,47] at hydrophobic self-assembled monolayers[48] and at diamond surfaces.[24,49,50] In the specific case of hydrophobic carbon materials, several recent reports have confirmed hydroxide adsorption. Härtl *et al.*[50] reported streaming potential measurements of H-terminated diamond yielding a pH_{iso} in the range 3–4; complementary surface conductivity measurements and simulations demonstrated that this can be attributed to the asymmetric adsorption of OH^- and H_3O^+ ions. Our results on a-C and a-C:H suggest that hydroxide ion adsorption is likely to be the dominant effect, given the absence of acidic groups at theses surfaces, thus yielding negative SZP, and pH_{iso} values similar to those observed at other carbon hydrophobic interfaces under similar conditions.

Surface ζ-potential results for a-C:O, the oxidized form of a-C, indicate that oxidation leads to more negative SZP values at all pH and to a decrease in isoelectric point. This is consistent with XPS results, which indicate that a-C:O possesses carboxylic groups, which are expected to impart greater surface acidity and increase the density of negative charges when deprotonated. Our results for a-C:O are also in good agreement with SZP and pH_{iso} values reported previously by our group and others for oxidized carbon particles.[18,19] Moreno-Castilla *et al.*[19] studied the effect of surface treatments on the SZP of carbon particles; they reported pH_{iso} in the range 3–4 after activation and $pH_{iso} < 2$ after oxidative treatments. Previous literature on SZP of carbon coatings is also in agreement with results presented in this work. Nitta *et al.*[17] showed a decrease in SZP for DLC films, reporting SZP values of −26 mV for a-C *versus* −50 mV for a-C:O at pH 5.8. Härtl *et al.*[50] reported a $pH_{iso} < 1.5$ at O-terminated diamond surfaces, in good agreement with the pH_{iso} of a-C:O surfaces presented in this work. Finally, Chakrapani *et al.*[49] showed how oxidation of diamond surfaces results in $pH_{iso} = 1$. In all cases, the SZP trends were attributed to the dominant effect of acidic O-containing surface groups that are created via oxidative processes.

Surface ζ-potential values obtained with SL and AL were found to display similar trends *versus* pH and only small differences at each of the pH values examined. This indicates that repulsive/attractive electrostatic interactions or acid/base interactions between the static surface and the tracer particles do not affect SZP determinations under the conditions used in our studies. Interestingly, the greatest divergence between SL and AL SZP values is observed at pH 7.4. This effect could be because AL particles possess a ζ-potential at pH 7.4 at the margin of colloidal stability, thus suggesting that this is a limiting pH for the application of AL suspensions as tracers. Beyond colloidal stability, it is worth mentioning that AL beads are chemically less stable than SL beads as amine groups oxidize when exposed to air. AL beads were found to yield more negative particle SZP values than those reported in Fig. 1 when measured after 30 days of storage. However, SZP determinations of carbon surfaces remained similar to those obtained with fresh AL suspensions, as long as the value chosen for the subtraction in Eqn (1) was the value obtained at 1000 μm displacement.

Conclusions

In this work, we focused on establishing, first, whether pH-dependent SZP determinations using the tracer particle method in combination with commercially available particle suspensions are comparable with those obtained with traditional streaming potential methods. We tackled this objective by measuring ζ-potential and isoelectric points of standard polymeric substrates and, indeed, found that results were comparable with reference values reported in the literature, thus confirming the applicability of the protocol.

Second, we investigated the tracer particle method for the characterization of carbon surfaces. Carbon coatings such as the ones investigated in this work are of relevance for applications in biomaterials, diagnostics and biosensing, and ζ-potential determinations are essential to understand their interactions with biomolecules, cells and organisms. Our results are the first determinations of pH-dependent ζ-potential and isoelectric points for sputtered carbon films; we present results for carbon with three different types of surface termination/chemistry: graphitic, hydrogenated and oxidized. We show that the two most hydrophobic surfaces display negative ζ-potential values over the range pH = 4–7; in the case of graphitic surfaces, the isoelectric point could be determined to

Copyright © 2017 John Wiley & Sons, Ltd.

be at pH < 4. These results are consistent with the ζ-potential being dominated by the asymmetric adsorption of hydroxide ions, a common finding for hydrophobic surfaces that is in agreement with prior electrokinetic results obtained on diamond materials. In the case of oxidation, we found that the presence of acidic ionizable groups leads to a significant lowering, with respect to the non-oxidized surface, of both the ζ-potential and the isoelectric point.

Finally, to the best of our knowledge, there is no information currently in the literature on whether the tracer particle chemistry might affect ζ-potential and isoelectric point determinations. This is an important issue in the case of carbon materials, as these can display a wide range of chemical groups and acid/base behaviour. In this work, we tackled this problem by carrying out measurements using suspensions of tracer particles that possess terminal groups at the two extremes of the basicity/acidity spectrum: strong acid (–SO_3H) and basic (–NH_2). Furthermore, we carried out measurements with carbon materials bearing both hydrophobic and acidic groups. Results obtained with the two types of tracer particles were found to be similar in trends and values, thus indicating that SZP determinations are not affected by the acid–base chemistry or the electrostatic interactions between the solid surface and the particle surface under our experimental conditions. However, sulfonic acid groups are more stable towards ambient oxidation than amine groups, and the corresponding suspensions possess greater SZP stability over time. We believe these results to be of interest for expanding applications of the tracer particle method to other surfaces with complex chemistry.

Acknowledgements

This publication has emanated from research conducted with the financial support of Science Foundation Ireland under Grant No. 12/IP/1273. SNS gratefully acknowledges support by SFI Grant No. 13/CDA/2213. JAB acknowledges support from grant GOIPG/2014/399. Use of the XPS of I. V. Shvets and C. McGuinness provided under SFI Equipment Infrastructure funds. The authors are grateful to S. Mills, Dr Esteban-Tejeda and Mr R. Cullen for support with instrumentation.

References

[1] S. R. P. Silva, G. A. J. Amaratunga, C. P. Constantinou, *J. Appl. Phys.*, **1992**, *72*, 1149.
[2] J. Robertson, *Surf. Coat. Technol.*, **1992**, *50*, 185.
[3] A. S. Barnard, *Analyst*, **2009**, *134*, 1751.
[4] O. Faklaris, V. Joshi, T. Irinopoulou, P. Tauc, M. Sennour, H. Girard, C. Gesset, J. C. Arnault, A. Thorel, J. P. Boudou, P. A. Curmi, F. Treussart, *ACS Nano*, **2009**, *3*, 3955.
[5] F. Liang, B. Chen, *Curr. Med. Chem.*, **2010**, *17*, 10.
[6] S. K. Bhunia, A. Saha, A. R. Maity, S. C. Ray, N. R. Jana, *Sci. Rep.*, **2013**, *3*, 1473.
[7] Y.-P. Sun, B. Zhou, Y. Lin, W. Wang, K. A. S. Fernando, P. Pathak, M. J. Meziani, B. A. Harruff, X. Wang, H. Wang, P. G. Luo, H. Yang, M. E. Kose, B. Chen, L. M. Veca, S.-Y. Xie, *J. Am. Chem. Soc.*, **2006**, *128*, 7756.
[8] A. K. Geim, K. S. Novoselov, *Nat. Mater.*, **2007**, *6*, 183.
[9] M. F. L. De Volder, S. H. Tawfick, R. H. Baughman, A. J. Hart, *Science*, **2013**, *339*, 535.
[10] R. K. Roy, K. R. Lee, J. Biomed, *Mater. Res., Part B*, **2007**, *83*, 72.
[11] M. Stüber, L. Niederberger, F. Danneil, H. Leiste, S. Ulrich, A. Welle, M. Marin, H. Fischer, *Adv. Eng. Mater.*, **2007**, *9*, 1114.
[12] L. An, Q. Fu, C. Lu, J. Liu, *J. Am. Chem. Soc.*, **2004**, *126*, 10520.
[13] K. Balasubramanian, R. Sordan, M. Burghard, K. Kern, *Nano Lett.*, **2004**, *4*, 827.
[14] J. Robertson, *Mater. Sci. Eng., R*, **2002**, *37*, 129.
[15] C. Werner, H. Körber, R. Zimmermann, S. Dukhin, H.-J. Jacobasch, J. Colloid Interface, *Sci.*, **1998**, *208*, 329.
[16] C. Werner, H. J. Jacobasch, *Int. J. Artif. Organs*, **1999**, *22*, 160.
[17] Y. Nitta, K. Okamoto, T. Nakatani, H. Hoshi, A. Homma, E. Tatsumi, Y. Taenaka, *Diamond Relat. Mater.*, **2008**, *17*, 1972.
[18] P. Duffy, L. M. Magno, R. B. Yadav, S. K. Roberts, A. D. Ward, S. W. Botchway, P. E. Colavita, S. J. Quinn, *J. Mater. Chem.*, **2012**, *22*, 432.
[19] C. Moreno-Castilla, M. A. Ferro-Garcia, J. P. Joly, I. Bautista-Toledo, F. Carrasco-Marin, J. Rivera-Utrilla, *Langmuir*, **1995**, *11*, 4386.
[20] A. V. Delgado, F. Gonzalez-Caballero, R. J. Hunter, L. K. Koopal, J. Lyklema, *J. Colloid Interface Sci.*, **2007**, *309*, 194.
[21] B. J. Kirby, E. F. Hasselbrink Jr., *Electrophoresis*, **2004**, *25*, 203.
[22] T. Nakatani, Y. Nitta, K. Okamoto, A. Mochizuki, *J. Photopolym. Sci. Technol.*, **2009**, *22*, 455.
[23] M. Jelínek, K. Smetana, T. Kocourek, B. Dvořánková, J. Zemek, J. Remsa, T. Luxbacher, *Materials Science and Engineering: B*, **2010**, *169*, 89.
[24] A. Voss, H. Wei, C. Müller, C. Popov, W. Kulisch, G. Ceccone, C. Ziegler, M. Stengl, J. P. Reithmaier, *Diamond Relat. Mater.*, **2012**, *26*, 60.
[25] D. Yan, C. Yang, N. T. Nguyen, X. Huang, *Electrophoresis*, **2006**, *27*, 620.
[26] J. C. W. Corbett, F. McNeil-Watson, R. O. Jack, M. Howarth, *Colloids Surf., A*, **2012**, *396*, 169.
[27] J. Corbett, F. Mcneil-Watson, R. Jack, Surface charge measurement, Patent No. WO2012172330 A1, **2012**.
[28] I. M. Tucker, J. C. W. Corbett, J. Fatkin, R. O. Jack, M. Kaszuba, B. MacCreath, F. McNeil-Watson, *Curr. Opin. Colloid Interface Sci.*, **2015**, *20*, 215.
[29] R. J. Cullen, D. R. Jayasundara, L. Soldi, J. J. Cheng, G. Dufaure, P. E. Colavita, *Chem. Mater.*, **2012**, *24*, 1031.
[30] J. M. Simmons, B. M. Nichols, S. E. Baker, M. S. Marcus, O. M. Castellini, C. S. Lee, R. J. Hamers, M. A. Eriksson, *J. Phys. Chem. B*, **2006**, *110*, 7113.
[31] P. E. Colavita, B. Sun, X. Wang, R. J. Hamers, *J. Phys. Chem. C*, **2009**, *113*, 1526.
[32] F. Zen, M. D. Angione, J. A. Behan, R. J. Cullen, T. Duff, J. M. Vasconcelos, E. M. Scanlan, P. E. Colavita, *Sci. Rep.*, **2016**, 24840.
[33] M. R. Gittings, D. A. Saville, *Colloids Surf., A*, **1998**, *141*, 111.
[34] F. Thielbeer, K. Donaldson, M. Bradley, *Bioconjug. Chem.*, **2011**, *22*, 144.
[35] F. Ganachaud, A. Elaïssari, C. Pichot, A. Laayoun, P. Cros, *Langmuir*, **1997**, *13*, 701.
[36] H. M. Rendall, A. L. Smith, *J. Chem. Soc. Faraday Trans.*, **1978**, 1179.
[37] X. L. Peng, Z. H. Barber, T. W. Clyne, *Surf. Coat. Technol.*, **2001**, *138*, 23.
[38] G. Dearnaley, J. H. Arps, *Surf. Coat. Technol.*, **2005**, *200*, 2518.
[39] E. Johansson, L. Nyborg, *Surf. Interface Anal.*, **2003**, *35*, 375.
[40] P. B. Leezenberg, W. H. Johnston, G. W. Tyndall, *J. Appl. Phys.*, **2001**, *89*, 3498.
[41] A. Zebda, H. Sabbah, S. Ababou-Girard, F. Solal, C. Godet, *Appl. Surf. Sci.*, **2008**, *254*, 4980.
[42] J. K. Beattie, *Lab Chip*, **2006**, *6*, 1409.
[43] L. S. McCarty, G. M. Whitesides, *Angew. Chem. Int. Ed. Engl.*, **2008**, *47*, 2188.
[44] H. J. Kreuzer, R. L. C. Wang, M. Grunze, *J. Am. Chem. Soc.*, **2003**, *125*, 8384.
[45] K. N. Kudin, R. Car, *J. Am. Chem. Soc.*, **2008**, *130*, 3915.
[46] R. Zangi, J. B. F. N. Engberts, *J. Am. Chem. Soc.*, **2005**, *127*, 2272.
[47] R. Zimmermann, S. Dukhin, C. Werner, *J. Phys. Chem. B*, **2001**, *105*, 8544.
[48] C. Dicke, G. Hähner, *J. Am. Chem. Soc.*, **2002**, *124*, 12619.
[49] V. Chakrapani, J. C. Angus, A. B. Anderson, S. D. Wolter, B. R. Stoner, G. U. Sumanasekera, *Science*, **2007**, *318*, 1424.
[50] A. Hartl, J. A. Garrido, S. Nowy, R. Zimmermann, C. Werner, D. Horinek, R. Netz, M. Stutzmann, *J. Am. Chem. Soc.*, **2007**, *129*, 1287.

Supporting information

Additional Supporting Information may be found online in the supporting information tab for this article.

Data S1 Supporting info item

Copyright © 2017 John Wiley & Sons, Ltd.